Optimising Molecular Radionuclide Therapy: The Role of Quantitative SPECT/CT & PET/CT and Radiation Dosimetry

Alkahtani, Tahani

Awarding institution:
King's College London

KING'S College LONDON

Optimising Molecular Radionuclide Therapy: The Role of Quantitative SPECT/CT & PET/CT and Radiation Dosimetry

Submitted by:

Tahani Omair Alkahtani

Supervisors:

Professor Valerie Lewington

Dr. Lefteris Livieratos

A thesis submitted in fulfilment of the requirements
for the degree of Doctor of Philosophy in the
School of Biomedical Engineering & Imaging Sciences
Faculty of Life Sciences & Medicine
King's College London

August 2023

Table of Contents

Declaration

I Tahani Omair Alkahtani confirm that no part of this thesis has been submitted in support of any other application for a degree or qualification of King's College London, or any other university or institute of learning. I confirm that this work is my own. Where information has been derived from other sources it has been indicated in this thesis.

Acknowledgement

List of Figures

List of Tables

List of Abbreviations

Abbreviation	Definition
CF	Calibration factor
CDR	Collimator-detector response
cm	Centimetre
CoV	Coefficient of variation
CPS	Counts per second
cRC	Concentration recovery coefficient
CT	Computerised tomography
CTCAE	Common Terminology Criteria for Adverse Events
Day (D)	Calendar day
2D	Two dimensions
3D	Three dimensions
DOTA	1,4,7,10-tetraazacyclodocecane-1,4,7,10-tetraacetic acid
DOTA-TATE	DOTA-octreotate
DOTA-TOC	DOTA-Tyr-3-octreotide
DTC	Differentiated Thyroid Cancer
^{18}F-FDG	Fluorine-18-fluorodeoxyglucose
FU	Follow-up
^{68}Ga	Radioisotope of Gallium
GBq	Giga Becquerel
GEP	gastro-entero-pancreatic
Gy	Gray
Hr	Hour
^{131}I	Radioisotope of Sodium Iodine
IAEA	International Atomic Energy Agency
ICRP	International Commission on Radiological Protection
IRMER	Ionising Radiation (Medical Exposure) Regulations
IRR99	Ionising Radiation Regulations (1999)
keV	Kilo-electron volt
^{177}Lu	Radioisotope of Lutetium
LTL	Lesion to liver
LTS	Lesion to spleen
m	Metre
MBq	Mega Becquerel
MGy	Milli Gray
MRT	Molecular Radiotherapy
µSv	Micro Sievert

mSv	Millie Sievert
MTV	Metabolic volume
NaI	Sodium iodide
NET	Neuroendocrine tumour
NEMA-IEC	National Electrical Manufacturers Association- International Electro-technical Commission
OSEM	Ordered subset of expectation maximisation
PERCIST	Positron Emission Tomography (PET) Response Criteria in Solid Tumours
PET	Positron emission tomography
PET CT	Positron Emission Tomography combined with Computerised Tomography
PRISMA	Preferred Reporting Items for Systematic Reviews and Meta-Analyses
PRRT	Peptide Receptors Radionuclide Therapy
PSMA	Prostate Specific Membrane Antigen
PVE	Partial volume effect
RAI	Radioactive iodine
RE	Relative error
RECIST	Response Evaluation Criteria in Solid Tumours
ROI	Region of interest
SPECT	Single Photon Emission Tomography
SPECT/CT	Single Photon Emission Tomography with Computed Tomography
SSA	Somatostatin Analogue
SSTR	Somatostatin receptor
SUV	Standardized Uptake Value
SUV_{mean}	Mean of Standardized Uptake Value
SUV_{max}	Maximum of Standardized Uptake Value
SUV_{peak}	Peak of Standardized Uptake Value
VOI	Volume of interest
WBS	Whole Body Scan
WHO	World Health Organisation

1st Author Abstract publications, arising from thesis work

1. *Alkahtani T, Livieratos L., Lewington V.* e-poster " Optimising Molecular Radionuclide Therapy: The Role of Patient-Led Whole-Body Retention Dosimetry ". Annual Congress of the European Association of Nuclear Medicine October 15-19, 2022, Barcelona, Spain. Eur J Nucl Med Mol Imaging 49 (Suppl 1), 1–751 (2022). Page 641. https://doi.org/10.1007/s00259-022-05924-4.

2. *Alkahtani T, Livieratos L, Lewington V.* Oral talk. " Is Quantitative Post-treatment SPECT/CT Useful to Assess Peptide Receptor Radiotherapy Response in Neuroendocrine Tumours (NETs)? ". 49th Annual Spring Meeting of the British Nuclear Medicine Society, SEC, Glasgow, UK, 16 – 18 May 2022.

3. *Alkahtani T, Livieratos L, Lewington V.* Oral talk "Patient-Led Whole-Body Retention Dosimetry in 131I-NaI Molecular Radiotherapy (MRT) for Thyroid Malignancies". 49th Annual Spring Meeting of the British Nuclear Medicine Society, SEC, Glasgow, UK, 16 – 18 May 2022.

4. *Alkahtani T, Lewington V, Livieratos L.* Oral talk " I-131 Quantitative SUV-SPECT/CT Standardisation and Validation''. European Association of Nuclear Medicine October 20-23, 2021, Virtual. Eur J Nucl Med Mol Imaging (2021). Page 230. https://doi.org/10.1007/s00259-021-05547-1.

5. *Alkahtani T, Livieratos L, Lewington V.* e-poster "Assessment of PRRT Response from SUV-SPECT & PET, Personal Dosimeter and Biochemical Metrics". European Association of Nuclear Medicine October 20-23, 2021, Virtual. Eur J Nucl Med Mol Imaging (2021).Page 467. https://doi.org/10.1007/s00259-021-05547-1.

6. *T. Alkahtani, J. Johnson, K. Adamson, V. Lewington, L. Livieratos. "*Standardisation and Validation of 177Lu Quantitative SUV-SPECT/CT*".* European Association of Nuclear Medicine October 22 – 30, 2020 Virtual. *Eur J Nucl Med Mol Imaging* 47 (Suppl 1), 1–753 (2020). Page 448. https://doi.org/10.1007/s00259-020-04988-4.

7. *Alkahtani T, Livieratos L, Lewington V.* e-poster "Neuroendocrine Tumours (NET) Quantitative SUV-SPECT/CT Change during 177Lu-DOTATATE MRT". European Association of Nuclear Medicine October 22 – 30, 2020 Virtual. Eur J Nucl Med Mol Imaging 47 (Suppl 1), 1–753 (2020). Page 688. https://doi.org/10.1007/s00259-020-04988-4.

Thesis Outline

The thesis is structured as follows:

Chapter 1 introduces molecular radiotherapy (MRT) theranostics use of ^{131}I and ^{177}Lu-DOTA-TATE, including the clinical background of neuroendocrine tumours (NET), differentiated thyroid cancer (DTC), and benign thyroid disease (Thyrotoxicosis). It describes the imaging dosimetry application of quantitative SPECT/CT and PET/CT. Finally, introduces the research significance, objectives, and null hypotheses.

Chapter 2 presents a systematic review to examine the role of quantitative SUV-SPECT/CT during ^{177}Lu-DOTA-TATE MRT to determine whether the standardised uptake value (SUV) changes in patients undergoing repeated radionuclide treatments.

Chapter 3 presents an investigation of an optimal protocols for quantitative ^{131}I and ^{177}Lu SPECT/CT by evaluating the accuracy of absolute SUV-SPECT/CT quantification using phantom measurements.

Chapter 4 then investigates the feasibility of ^{177}Lu- DOTA-TATE SUV-SPECT/CT and whether serial SUV-changes derived from quantitative SPECT/CT and PET/CT correlated with clinical response in neuroendocrine tumours (NETs). This investigation was carried out using retrospective data acquired from patients undergoing four cycles of peptide receptor radionuclide therapy (PRRT).

Chapter 5 presents a novel study on the development and feasibility assessment of dosimetry in MRT using patient-led whole-body radiation monitoring. Long-term whole-body retention data were derived from patient-led measurements combined with post-treatment early distribution planar whole-body and SPECT/CT imaging. This chapter aims to provide reliable whole-body retention and absorbed dose estimates. This investigation was carried out using

phantom, retrospective data obtained from NET patients undergoing ^{177}Lu- DOTA-TATE - PRRT and prospective data from patients with benign and malignant thyroid disease undergoing ^{131}I therapy.

Chapter 6 In this section, results of tailored radiation restrictions using patient-led data model fitting are presented for each MRT group (^{177}Lu-Dota-Tate, ^{131}I-DTC, and ^{131}I-Thyrotoxicosis). Then results of the correlation between early-prediction (8-days) and longer-term (28-day) model fitting are presented in view of a realistic clinical implementation.

Chapter 7 finally summarises the main findings and limitations described in the thesis, with recommendations for potential future work.

Abstract

Introduction/Aims:

Molecular radiotherapy (MRT) describes the use of radiopharmaceuticals to treat benign and malignant diseases. For practical reasons, MRT is conventionally prescribed as a standard administered activity regardless of differences in disease burden, disease distribution and physiology between individuals. If post-treatment imaging is performed, this is usually undertaken 24-48 hours after MRT administration, which limits the reliability of dose estimates and results in patients being provided with generic radiation safety advice. Optimising the outcome of MRT requires reliable measurement of absorbed radiation doses delivered to target tissues and healthy organs, and, from the patients' perspective, the provision of tailored radiation protection advice particularly for therapies that account for a high percentage of treatments such as [^{131}I] NaI-Sodium iodide and [^{177}Lu] Lu - DOTA-TATE.

This study aims to investigate:

- The comparative results of quantitative SPECT/CT & PET/CT imaging.
- Whether serial changes in PET and SPECT-derived standardised uptake value (SUV) are correlated in patients undergoing MRT.
- Whether combining data from early (quantitative imaging) and late (whole-body-retention data) could support individual treatment planning for patients undergoing repeated cycles of MRT.
- Whether current MRT radiation protection advice is appropriate.

Methods

1. 2D/3D-Quantitative Optimisation and Validation

We examined multiple factors to achieve optimum quantitative ^{177}Lu and ^{131}I performance using:

    a. A cylindrical homogeneous phantom was used to assess the scintillation camera calibration factor (CF) (cps/MBq).

    b. A NEMA-IEC-Body Phantom incorporating six spheres of various sizes to calculate the concentration recovery coefficients (cRC).

2. PRRT Quantitative-SUV Assessment

We analysed retrospective data from 19 patients with histologically confirmed, unresectable metastatic NETs treated with PRRT over 4 cycles. SUV_{max}, lesion-to-liver (LTL) and lesion-to-spleen (LTS) ratios were measured using ^{68}Ga-PET/CT and ^{177}Lu-SPECT/CT images.

3. Patient-Led Whole-Body-Retention and Tailored Radiation Restrictions

Patients undergoing molecular radionuclide therapy using [^{177}Lu] Lu- DOTA-TATE for PRRT and [^{131}I] NaI for benign and malignant thyroid disease therapy were included. Planar whole-body images at 24-48 hr following MRT were acquired to assess early uptake. Patient-led whole-body retention measurements obtained using a hand-held radiation monitor were used to follow the time course of radioactivity clearance in each patient for four weeks post-therapy. For tailored radiation restriction calculation, bi-exponential fitting parameters were used for NET and DTC patients and mono-exponential parameters for Thyrotoxicosis patients.

Results

HERMES-Hybrid3D-3.01 software was used to estimate CF and SUV values. ^{177}Lu and ^{131}I showed an optimal CF of 11.1 cps/MBq and 41cps/MBq, respectively, resulting in the most accurate activity. OSEM updates(iteration*subsets) for optimised activity concentration values was observed at 80-updates for ^{177}Lu and 48-updates for ^{131}I.

A significant correlation was shown between SPECT- and PET-derived SUV measurements (r_s=0.8, p<0.01). The average SPECT-SUV_{max} at cycle-1 PRRT was comparable to PET-SUV_{max} at baseline pre-PRRT (30±24 and 35±18, respectively). Following PRRT, SPECT- and PET-derived SUV_{max} reduced by 45±29% and 34±27% respectively. LTS and LTL change showed a significant, robust positive linear correlation (r_s=0.8, p<0.05) using both SPECT and PET.

A significant correlation was shown between patient-led and whole-body imaging derived whole-body retention (A_r) measurements (R=0.8, p<0.05) for all MRT groups. Patients showed variable restrictions to follow after MRT administration among the same group.

Conclusion

This study supports the following:

Quantitative-SUV estimates can be derived from I-131 and Lu-177 phantom SPECT/CT images and applied to clinical data.

Quantitative SPECT/CT was reliable in evaluating PRRT response and can be used as an early clinical response indicator between PRRT cycles.

Integrating patient-led radiation monitoring into MRT planning is feasible and is a valid dosimetry tool. The accuracy of this approach is comparable to that of serial quantitative imaging for whole-body activity estimates.

Tailored radiation restriction using patient-led whole-body retention measurements proved to be feasible to follow the time course of radioactivity clearance.

CHAPTER 1

1. Introduction

1.1. Clinical Background

Molecular radiotherapy (MRT) is the systemic administration of radiopharmaceuticals that are intended to selectively target specific tissues. Moreover, it describes the use of radiopharmaceuticals to treat benign and malignant diseases by delivering continuous, variable low dose-rate radiation to the target tissue (often a tumour). In oncology, this approach aims to deliver radiation doses directly to tumours while avoiding the irradiation of healthy organs and may also target occult disease that expresses the same uptake mechanism. A further significant advantage of MRT relative to other systemic treatments such as chemotherapy is the opportunity to perform a pre- and post-therapy scan to help plan patient-specific treatment, optimise the activity to be administered and predict the effectiveness of the therapy for a given patient (Saw, 2013).

Many radionuclides have been produced and labelled to specific compounds to perform MRT targeting specific cancer tissues. The majority of therapeutic radionuclides are beta-minus particle (β^-) emitters (e.g., phosphorus-32 [^{32}P], copper-67 [^{67}Cu], strontium-89 [^{89}Sr], yttrium-90 [^{90}Y], rhodium [^{105}Rh], iodine-131[^{131}I], promethium [^{149}Pm], holmium-166 [^{166}Ho], lutetium-177[^{177}Lu], rhenium-186 [^{186}Re], rhenium-188 [^{188}Re], gold-199 [^{199}Au]) (Table 1-1). The high energy beta particle emissions of ^{90}Y, ^{186}Re and ^{188}Re have a relatively long range of several millimetres in tissue. Therefore, energy might be delivered beyond the target, causing toxicity to healthy neighbouring tissues. In contrast, ^{177}Lu emits lower-energy, shorter range β^- particles and is less likely to damage surrounding healthy tissue (Velikyan, 2014). The most used radionuclides are ^{131}I, ^{177}Lu and ^{90}Y, the β^- particle emissions of which have a range of between 2-11 mm in tissue and maximum beta energies ($_\beta$E-max) between 0.49-2.29 MeV (Drude et al., 2017). The choice of the radionuclide that is most advantageous for therapy depends on a range of factors, including 1) radionuclide physical properties; 2) radionuclide chemical labelling properties and in vivo stability; 3) radiolabel conjugate biological half-life;

4) the resultant target (tumour) non-target (normal tissue) time-dependent localisation ratio (Carollo et al., 2015; Zaidi, 2005). In addition, radionuclides with gamma-emitting photons allow the pre and post-MRT imaging of the radiopharmaceutical's distribution to be assessed and quantified in vivo.

*Table 1-1: **Examples of radioisotopes used for MRT.***

Radioisotopes	Beta E-max($_\beta$E-max) (MeV)	Max Range in soft tissue (mm)	Gamma E-max (γE-max) (keV)	Half-Life (hr)
^{131}I	0.61	2.4	364	193
^{177}Lu	0.49	2	208	162
^{90}Y	2.28	11	-	64.1
^{186}Re	1.08	4.5	137	90.7
^{188}Re	2.21	10	155	17
^{32}P	1.71	8.7	-	342

Molecular imaging allows visual representation, characterisation, and quantification of the biological characteristics of cells and tissues within intact living organisms (Ahn, 2016). Established radiological modalities such as computed tomography (CT) can identify a tumour's location, dimensions, and relationship to adjacent anatomical structures. By comparison, molecular imaging allows non-invasive, in vivo characterisation of the molecular features of target cells and enables the visualisation, classification, and measurement of cell function (Colombo et al., 2017).

Molecular image-guided therapy is of proven value for prognosis, management planning and response monitoring. Radionuclide imaging, such as positron emission tomography (PET) and single-photon emission-computed tomography (SPECT), are the most sensitive molecular modalities that provide target-specific information about physiology, pathway activities and cell migration in the whole organism (H. Zhang et al., 2015). Both imaging methods offer clinically relevant quantitative and functional information about normal tissues and pathological conditions (Kramer-Marek & Capala, 2012).

The concept of "theranostics" in nuclear medicine describes the use of a specific targeting vector that can be labelled with either diagnostic or therapeutic radionuclides and used both for imaging and treatment. ^{131}I is the oldest and most used isotope applied for theranostics applications. This means that the same radioisotope ^{131}I serves diagnostic and therapeutic purposes based on using the same target such as the sodium iodide symporter protein (NIS). NIS expression on thyroid follicular cells allows the transport of iodine from the bloodstream to the thyroid cell cytoplasm. Moreover, NIS can transport not only iodine but also radioactive isotopes such as technetium-99m pertechnetate ($^{99m}TcO4^-$) (Choudhury & GupTa, 2018; de la Vieja & Riesco-Eizaguirre, 2021). Another example is the somatostatin receptor (SSR) because of its expression by neuroendocrine tumour cells, which serves as a foundation for targeting these receptors with synthetic octreotide somatostatin analogues (SSA) such as DOTA-Tyr3-octreotide (DOTATOC), 1-Nal3-octreotide (DOTANOC) and DOTA-(Tyr)-octreotate (DOTATATE). DOTATATE and DOTATOC are routinely chelated to gallium-68 [^{68}Ga] for PET diagnostic imaging and subsequently to ^{177}Lu for therapy (Bozkurt & Özcan, 2018; Harris & Zhernosekov, 2022; Ilan et al., 2020; Kapoor & Kasi, 2022; Poeppel et al., 2011, 2013; Thuillier et al., 2021; Velikyan et al., 2014).

Novel theranostic probes have been developed to combine imaging and therapeutic functions. In SPECT and PET, many small molecules, antibodies, receptors, and enzymes can be labelled using radioisotopes for imaging and therapy purposes, e.g., ^{68}Ga ($T_{1/2}$ = 68 minutes), zirconium-89 [^{89}Zr] ($T_{1/2}$ = 3.3 days), indium-111 [^{111}In] ($T_{1/2}$ = 2.8 days), ^{198}Au ($T_{1/2}$ = 2.69 days) (Andreou et al., 2017). The improved understanding of molecular alterations driving cancer progression has made a significant contribution toward guiding probe development and selecting the preferred target of cancer cells for imaging (Colombo et al., 2017). These challenging developments associated with theranostic SPECT and PET probes led to the initiation of MRT and optimisation of quantitative imaging and dosimetry.

The outcome of MRT depends on the absorbed radiation dose delivered to target tissues and healthy organs. For practical reasons, post-treatment imaging is rarely performed beyond 48 hours after MRT administration (European Association of Nuclear Medicine (EANM), 2017). This limits the reliability of absorbed dose and cumulative activity estimates and results in patients being provided with generic radiation safety advice based on worst-case assumptions of radiopharmaceutical retention. Personalised treatment requires the development and validation of dosimetry-based MRT, especially for therapies such as ^{131}I-iodide and ^{177}Lu-DOTA-TATE. This approach would also allow radiation protection advice to be tailored to individual patients, which might significantly improve the patient experience.

1.1.1. ^{131}I-NaI Theranostics

Sodium iodide was the first compound to meet the requirements of a theranostic using radioisotopes applicable both for diagnosis and for therapy in the 1940s (Velikyan, 2014). Saul Hertz was a prominent American radiologist who is credited with the first successful use of radioactive iodine for the treatment of hyperthyroidism. In 1941, Hertz and his team at Massachusetts General Hospital in Boston began reported successive treatment of young female with hyperthyroidism using mixture ^{130}I/^{131}I (Fahey et al., 2017). Benedict, in 1950, was the first to develop the rectilinear scanner and successfully image the thyroid gland, revealing the biological characteristics of thyroid tissues using radioiodine before the period of tomography imaging. Thus, the visualisation of the therapeutic targets of certain diseases became possible (Ahn, 2016). Radioiodine is considered a gold standard for diagnostic evaluation and therapy in radioiodine-avid thyroid disease and benign and malignant tumours.

The thyroid gland can suffer from a variety of benign or malignant diseases that can be treated using ^{131}I. Examples of benign thyroid disease include non-toxic goitre, diffuse toxic goitre

(Graves' disease), solitary autonomous nodule, multinodular change, viral and autoimmune thyroiditis. Diagnosis should be confirmed clinically by evaluating thyroid hormonal function, ultrasound scan, and nuclear medicine uptake and scan. For patients who are diagnosed with thyroid nodules and a low serum thyroid-stimulating hormone (TSH), the nodule needs to be assessed to determine whether it is functional. Thyroid scintigraphy using radioiodine (^{123}I) or technetium pertechnetate (^{99m}TcO4$^-$) is useful to determine the functional status of a nodule. This diagnostic procedure can accurately assess timed radioisotope thyroid uptake. The uptake of radioisotopes is selectively increased in hyper-functioning and low in hypo-functioning nodules (Tamhane & Gharib, 2016). ^{131}I sodium iodide can be used to treat hyperfunctioning thyroid nodules and is an alternative to surgical excision.

Malignant thyroid lesions include papillary cancer, follicular cancer, Hurthle cell (oncocytic) cancer, anaplastic cancer, medullary cancer, thyroid lymphoma, and metastases (Popoveniuc & Jonklaas, 2012; Tamhane & Gharib, 2016). ^{131}I is used mainly to treat differentiated papillary and follicular carcinomas following thyroidectomy, both to ablate normal thyroid tissue in the thyroid bed and to manage recurring and/or metastatic disease indicated by persisting detectable or elevated serum thyroglobulin (Tg) levels (>0.7µg/L). Radioiodine therapy is based on beta radiation emissions from ^{131}I that deliver a high radiation dose to functioning thyroid tissue. Patients receive a specific oral ^{131}I activity based on clinical findings and the stage of their disease (Jadvar, 2014). To reach optimal ^{131}I uptake by remnant thyroid tissue and metastatic disease, patients should be on low-iodine diet (1-2 weeks) and should undergo TSH measurement ≥30 mIU/L (1–3 day) prior to ^{131}I administration. TSH stimulation is achieved by either thyroid hormone withdrawal (THW) or recombinant human TSH (rhTSH) stimulation (Avram et al., 2022; Luster et al., 2008, 2017; Silberstein et al., 2012).

Benign and malignant thyroid diseases for which ^{131}I is a treatment option are illustrated here.

^{131}I-NaI for Hyperthyroidism Therapy (Thyrotoxicosis)

^{131}I has been employed since 1958 to treat benign thyroid disease, such as Graves' disease based on biochemical and/or clinical hyperthyroidism (Fig. 1-1).

Hyperthyroidism (hyperfunction of the thyroid gland) is a common thyroid disease that may be associated with significant morbidity, such as cardiovascular symptoms. It may also contribute to an increased incidence of circulatory mortality (Lewis et al., 2013).
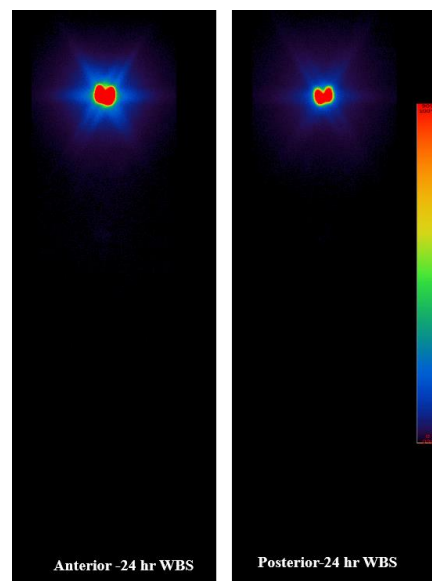
Figure 1-1: 2D whole-body scan 24-hour following 131I administration for thyrotoxicosis therapy.

At first, ^{131}I therapy was used to achieve a euthyroid state using low or adjusted activity regimens; however, RAI outcome can be affected by several factors such as disease aetiology and goitre size. Consequently, an alternative approach would   administer a high ablative ^{131}I activity in early hyperthyroidism with the intention of establishing rapid hypothyroidism treated with long-term thyroid hormone replacement. This was confirmed by Lewis et al. (2013) after treating 449 hyperthyroidism patients with a fixed activity of ^{131}I 550 MBq, which resulted in 94% of the patients being cured after the first dose, whereas 6.7% required further radioiodine (Lewis et al., 2013). Fixed-activity methods are usually based on an estimation of the size of the thyroid by palpation, ultrasound, or nuclear medicine radioiodine (^{123}I) or

technetium pertechnetate ($^{99m}TcO4^-$) uptake and scan. The range of activities prescribed in the UK, regardless of the rationale used, varies between 200 and 800 MBq, 400–600 MBq being most widely used (Stokkel et al., 2010).

In general, benign nodules do not require specific intervention unless they cause compressive symptoms from significant enlargement, such as dysphagia, choking, shortness of breath, hoarseness, or pain, in which case surgical intervention (partial or complete thyroidectomy) should be performed. In addition, the presence of single or multinodular goitre might be an indication for surgery. Radioiodine therapy needs to be approached with caution in individuals with uncontrolled thyrotoxicosis (Popoveniuc & Jonklaas, 2012), and it is often advisable to achieve biochemical control using antithyroid drugs prior to administering I-131 (Stokkel et al., 2010). ^{131}I therapy can be used to treat toxic nodular goitres; however, they are frequently more radioresistant than toxic diffuse goitres and may therefore require higher administered activities to achieve biochemical euthyroidism (Silberstein et al., 2012).

^{131}I-NaI for Differentiated Thyroid Cancer (DTC) Ablation and Recurrent Therapy

Thyroid cancer is the most common endocrine malignancy and is ranked seventh among the most frequently diagnosed cancers in females. In Europe, the incidence of thyroid cancer is three times higher in females than males. The estimated ten-year relative survival from 86,690 adult thyroid cancer patients (29 European countries) was 89% in women and 79% in men (Dal Maso et al., 2017).

Cancer of the thyroid gland may be primary (arising from follicular or papillary cells within the thyroid gland) or secondary due to malignant cells that have spread from other tissues. Medullary thyroid cancer arises from para-follicular cells, secrete calcitonin (Nussey S., 2001). As medullary tumours do not express NIS, radioiodine has no role in post operative management.

A study by Ahn (2016) in patients with papillary and follicular DTC reported that radioiodine-avid metastatic lesions on imaging predicted a high probability of favourable response after ^{131}I therapy. In contrast, patients who had a radioiodine non-avid metastasis on nuclear medicine imaging had progressive disease after ^{131}I treatment (Ahn, 2016).

[123]I/[131]I 2D whole-body as shown in figure 1-2 and 3D SPECT/CT pre-therapy scanning can be used to assess iodine-avidity prior to planned ^{131}I radionuclide therapy of thyroid cancer (Haddad et al., 2022). [124]I-PET/CT has theoretical advantages offering accurate localisation and quantification of iodine-concentrating tissue, which is required for disease staging, dosimetry, and therapeutic dose planning (de Pont et al., 2013; Freudenberg et al., 2008; Khorjekar et al., 2014; Velikyan, 2014) but is not advised for routine use internationally. In the UK, ^{131}I-NaI is administered orally with a fixed activity of 1–5 GBq for DTC ablation; however, multiple centres empirically support the use of 1.11, 1.85, or 3.7 GBq (Luster et al., 2008). There are several approaches to the selection of ^{131}I activity. According to the joint European Association of Nuclear Medicine (EANM) and Society of Nuclear Medicine and Molecular Imaging (SNMMI) guidelines (2022),[131]I activity for post-thyroidectomy ablation of thyroid bed remnants is prescribed in the range of 1.11–3.7 GBq (30–100 mCi); 3.7-5.6 GBq (100-150 mCi) for treatment of small volume locoregional disease and 5.6–7.4 GBq (150–200 mCi) for treatment of advanced locoregional disease and/or small-volume distant metastatic disease. Activities of ≥7.4 GBq (200 mCi) are administered for treatment of known distant metastases, empirically or guided by dosimetry calculations (Avram et al., 2022).

In a retrospective study, 1,229 DTC patients were treated with [131]I. Complete response was achieved with a median cumulative activity of 3700 MBq (range 970 to 47,900 MBq) (Thies et al., 2014). When complete remission was achieved after the first ^{131}I ablative therapy, the risk of recurrence was low.
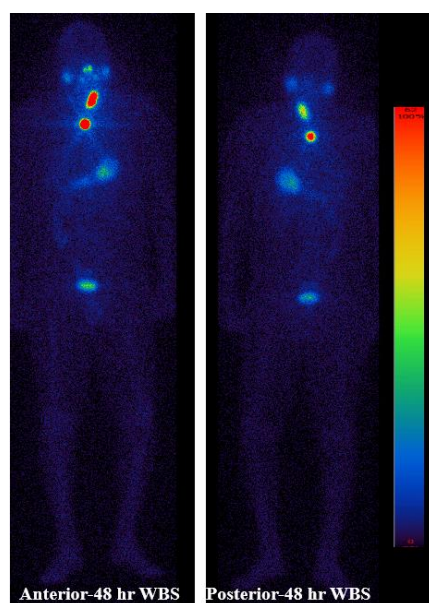
Figure 1-2: 2D whole-body scan 48-hour following 131I administration for thyroid cancer ablation therapy.

Klubo-Gwiezdzinska et al. (2011) addressed the issue of using dosimetry-based instead of empirically prescribed ^{131}I activity. Based on their results, which confirmed the greater effectiveness of dosimetry-based prescribed RAI ablation with a similar safety profile as the empiric alternative, they recommended employing individually prescribed activity in DTC patients with distant metastases and local advanced disease (Klubo-Gwiezdzinska et al., 2011). Ma et al. (2005) confirmed the recommendation for individualised RAI prescription based on clinical characteristics, reporting that it could be justified in DTC patients with Tg levels <10 µg/L, a negative whole-body scan, and a high risk of recurrence (Ma et al., 2005).

Zidan et al. (2004) suggested that patients with DTC receive an optimum activity of ^{131}I therapy with a successful ablation rate of 94% (95% CI: 89–100%) if the ^{131}I activity is calculated based on the percentage of residual neck uptake on 24-hour diagnostic whole-body imaging (Zidan et al., 2004).

5–15% of treated patients become refractory to RAI; the 5-year survival rate among these refractory patients is 66%, and the 10-year survival rate is approximately 10% (Wang et al., 2016).

1.1.2. ^{177}Lu-DOTA-TATE Therapy for NETs

Diagnosis

The World Health Organisation (WHO) defined neuroendocrine neoplasms (NENs) as an abnormal growth with recognised neuroendocrine differentiation and biomarkers expressing normal neuroendocrine cells or neurons. The new classification of NENs proposed by the WHO (2022) was based on a differentiation and proliferation grading system. NENs classified as epithelial well-differentiated neoplasms are defined as neuroendocrine tumours (NETs) whereas poorly differentiated neoplasms are defined as neuroendocrine carcinomas (NECs). Generally, NETs over express surface somatostatin receptors (SSTR), and exhibit immunohistochemical staining for several antibodies (INSM1), synaptophysin and chromogranin A, chromogranin B and/or chromogranin C being more variable. By contrast, NECs typically demonstrate lower expression of SSTR and are often not targetable for PRRT (Rindi G. et al., 2022).

Many NETs first appear in the lungs or the gastrointestinal tract, including the stomach, pancreas, appendix, intestines, colon, and rectum. NETs can also arise from the thymus, thyroid gland, adrenal gland, and pituitary gland (American Cancer Society, Accessed 08 August 2022).

Previously, NETs were referred to as carcinoid tumours; today the term 'carcinoid' refers to specific NETs of the small bowel that secrete 5-hydroxytryptamine and NETs of the lung. The slow growth of most well differentiated NETs leads to late detection by which time most have already metastasised. The characteristics of NETs define the therapy method and prognosis, key characteristics being tumour location, grade, differentiation, stage, and hormone secretory profile.

Nuclear Medicine imaging of NETs is based on radiolabelled SSR analogues composed of a radioisotope and SSA linked together by chelator. The first SSR scintigraphy used the gamma-emitter radioisotope, indium [^{111}In]^{111}In-DTPA (diethylenetriamine pentaacetate)-D-Phe-1-octreotide. This was followed by the development of gallium-68 SSR- PET compounds such as ^{68}Ga-DOTATOC, ^{68}Ga-DOTATATE, and ^{68}Ga-DOTANOC, which have varying affinity to different SSRs (Kapoor & Kasi, 2022; Navalkissoor et al., 2017; Yang et al., 2014).

^{68}Ga-DOTA-TATE exhibited a sensitivity of 96% compared with 65% for ^{111}In-pentetreotide (Srirajaskanthan et al., 2010). Kayani et al. (2009) reported that ^{68}Ga-DOTA-TATE was more sensitive for detecting typical pulmonary NETs than fluorine-18-fluorodeoxyglucose (^{18}F-FDG). In contrast, atypical carcinoid and higher-grade tumours had lower uptake of ^{68}Ga-DOTA-TAE compared with ^{18}F-FDG (Kayani et al., 2009) reflecting poor SSR expression.

^{68}Ga-DOTA-TATE has higher sensitivity for low-grade tumours and greater avidity for well-differentiated NETs than FDG, ^{18}F-FDG uptake being typically low for tumours with a low proliferation index, slow growth rate, and low glucose consumption, such as well differentiated NETs (Saw, 2013).

Therapy

Peptide-receptor radionuclide therapy (PRRT) is an effective treatment for advanced, well-differentiated NETs, the majority of which express elevated levels of SSR to which somatostatin analogues (SSA) bind (Fig. 1-3).

The main three identified PRRT radiopharmaceuticals used for the treatment of NETs are described in the following section (Bodei et al., 2016).
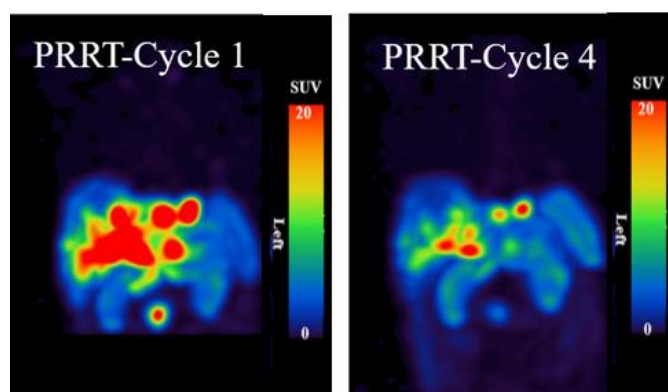
Figure 1-3: Maximum-intensity projection (MIP) SPECT/CT images 24-hour following administration of 177Lu-DOTA-TATE at PRRT-cycles 1and 4. Multiple NET lesions showed decreased somatostatin expression after four cycles of PRRT.

- ### ^{111}In-Pentetreotide (PRRT)

In the 1990s, ^{111}In-pentetreotide underpinned the development of PRRT by transforming a diagnostic into a therapeutic approach. The foundation of this approach reflects the internalisation of the peptide or receptor complex, exploiting the cytotoxic effects of Auger and conversion electrons emitted by ^{111}In which decayed in close proximity to the cell nucleus. However, as a consequence of the development of tetra-azacyclododecane-N,N′,N″,N‴-tetra-acetic acid-chelated octreotide, β-emitting radiolabels, such as the pure β-emitter ^{90}Y, with higher energy and longer particle range emerged as a preferred choice.

- ### ^{90}Y-Somatostatin Analogues (PRRT)

In 1996, (^{90}Y-DOTA^0, Tyr^3)-octreotide, ^{90}Y-DOTATOC, or ^{90}Y-octreotide were primarily used for the treatment of metastatic NETs. [90]Y appeared to be a more suitable radiolabel than ^{111}In for PRRT due to high-energy β emission (maximum energy $E_{\beta max} = 2.27$ MeV, penetration range $R_{\beta max} = 11$ mm, and half-life $T_{1/2} = 64$ h). Based on promising preliminary results, ^{90}Y-octreotide became the most used radiopeptide for PRRT in the early 2000's.

- ### ^{177}Lu-Somatostatin Analogues (PRRT)

In 2000, octreotate (Tyr^3, Thr^8-octreotide) was introduced as a newly developed analogue that exhibited a six- to nine-fold higher affinity for somatostatin receptor subtype 2 (SSTR2), which is commonly expressed by the majority of NETs. To mitigate renal retention and reduce the

risk of nephrotoxicity, the chelated analogue [DOTA]^0-Tyr^3-octreotate, or DOTA-TATE, was radiolabelled with a dual β-γ-emitter (^{177}Lutetium) ($E_{\beta max}$ = 0.49 MeV, $R_{\beta max}$ = 2 mm, and $T_{1/2}$ = 6–7 days) rather than ^{90}Y. The gamma emission allowed scintigraphy images and dosimetry studies to be performed simultaneously. For these reasons, ^{177}Lu- DOTA-TATE is the most widely used radiopeptide in PRRT today (Strosberg et al., 2017, 2021).

^{177}Lu-DOTA-TATE is a radiolabelled SSA consisting of a radionuclide (^{177}Lu) and a peptide–chelator complex [DOTA0, Tyr3-]-octreotate (DOTA-TATE). Tyr3-octreotate binds to malignant cells that overexpress SSTR2. Once bound, ^{177}Lu-DOTA-TATE accumulates within the tumour cells, delivering cytotoxic radiation that kills them. The standard protocol for administering ^{177}Lu-DOTATATE is through an intravenous infusion followed, in most centres by 24 hours whole-body ± SPECT/CT scan. Typically, four treatment cycles are administered over a total of 8–10 months (Mujica-Mota et al., 2018).

In the NETTER-1 phase 3 trial (2017), investigators compared ^{177}Lu-DOTATATE (four cycles at 8-week intervals of 7.4 GBq [200 mCi] of ^{177}Lu- DOTA-TATE infused intravenously for 30 minutes with cumulative radioactivity, 29.6 GBq [800 mCi]), plus 30 mg octreotide long-acting release (LAR) 4 weekly, with monthly injections of 60 mg octreotide LAR in patients with progressive small bowel NETs. This study concluded that ^{177}Lu- DOTA-TATE therapy led to significantly longer progression-free survival than high-dose octreotide LAR and was associated with limited severe toxic effects among the study population (Strosberg et al., 2017, 2021) .

A retrospective study was conducted on 68 patients diagnosed with advanced well-differentiated pancreatic neuroendocrine tumours (pNETs). The study demonstrated the effectiveness of PRRT with [^{177}Lu-DOTA^0, Tyr^3] octreotate for treating advanced Grade 1 and

2 pNET, with median overall survival (OS) and progression-free survival (PFS) of 53 months and 34 months, respectively (Ezziddin et al., 2014).

Bergsma et al. (2016) reported that the incidence of subacute haematological toxicity post-PRRT with ^{177}Lu-DOTATATE was low (11%). Furthermore, they concluded that the bone marrow dose limit of 2 Gy adopted from ^{131}I does not appear to be applicable to PRRT with ^{177}Lu-DOTATATE (Bergsma et al., 2016).

The NETTER-1 Phase-3 trial investigated the incidence, severity, and reversibility of long-term hematotoxicity in a large cohort of patients (n=116) undergoing PRRT with ^{177}Lu-DOTATATE. The trial reported grade 3 or 4 neutropenia (1%), thrombocytopenia (2%), and lymphopenia (9%) (Strosberg et. al., 2017, 2021).

PRRT is performed using 7.4 GBq (150-200 mCi) ^{177}Lu-DOTATATE-octreotate per treatment cycle, aiming for 4 cycles with standard intervals of 8 weeks. Amino acid, such as L-lysine and/or L-arginine, should be infused 30-60 min before PRRT to reduce the high kidney retention of radiopeptides and maintained for 4 hours post-PRRT. Prior to amino acid infusion, antiemetics (e.g., ondansetron) should be injected intravenously to prevent nausea and vomiting. Corticosteroid (e.g., Dexamethasone) may be administered post-^{177}Lu-DOTATATE to reduce inflammation and swelling of the liver in patient with bulky or diffuse disease (Bodei et al., 2013).

1.1.3. Imaging Dosimetry for MRT

In molecular radionuclide therapy, radiation dosimetry may involve: 1) use of quantitative imaging, including appropriate corrections for photon attenuation, scatter, camera limitations; 2) image analysis, such as image registration, image segmentation, and classification of normal tissue structures and tumours in the images; and 3) application of modelling to data obtained

from images acquired at different time-points to calculate the total amount of deposited radiation energy during the whole course of treatment (Ljungberg & Sjögreen Gleisner, 2016). The development of the Response Evaluation Criteria in Solid Tumours (RECIST 1.0) guidelines in 2000 and their revised version (RECIST 1.1) in 2009 were additional evolutionary steps for more robust treatment response appraisal schemes. However, neither RECIST 1.0 nor RECIST 1.1 criteria included functional assessment because the working group felt that there was still insufficient standardisation and access to imaging technologies, such as PET, to merit such inclusion (Jadvar, 2014). PERCIST (PET Response Criteria in Solid Tumours) is a set of criteria specifically designed for assessing tumour response using PET scans with FDG (Fluorodeoxyglucose) as the radiotracer. Unlike RECIST, which primarily focuses on tumour size changes, PERCIST considers the metabolic activity of the tumour. It evaluates changes in the standardized uptake value (SUV) of FDG uptake in the tumour and surrounding tissues Joo Hyun et al., 2016).

MRT delivers continuous, variable, low-dose rate radiation to normal and target tissues such as tumour. Response to MRT is influenced by numerous factors, such as the perfusion of the tumour, the affinity of the vector, the cellular washout rate, and the half-life of the radionuclide. Dose rate increases during the uptake phase and decreases afterwards, which requires the determination of a time–activity curve.

2D quantitative whole-body planar imaging

Planar imaging can be used to measure the whole-body clearance and retention of radiopharmaceuticals over several days post-therapy. A two-dimensional (2D) quantitative approach has been applied to produce quantitative data from whole-body planar images (Bailey et al., 2015). However, the accuracy of 2D quantification from planar images is limited, with high systematic errors despite the application of scatter and attenuation correction (Hänscheid et al., 2018; Zimmerman et al., 2017).

3D Quantitative SPECT/CT

Nuclear medicine provides a means of evaluating the biological function of cells and organs, producing 3D images of the bio-distribution of radiopharmaceuticals into the patient's body. Both SPECT and PET imaging techniques examine the uptake of radiolabelled molecules in regions of interest, revealing metabolic and functional information in vivo. The most recent technological advances in image processing software applied to SPECT/CT and PET/CT incorporate iterative reconstruction algorithms with attenuation and scatter correction to facilitate accurate, non-invasive quantitative imaging. These data can be applied to calculate the activity uptake in areas of interest in absolute or relative units of activity concentration.

One of the key differences between SPECT and PET is how emitted photons are attenuated. In SPECT, the distinguished photon event rate is a combination of both the unknown strength of each single-point source emitter of gamma rays and its attenuation through the object from source to detector. This led to the first implementation of an estimated algorithm for photon attenuation correction using filtered back-projection image reconstruction for SPECT by Chang. Chang's attenuation correction is based on the linear attenuation coefficient (μ) of the tissue being imaged calculated using a computed tomography (CT) transmission scan. Today, attenuation correction is performed using a CT scan, which provides an anatomical image of the body that can be used to correct for attenuation of the PET and SPECT signals caused by tissue. The CT image is co-registered with the PET and SPECT images, and the attenuation correction factors are applied to the SPECT and PET images data during reconstruction to compensate for attenuation caused by the body tissue. In PET, the two emitted photons post-annihilation both pass through the full cross-sectional thickness of the body before detection (Bailey & Willowson, 2013).

Sanders et al. (2015) reported that complete quantification of ^{177}Lu in patients for the purpose of personalised SPECT/CT PRRT dosimetry is achievable and that upcoming efforts to

improve physics modelling and facilitate the clinical workflow will only develop this capability. In their project, they applied the quantification protocol established for [99mTc] SPECT/CT to [177Lu] to quantify the radioactivity concentration in small spheres contained within a sphere phantom. They then validated the in vivo applicability of the method in patients by comparing radioactivity concentrations resulting from quantitative SPECT/CT to urine concentrations measured in vitro (Sanders et al., 2015).

Regarding [177Lu], several studies have investigated the accuracy of quantitative SPECT/CT using different reference geometries to calibrate the system. Concentration recovery coefficients (cRCs), coefficient of variation (CoV), and correction factor (CF) or sensitivity comprised the reference geometry used for 3D SPECT/CT quantification (Hippeläinen et al., 2016; Mezzenga et al., 2017; Zhao et al., 2018).

Dosimetry data calculated from 3D images increases the accuracy of dose estimates. Imaging at multiple time points such as 4-, 24-, and 96-hours post-injection is recommended (Ahn, 2016; Emmett et al., 2017). While feasible for research purposes, this approach is too resource intensive and onerous for patients to be applied in routine practice. We hypothesise that data derived from home-based, patient-led dose rate monitoring could be combined with a single post-treatment scan to provide reliable absorbed dose estimates for normal and abnormal tissues.

3D Quantitative PET/CT

Quantitative PET can be used to measure the intensity of positron-emitting radionuclide-labelled radiopharmaceutical uptake in a volume of interest (Verburg et al., 2017). For [18F]-FDG, the standardised uptake value (SUV) is a recognised surrogate of tissue function in a region of interest and is defined mathematically as the concentration of the radionuclide in the volume of interest divided by the injected activity normalised to the patient's body weight,

usually total body weight or lean body mass (Kozak et al., 2005). Elevated SUVs derived from ^{18}F-FDG PET are likely to correspond to pathological conditions, from inflammation and infection to cancer, with higher values being suggestive of cancer (D'Arienzo & Cox, 2017; Jadvar, 2014). While various SUV-related parameters have been recommended (e.g., SUVmax, SUVmean, SUVpeak), SUVmax is considered the most useful in routine clinical practice. It is essentially a single-pixel value in the region of interest that most likely reflects the most metabolically active component of the region of interest (usually tumour) (Verburg et al., 2017). SUV_{max} changes can be monitored on pre- and post-treatment ^{68}Ga-DOTA-TATE PET scans and used to assess treatment response (Opalińska et al., 2022, Sharma et al., 2019). We hypothesise that this may also be true of serial post-therapy SPECT scans.

Although SUV_{max} may be affected by image noise, it has been widely used in PET literature because of its simplicity and low interobserver inconsistency (Jadvar, 2014). In molecular imaging, quantitation is useful for the evaluation of therapeutic response, such as the assessment of biodistribution as a potential means of determining a lesion and healthy tissue dosimeter following radionuclide therapy (Beauregard et al., 2011). In addition to SUV, other factors, such as the signal-to-noise ratio (SNR), noise-bias curve, and normalised mean-square error (NMSE), affect the accuracy of quantitative PET/CT (Lu et al., 2019).

1.2. Research Significance

For practical reasons, MRT is conventionally prescribed empirically as a standard administered activity regardless of differences in disease burden, disease distribution, and physiology between individuals. Evidence to support personalised activity prescription is very limited. Current evidence showed the effectiveness of dosimetry-based high-activity ^{131}I individualisation compared to the empirical use of MRT (Verburg et al., 2017).

This research will examine how differences in disease burden and distribution influence radiopharmaceutical kinetics and the absorbed dose delivered to normal and abnormal tissues. We will explore how patient-led radiation monitoring can be integrated into treatment planning, dose calculation, outcome assessment, and radiation protection guidance.

In this study, we will use imaging to measure the early distribution of targeted MRT drugs and combine this information with long-term retention data obtained from recordings taken by patients at home using a patient-led radiation monitor. The patient-led monitor is a mobile phone-sized, hand-held Geiger counter (ATOMTEX model AT6130, Belarus). Patients will be taught to operate the monitor and instructed to record their external dose rate at a fixed geometry twice daily after MRT. Measurements will commence immediately following treatment administration and continue for 28 days. Patient-acquired dose rate readings will be integrated with quantitative post-treatment images to obtain absorbed radiation dose estimates. This data will provide a unique, personal record of long-term radiation exposure following MRT and will allow radiation protection advice to be tailored to an individual patient's physiology. Patient-led data, if used in combination with sparse imaging and pharmacokinetic modelling, may replace the requirement for multiple time-point imaging for dosimetry purposes. In addition to improving convenience, this is especially relevant to reducing the risk of repeated hospital visits during the coronavirus (COVID-19) pandemic.

1.3. Research Objectives and Outcomes

Primary Objective	Endpoint
• To assess the feasibility of quantitative SPECT/CT and PET/CT imaging.	• Development and validation of SPECT quantification method (using a phantom study).
• To combine quantitative SPECT/CT imaging with post-treatment, patient-led, whole-body dose rate measurements to support individual MRT treatment planning.	• Comparison of SPECT quantification changes during therapy. • Comparison of pre- and post-therapy gallium PET-derived SUVmax. • Evaluation of changes in MRT uptake/retention after repeated therapy as a surrogate response indicator. • Integration of patient-led dose rate measurements with post-treatment 3D SPECT/CT and 2D whole-body scan imaging data.

Secondary Objective	Endpoint
• To apply patient-led, whole-body dose rate measurements to provide personalised radiation protection advice for patients undergoing MRT.	• Comparison with gamma camera-derived whole-body retention. • Evaluation of sequential dose rate changes after repeated treatment. • Evaluation of the consistency of patient-led self-radiation monitoring data.
• To evaluate the reproducibility and acceptance of patient-led self-radiation monitoring.	• Assessment of patient satisfaction (patient-led questionnaire).

Keynote Outcomes

Quantitative SPECT and PET:

Determine the potential of monitoring MRT impact prospectively based on post-treatment quantitative imaging.

Patient-led:

Impact of patient-led external dose rate monitoring versus standard, generic, post-treatment radiation protection advice in terms of restriction duration and patient satisfaction.

1.4. Research Null- Hypotheses

Quantitative SUV Null-Hypothesis:

1. PRRT Cycle 4 lesion SUV-SPECT does not change from Cycle 1.

2. There is no correlation between SUV-max, mean, and peak.

3. Lu- DOTA-TATE SPECT functional volume change (target and non-target structures) defined using relative to maximum threshold does not correlate with anatomical volume change.

4. PRRT of the normal organ (liver, kidneys, and spleen) SUV-SPECT does not change between PRRT-Cycle 1 and Cycle 4.

5. SUV-SPECT following PRRT Cycle 1 and Cycle 4 does not correlate with changes in biochemical metrics.

6. SUV-SPECT changes during PRRT do not correlate with SUV-PET pre- and post-PRRT changes.

7. ^{68}Ga- DOTA-TATE SUV-PET pre- and post-MRT does not correlate with changes in biochemical metrics.

Patient-led Dosimetry Null Hypothesis:

1. ^{177}Lu- DOTA-TATE and I-131 MRT whole-body dosimetry from patient-led measurements do not correlate with the whole-body dose derived from a single time-point whole-body scan detailed dosimetry.

2. ^{177}Lu- DOTA-TATE and I-131 MRT whole-body dosimetry from patient-led measurements do not correlate with 2-metre external dose rate measurements.

3. Patient-led measurements do not introduce any changes to generic radiation restrictions.

4. Patient-led non-linear curve regression for eight days do not correlate with 28 days curve fitting parameters.

5. Patients do not accept using patient-led recording for 28 days.

CHAPTER 2

2. Quantitative SUV-SPECT/CT to Assess Response of Neuroendocrine Tumours (NET) to PRRT: A Systematic Review

Abstract

Aim/Introduction: Quantitative molecular imaging for NET response assessment is performed before, after and during peptide receptor radiotherapy (PRRT). SPECT/CT imaging is used to verify radiopharmaceutical distribution in patients undergoing PRRT. However, evidence of the role of image quantification in monitoring changes induced by PRRT is limited. This systematic review aims to examine the role of quantitative SUV-SPECT/CT during ^{177}Lu-DOTA-TATE PRRT to determine whether the standardised uptake value (SUV) changes in patients undergoing repeated radionuclide treatments.

Method: A systematic review was conducted following PRISMA guidelines. The data sources were MEDLINE/PubMed of relevant articles from May 2016 to October 2022. The inclusion criterion was quantitative SUV-SPECT/CT performed during NET ^{177}Lu-DOTA-TATE PRRT. For data extraction and analysis, three reviewers screened the records independently for eligibility. The first reviewer extracted all data, and the other two reviewed the data for accuracy. Abstracts of 455 records were screened, and 423 were excluded due to non-relevance to the main scope; the full text of 32 papers were retrieved and assessed for eligibility (two systematic reviews and 30 original papers). Most of the papers (n=31) assessed the absorbed dose for renal, normal organs, and NET lesions. Only one original paper investigated changes in SUV metrics during ^{177}Lu-DOTA-TATE PRRT.

Results: Included study (n=1), published in 2021, investigated the SPECT and PET parameters including SUV_{max}, averaged SUV_{max}, SUV lesion to liver and lesion to spleen ratio, and metabolic volume. They reported a strong Pearson correlation between ^{177}Lu and ^{68}Ga SUV_{max}, SUV_{peak}, and SUV_{mean} (r = 0.79, 0.84, and 0.79 respectively). The authors concluded that SPECT and PET SUV_{peak} should be considered the most valuable metrics to assess responses to PRRT that are least affected by MTV.

Conclusion: There is a need to initiate a quantitative SUV-SPECT/CT protocol in PRRT describing the acquisition and processing factors toward optimisation. Investigating the role of SUV- 177Lu-DOTA-TATE change during PRRT as a response to therapy metrics is urgently needed.

2.1. Introduction

Specific therapies for inoperable NETs include peptide receptor radionuclide therapy (PRRT), which has provided effective treatment for advanced, well-differentiated tumours. The majority of NETs express elevated levels of somatostatin receptors to which somatostatin analogues bind.

^{177}Lu-DOTA-TATE was approved by the European Medicines Agency (EMA) in 2017 (EMA, 2017) and the United States of America (USA) Food and Drug Administration (FDA) in 2018 to treat somatostatin receptor (SSTR) positive metastatic NETs. It is a radiolabelled somatostatin analogue (SSA) consisting of a radionuclide Lutetium-177 (^{177}Lu) and the peptide–chelator complex [DOTA0, Tyr3-]-octreotate (DOTA-TATE) (Hennrich & Kopka, 2019). The (Tyr3)-octreotate complex binds to malignant cells that overexpress SSTR subtype 2. ^{177}Lu has a physical half-life of 160 h and maximum beta particle range of 2mm in tissue; it also emits gamma photons 208keV 11% and 113keV 6.4% (Strosberg et al., 2017,2021).

Once bound, the ^{177}Lu-DOTA-TATE accumulates within the tumour cells, delivering cytotoxic radiation. The standard protocol for the administration of ^{177}Lu-DOTA-TATE is by intravenous infusion. Typically, four cycles are administered over a total of 8 to 10 months (Mujica-Mota et al., 2018).

Currently, several types of quantitative molecular imaging for NET diagnosis and molecular response assessment can be performed before and after PRRT. Pre and post treatment PET is the most useful quantitative tool to assess molecular response. The PET scanner is fundamentally capable of generating cross-sectional images in units of $kBq.ml^{-1}$ (Bailey & Willowson, 2013). It uses the standardised uptake value (SUV) as a marker for quantitative data. Known as a surrogate of tissue function in a region of interest, SUV is defined mathematically as the radionuclide concentration in a volume of interest divided by the injected

activity normalised for the patient's body weight (usually total body weight or lean body mass) (Kozak et al., 2005). Elevated ^{18}F-FDG SUV values in PET imaging are likely to correspond to pathological conditions, from inflammation to infection to cancer, with higher numbers suggestive of cancer (D'Arienzo & Cox, 2017; Jadvar, 2014).

The role of SPECT/CT derived SUV as a quantitative means of assessing response to PRRT has not been extensively investigated. The primary objective of this review was to determine the role of quantitative SUV-SPECT/CT for NET molecular response assessment over the course of 4 ^{177}Lu-DOTA-TATE treatment cycles.

2.2. Methods

This systematic review followed PRISMA guidelines as presented in figure 2-1 (Page et al., 2021). We included all original and systematic review papers published in English between 21st June 2016 and 13th October 2022 (the last 6 years).

2.2.1. Eligibility criteria

To be eligible, patients in the studies were required to meet all of the following criteria: 1) 18 years or older with metastasised, inoperable NETs, 2) received ^{177}Lu-DOTA-TATE MRT, and 3) subjected to quantitative SUV analysis using SPECT/CT. Records were identified from MEDLINE/PUBMED (Accessed 13/10/2022 https://pubmed.ncbi.nlm.nih.gov/advanced/).

2.2.2. Search strategy

The search query covering the field of titles and abstracts was:

1- Search for free and none free access full text ((((((("quant*"[Title/Abstract] OR "suv"[Title/Abstract] OR ("standard*"[All Fields] AND "uptake value"[Title/Abstract])) AND

"SPECT"[Title/Abstract]) OR "single photon emission tomography"[Title/Abstract]) AND "dota*"[Title/Abstract] AND "net"[Title/Abstract]) OR "neuroendocrine tumo*"[Title/Abstract]) AND "lu"[All Fields] AND "2016/06/21 00:00":"3000/01/01 05:00"[Date - Publication]) AND ((ffrft[Filter]) AND (fft[Filter]))

2- Search for free access full-text only (((((("quant*"[Title/Abstract] OR "suv"[Title/Abstract] OR ("standard*"[All Fields] AND "uptake value"[Title/Abstract])) AND "SPECT"[Title/Abstract]) OR "single photon emission tomography"[Title/Abstract]) AND "dota*"[Title/Abstract] AND "net"[Title/Abstract]) OR "neuroendocrine tumour*"[Title/Abstract]) AND "lu"[All Fields] AND "2016/06/21 00:00":"3000/01/01 05:00"[Date - Publication]) AND (fft[Filter])

3- Search for abstracts only ("quant*"[Title/Abstract] OR "suv"[Title/Abstract] OR ("standard*"[All Fields] AND "uptake value"[Title/Abstract])) AND ("SPECT"[Title/Abstract] OR "single photon emission tomography"[Title/Abstract]) AND "dota*"[Title/Abstract] AND ("net"[Title/Abstract] OR "neuroendocrine tumo*"[Title/Abstract]) AND "lu"[All Fields] AND "2016/06/21 00:00":"3000/01/01 05:00"[Date - Publication]

All studies including adults ≥ 18 years of age, male and female, diagnosed with a NET and eligible for PPRT using ^{177}Lu-DOTA-TATE, and response to therapy outcome assessed using quantitative SUV-SPECT/CT were included in this search. We excluded studies with patients that did not match all inclusion criteria, such as phantom studies or those focussing on normal organs and tumour absorbed dose calculation.
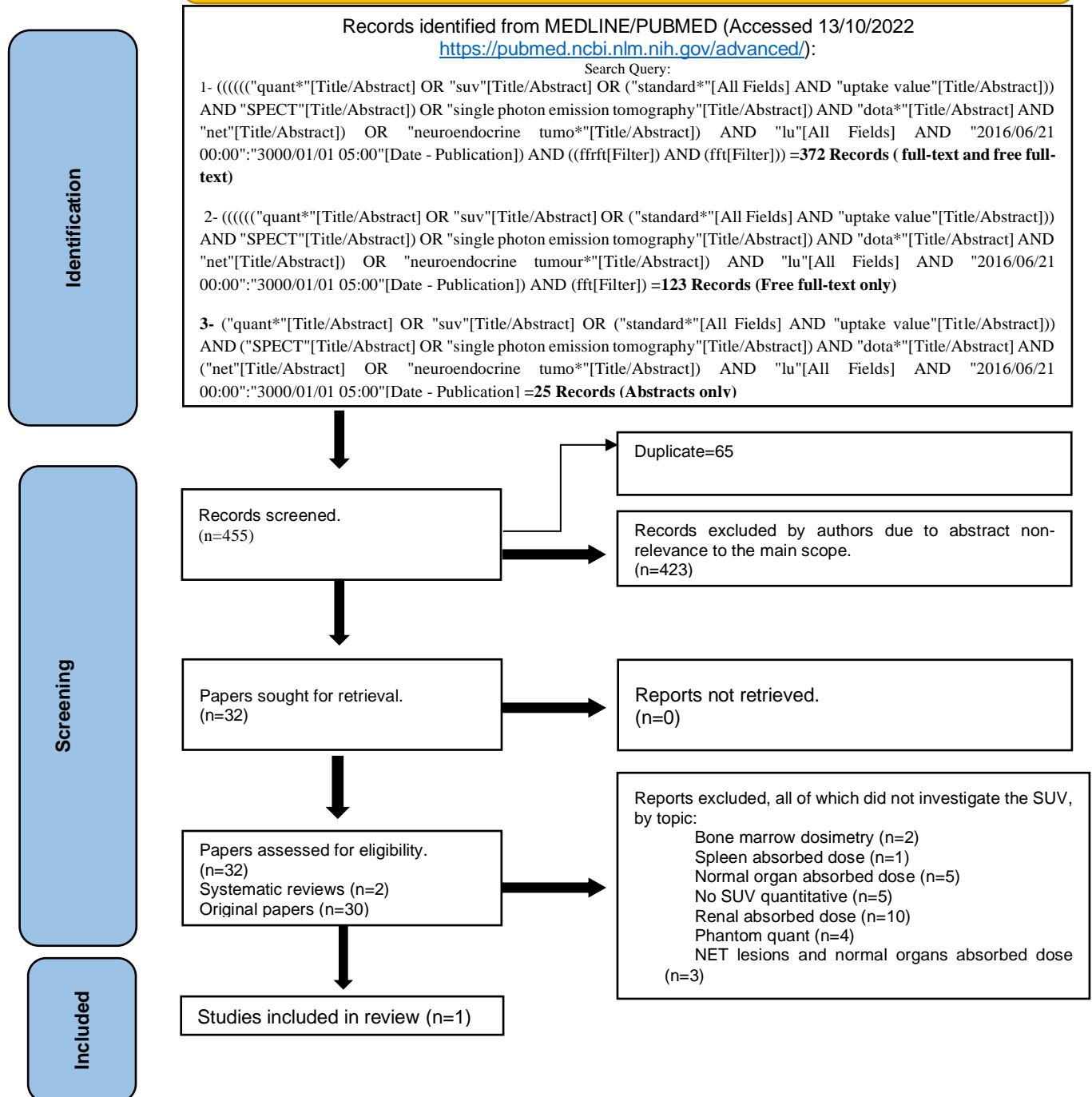
Figure 2-1: Search method using PRISMA flow diagram.

2.2.3. Data extraction and analysis

All reviewers screened the records independently for eligibility. T. Alkahtani extracted all data, and two other reviewers (L. Liveratos and V. Lewington) reviewed the data for accuracy. Abstracts of 455 records were screened, and 423 excluded due to non-relevance to this review's main scope, such as normal organ and NET lesion absorbed dose calculation without quantitative SUV data. Thirty-four full-text papers were retrieved and assessed for eligibility (2 systematic reviews and 30 original papers). Most of the papers assessed the absorbed dose for normal organs including the kidneys and NET lesions (n=31). Only one original paper investigated SUV metrics during ^{177}Lu-DOTA-TATE PRRT in NET.

2.2.4. Study risk of bias assessment

The three authors of this review independently assessed the risk of bias in the studies included. We used the Risk of Bias in Non-randomised Studies - of Interventions (ROBINS-I) tool to address the following risks of bias domains: (1) bias arising from the SPECT/CT reconstruction process, (2) bias due to deviations from intended PRRT, (3) missing outcome data, (4) measurement of the outcome and (5) selection of the reported result. We summarised an overall risk of bias judgement (low=1, intermediate=2 and high=3) for each specific outcome (Table 2-1). The highest ROBINS-I level determined the overall ROBINS-I for each study in any assessed domain (Sterne et al., 2016).

Table 2-1: Risk of bias assessment using ROBINS-I tool.

Bias	Thuillier et al., 2021
SPECT/CT reconstruction process	low
Deviations from intended PRRT	low
Missing outcome data	low
Measurement of the outcome	low
Selection of the reported result	low
Overall ROBINS-I (low=1, intermediate=2, high=3)	low

2.2.5. Effect measures

We evaluated evidence supporting the use of quantitative SUV-SPECT/CT as a validated tool for PRRT response assessment.

2.2.6. Synthesis methods

Studies presenting quantitative SUV data were analysed. Meta-analysis was not applicable in this review due to the small body of SUV-SPECT/CT evidence for comparing studies. Instead, we used a qualitative assessment of included papers.

2.3. Results

Our search of MEDLINE/PubMed identified (n=455) records. Abstracts of 455 records were screened, and 423 were excluded due to non-relevance to the main scope; 32 full-text papers were retrieved and assessed for eligibility (two systematic reviews and 30 original papers). Most of the papers assessed the absorbed dose for the kidneys, normal organs, and NET lesions (n=31). Only one original paper investigated SUV metrics during ^{177}Lu-DOTA-TATE PRRT for NET (Thuillier al., 2021). As a result, only one study was included in this review, as shown in Table 2-2. The low number of publications reporting SUV-SPECT within the search criteria was an unexpected finding. This may be partly explained by the vast inhomogeneity of peptides used for PRRT and the strong precedence of SUV-PET quantification.

Table 2-2: Summarised reviewed eligible papers.

Authors/ Year	Study type	Sample size	SPECT/CT	PET/CT	Quantitative method	Objective	SPECT/ CT Phantom
(Thuillier et al., 2021)	Prospective	10	^{177}Lu- DOTA-TATE (24 hours post 1st PRRT cycle, 128 OSEM updates)	^{68}Ga-DOTA-TOC (Avg. 50 days interval post PRRT)	SPECT and PET (SUV$_{max}$, averaged SUV$_{max}$, and SUV LTL &LTS ratio, MTV)	SPECT and PET SUVpeak are considered the most valuable metrics to assess response to PRRT that are least affected by MTV (r=0.84)	Uniform cylindrical phantom (^{177}Lu)

In 2021 Thuillier et al. conducted a feasibility study using quantitative SUV derived from ^{177}Lu-DOTA-TATE and ^{68}Ga-DOTA-TOC PET. Their prospective study included 10 NET patients with pre-PRRT ^{68}Ga-DOTA-TOC PET/CT (median time interval=50 days) and ^{177}Lu-DOTA-TATE SPECT/CT at 24 hours after the first PRRT cycle. A SPECT/CT calibration factor of 9.4 cps MBq^{-1} was calculated using uniform cylindrical phantom and 128 updates (16 iterations and eight subsets) for ordered subset expectation maximisation (OSEM) reconstruction was applied. Both SUV-SPECT and SUV-PET maximum and mean values were estimated for liver (3cm sphere VOI) and spleen (1cm sphere VOI). For metabolically active abnormal lesions, a fixed spherical VOI relative to the max threshold of 40% was applied for a maximum of 10 lesions per patient. In addition, the authors calculated the lesion to liver (LTL) and lesion to spleen (LTS) ratios as the lesion SUV$_{max}$ corrected for liver and spleen SUV$_{mean}$. A total of 81 lesions, four liver, and eight splenic SPECT and PET SUV metrics (mean, max and peak) were analysed using a signed Wilcoxon-rank test and Pearson linear regression. A 3 mL VOI metabolic tumour volume (MTV) was used to assess the partial volume effect (PVE) in SUV-SPECT. The authors reported that for lesions with an MTV > 3 mL, the median SUV and MTV SPECT and PET were comparable. However, MTV < 3 mL showed a significant difference between SPECT and PET values (P < 0.001). LTL and LTS SUV ratios were comparable in SPECT and PET only when MTV was less than 3 mL. A strong

linear correlation was observed between SUV metrics and MTV (r=0.77–0.84). ^{177}Lu-LTL and LTS values were significantly higher than ^{68}Ga-LTL and LTS (P < 0.02 and P < 0.001, respectively). The authors proposed that SPECT and PET SUV$_{peak}$ should be considered the most useful metrics to assess response to PRRT least affected by MTV (r=0.84) (Thuillier et al., 2021).

2.4. Discussion

As outlined in this systematic review of eligibility criteria and objectives, very few papers have explored the feasibility of applying quantitative SUV-SPECT/CT to assess ^{177}Lu-DOTA-TATE PRRT response. The prospective study of Thuillier et al., 2021 was the first to investigate the role of quantitative SUV-SPECT/CT and MTV as a metric to assess response to PRRT. SUV-SPECT/CT derived from ^{177}Lu-DOTA-TATE was shown to be comparable to SUV-PET/CT derived from ^{68}Ga-DOTA-TATE scans. One of the limitations of Thuillier study was the use of different somatostatin receptors analogous such as DOTA-TATE and DOTA-NOC labelled with ^{177}Lu and ^{68}Ga. Poepple et al. (Poeppel et al., 2011) reported significant differences between ^{68}Ga-DOTA-TOC and ^{68}Ga-DOTA-TATE SUV$_{max}$, the DOTA-TOC analogue showing higher SUV$_{max}$ than the DOTA-TATE (Poeppel et al., 2011). SSA uptake variation might be due to binding preference to specific SSTR subtypes. More reasons for binding variation could be the non-standardised scanning and amount of administered peptide activity (Velikyan et al., 2014). For example, ^{68}Ga-DOTA-TATE binding to SSTR2 is 10-fold higher than that of ^{68}Ga-DOTA-TOC (Reubi et al., 2000). The second limitation of the Thuillier study was failure to undertake phantom studies. The NEMA phantom with different sphere sizes can standardise and validate the SUV-SPECT/CT reconstruction method and assess the impact of the partial volume effect. In the end, they recommended adding more value to SUV-

SPECT/CT as a response to therapy assessment metrics by combining them with newly developed PRRT Predictive Quotient (PPQ) scoring systems by Bodei et al. (Bodei et al., 2020).

Del Prete and colleagues published quantitative SPECT/CT-based dosimetry data in 2017 (del Prete et al., 2017). Primarily, they aimed to propose a personalised protocol for PRRT based on individual actual dosimetry simulation. Thirty-six NET patients treated with at least one ^{177}Lu-DOTA-TATE PRRT cycle were included in their study. The calibration factor (cps/MBq) was estimated using serial SPECT/CT imaging of a ^{177}Lu point source. Quantitative SPECT/CT (32 updates, OSEM reconstruction) was performed at three time points (4, 24, 72 hr) post-PRRT administration. A 2 cm sphere VOI was placed over both kidneys and up to five dominant lesions that were ≥ 2 cm in size. Although their results reported the absorbed doses of renal, bone marrow, and lesions per unit of injected PRRT activity, the SUV was not reported even though it was mentioned in their methods. Furthermore, they described SUV$_{mean}$ measurements in their methods, but no results were reported. As a result, their study was excluded from this review.

The Hänscheid et al., (2012) pilot trial showed evidence of a strong positive correlation between ^{177}Lu-PRRT lesion uptake and ^{68}Ga-somatostatin receptor analogues. However, SUV-PET/CT was assessed after one cycle of PRRT, different peptide receptor analogues were used and PRRT was followed by external beam radiotherapy. Notably, ^{68}Ga-PET/CT SUV$_{max}$ values presented in their study were higher post-therapy than at baseline (Hänscheid et al., 2012). Uptake variations were reported to result from using two different peptides and PET scanners before and after therapy.

The SUV metrics of ^{68}Ga-somatostatin receptor analogues were studied broadly to predict PRRT therapeutic response (Aloj et al., 2021; Chang et al., 2016; Gålne et al., 2019; Ilan et al.,

2020; Opalińska et al., 2022; Ortega et al., 2021; Panagiotidis et al., 2017; Poeppel et al., 2013; Ragab et al., 2022; Sharma et al., 2019; Zhu et al., 2020). A comparative study between SUV-PET/CT using ^{68}Ga-somatostatin receptor analogues after somatostatin analogue injection therapy (SSA) and ^{177}Lu PRRT was conducted in 2019 by Sharma et al. The authors reported that the baseline SUV_{max}-PET of a single lesion (threshold ≥ 13) could predict treatment response and progress-free survival following PRRT (Sharma et al., 2019). Moreover, the difference between SUV normalised for body weight (SUV_{bw}) and lean body mass (SUL) on liver and spleen was previously reported (Ragab et al., 2022). More recently, Opalińska et al., 2022 reported the potential of measuring changes in ^{68}Ga- DOTA-TATE SUV_{max} and SUV_{mean} before and after PRRT as a treatment response indicator (Opalińska et al., 2022).

Current evidence supports the role of ^{68}Ga-DOTA PET/CT for staging, treatment planning, and prognosis assessment in NET (Ambrosini V. et al., 2022; Lee O. et al., 2022). PET/CT radiomics with tumour texture analysis and histograms may offer advantages for diagnosis, tumour risk stratification and PRRT response assessment (Liberini et al., 2021; Jha et al., 2022; Prosperi et al., 2022; Saleh et al., 2022). Texture analysis of tumour heterogeneity showed a significant relationship to prognosis and outcomes following PRRT that exceeded conventional quantitative metrics (Atkinson et al., 2021). Consequently, more studies are looking to develop PET/CT radiomic features modelled to ^{68}Ga-radiopeptide PET/CT to predict progression-free and survival rate following PRRT (Atkinson et al., 2021; Bevilacqua et al., 2021; Fournier et al., 2021; Jha et al., 2022; Laudicella et al., 2022; Liberini, de Santi, et al., 2021; Liberini, Rampado, et al., 2021; Opalińska et al., 2022; Prosperi et al., 2022). Accurate response to PRRT assessment requires the use of optimised and validated reproducible image acquisition, reconstruction, and standardised quantitative metrics (Liberini et al., 2020).

In our search, we found many dosimetry studies that examined the absorbed dose of normal organs and lesions using whole-body scan or SPECT/CT but without investigating quantitative

SUV values (Chicheportiche et al., 2021; del Prete et al., 2019; Desy et al., 2020; Devasia et al., 2021; Gosewisch et al., 2018; Hänscheid et al., 2018; Hou et al., 2021; Huizing et al., 2020; Roth et al., 2022; Santoro et al., 2021; Svensson, Hagmarker, et al., 2016; Svensson, Rydén, et al., 2016; Vergnaud et al., 2022; Willowson, Eslick, et al., 2018; Willowson, Ryu, et al., 2018; Zhao et al., 2019). In addition, there have been two systematic reviews, one of which evaluated the efficacy of ^{177}Lu-DOTA0-Tyr3-octreotate, but no quantitative data were presented (J. Zhang et al., 2020). The second review investigated the correlation between kidney absorbed dose and toxicity (Cremonesi et al., 2018).

A very low rate of reporting SUV-SPECT in PRRT publications may be partly explained by the strong precedence of SUV-PET quantification and weak reliance on SPECT quantification due to historical reasons (e.g., lack of accurate attenuation correction before iterative reconstruction was computationally feasible at a clinical setting). Perhaps, lack of defined criteria and protocols for measuring and reporting SUV-SPECT can also be added as possible explanation.

2.5. Conclusion

There is a paucity of studies using SUV-SPECT/CT in ^{177}Lu-DOTA-TATE as surrogate metric of PRRT treatment therapy response. This could be remedied by initiating a quantitative SUV-SPECT/CT protocol in PRRT describing the acquisition and processing factors toward optimisation. Such a protocol would rely on phantom imaging to assess the reliability of SUV values, standardise, and validate the quantification method. Additionally, the VOI delineation method and threshold would need to be identified clearly in the quantitative method using both phantom and patient's data.

CHAPTER 3

3. Optimisation and Validation of Quantitative 2D and 3D Imaging Protocols for Lutetium-177 (^{177}Lu) and Iodine-131 (^{131}I)

Abstract

Aims/Introduction: Imaging as part of the patient workup for molecular radiotherapy (MRT) is often used in the evaluation, verification, and follow-up of treatment. Beyond its role as a visual assessment tool, image quantification may have a role in monitoring change as part of MRT. Recent advancements in SPECT imaging, such as improved image reconstruction and scatter and attenuation correction, allow for precise quantitative analysis and the calculation of standardised uptake value (SUV). This study aims to investigate optimal protocols for quantitative ^{131}I and ^{177}Lu SPECT/CT by evaluating the accuracy of absolute SUV-SPECT/CT quantification.

Materials and Methods: As part of setting optimal 3D quantitative SUV-SPECT/CT protocol, since there are different quantitative tools proposed, phantom imaging was conducted to develop and validate the image quantification method using ^{177}Lu, including:

Cylindrical homogeneous phantom to assess scintillation camera calibration factor (CF) (cps/MBq) for planar and SPECT imaging. CF value was used by HERMES to estimate the SUV in the volume of interest (VOI).

The NEMA IEC Body Phantom consisting of a body/thorax-size compartment and six spherical inserts of various sizes (from 10mm to 37mm in diameter), was used to validate the accuracy of quantitative SUV by calculating the concentration recover coefficients (cRC) at various object sizes.

Results: HERMES Hybrid3D 3.01 software (HERMES Medical Solutions, Sweden) was used to estimate CF and SUV values. ^{131}I and ^{177}Lu total activity convergence reached 90% at 48 and 80 updates (iteration*subsets), respectively. Regarding ^{131}I and ^{177}Lu activity concentration, good precision was observed at 48, and 80 updates, respectively, as the coefficient of variation (CoV) became <10% & relative error (RE) <5%. Spheres cRC and SUV_{max} of the largest sphere reached the optimum cRC of 1 and SUVmax of 10 at 48 and 80 updates for ^{131}I and ^{177}Lu, respectively.

Conclusion: Reproducible, quantitative SUV estimates can be derived from I-131 and Lu-177 SPECT/CT images using appropriate reconstruction and compensation methods. Accuracy relies upon optimising calibration factors and OSEM updates for accurate recovery (cRC, CoV, and RE). This method will be applied to retro- and prospective patients' samples in this research to measure normal and abnormal tissue SUVs in patients undergoing SPECT/CT following MRT using ^{131}I and ^{177}Lu- DOTA-TATE.

3.1. Introduction

SPECT and PET imaging techniques examine the uptake of radiolabelled molecules in regions and volumes of interest (ROI and VOI), offering clinically relevant quantitative and functional information regarding tissues under both physiological and pathological conditions (Kramer-Marek & Capala, 2012). SPECT/CT and PET/CT imaging techniques can be used to calculate the standardised uptake value (SUV) of the ROI to measure absolute or relative activity (kBq/ml). The accuracy of absolute SUV quantification obtained from SPECT/CT images should be verified, especially for MRT planning purposes and advanced kinetic analyses (IAEA, 2014). In quantitative PET/CT studies, SUV is used as a surrogate measure of tissue function within an ROI and is defined mathematically as the ratio between the radionuclide concentration in the ROI (kBq/ml) and the total injected activity (kBq), normalised for the patient's body weight (in g, either the total body weight or lean body mass) (Kozak et al., 2005). The SUV can be calculated using Equation 3-1:

$$\text{SUV (g/ml)} = \frac{\text{VOI uptake (kBq/mL)}}{\text{Injected Activity (kBq)/ Patient's weight (g)}} \qquad \text{Eq. 3-1}$$

Elevated SUV compared with body background or normal organs values are likely to correspond to pathological conditions, including inflammation, infection, and cancer (D'Arienzo et al., 2016; Jadvar, 2014). Various SUV-related parameters have been recommended to assess response to MRT, including SUV_{max}, SUV_{mean}, and SUV_{peak}. SUV_{max}, which represents a single-pixel value in the ROI, is typically considered to be the most valuable (Verburg et al., 2017) because it most likely reflects the most metabolically active component of the ROI (characteristic of a tumour) and changes between pre- and post-therapy for both PET/CT and SPECT/CT scans. Although SUV_{max} might be affected by image noise, it has been widely used in the PET literature due to its simplicity, relative resistance to partial volume

effects and high inter-observer consistency (Jadvar, 2014). In molecular imaging, activity quantification can evaluate the therapeutic response. For example, imaging the bio-distribution of a radiolabelled molecule can be used as a dosimeter for lesions and healthy tissues (Beauregard et al., 2011).

To optimise absolute quantification, appropriate standardisation and validation methods should be identified and performed for each radionuclide, scintillation camera, collimator, and relevant energy window before quantification (Frey et al., 2012; IAEA, 2014). Several studies have investigated the accuracy of quantitative SPECT/CT using various reference geometries to calibrate the system, such as the concentration recovery coefficients (cRC), coefficient of variation (CoV), and calibration factor (CF), a measure of system sensitivity (Hippeläinen et al., 2016; Mezzenga et al., 2017; Zhao et al., 2018).

A multi-centre study performed by Zimmerman et al. (2017) attempted to evaluate the accuracy and variability of absolute activity measurements by comparing planar and SPECT images of a cylindrical phantom, which showed that SPECT/CT quantification was applicable and superior to planar images (Zimmerman et al., 2017).

MRT protocols often use imaging to evaluate, verify, and follow-up treatment. In addition to visual assessment, image quantification might play a role in monitoring the change in response to MRT. Recent advancements in SPECT/CT imaging, such as improved image reconstruction and scatter and attenuation correction, allow for the precise quantitative analysis and calculation of SUV.

3.2. Aims

This study aims to investigate the optimal protocols for quantitative ^{177}Lu and ^{131}I SPECT/CT by evaluating the accuracy and precision of absolute SUV-SPECT/CT quantification.

3.3. Methods

This study conducted 2-dimensional (2D) whole-body scans (WBS) and 3-dimensional (3D) SPECT/CT quantitative image acquisitions and reconstructions using phantom data and evaluated for accuracy and precision. We examined multiple factors to achieve the optimum quantitative performance, such as gamma-ray attenuation, scatter, collimator–detector response, dead-time, partial volume effect (PVE), and ordered subsets expectation maximisation (OSEM) sub-iterations. The main factor to start with was the assessment of whole-body and SPECT/CT systems calibration factor (CF) (cps/MBq). All phantoms' activities were calibrated using a dose calibrator (CRC-15R serial number 151976) that is routinely used for patient activity measurement; This is annually calibrated against the National Physics Laboratory (NPL) standard and tested daily under the departmental Quality Control system in place.

Several different quantitative tools have been proposed in the literature. In this study, the 3D quantitative SUV-SPECT/CT protocol was optimised using phantom imaging mimicking the patient's body habitus to develop and validate an image quantification method for the use of ^{177}Lu and ^{131}I, including the following:

- A cylindrical homogeneous phantom was used to assess the scintillation camera volume CF (cps/MBq) for ^{177}Lu whole-body and ^{177}Lu, and ^{131}I SPECT imaging. We used the CF value to calculate the SUV in the VOI.

- Thyroid uptake neck phantom was used to assess the ^{131}I whole-body scintillation camera CF (cps/MBq).

- A National Electrical Manufacturers Association (NEMA), International Electro-technical Commission (IEC), Body Phantom consists of a body phantom into which six spheres with various sizes are inserted to validate the accuracy of quantitative SUV by calculating the concentration recovery coefficients (cRC) for each sphere.

The 3D quantitative SPECT/CT phantom results were then tested for the accuracy and precision of the SUV. Accuracy refers to the deviation for a given VOI between the measured mean and the actual mean and can be expressed in terms of bias or relative error (RE, Equation 3-2). Precision refers to the range of repeated measurements around the mean and can be expressed as the standard deviation or the CoV (Equation 3-3) (Frey et al., 2012; IAEA, 2014).

$$b = m - t \qquad\qquad \text{Eq.3-2}$$

Where:

b: bias
m: measured mean in VOI
t: true value

Relative error (RE) $= \dfrac{b}{t}$

$$CoV = \frac{\sigma}{m} \qquad\qquad \text{Eq.3-3}$$

Where:

σ: standard deviation
m: measured mean in VOI

3.3.1. 2D Whole-Body Quantitative Imaging Study

Calibration factor (CF)

For the 2D ^{177}Lu and ^{131}I whole-body scan quantification, we calculated the whole-body CF (cps/MBq), which was used to convert acquired counts into activity following the whole-body scan using different systems, as listed in table 3-1 following MIRD 24 and 26 acquisition guidelines (Dewaraja et al., 2013, and Ljungberg et al., 2016). We used a cylindrical homogeneous (Figure 3-1, a), Perspex phantom (length = 29.7 cm, diameter = 18.75 cm, volume = 8,200 ml) filled with water and known amount of ^{177}Lu –DOTA-TATE activity (Table 3-1). For ^{131}I-WBS, we used a Lucite cylinder thyroid uptake neck phantom (length = 12.7 cm, diameter = 12.7 cm) fitted with a vial holder at the anterior part of the phantom (length = 10 cm, diameter = 5 cm). A vial containing 4 ml of ~ 55 MBq of ^{131}I-NaI activity was placed in the vial holder (Figure 3-1, b).

Whole-body images were acquired using existing clinical protocols for MRT patients receiving ^{177}Lu-DOTA-TATE for neuroendocrine tumours and ^{131}I-NaI for thyroid cancer therapy. The 2D ^{177}Lu-WBS imaging was obtained using dual-head scintillation cameras from the two manufacturers (SymbiaT16-Siemens, Erlangen, Germany and Precedence-Philips, Netherlands) representing locally available systems for current and retrospective patient data, respectively. Lu-177 whole-body acquisitions were performed with a medium-energy on Precedence scanner and low-energy on Symbia scanner, energy window centred at 113 keV (101.7-124.3KeV) and 208 keV (187.2-228.8KeV), and 15 cm/min bed speed.

We used Siemens's systems for ^{131}I-WBS (SymbiaT16 and INTEVO BOLD-Siemens, Erlangen, Germany) as the systems available for high-energy imaging at the time (Table 3-1).

I-131 acquisitions were performed with a high-energy (HE) collimator, energy window centred at 364 keV ± 15%, and 8 cm/min bed speed.

The 2D whole-body CF of each system was calculated according to the following equation:

$$CF(\frac{cps}{MBq}) = \frac{Counts\ in\ ROI}{T(s) * A(MBq)}$$

Eq.3-4

Where T is the acquisition duration in seconds, and A is the true activity in the phantom as measured by the radionuclide calibrator in MBq. We calculated the CF from geometric mean counts for both anterior and posterior detectors and each detector separately. A geometric-mean whole-body count, GM, was calculated by region of interest (ROI) multiplication of anterior counts (C_A) and the mirrored ROI posterior counts (C_P) (Eq.3-5) (Ljungberg & Sjögreen Gleisner, 2016; Sjögreen et al., 2002; Zaidi, 2005).

$$GM_{counts} = \sqrt{C_A \times C_P}$$

Eq.3-5

Table 3-1: Parameters of whole-body scan (WBS) acquisition and sources activities used in cylindrical homogeneous phantom experiments to calculate CF

Radioisotopes	System	Speed (cm/m)	Collimator	True Activity at scan time (MBq)	Scan duration (s)	Matrix	Energy window
^{177}Lu	PRECEDENCE (Philips)	15	MEGP	1441	444	512x1024	W1 = 113 keV (101.7-124.3KeV), W2 = 208 keV (187.2-228.8KeV)
	Symbia T16 (Siemens)	15	LEHR	1432	491	256x1024	W1 = 113KeV (101.7-124.3 KeV), W2 = 203KeV (182.7-223.3 KeV)
^{131}I	Symbia T16 (Siemens)			355	857		
	INTEVO BOLD (Siemens)	8	HEGP	325		256x1024	364 KeV ±15%
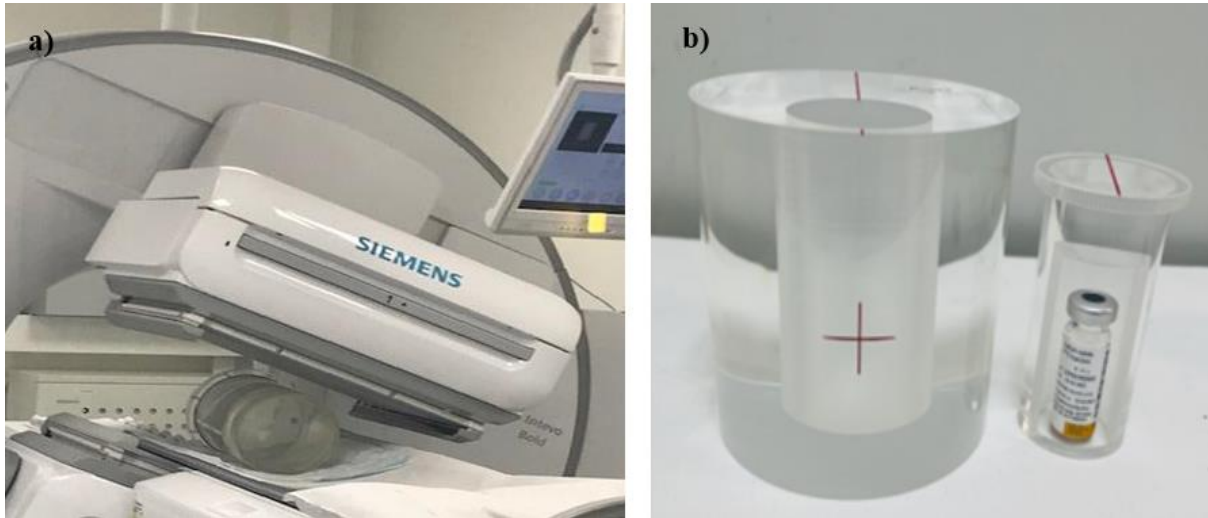
Figure 3-1: System calibration using a) cylindrical phantom SPECT/CT & whole body and b) Thyroid neck phantom whole-body acquisitions.

Dead-Time

Dead-time (Dτ) is defined as the ratio between the true count rate (Ct) and the measured count rate (Cm) of a detector (Eq.3-6).

$$Dτ = \frac{Ct}{Cm}$$

Eq.3-6

In MRT, count rate losses due to the dead-time effect can be considered especially when high activities of ^{131}I are imaged. However, in ^{177}Lu imaging, this effect is relatively small because of the low yield of γ-photons emitted during the decay of ^{177}Lu and the negligible bremsstrahlung influence (Ljungberg et al., 2016). Scans performed shortly after injection are the most likely to be affected. Therefore, we aimed to estimate the dead-time effect. A series of phantom tests were performed using different ^{177}Lu activity levels using the acquisition applied for a patient study (Table 3). The count rate (cps) was then analysed to estimate count rate losses (Dewaraja et al., 2012, 2013; Ljungberg et al., 2016).

This study will use two systems for patient scan post-^{131}I-NaI MRT (INETVO BOLD and Symbia T16). Considering the high risk of radiation exposure and contamination due to [131]I

high photon energy and beta emission particles from ~ 8 days half-life, we used the dead time for the scanners recommended by recent studies (Gregory et al., 2019; Taprogge et al., 2020). Dead-time factors showed an agreement in two different studies for the same scintillation camera manufacturers and models. However, the dead-time compensation is applied when a scan is performed before 48 hr post-^{131}I-NaI MRT for thyroid cancer patients. In our prospective malignant thyroid patients, imaging will be acquired at 48 hr post MRT. For Benign thyroid disease patients who will receive less than 1.1 GBq of ^{131}I-NaI activity, the scan will be acquired 24 hr post-MRT. Benign and malignant thyroid disease will be scanned when their activities are less than 1.1GBq. Taprogge et al. reported minimal dead-time effect when the actual count rate is < 30 kcps for both Siemens systems (Symbia 16T and INTEVO BOLD) (Taprogge et al., 2020). Moreover, MIRD 24 recommended imaging with counts < 50 kcps to overcome dead-time effects (Dewaraja et al., 2013).

3.3.2. 3D SUV-SPECT/CT Quantitative Imaging Study

- **Cylindrical Homogenous Phantom**

Calibration factor (CF)

The 3D ^{177}Lu-SPECT/CT imaging was acquired using dual-head scintillation cameras from two manufacturers (INTEVO BOLD-Siemens, Erlangen, Germany, and Precedence-Philips, Netherlands), for quantitative ^{131}I-SPECT/CT imaging was acquired on a cylindrical phantom only using two INTEVO BOLD systems.

Quantitative 3D SPECT/CT system volume CF (cps/MBq) was calculated using a cylindrical, homogeneous, Perspex phantom (length = 29.7 cm, diameter = 18.75 cm, volume = 8,200 ml) filled with water and various ^{177}Lu –DOTA-TATE activities and single ^{131}I-NaI activity, as shown in table 3-2, this phantom same as used for 2D calibration. The phantom was placed on

the imaging pallet on the axis of rotation and in the centre of the detector field of view. First, SPECT/CT images were acquired using existing clinical protocols for an MRT patient receiving ^{177}Lu-DOTA-TATE for neuroendocrine tumours and ^{131}I-NaI for thyroid cancer therapy.

Two ^{177}Lu energy windows were acquired and saved separately for the PRECEDENCE system, enabling us to reconstruct and calculate SPECT/CT CF using both energy windows (centred at 113 and 208 keV) and the higher energy window alone (208 keV). The pilot qualitative assessment by an expert nuclear medicine physician showed that there are no observed differences regarding quality and resolution between the two sets. This is reassuring as clinical data acquisition in the department moves to the Siemens platform, which doesn't support concurrent multiple energy windows as the previously locally established Philips Precedence system. ^{177}Lu-SPECT/CT was acquired for the Siemens INTEVO BOLD system using only the upper energy window (208 keV) as per clinical protocol.

For analysis and reconstruction purposes, only the upper energy window was used as a reference for both CF and SUV-SPECT calculations, as described by the EANM/MIRD 23,24, and 26 Guidelines for Quantitative ^{131}I and ^{177}Lu-SPECT (Dewaraja et al., 2012, 2013; Ljungberg et al., 2016). ^{131}I-SPECT/CT was acquired by INTEVO BOLD system using 364 keV energy window with 15% upper and lower scatter.

The SUV-SPECT calibration application in HERMES Hybrid 3D 3.01 beta software program (HERMES Medical Solutions, Stockholm, Sweden) was used to calculate CF by applying for automated image registration of SPECT/CT image. The CF estimation for each system was based on the attenuation correction, scatter correction, and collimator–detector response, as shown in table 3-3. The Volume of interest (VOI) was drawn in the middle of the cylindrical phantom, covering 70% of the size of the phantom.

Once each CF was identified, the SPECT/CT data were registered for the SUV-SPECT reconstruction application. The CF value was entered for each system, including attenuation correction, scatter correction and collimator–detector response. Finally, the phantom details, including total and residual injected activity, scan time, phantom dimension, and weight, were accurately entered to generate accurate CF and SUV values. For all systems, OSEM with CT-based attenuation correction, ten iterations, eight subsets, and a 9mm 3D Gaussian post-filter was applied as optimum outcome for SUV based on the study assessment. We generated a CF for each phantom experiment presenting a different ^{177}Lu activity for the PRECEDENCE system.

Table 3-2: SPECT/CT acquisition Parameters and sources activities used in cylindrical homogeneous phantom experiments. Four phantoms' experiments were performed using gradually increased activity for the PRECEDENCE system.

	^{177}Lu-SPECT/CT		^{131}I-SPECT/CT
System	**INTEVO BOLD (Siemens) Systems 1&2**	**PRECEDENCE (Philips)**	**INTEVO BOLD (Siemens) Systems 1&2**
Total phantom true Activity at scan time (MBq)	System1 -1415 MBq (Cylinder activity) -428MBq (point source activity, 1mL sphere in the air) System2 -1423MBq (Cylinder activity) -428MBq (point source activity, 1mL sphere in the air)	57 MBq 114MBq 242MBq 1137 MBq	55MBq
Energy Window	TEW (208 keV 20%, Lower & Upper Scatter 10%)	Two energy windows (113keV & 208keV, 15%)	364 keV, 20% window, 15% upper and lower scatter
Collimator	MELP	MEGP	HE
Crystal thickness	3/8"	3/8"	3/8"
Matrix Size	256x256	128x128	128x128
Zoom	1	1	1
Number of views/Detector	64	64	32
degree of rotation	180	180	180
Mode	step & shoot	step & shoot	step & shoot
Time per View	20s	20s	25s
CT			
mAs	31(Eff.mAs)	100	20 (Eff.mAs)
Kev	130	120	130
Matrix Size	512x512	512x512	512x512
Slice	1.5mm	1.5mm	1.5mm

		^{177}Lu		^{131}I
HERMES SUV-SPECT reconstruction parameters		**PRECEDENCE**	**INTEVO**	**INTEVO**
Scatter correction	Energy resolution @140keV	9.9		
	Simulated photon	100000		
	Update iteration	2		
	Down-scatter photon	100000		
Collimator-detector response (Resolution Recovery, RR)	Hole diameter (cm)	0.295	0.294	0.4
	Hole length (cm)	4.8	4.064	5.97
	Detector resolution @140 kV(cm) 9.5mm Crystal Thickness	0.38		
	Radius of rotation offset (cm)	0.0	4.864	6.77
Attenuation Correction	Mu-map type	CT		
	Mu-map source	INTERNAL		
	HU offset	1000		
	Intercept 1st eq.	0.151		
	Slope 1st eq.	0.00015		
	Intercept 2nd eq.	0.156		
	Slope 2nd eq.	0.000107		

Iterative Reconstruction

Iterative reconstruction algorithms, such as the ordered subsets expectation maximisation (OSEM), were used to compensate for image degrading factors to optimise activity quantification. A certain number of iterations was applied using the OSEM reconstruction method until we reached convergence at 90% recovery, reflecting the optimum reconstruction accuracy. (Dewaraja et al., 2012, 2013). The image is updated by predefined iterations for each subset of evenly- distributed angles that has been processed.

Image resolution improved when using OSEM or the maximum likelihood estimation method (MLEM), and the noise increased with increasing updates. However, the image was considered optimised to estimate activity in VOIs (IAEA, 2014).

This study delineated five spherical VOIs with fixed 5-cm diameters in the middle trans-axial view of phantom SPECT/CT data (Fig. 3-2). The activity concentration (kBq/ml) was then plotted as a function of the number of OSEM updates (number of subsets multiplied by the number of iterations).

Additionally, we investigated reconstruction parameters as several updates by using ^{177}Lu-SPECT/CT data from a sample patient, which were evaluated visually to examine the effects of updates on image noise and quality (Ljungberg et al., 2016).
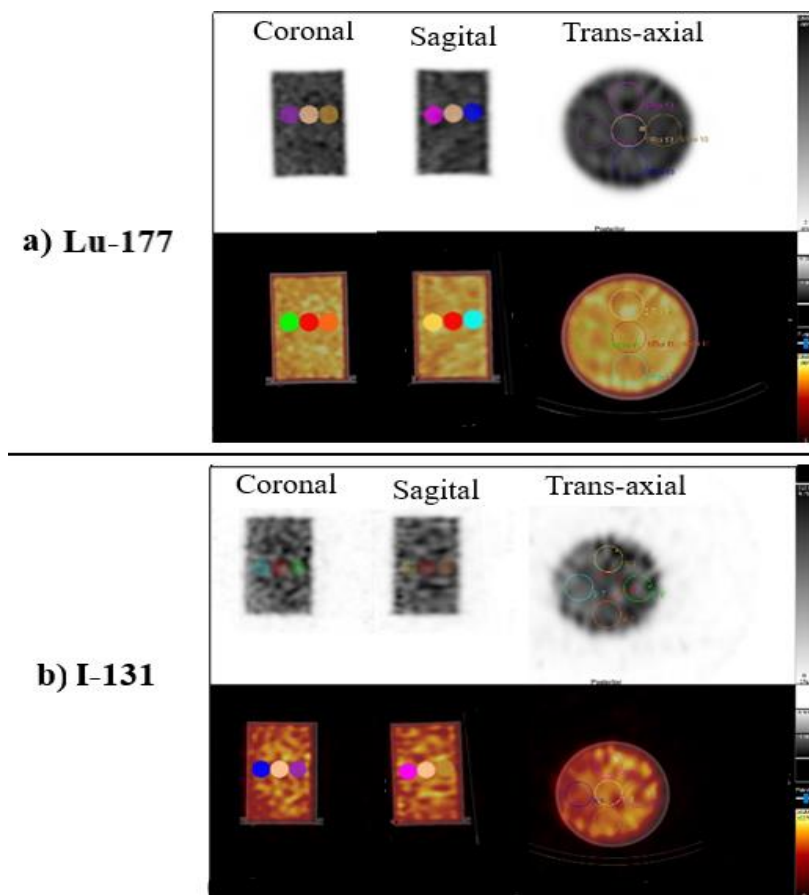
Figure 3-2: Five spherical VOI with fixed 5-cm diameter delineated in the middle trans-axial view of homogenous phantom SPECT data at the top row and fused SPECT/CT data at the lower row ^{177}Lu (a) and ^{131}I (b)

ROI & VOI Definition

The 2D ROI from a planar image or the 3D VOI from a SPECT/CT image should be appropriately defined to obtain a reliable estimate of quantitative activity. Three methods can be used to identify ROI and VOI: manual, semi-automated, and automated. Multiple ROI are drawn over phantom diameter (18 cm) trans-axial image in the manual method, and then a 3D VOI is created from these ROI. The semi-automated process determines the threshold value as a percentage of the maximum pixel activity manually entered. In the automated method, the software will use contours to define the whole VOI using an automatic algorithm without user interaction. Only the manual and semi-automated approaches were used and tested in this study. VOI were placed in the whole phantom using the CT trans-axial image as a reference to calculate the total activity at each update. For CoV and RE calculations, five spheres were drawn at the mid-trans-axial view of the phantom.

Photon Attenuation

Photon attenuation is a leading cause of degradation when SPECT/CT quantification is performed. The absolute estimation of a region's activity will be underestimated by factors of 5–20 in the absence of attenuation correction (IAEA, 2014). An attenuation map that provides an attenuation coefficient for each pixel is required as an input for attenuation correction. Today, using a state-of-the-art SPECT/CT system, an attenuation map derived from a CT image can be registered with an emission image to apply attenuation correction. This study obtained CT images in Hounsfield units and converted them into linear attenuation coefficient (μ) values before attenuation correction. HERMES provided standard SUV-SPECT/CT calibration and reconstruction settings, as shown in table 3-3.

Compton Scatter

Many factors affect scatter, including photon energy, source depth, energy windows, and the energy resolution of the system, which can lead to a loss of image contrast and degraded

quantitative data (Frey et al., 2012). HERMES SUV-SPECT/CT performs scatter correction within the patient using a Monte Carlo-based approach, which uses the initial point of photons to be simulated from the SPECT data, the electron density of the medium from the CT image, and the energy resolution of the system.

Collimator–Detector Response (CDR)

We used a CDR factor to improve the resolution model of the reconstructed images and the quantitative accuracy by reducing the noise and resolution effects. Two CDR methods exist: iterative and non-iterative methods. The non-iterative method is not as well-established because it is not as effective as the iterative method (Ljungberg et al., 2016). HERMES SUV-SPECT software applies the geometric components of the CDR, including collimator hole diameter and length, detector resolution at 140keV, and the radius of rotation for each system (Table 3-3).

The Standardised Uptake Value (SUV)

The SUV refers to the standardised activity concentrations for a given VOI, corrected for injected radiopharmaceutical activity, the physical decay of the radionuclide, and the object's distribution volume (Eq. 3-1). The SUV of a defined VOI will be reported as the SUV_{max}, SUV_{mean}, and SUV_{peak}. For a cylindrical, homogenous phantom test, because the activity is distributed uniformly, SUV_{mean} should be equal to 1 (IAEA, 2014; Ljungberg et al., 2016). An 8-cm sphere's diameter VOI was drawn at the phantom's centre, and different VOI delineations and thresholds were tested to obtain an optimal SUV value. The OSEM update and threshold effect assessments were analysed using the VOI for the whole phantom.

For validation purposes, these measurements were also applied to a NEMA IEC. A cRC curve was generated for each sphere, showing the effects of OSEM update numbers and VOI delineation using spherical and threshold delineation methods.

- **NEMA-IEC Body Phantom Validation Test**

The standardised acquisition and reconstruction method used to generate the 3D SUV-SPECT quantitative data was validated for SUV accuracy, and cRC values were evaluated by measuring the activity from different sized objects. The NEMA IEC body phantom, without the lung insert (10,150 ml), was equipped with six inserts of different diameters (10, 13, 17, 22, 28, and 37 mm) and volumes (0.5, 1.1, 2.5, 5.5, 11.5, and 26.5 ml, Figure 3). The aim was for the spheres to have activity concentration ten times that of the background activity (10:1) (Tran-Gia & Lassmann, 2019). We filled the total volume of the spheres (47.8 ml) with 80.6 MBq ^{177}Lu, which was equivalent to 1.78 MBq/ml. We filled the background with 1,812 MBq ^{177}Lu (0.178 MBq/ml). SPECT/CT acquisition was performed using standard clinical settings (Table 3-2).

For ^{131}I, sphere-to-background activity concentration ratio was based on published data of ~ 11.4 mean lesion-to-background ratio in 98 lesions of 31 patients using ^{131}I-whole-body scan post MRT (Rubello et al., 2007). We filled the total volume of the spheres (47.8 ml) with 16.2 MBq ^{131}I-NaI, which was equivalent to 0.3 MBq/ml. We filled the background with 318 MBq ^{131}I (0.03MBq/ml) to achieve 10:1 sphere-to-background activity concentration ratio. SPECT/CT acquisition was performed using standard clinical settings (Table 3-2).

The images were reconstructed using the HERMES SUV-SPECT reconstruction settings. The CF, phantom/radionuclide, and activity/time information, as well as the attenuation correction/resolution recovery (RR)/scatter correction was appropriately entered for each system.

SUV$_{mean}$, SUV$_{max}$, and SUV$_{peak}$ were measured for each sphere by placing spherical VOIs equal to the spheres' inner diameters (37, 28, 22, 17, 13, and 10 mm) using CT data to guide the positioning. Then five 3-cm diameter spherical VOIs were placed in the background (Fig. 3-3). Ideally, the background SUV$_{mean}$ value should equal 1, and the largest sphere should have an SUV$_{max}$ value of 10, which would confirm that the activity concentration ratios are those detailed in the procedure. However, we expected the SUVs to drop in value with decreasing sphere size due to the PVE, which can be compensated for by determining the cRC curve defined by the following equation:

$$cRC = \frac{C(Sph)/C\ (Bkg)}{A(Sph)/A(Bkg)} \qquad\qquad Eq.3\text{-}5$$

Where:

C (Sph): all counts measured in the hot sphere VOI.
C (Bkg): average counts from three background VOIs.
A (Sph)/A (Bkg): the ratio of the hot sphere and background true activities.
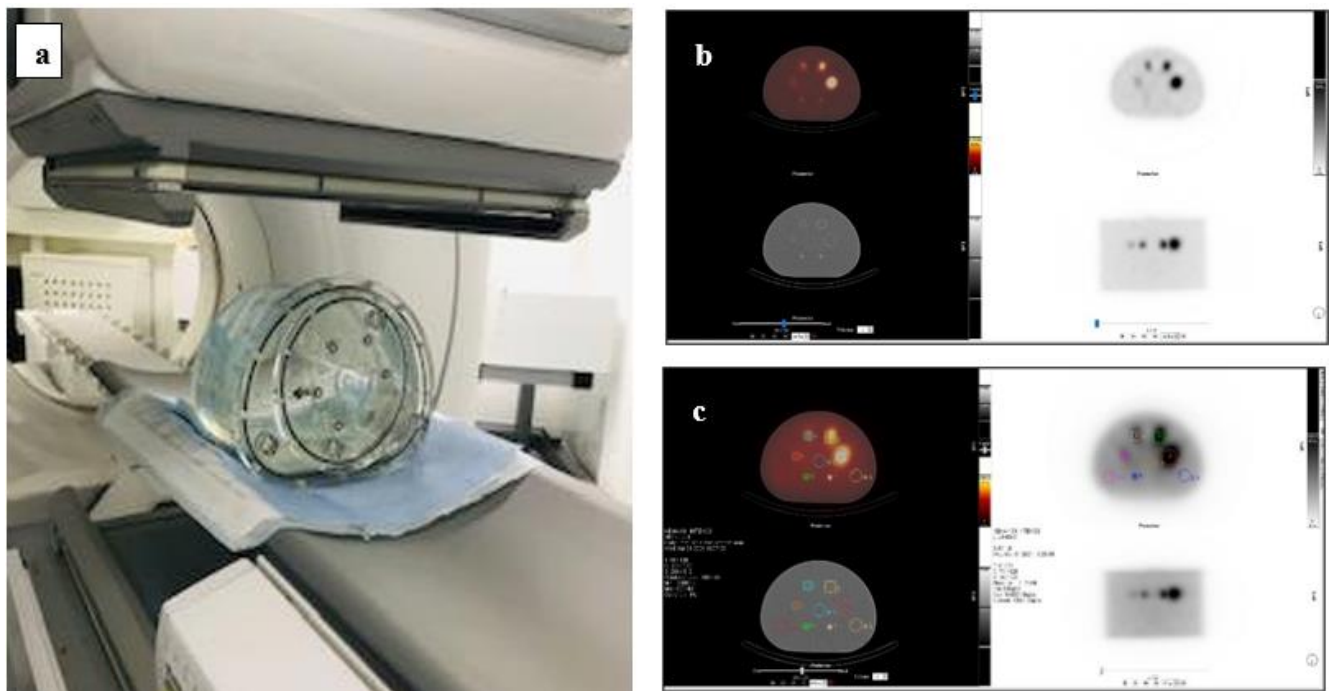
Figure 3-3: SPECT/CT acquisition of NEMA IEC body phantom with six inserts, reconstructed fused, SPECT, and CT transaxial image of b)^{177}Lu, and c)^{131}I NEMA phantoms. VOI delineated using CT transaxial image reference copied to SPECT data.

3.4. Results

3.4.1. ^{177}Lu-DOTA-TATE 2D and 3D Image Optimisation and Validation

System Sensitivity (Calibration Factor, CF) and Dead time

The CF was generated using Eq. 3-4 for a whole-body image. Table 3-4 shows the geometric mean CF for the whole-body phantom scan and the CF per detector. HERMES SUV-SPECT software was used to calculate the CF for different systems (Table 3-5). Multiple SPECT/CT phantom tests using different levels of ^{177}Lu activities were measured using the PRECEDENCE system, as illustrated in figure 3-4. The CF (11.1 cps/MBq) for 1,137 MBq activity was standardised as the closest value to that observed for patient activity during a 24-hour scan. The manual calculation of CF for each activity level was compared against the HERMES calculation, as shown in figure 3-5. The manually calculated CF for the highest activity (1,137 MBq) was 9.4, whereas a CF of 10 was calculated for the lower three activity levels. The three systems CFs were used to estimate the phantom activity, and these values were compared against the true activity value (Table 3-5). The volume CF of 11.1 cps/MBq resulted in the most accurate activity estimate (1,124 MBq), which differed from the actual activity by only 1%.

Table 3-4: Systems sensitivity using ^{177}Lu whole-body cylindrical phantom imaging.

ID	Detector	CF (cps/MBq)	Geometric Mean CF (cps/MBq)
Precedence (Philips) System	Anterior	3.3	3.1
	Posterior	3	
Symbia T16 (Siemens) System	Anterior	3.5	3.4
	Posterior	3.3	

Table 3-5: ^{177}Lu radionuclide (208 keV, energy window) calibration factor (cps/MBq) for three SPECT/CT scanners. CF generated using HERMES SUV-SPECT software (OSEM, scatter and attenuation correction, CDR, 80 updates (10 iterations& 8 subsets).

ID	CF (cps/MBq)	Measured activity concentration (kBq/ml) Hermes	True activity concentration at scan time (kBq/ml) Dose-calibrator
PRECEDENCE (Philips)	11.1	132	138.6
INTEVO BOLD (Siemens)System 1	11.7	172.2	172.5
INTEVO BOLD (Siemens)System 2	10.8	171.2	173.5
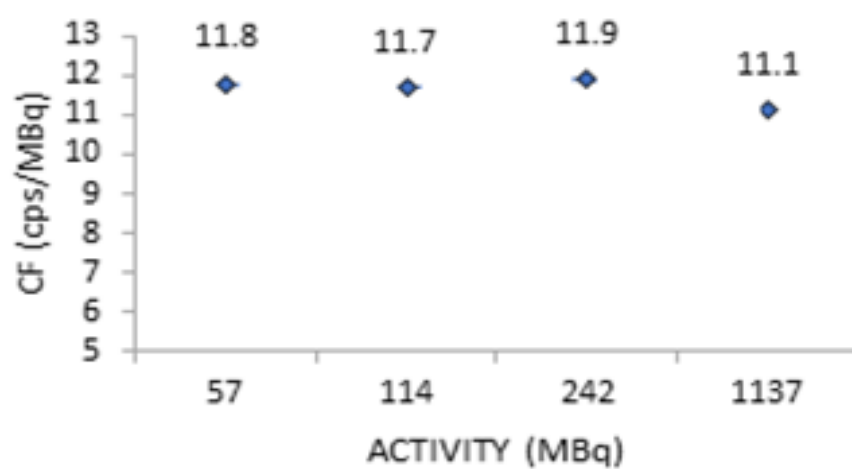
Figure 3-4: 177Lu volume Calibration factor (CF)for different phantom activities calculated using HERMES SUV- SPECT
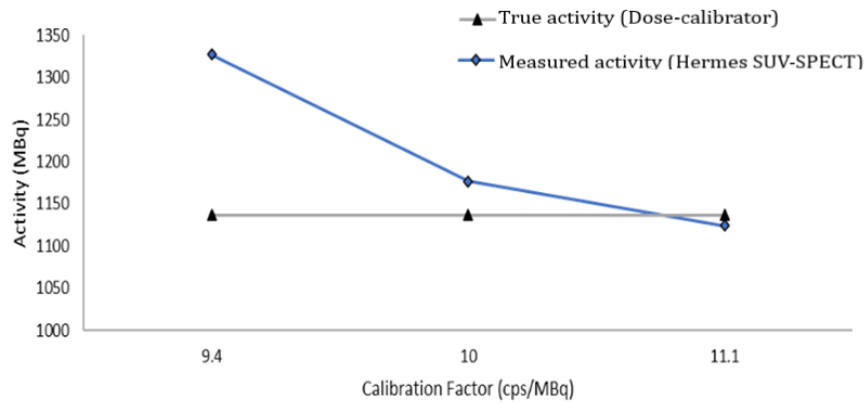
Figure 3-5: Phantom dose-calibrator true activity (1137MBq) compared to Hermes measured one using different CF. 11.1cps/MBq (HERMES calculation) and 9.4 & 10 cps/MBq were calculated manually from DICOM header total counts without compensation, respectively, presenting high and low activity

Figure 3-6 illustrates the count rate (cps) losses difference using a CF of 11.1 cps/MBq compared with the true count rate regarding the dead-time effect. The highest difference of 17.5% was recorded at 1137MBq.
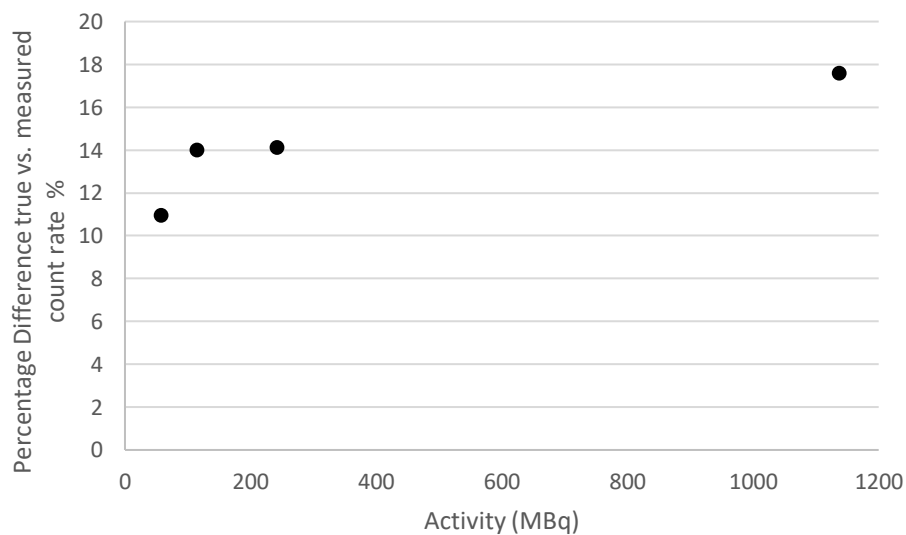
Figure 3-6: ^{177}Lu-Cylindrical homogeneous phantom count rate difference scatter plot presenting dead time effect as the difference percentage between the true count-rate and the measured count-rate of a detector, is used to correct the acquired image counts for counts lost due to detector.

Iterative Reconstruction

OSEM updates starting from 8 to 280 were plotted against the normalised total activity and activity concentration (Fig. 3-7). In this study, we acquired a 64-angle SPECT acquisition from each detector (a total of 128 angles). This means 128 angles can be distributed evenly to 2,4,8, & 16 subsets. We used eight subsets, so the reconstructed images are updated 16 times for each iteration. Increasing updates increased total activity towards convergence, and 90% convergence was obtained at approximately 80 updates.

The CoV and RE values were calculated to estimate the precision and accuracy of OSEM updates for quantitative purposes. Figure 3-8 illustrates that CoV, as a percentage, increased with increasing updates for both systems (INTEVO BOLD & PRECEDENCE). For the SUV-SPECT quantitative calculations, activity concentrations in kBq/ml were considered the principal representative value, optimised with increasing precision at 80 updates, when the CoV fell below 10% (3% CoV for INTEVO BOLD and 8.5% CoV for PRECEDENCE cameras).
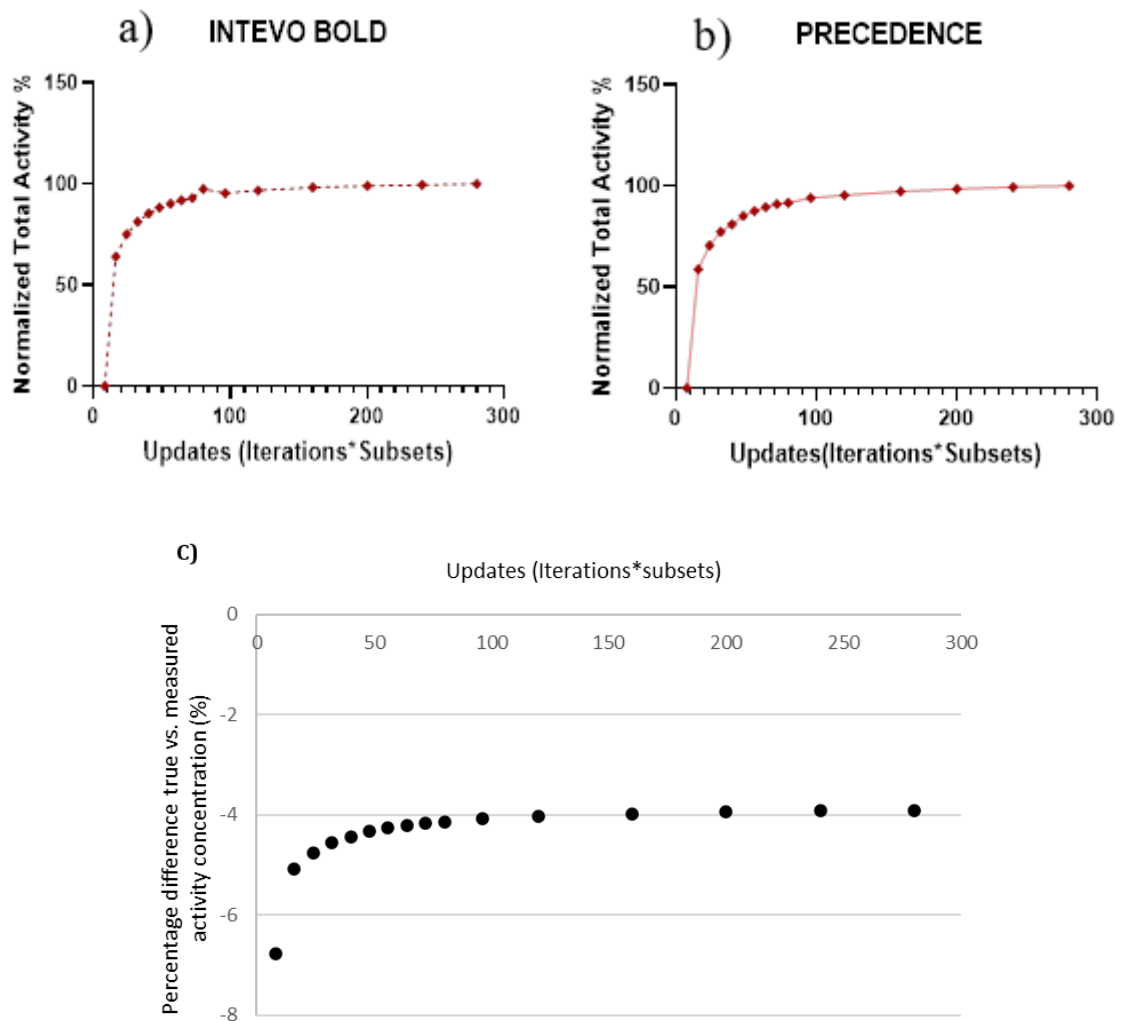
Figure 3-7: Iterative reconstruction using OSEM starting from 8 to 280 updates for ^{177}Lu cylindrical phantom experiment filled with 1137 MBq. VOI delineated in consecutive ROIs over phantom trans-axial view on CT image and copied to SPECT data. Normalized Total counts increased with more updates, and convergence reached 80 updates for both scanners a) and b). c) Measured & true activity concentration (kBq/ml) difference (%).
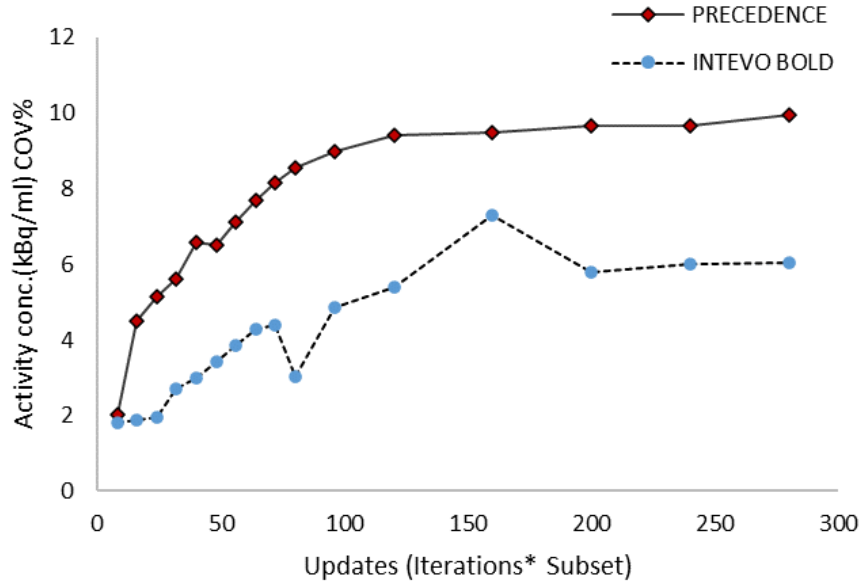
Figure 3-8: Increasing updates on activity concentration using CoV as precision measurement.

As shown in figure 3-9, the obtained RE reached a minimum value of 1% at 80 updates for the PRECEDENCE system. However, the INTEVO BOLD system showed a higher RE (6%) than the PRECEDENCE at 80 updates. A seemingly smoother variation of noise with increasing updates on the PRECEDENCE reconstruction platform seems to indicate some sort of regularisation in the implementation of the algorithm.

Moreover, the effects of the OSEM updates on the noise level of the SPECT/CT images were investigated visually using data from an MRT patient study performed 24 hours post-administration of ^{177}Lu-DOTA-TATE. Figure 3-10 illustrates increased image noise as more counts were recorded with more updates.
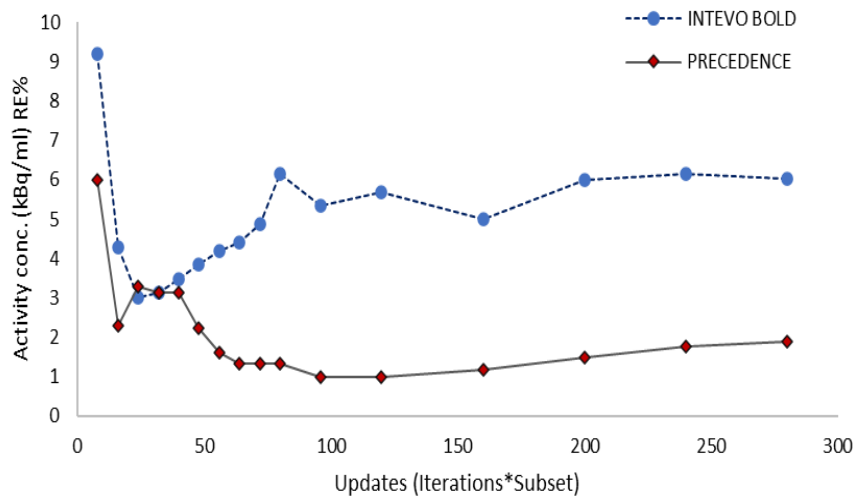
Figure 3-9: Increasing updates on total counts, count rate, and activity concentration. Relative error was obtained as an accurate measurement. VOI were delineated manually using CT image reference
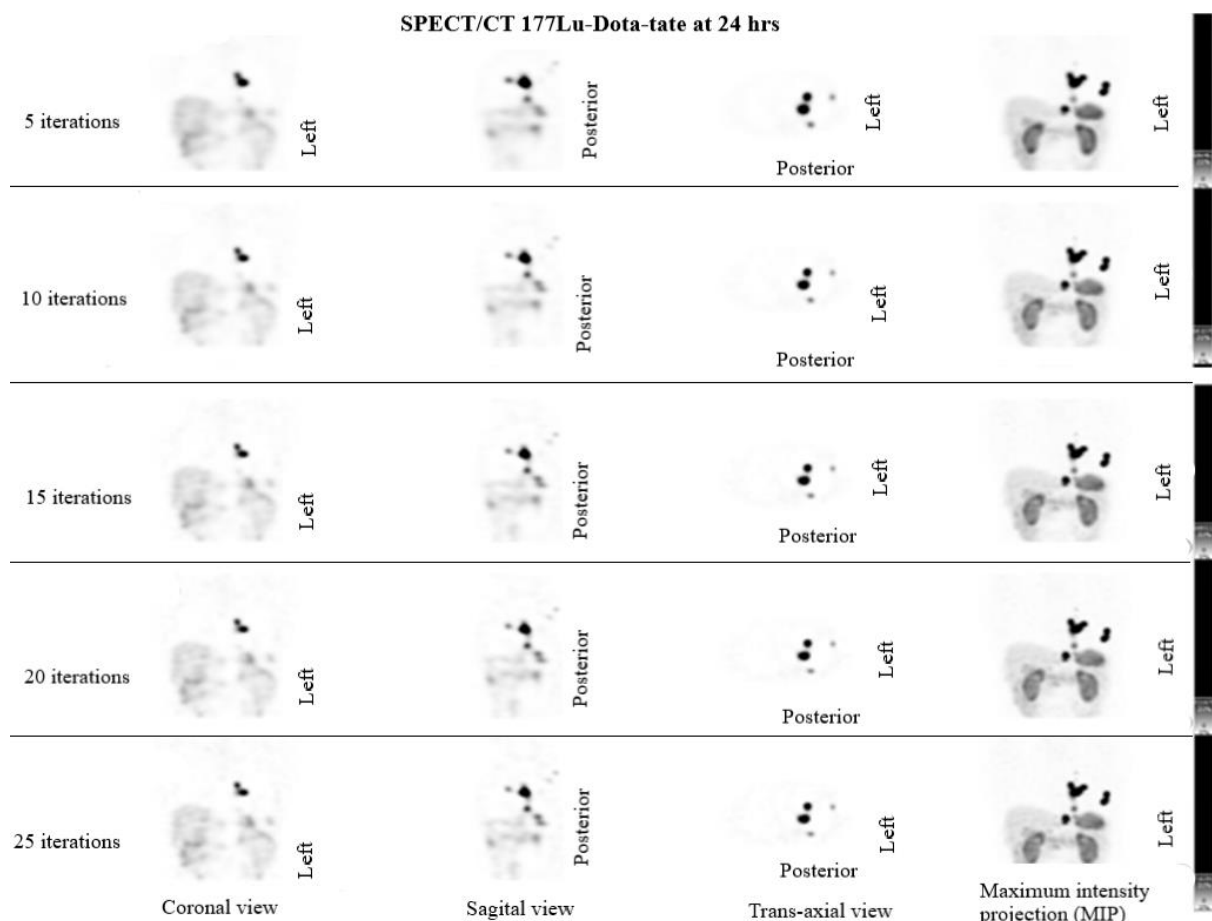
Figure 3-10: Visual evaluation of noise level using OSEM (5,10,15,20,25 iterations and eight subsets) reconstructed SPECT images from MRT patient study 24 hours post-administration ^{177}Lu-DOTA-TAT

SUV-SPECT Analysis

SUV-SPECT values presented an optimal SUV_{mean} equal to 1 and a measured activity concentration using HERMES with a less than 5% difference compared with the true activity from the dose-calibrator for the PRECEDENCE system and a less than 2% difference compared with the value for the INTEVO BOLD system (Table 3-6). More factors that might affect the SUV value, including several OSEM updates and thresholds, were analysed and presented in figure 3-11. Several OSEM updates showed no effects on the SUV_{mean}, but the SUV_{max} and SUV_{peak} values increased slightly with more updates. In contrast, the relative to max threshold method (VOI with an isocontour percentage growing for the maximum voxel position) presented no effects on SUV_{max} and SUV_{peak}, whereas the SUV_{mean} achieved an outstanding value at a 45% threshold. Figure 3-12 confirms that a 40%–45 % of maximum SUV threshold showed a more reliable estimation of the actual phantom activity with minimum relative errors of 0.1% and 1%, respectively.

Table 3-6: Cylindrical homogeneous phantom SUV values generated using HERMES SUV-SPECT software for three SPECT/CT systems using 80 updates OSEM.

System		SUV_{mean}	SUV_{min}	SUV_{max}	SUV_{peak}	Measured activity concentration (kBq/ml) Hermes	True activity concentration (kBq/ml) Dose-calibrator	Difference %
PRECEDENCE (Philips)		1.00	0.78	1.37	1.35	132	138.6	5
INTEVO (Siemens)1	BOLD	1.02	0.81	1.19	1.16	172.2	172.5	0.2
INTEVO (Siemens)2	BOLD	1.01	0.87	1.24	1.2	171.2	173.5	1.3
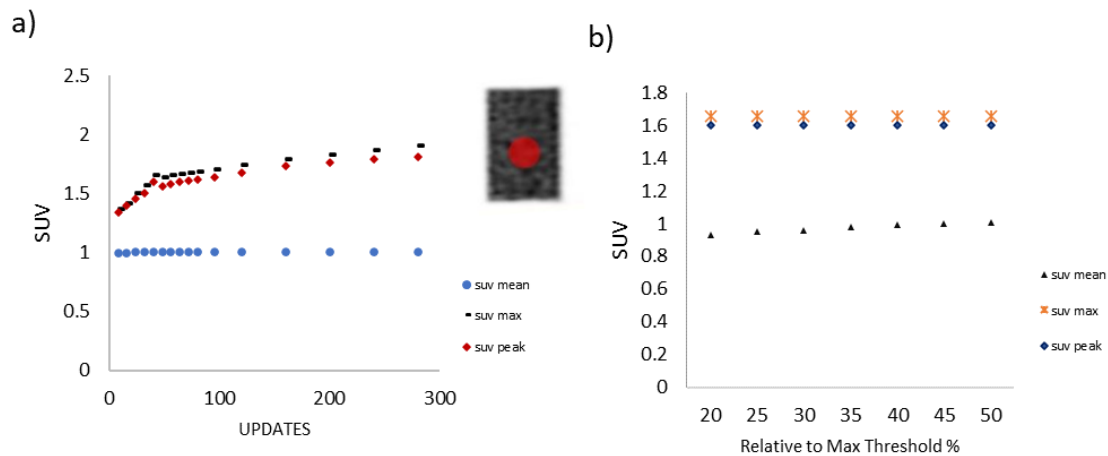
Figure 3-11: Effect of a) OSEM updates and b) relative to maximum SUV threshold% on SUVmean, SUVmax, and SUVpeak.8-cm sphere VOI was delineated at the middle of the phantom.

.
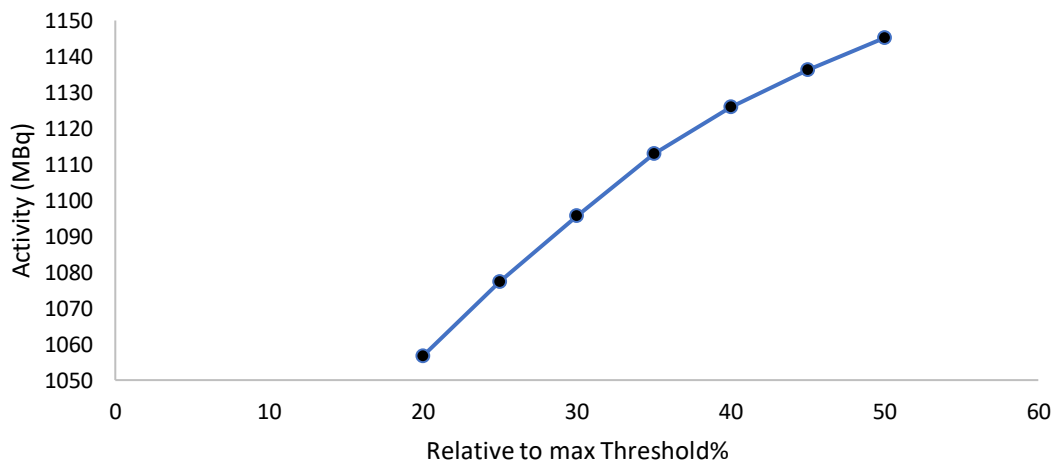
Figure 3-12: Threshold effects on total cylindrical homogenous phantom activity (scan time was 1137 MBq).

.

Concentration Recovery Coefficient (cRC)

For validation purposes, these measurements were also performed on the NEMA IEC. The cRC

curve created for each sphere showed the effects of increasing OSEM update numbers and VOI

delineation using spherical and threshold methods.

We estimated the SUV value and RC for each object to correct the PVE and accurately quantify the VOI. The cRC tends to increase with increasing sphere sizes and update numbers. With a 37-mm diameter, the ^{177}Lu immense sphere showed an almost optimal cRC, equal to 1 at 80 updates (Fig. 3-13a). At 80 updates, the SUV_{max} presented the closest value to the true SUV_{max} (Fig. 3-13, b).

We identified the optimal percentage threshold of the maximum voxel value to define sphere volume accurately using various relative to max threshold values. The VOI delineation method had no effects on SUV_{max} or SUV_{peak}, whereas SUV_{mean} reached an excellent value equal to 1 at a 45% threshold. Figure 3-14 confirmed that a 33%–34 % threshold value resulted in a more reliable estimation of the actual sphere volume for the ^{177}Lu immense sphere (37 mm diameter).
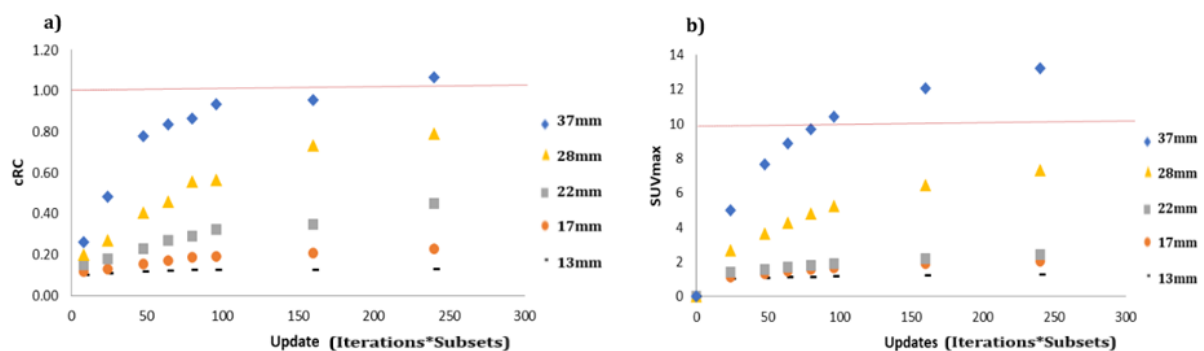
Figure 3-13: a) Recovery coefficient (RC) of mean activity concentration (kBq/ml) and b) SUVmax versus updates for the 13mm, 17mm, 22mm, 28mm, & 37mm. SUV sphere-to-background ratio was 10:1 for all spheres. 10mm sphere was excluded due to low activity contrast compared to the background.

.
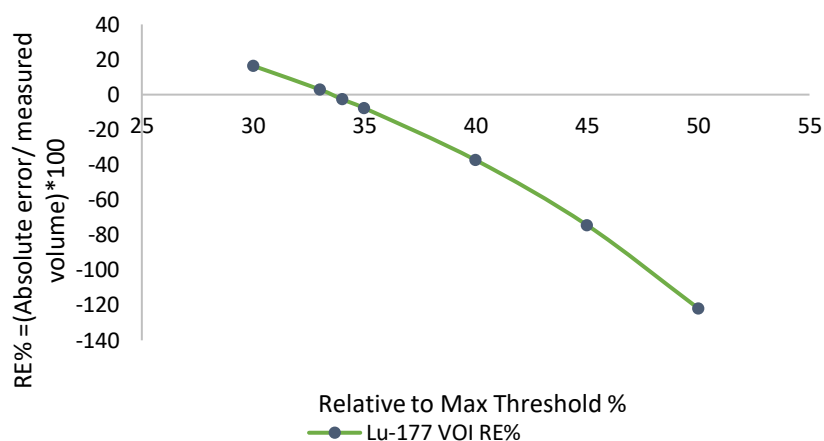
Figure 3-14: Effect of VOI delineation method using relative to max Threshold % on 37mm sphere volume.

3.4.2. ^{131}I-NaI 2D and 3D Image Optimisation and Validation

System Calibration Factor (CF)

Both Siemens systems showed comparable CF/detector using the thyroid neck phantom (Table 3-7). Both systems' CF geometric mean was equal to 6cps/MBq/detector.

Table 3-7: Systems whole-body calibration factors (CF, cps/MBq) per detector and geometric mean (GM) using ^{131}I whole-body thyroid uptake neck phantom imaging.

ID	Detector	CF (cps/MBq)	Geometric Mean CF (cps/MBq)
INTEVO BOLD (Siemens) System	Anterior	10	6.3
	Posterior	4	
Symbia T16 (Siemens) System	Anterior	9	6
	Posterior	4	

HERMES SUV-SPECT software was used to calculate the volume CF for ^{131}I-SPECT/CT. The CF (41 cps/MBq) was standardised for the INTEVO BOLD system. Both systems' CFs were used to estimate the phantom activity, and these values were compared against the true activity value (Table 3-8). The CF of 41 cps/MBq resulted in the most accurate activity estimate (51.6 MBq), which differed from the true activity (calibrator) by < 1%.

Table 3-8: ^{131}I radionuclide calibration factor (cps/MBq) for three SPECT/CT scanners. CF generated using HERMES SUV-SPECT software (OSEM, scatter and attenuation correction, CDR, 48 updates (6 iterations & 8 subsets)

ID	CF (cps/MBq)	Measured activity concentration (kBq/ml) Hermes	True activity concentration at scan time (kBq/ml) Dose-calibrator
INTEVO BOLD (Siemens)System 1	41	6.3	6.2
INTEVO BOLD (Siemens)System 2	42	6.4	6.2

Iterative Reconstruction

OSEM updates starting from 8 to 280 were plotted against the normalised total activity and activity concentration (Fig. 3-15). Subsets of 8 were used for all iterations to reconstruct 64 acquired projections. Total activity increased with increasing updates, and 90% convergence was obtained at approximately 48 updates.

Figure 3-16-a illustrates that CoV, as a percentage, increased with increasing updates. For the SUV-SPECT quantitative calculations, activity concentrations in kBq/ml were considered the principal representative value, which was optimised with increasing precision and plateaued at a minimum CoV value of 3% between 16 and 48 updates. As shown in figure 3-16-b, the obtained RE reached the peak RE of 4% at 32 updates and declined gradually to 0.5% at 280 updates.

INTEVO BOLD
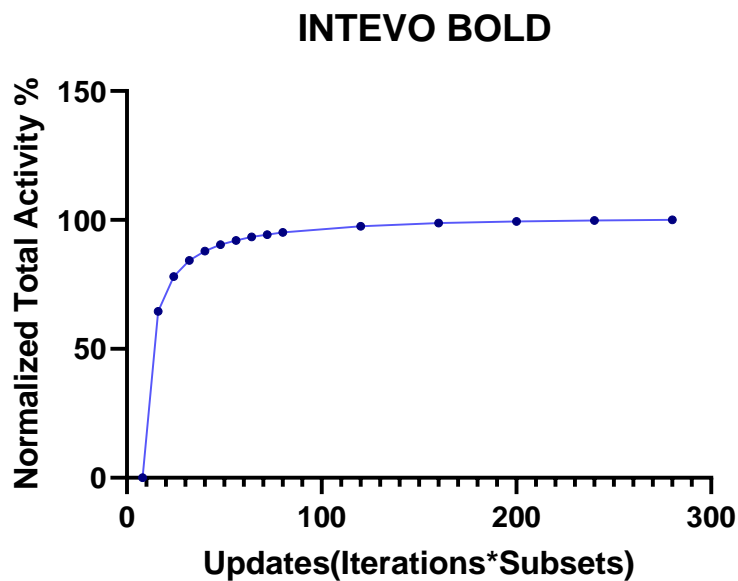
Figure 3-15: Iterative reconstruction using OSEM starting from 8 to 280 updates for ^{131}I-cylindrical phantom experiment filled with ~51 MBq. VOI delineated in consecutive ROIs over phantom trans-axial view on CT image and copied to SPECT data. Normalised total activity increased with more updates, and 90% total activity convergence was reached with 48 updates.
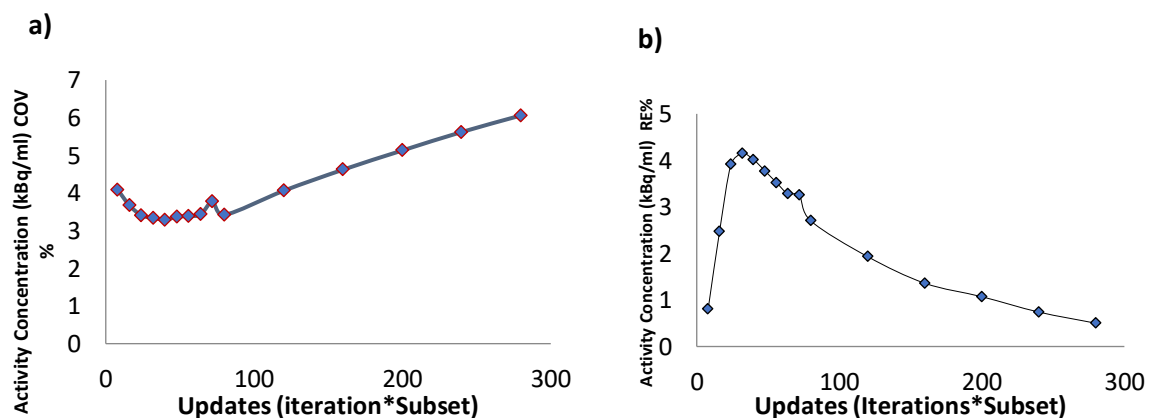
Figure 3-16: Effects of an increasing number of updates on activity concentration using a) Coefficient of variation (CoV) as precision measurement and Relative error (RE) obtained as an accurate measurement. VOI were delineated manually using CT image reference.

SUV-SPECT Analysis

SUV-SPECT values presented an optimal SUV_{mean} equal to 1 and a measured activity concentration with less than a 1% difference compared with the actual value for INTEVO BOLD system (Table 3-9). More factors that might affect the SUV value, including several OSEM updates and thresholds, were analysed and presented in figure 3-17. Several OSEM updates showed no effects on the SUV_{mean}, but the SUV_{max} and SUV_{peak} values increased slightly with more updates. In contrast, the threshold method presented no effects on SUV_{max} and SUV_{peak}, whereas the SUV_{mean} achieved an outstanding value at a 45% threshold. Regarding estimated sphere volume, figure 3-18 confirmed that the 30 % threshold showed a more reliable estimation of accurate volume for the immense sphere (37mm diameter).

Table 3-9: Cylindrical homogeneous phantom SUV values generated using HERMES SUV-SPECT software for three SPECT/CT systems using 48 updates OSEM.

Radiopharmaceutical	CF (cps/MBq)	SUV_{mean}	SUV_{max}	SUV_{peak}	Measured activity concentration (kBq/ml)	True activity concentration (kBq/ml)
^{131}I	41	1.02*	1.21	1.17	6.3	6.22

a)

b)
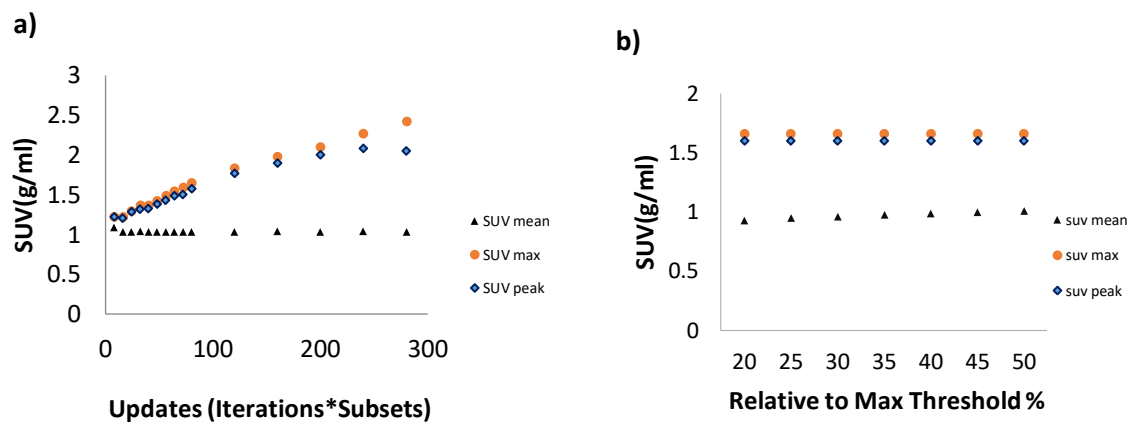
Figure 3-17: ^{131}I-NEMA Phantom, Effect of a) increasing updates and b) increasing relative to max threshold on SUVmean, SUVmax, and SUVpeak.

.
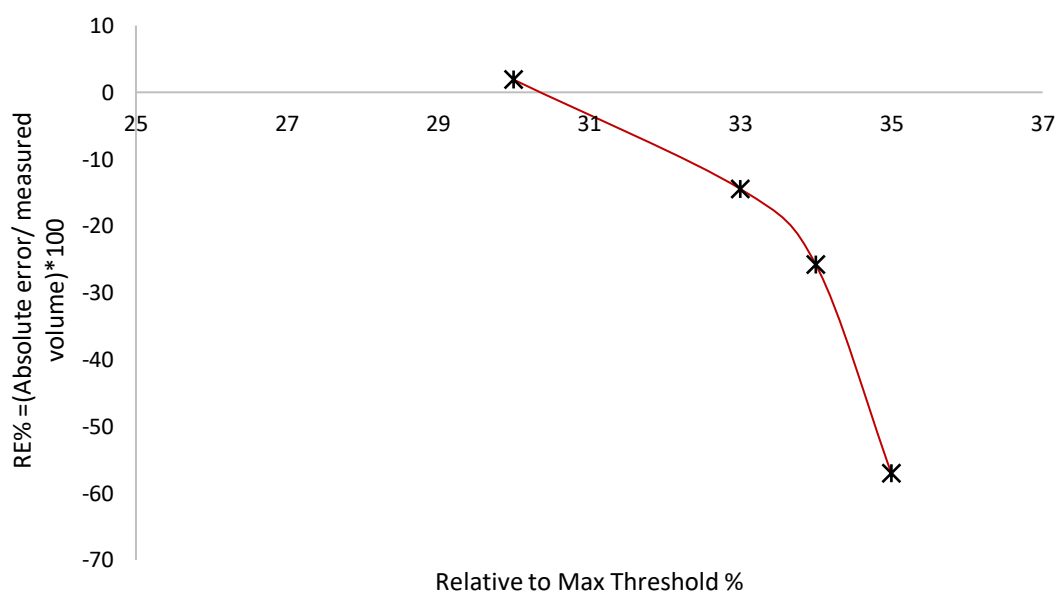
Figure 3-18: Effect of VOI delineation method using relative to max Threshold % on 37mm sphere volume (131I-NEMA Phantom) (True volume is 26 cc)

Concentration Recovery Coefficient (cRC)

The cRC tends to increase with increasing sphere sizes and update numbers. With a 37-mm diameter, the largest sphere showed an almost optimal cRC, equal to 1 at 48 updates (Fig. 3-19-a). At 48 updates, the SUV_{max} presented the closest value to the true SUV_{max} (Fig. 3-19-b).
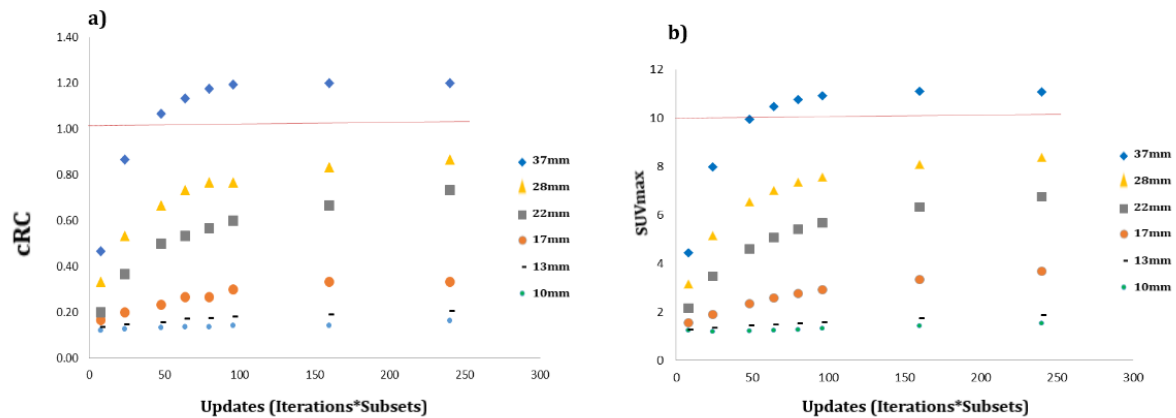
Figure 3-19: ^{131}I-NEMA Phantom a) Recovery coefficient (RC) of mean activity concentration (kBq/ml) and b) SUVmax versus updates for the10mm, 13mm, 17mm, 22mm, 28mm, & 37mm. SUV sphere-to-background ratio was 10:1 for all spheres.

3.5. Discussion

The standardisation and validation methods presented in this study confirmed the feasibility of performing ^{177}Lu and ^{131}I quantitative SUV-SPECT/CT with optimised reliability. This study investigated the quantitative accuracy and precision of both reconstructed activity concentrations and SUV. The protocol was based on MIRD23, MIRD24 MIRD26, and IAEA (2014) guidelines and recommendations (Dewaraja et al., 2012, 2013; IAEA, 2014.; Ljungberg et al., 2016). The primary aim was to estimate the optimum system sensitivities (CF) and the cRC. Accuracy was evaluated using several compensation methods, such as OSEM updates and defining the VOI (Table 3-10).

Table 3-10: Standardised SPECT/CT acquisition and processing parameters for ^{177}Lu and ^{131}I

Radiopharmaceutical	System	Number of views/ Detector	Acquisition time/View (second)	Energy window	Collimator	CF (cps/MBq)	OSEM Updates (iterations *subsets)	VOI segmentation (Percentage threshold of maximum SUV)
^{177}Lu	PRECEDENCE (Philips)	64	20s	208 keV	ME	11.1		
	INTEVO BOLD (Siemens)System 1					11.7	80 (i10*s8)	33%
	INTEVO BOLD (Siemens)System 2					10.8		
^{131}I	INTEVO BOLD (Siemens)System 1	32	25s	364 keV	HE	41	48 (i6*s8)	30%
	INTEVO BOLD (Siemens)System 2					42		

A key factor that can affect activity recovery is the number of OSEM updates; As updates increase, the image noise increased, and image voxels converged to higher values. The CoV values were measured and tended to increase with increasing updates. However, a slight reduction in the ^{177}Lu CoV by almost 1% was observed at 80 updates for the INTEVO BOLD system, which recovered to 2% with additional updates. This finding was comparable to the results reported by Mezzenga et al. (2017), who reported a relationship between the CoV of a Jaszczak homogeneous phantom and the number of updates (Mezzenga et al., 2017). The most noticeable difference observed between the present study results, and those of Mezzenga et al. (2017) was that the ^{177}Lu activity concentration CoV in the present study ranged between 2% and 10% for both systems. However, their study reported a CoV's 10% to 20% range. They suggested that the CoV difference between a homogeneous and a Jaszczak phantom could be due to differences in VOI positioning (Mezzenga et al., 2017). The VOI delineation method can significantly alter both CoV and RE values. To overcome this issue, a standardised method was used to define VOIs, as described in the present study's Methods. Fortunately, this provided us with a more reliable estimate of activity for each VOI at different update levels. In terms of the quantitative precision and accuracy of SPECT, increasing updates reduced the precision

but increased the accuracy. MIRD pamphlet no. 23 agree with CoV and RE findings and the number of updates (Dewaraja et al., 2012). This study used 80 updates as the optimum OSEM reconstruction as almost 90 % of ^{177}Lu total activity convergence was reached.

Representative patient ^{177}Lu-DOTA-TATE SPECT/CT images were used to evaluate the noise levels as a function of update numbers. The noise level appeared to increase with an increasing number of OSEM updates. At 80 updates, acceptable image contrast, noise level, resolution, and quantification were achieved, as shown in figure 3-10. Consequently, optimum diagnosis and quantitative assessment support MRT follow-up and interpatient comparisons. MRT optimisation to obtain clinically meaningful results was expressed by using SUV values. SUV is considered a convenient method for quantifying SPECT uptake that has been normalised against the injected activity and body habitus. Our phantom study showed a steady SUV_{mean} with an ideal value equal to 1, indicating the homogeneous distribution of activity for both radioisotopes ^{177}Lu and ^{131}I.

To evaluate PVE correction, we reported the cRC from six spherical inserts of various sizes. The highest recovery was observed with higher update numbers. The largest two inserts (26.5 ml and 11.5 ml) achieved 95% and 57% ^{177}Lu activity concentration recovery rates after 96 updates. The maximum cRC values for these inserts increased 100% and 80%, respectively, at 240 updates, and these values are similar to the reported 85% and 75% values (Hippeläinen et al., 2016).

Three SUV metrics are used to evaluate PET images, including the SUV_{mean}, SUV_{max}, and SUV_{peak}. SUV_{max} is the most used metric for PET quantification, representing the maximum SUV within a volume. The SUV_{mean} represents the mean value of all SUVs within a segmented volume. The SUV_{mean} depends on the threshold technique for VOI delineations, and higher sensitivity to PVEs makes it less usable (Frey et al., 2012). SUV_{peak} has become more widely used because it is less affected by VOI delineation than SUV_{mean} and less affected by PVE than

SUV$_{mean}$. SUV$_{peak}$ refers to the maximum activity concentration in a 1 cm^3 volume within a VOI. Because the VOI delineation method can affect SUVs, the standardised method was assessed using a NEMA body phantom. Using CT images as a reference to define VOI is the preferred method due to its high-resolution anatomic image set. However, if the VOI cannot be determined on a CT image, relative to the max threshold and manual methods can be used. Concerning ^{131}I, the calibration factor has been tested using the same method applied in many studies (Dewaraja et al., 2005; Gear et al., 2020; Gregory et al., 2019; Zhao et al., 2018). Variations of reported CF were reported between different manufacturers and detector physical properties and collimator types for ^{177}Lu and ^{131}I (Lassmann & Eberlein, 2018; Zhao et al., 2018). In addition, the reconstruction software algorithm can cause a considerable difference in CF for the same SPECT/CT scanner model and manufacturer. A recent study reported ^{131}I-CF of 74cps/MBq for the INTEVO BOLD system using Vendor-specific reconstruction software/algorithm (Taprogge et al., 2020). Moreover, only a 1.5% difference was reported for the ^{131}I-CFs when different source geometries, such as a cylindrical phantom, a sphere in cold cylindrical phantom, a sphere in air and a point-source, were applied (Morphis et al., 2021). Our study obtained the volume CF using a homogeneous cylindrical phantom that mimics the patient's habitus scatter and attenuation conditions (Dewaraja et al., 2013).

Both radioisotopes ^{131}I and ^{177}Lu SPECT/CT quantification are feasible with high accuracy and can be optimised using standardised acquisition and reconstruction methods, as shown in our results. Quantitative image optimisation and a validation process must be developed and tested for each radioisotope, system model, physical detector properties, crystal thickness, and collimator type.

Iterative reconstruction of 48 and 80 updates for ^{131}I and ^{177}Lu was chosen to apply to prospective patient data. This selection was based on 90% total activity convergence, and cRC for the immense sphere (37 mm) met the ideal value of 1. Moreover, a 30% VOI threshold for

[131]I will define lesion or remnant thyroid tissue for differentiated thyroid cancer MRT. This agreed with a reported study that showed a robust linear correlation (R=0.99) in determining volume activity concentrations using 30% VOI threshold and maximum-voxel dosimetry methods (activity per voxel) (Mínguez et al., 2016).

The major challenge in quantitative MRT imaging is the partial volume effect (PVE). It is more considerable in ^{131}I due to the high energy collimator's septal scatter and penetration. The PVE can be compensated partially by applying CDR in reconstruction. However, the NEMA phantom with spheres validation method can compensate for the spill-in or spill-out effect using the mean concentration recovery coefficient (Morphis et al., 2021; van Gils et al., 2016).

3.6. Conclusion

SUV-SPECT/CT quantification can be optimised with implemented compensation protocols. This study investigation showed the optimal accuracy and precision of absolute SUV-SPECT/CT quantification protocols for ^{177}Lu and ^{131}I SPECT/CT. Optimised and validated SUV metrics can be considered for monitoring a treatment response during MRT using ^{177}Lu and [131]I.

CHAPTER 4

4. Neuroendocrine Tumour (NET) PRRT Response Assessment Using Quantitative SUV-SPECT-PET & Biochemical Metrics

Abstract

Aim/Introduction: Single-photon emission computed tomography (SPECT)/computed tomography (CT) and positron emission tomography (PET)/CT imaging are routinely used to verify radiopharmaceutical distribution in patients undergoing peptide receptor radiotherapy (PRRT). We used quantitative imaging, combined with clinical metrics, to investigate whether serial changes in standardised uptake values (SUVs) correlated with clinical response in neuroendocrine tumours (NETs).

Method: Retrospective data from 20 patients with histologically confirmed, unresectable metastatic NET were analysed. Patients received four cycles of 7.4 GBq Lutetium-177 [^{177}Lu] Lu-DOTA-TATE therapy and had pre-treatment and post-treatment PET/CT images using Gallium-68 [^{68}Ga] Ga-DOTA-TATE. SUV was measured in individual lesions and normal tissues from 40 SPECT/CT images (24 h post-PRRT Cycles 1 and 4) and 39 PET/CT scans. Haematological parameters and biochemical markers (including chromogranin A [CgA] and chromogranin B [CgB]) were assessed before Cycles 1 and 4.

Results: A significant correlation was shown between SPECT/CT- and PET/CT-derived SUV measurements ($r_s = 0.8$, $p < 0.05$). The SUV_{max}-SPECT/CT for Cycle 1 PRRT varied from 2.5 to 141.7 (mean 30 ± 24). The SUV_{max}-PET/CT at baseline before PRRT ranged from 11.5 to 105 (35 ± 18). A decrease in the SUV_{max}-SPECT/CT, ranging from -0.25% to -98% (mean $-45\% \pm 29.6\%$), was observed in 89% of lesions following PRRT. The PET/CT SUV_{max} was reduced by $34\% \pm 27.5\%$ in 66% of lesions. Lesion to spleen (LTS) and lesion to liver (LTL) ratios showed a strong, positive, linear correlation ($r_s = 0.8$, $p < 0.05$) in both SPECT/CT and PET/CT imaging. CgA and CgB showed moderately positive correlations with changes in SUV-SPECT/CT metrics.

Conclusion: Measurement of SUV changes derived from quantitative SPECT and PET/CT is useful and feasible to evaluate response to radionuclide therapy. SUV-SPECT/CT can be used as an early assessment metric between successive PRRT cycles.

4.1. Introduction

Neuroendocrine tumours (NETs) are abnormal growths originating from enterochromaffin cells in the bronchial and gastrointestinal tracts. Gastroenteropancreatic (GEP) NETs are tumours that originate in the gastrointestinal tract and pancreas. The classification of neuroendocrine tumours is discussed in more detail in Chapter 1, section 1.1.2. NETs are grouped according to their proliferation index (Ki67) into three main grades for prognosis stratification. Grades 1 and 2 (G1 and G2) NETs are well-differentiated, with benign behaviour for G1 and low-grade malignant behaviour for G2. Grade 3 (G3) NETs are characterised by poor differentiation and high-grade malignant behaviour. NET differentiation indicates how similar neoplastic cells are to non-neoplastic ones (Feelders et al., 2012; Rindi et al., 2022).

Generally, NET development involves the overexpression of somatostatin receptors (SSTRs), and the SSTR subtypes SSTR2, SSTR3, and SSTR5 are characterised by a high binding affinity for structural SST analogues (SSAs), such as octreotide and lanreotide (Feelders et al., 2012; Rindi et al., 2022). Octreotate (Tyr^3, Thr^8-octreotide), is a newly developed SST analogue with a 6- to 9-fold higher affinity for SSTR2 than octreotide. The chelated analogue, [DOTA]^0-Tyr^3-octreotate (DOTA-TATE), is labelled with a gallium-68 (^{68}Ga) to perform positron emission tomography (PET) scans to facilitate NET localisation and with the dual β-γ-emitter lutetium-177 (^{177}Lu; $E_{\beta max} = 0.49$ MeV, $R_{\beta max} = 2$ mm, and $T_{1/2} = 6–7$ days) for molecular radiotherapy (MRT) (Kapoor & Kasi, 2022; Navalkissoor et al., 2017; Yang et al., 2014). The longer tumour residence time of radiolabelled octreotate delivers a higher absorbed tumour dose than octreotide (Esser et al., 2006).

[^{177}Lu] Lu-DOTA-TATE binds to NET cells that overexpress SSTR2 and is administered through four intravenous cycles over a total of 8 to 10 months for PPRT (Bodei et al., 2016;

Mujica-Mota et al., 2018). [^{177}Lu] Lu-DOTA-TATE molecular imaging and dosimetry studies can be performed simultaneously, and the [^{177}Lu] Lu-DOTA-TATE compound is the most used theranostic form of peptide receptor radiotherapy (PRRT) today (Bodei et al., 2016).

PRRT is used for the treatment of unresectable or metastatic, well-differentiated NETs, delivering highly localised radiation by targeting SSTR expressing tumour cells (Sorbye et al., 2020) . [^{177}Lu] Lu-DOTA-TATE has been shown to be effective for treating advanced Grade 1 and 2 pancreatic and midgut NETs, resulting in increased overall and progression-free survival (Ezziddin et al., 2014; Strosberg et al., 2017,2021).

PET/CT is a fundamental type of quantitative imaging modality that can be used to determine the standardised uptake value (SUV), which represents the radionuclide concentration in a target volume divided by the injected activity (IA) and normalised according to body weight, body mass, or lean mass as shown in chapter-3 equation 3-1 (Bailey & Willowson, 2013; Kozak et al., 2005). In ^{18}F-FDG PET imaging, high SUV values correspond to the metabolic activity levels of several diseases, particularly cancer (D'Arienzo & Cox, 2017; Jadvar, 2014). PET-peptide imaging demonstrates the SSTR expression status of NET cells that are not visualised on PET-FDG due to their low metabolic rate. PET-peptide avidity is essential in selecting patients for PRRT (Campana D. et al., 2010). Although the role of ^{68}Ga- DOTA-TATE PET/CT-derived SUV as a quantitative means of assessing response to PRRT has not been extensively investigated, a recent review showed that quantitative molecular [^{68}Ga] Ga-DOTA-TATE can be applied during PET/CT imaging to assess the PRRT response (Lee O. et al.,2022). Different SUV metrics were proposed for ^{68}Ga- DOTA-TATE imaging, such as lesional SUV_{max}, mean SUV_{max}, SUV_{max} lesion to the liver ratio, and SUV_{max} lesion to spleen ratio (Ortega et al., 2021; Sharma et al., 2019).

Depending on the half-life of the radiolabel used, nuclear medicine imaging can estimate the whole-body clearance and retention of a therapeutic radiopharmaceutical by both target and non-target organs over several days. A 2-dimensional (2D) gamma camera quantitative approach was applied to generate quantitative data from whole-body planar images (Bailey et al., 2015). However, the accuracy of 2D quantification from planar images is limited by systematic errors, even with the application of scattering and attenuation corrections (Hänscheid et al., 2018; Zimmerman et al., 2017). SUV measured by single-photon emission computed tomography (SPECT) has not been widely investigated as a quantitative tool for assessing MRT response, such as changes resulting from PRRT in NETs. This may be due to limited use of SUV-SPECT in general, potentially related to lack of hardware (e.g., CT for attenuation map derivation) or software resources (e.g., attenuation, scatter, and resolution recovery compensations as part of iterative reconstruction) or lack of established calculation protocols and reporting standards.

SPECT/CT-derived SUV changes have never been investigated or correlated with other well-evaluated PET/CT SUV metrics and biochemical tumour markers, which are currently used to assess the NET response to PRRT. Chromogranin A (CgA) is an accepted biochemical marker used to assess the efficacy of PRRT in NETs. Chromogranin B (CgB) is used as a secondary marker when CgA is within the average reference levels (Monaghan et al., 2016; Ramage et al., 2012). Other NET biomarkers, such as insulinoma-associated protein 1 (INSM1), synaptophysin, neuron-specific enolase, pancreatic polypeptide and SSTR (Rindi et al., 2022) are associated with specific NET subtypes. Paraganglioma, a rare NET type arising from neuroectodermal tissues secretes catecholamines such as dopamine, norepinephrine (noradrenaline), and epinephrine (adrenaline) (Rindi et al., 2022, Mete O. et al., 2022).

4.2. Aims

Image quantification may play a role in monitoring the changes induced by MRT. We hypothesise that, in well differentiated NETs, a decrease in radiopeptide uptake on serial quantitative imaging may correlate with treatment response in NET patients undergoing PRRT.

We assessed the role of quantitative SUV-SPECT/CT [^{177}Lu] Lu-DOTA-TATE response to PRRT in NET, which we compared with pre-therapy and post-therapy [^{68}Ga] Ga-DOTA-TATE SUV-PET/CT values. As there are no published guidelines for using SUV-SPECT metrics, we evaluated all the metrics proposed for PET-peptide imaging, including lesional SUV_{max} and mean SUV_{max}. Lesional SUV_{max} measurements were compared with the homogeneous healthy background SUV_{mean} and SUV_{max} of the liver and spleen tissue. Finally, SUV correlations were compared with the biochemical markers CgA and CgB.

4.3. Methods

SPECT/CT and PET/CT images obtained from 20 NET patients (mean age 62.3 ± 8.8 years) treated at Guy's & St. Thomas' NHS Foundation Hospitals Trust were analysed retrospectively. All patients (9 male and 11 female) were diagnosed with histologically confirmed, unresectable, metastatic NETs. [^{68}Ga] Ga-DOTA-TATE PET/CT imaging was performed before (60 ± 38.5 days) the first cycle and after (100 ± 49 days) the fourth cycle of PRRT (Table 4-1). The biochemical markers CgA and CgB were analysed 3 ± 5.8 days before the first and 102 ± 25.3 days after the fourth cycle of PRRT (Table 4-1).

Table 4-1: Summary of patients' demographics and injected activity descriptive statistics.

	Minimum	Maximum	Mean	Std.
Age (year)	38	78	62	8.8
Weight (kg)	48	122	81	16.8
Height (cm)	157	183	172	7.8
^{177}Lu-Dotatate Injected activity at cycle 1(MBq)	7081	8000	7644	227.2
^{177}Lu-Dotatate Injected activity at cycle 4(MBq)	3780	7843	7317	861.9
^{68}Ga-Dotatate Injected activity Pre-PRRT(MBq)	46	249	149	65.3
^{68}Ga-Dotatate Injected activity Post-PRRT (MBq)	46	215	129	50.4
Analysed lesions number/Patient	2	5	3.55	0.94
Interval between cycle1 PRRT & Pre-PET scan(days)	-167	-1	-60	38.5
Interval between cycle4 PRRT & Post-PET scan(days)	77	169	102	25.3
Interval between cycle1 PRRT & Pre-biochemical tests(days)	0	27	3	5.8
Interval between cycle4 PRRT & Post-biochemical tests(days)	45	273	100	49

All tumours were inoperable, well-differentiated neuroendocrine neoplasms with distant metastases (Table 4-2). 40 SPECT/CT images were acquired 24 hours post PRRT administration, and 39 PET/CT scans (patient Dota-20 had no pre-PRRT ^{68}Ga-DOTA-TATE scan) before and/or after completion of PRRT were analysed. We applied the PERCIST 1.0 protocol for selecting target lesions (Joo Hyun et al., 2016; Wahl et al., 2009) evaluating the single lesion with maximal uptake and up to five lesions per patient (maximum two target lesions per organ) which showed higher uptake than the designated threshold. PERCIST defined the threshold of the lesion to be measurable at baseline to be greater than or equal to one and a half times the liver SUV_{mean} in a 3-cm diameter spherical VOI plus two times its standard deviation (Eq.4-1).

$$Lesion_{Threshold} = Liver_{BKg}(SUV_{mean}) \cdot 1.5 + 2SD \qquad \text{Eq. 4-1}$$

The same target lesions and normal organ delineation method were applied to post-PRRT PET and SPECT following cycle four PRRT to assess changes in SUV. Seventy-one individual SPECT/CT lesions, 63 PETC/CT lesions and non-target organs (liver, spleen, and kidneys) were analysed to assess SUV_{mean}, SUV_{max}, SUV_{peak}, and metabolic volume (MTV). Eight

lesions were not identified in PET due to missing post-PRRT PET in one patient (3 lesions), one patient with a splenic lesion was identified on SPECT but not on PET, and the remaining four lesions were not identified in post-PRRT PET/CT. The whole liver was defined as the ROI for five patients with conglomerate hepatic metastases.

Finally, SUV-SPECT/CT and SUV-PET/CT changes were tested for correlations with the biochemical markers CgA and CgB changes.

Table 4-2: Patients' clinical diagnosis and imaging characteristics

ID	PET scanner- pre/post-PRRT	SPECT/CT scanner for cycle ¼ PRRT	Number of lesions analysed	Disease Distribution	SITE OF ORIGIN	PET outcome after cycle-4 PRRT
DOTA1	Siemens	Precedence	5	Skeletal & liver	Unknown	SD and Skeletal PD
DOTA2	GE	Precedence	4	Liver	Paraganglioma	PD
DOTA3	GE/ Siemens	Precedence	3	Liver & peritoneum	Small Bowel	PD
DOTA4	GE	Precedence	4	Liver, lung, and soft tissue	Atypical Pulmonary Carcinoid	PR
DOTA5	GE/ Siemens	Precedence	5	Liver, bone, and peritoneum	Small Bowel	PR
DOTA6	GE/ Siemens	Precedence	3	Liver, bone, and peritoneum	Small Bowel	PD
DOTA7	GE/ Siemens	Precedence	4	Liver, spleen, and bone	Rectal	PR
DOTA8	GE/ Siemens	Precedence	2	Liver and bone	Atypical Pulmonary Carcinoid	PR
DOTA9	GE/ Siemens	Precedence	4	Liver & peritoneum	Small Bowel	SD
DOTA10	GE/ Siemens	Precedence	2	Liver & peritoneum	Small Bowel	SD
DOTA11	GE/ Siemens	Precedence	4	Liver, peritoneum, and bone	Unknown	PR
DOTA12	Siemens	Precedence	3	Liver and soft tissue	Olfactory	SD
DOTA13	GE/ Siemens	Precedence	4	Liver	Small Bowel	SD
DOTA14	Siemens	Precedence	3	Liver	Pancreatic	PR
DOTA15	GE/ Siemens	Precedence	4	Liver, peritoneum, spleen, and bone	Small Bowel	Mixed Response
DOTA16	Siemens	Precedence	4	Liver, peritoneum, lung, and bone	Small Bowel	SD
DOTA17	Siemens	Precedence	3	Liver, adrenal, and lung	Small Bowel	SD
DOTA18	GE/ Siemens	Precedence	2	Liver, peritoneum	Small Bowel	PR
DOTA19	Siemens	Precedence/INTEVO	5	Liver, pleural, and bone	Lung	PR
DOTA20	*	Precedence	3	Liver and bone	Paraganglioma	PR

*Dota20 patient had FDG PET/CT pre-PRRT and Ga68-DOTA-TATE post-PRRT.
SD=stable disease, PD=progress disease, PR=partial response.

4.3.1. 3D Quantitative SPECT/CT and PET/CT SUV measurements

SPECT/CT images were acquired 24 hr after [^{177}Lu] Lu-DOTA-TATE infusion (7480±231 MBq) using a Precedence (Philips, Netherlands) system for both cycles, except for one patient (DOTA19) who was imaged for the fourth cycle SPECT/CT using an Intevo Bold system (Siemens, Erlangen, Germany). Medium energy general purpose (MEGP) collimators were used at 180°, with a 128 × 128 matrix, 15% energy window (centred on 208 keV) and a zoom of 1.0. 128 projections were acquired for 20 seconds per angle (64 angles per camera head).

For CT acquisition, the following parameters were used: 1.5 mm thickness, 0.75 mm increments, 120 kV, 100 mA/slice, 1.188 pitch, 0.75 rotation time, 512 × 512 matrix.

For PET/CT, a Siemens Biograph64 mCT (Siemens, Erlangen, Germany) and GE Discovery 710 (GE Healthcare, Chicago, US) were used, as shown in Table 2. Scans were performed one hour after [^{68}Ga] Ga-DOTA-TATE injection (mean IA 138.9 ± 14.2). The average interval between pre-PRRT PET/CT and PRRT was 2 months, and the mean interval between the last PRRT cycle and the post-PRRT PET/CT was three months. For GE system, scan times were 4 min per bed and 5 min per bed for over 100 Kg and 11 overlap slices. For helical, low-dose CT acquisition, the following parameters were used: 2.5 mm thickness, 3.27 mm intervals, 140 kV, auto + smart mA, noise Index of 40, range 15 –100 mA, 1.375 pitch, 0.5s rotation speed, detector coverage of 40 mm (64 × 0.625), and 512 × 512 matrix size. For Siemens system, scan times were 4 min per. For helical, the following parameters were used: 2 mm thickness, 2 mm intervals, 140 kV, 20 mA, Care Dose 4D (ref. 30 mAs), 1.35 pitch, 0.5s rotation speed, detector coverage of 19.2 mm (64 × 0.6), and 512 × 512 matrix size.

4.3.2. 3D Image Reconstruction

SPECT data were reconstructed using the Hermes Hybrid 3D 3.01 beta software program (Hermes Medical Solutions, Stockholm, Sweden). The quantification method was tested and validated using cylindrical and National Electrical Manufacturers Association (NEMA) International Electro-technical Commission (IEC) body phantom.

The patients' SPECT/CT images were reconstructed based on a phantom-optimised protocol, using iterative reconstruction algorithms, ordered subset expectation maximisation (OSEM) with 80 updates (10 iterations and eight subsets), attenuation, scatter, and collimator-detector response correction. The PET/CT images were reconstructed using manufacturers' recommended scanner settings and calibration. The PET/CT reconstruction method for the Siemens Biograph64 mCT was OSEM3D+TOF, 2 iterations, and 21 subsets, whereas 2 iterations with 24 subsets VPFX was used for the GE PET/CT scanner. Similar phantom-based calibration processes to those described in chapter 3 were previously undertaken for PET imaging outside the current study.

The Hermes Hybrid viewer was utilised to calculate SPECT/CT and PET/CT SUV values for both target and non-target tissues (liver, spleen, and kidneys). The VOI for individual lesions was defined using 33% of the maximum SUV threshold for SPECT/CT, as explained in chapter 3 (section 3.4.1). CT trans-axial imaging was used as a reference to delineate the VOI of the spleen, liver, and kidneys (Figure 4-1). For the liver and spleen background, a sphere with a 3 cm diameter was placed at homogenous background intensity of the right hepatic lobe and spleen.

For ^{68}Ga-PET/CT, NEMA phantom imaging was completed as part of departmental routine quality assurance, and we retrieved images to validate the VOI threshold method. The spheres

had activity concentration eight times that of the background activity (8:1). The optimum SUV$_{max}$ values of eight were reached at 42 and 45% of the maximum SUV threshold.
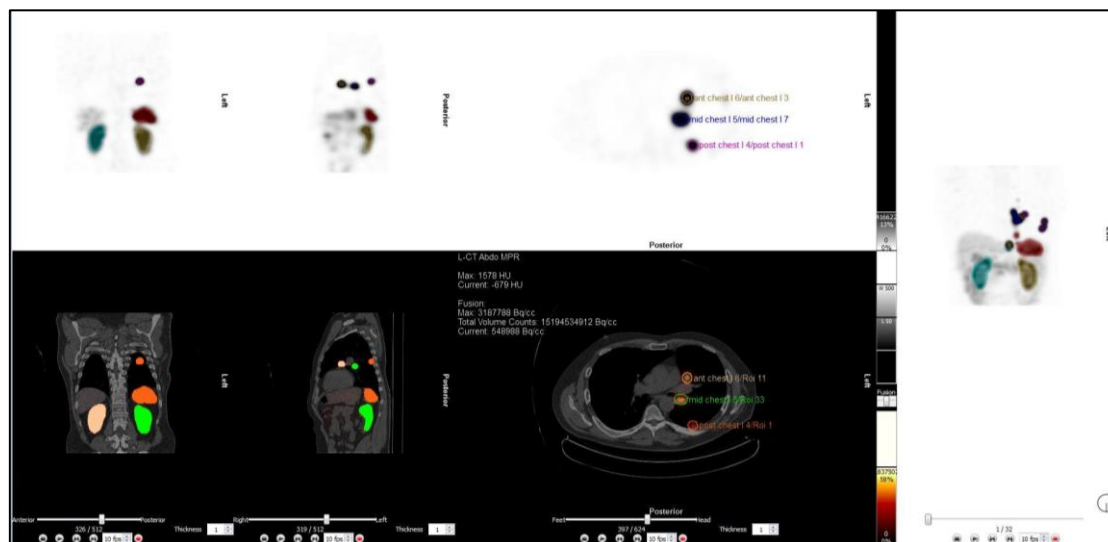
Figure 4-1: SPECT/CT images with defined volume of interest (VOI) in the first cycle of [^{177}Lu] Lu-DOTA-TATE at 24-hr post-PRRT injection using HERMES SUV reconstruction software.

4.3.3. Biochemistry, Haematology, and Tumour Marker Data

Toxicity was recorded using Common Terminology Criteria for Adverse Events v3.0 (CTCAE) (Cancer Therapy Evaluation Program, 2017). Blood sample analysis was performed less than one month before each therapy cycle and 3.3±1.6 months after the final cycle, which aligned with the timing of follow-up PET. Routine haematology, including full blood count [Haemoglobin (Hb), red blood cells (RBCs), white blood cells (WBCs), platelet (PLTs)] and biochemical tests of kidney function parameters [estimated glomerular filtration rate (eGFR) and creatinine], liver function tests [alanine transaminase (ALT), alkaline phosphatase (ALP), bilirubin, and albumin], and the biochemical tumour markers CgA and CgB were measured before and after PRRT (mean interval: 3 ± 5.8 days before and 100 ± 49 days after PRRT). The tumour markers nor-metadrenaline and metadrenaline were substituted for CgA and CgB for patients with metastatic neuroblastoma and paraganglioma. Metadrenaline and nor-

metadrenaline, the inactive metabolites of the catecholamines adrenaline and noradrenaline, showed superior diagnostic sensitivity of paraganglioma over measurement of the parent catecholamines (Därr et al., 2017).

4.3.4. Statistical Analysis

SPSS software (IBM SPSS Statistics *2019* v26.0 for Windows; Armonk, NY) was used for descriptive (mean ± standard deviation,SD) and inferential analyses. The one-sample Kolmogorov–Smirnov normality test was used to verify the normal distribution of data. A paired-sample t-test was used to evaluate the differences among normally distributed data, such as non-target organs, while the Wilcoxon signed-rank test was used to evaluate differences among non-normally distributed data. The Wilcoxon signed-rank test was used to precisely test the null hypothesis that no significant difference exists between SUV values obtained during PRRT. Spearman's correlation coefficient (r_s) was evaluated for nonparametric data, whereas Pearson's correlation coefficient (r) was evaluated for normally distributed data. A *p* value <0.05 was considered significant.

4.4. Results

4.4.1. Target Tissues (Lesions) SUV Changes

SPECT and PET SUV metrics, including the mean, maximum, and standard deviations for all lesions are presented in Table 4-3. Significant differences were observed for SUV-SPECT/CT measurements between Cycles 1 and 4 and for PET/CT SUV measurements between pre-and post-PRRT scans ($p < 0.05$). In addition, strong positive correlations were reported between all SPECT/CT metrics (r_s=0.9, p<0.05). The SPECT/CT MTV metrics showed no significant differences from the SUV metrics (mean, max, and peak, p>0.05). Lesion functional and

anatomical volumes were assessed in 26 lesions and showed no significant differences in cycles 1 and 4 (p=0.29 and 0.5, respectively).

Table 4-3: Descriptive statistics of Lesions SUV metrics at cycle one and four [^{177}Lu] Lu-DOTA-TATE PRRT and pre & post-PRRT [^{68}Ga] Ga-DOTA-TATE. SPECT/CT and PET/CT-SUV

Target tissues (Lesions) SUV	SPECT/CT-PRRT Cycle 1			SPECT/CT-PRRT Cycle 4			
	Maximum	Mean	±SD	Maximum	Mean	±SD	Mean Change %
SUVmean	49	14	10	51	9	9	-34
SUVmax	142	30	24	92	19	18	-39
SUVpeak	131	27	22	88	17	17	-38
MTV*	9223	1304	3066	8584	764	1868	-41

Target tissues (Lesions) SUV	PET/CT Pre-PRRT			PET/CT Post-PRRT			
	Maximum	Mean	±SD	Maximum	Mean	±SD	Mean Change %
SUVmean	63	19	12	66	17	13	-11
SUVmax	105	35	18	103	31	21	-13
SUVpeak	100	28	17	96	24	18	-15
MTV*	9223	1518	3695	9223	1181	3002	-22

*MTV=Metabolic volume (SUVmean*Volume)

Lesions having SUV_{max} higher than the liver-background (Bkg) on baseline PET (Bkg SUV_{mean} =5.5±1.7) and on SPECT (Bkg SUV_{mean}=1.05±0.47) were considered as target lesions.

The estimated threshold (Eq.4-1) for SUV-SPECT was ≥2.5 based on liver background SUVmean=1.04±0.47. The SPECT/CT lesional SUV_{max} after Cycle 1 of PRRT varied from 2.5 to 141.7 (mean: 30 ± 24). A decrease in the SUV_{max}-SPECT/CT was seen in 89% of 71 lesions on completion of PRRT, ranging from −0.25% to −97% (mean: −45% ± 29%). SUV_{max}-SPECT/CT in the remaining eight lesions (12%) increased by 32% ± 47%.

The estimated threshold (Eq.4-1) for SUV-PET was ≥11.5 based on liver background SUVmean=5.5±1.7. Lesional SUV_{max}-PET/CT at baseline before PRRT ranged from 11.5 to 105 (mean: 35 ± 18). The SUV_{max} measured by PET/CT was reduced by a mean of 34% ± 27%

in 66% of lesions (42 lesions). However, 21 lesions showed an increase in the SUV_{max}-PET/CT of 50% $\pm$ 58%.

The mean lesional ^{68}Ga-DOTA-TATE SUV_{max} percentage change was used to assess if the patient responded or not to PRRT. Patients were grouped into four main categories following PERCIST 1.0 guidelines (Complete Response, Partial Response, Stable Disease, and Progressive disease) based on the observed SUV_{max} response to PRRT. Complete response was defined when activity in all lesions was lower than mean liver activity and no new lesions had developed. Partial response was a reduction of $\geq$30% SUV_{max} in target measurable tumour. Stable disease was reported if no new lesions developed and SUV_{max} changes of 0 to < 30% were observed. Progressive disease was defined as an increase of target lesions SUV_{max} >30% (Joo Hyun et al., 2016).

Fifty-five per cent (n=11) of the included sample showed partial response with decreased mean lesional SUVmax $\geq$30%, seven patients showed stable disease with SUV_{max} reduction <30%, and two patients showed a mixed response. Figures 4-2 and 4-3 show examples of patients with different responses to PRRT using SPECT and PET-derived SUV_{max}.
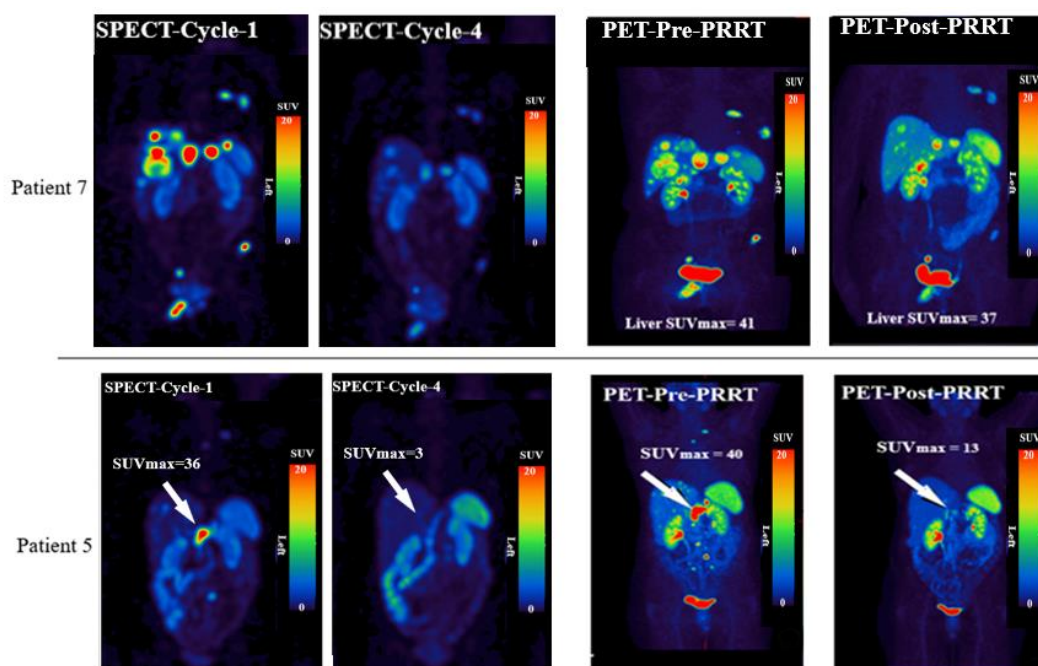
Figure 4-2: Examples of MRT response in two NET patients Dota7 (top) and Dota5 (bottom) with different disease burden. SPECT/CT at 24-h following PRRT cycles 1 and 4 and PET/CT pre- and post PRRT MIP images showing changes in PET and SPECT-derived SUV are visually correlated. Patient 7 (top) shows partial response in both SPECT and PET as SUV reduced by >70%. Patient 5 (bottom) shows>70% reduction in the mid-abdomen lesion(arrow) in both SPECT and PET.
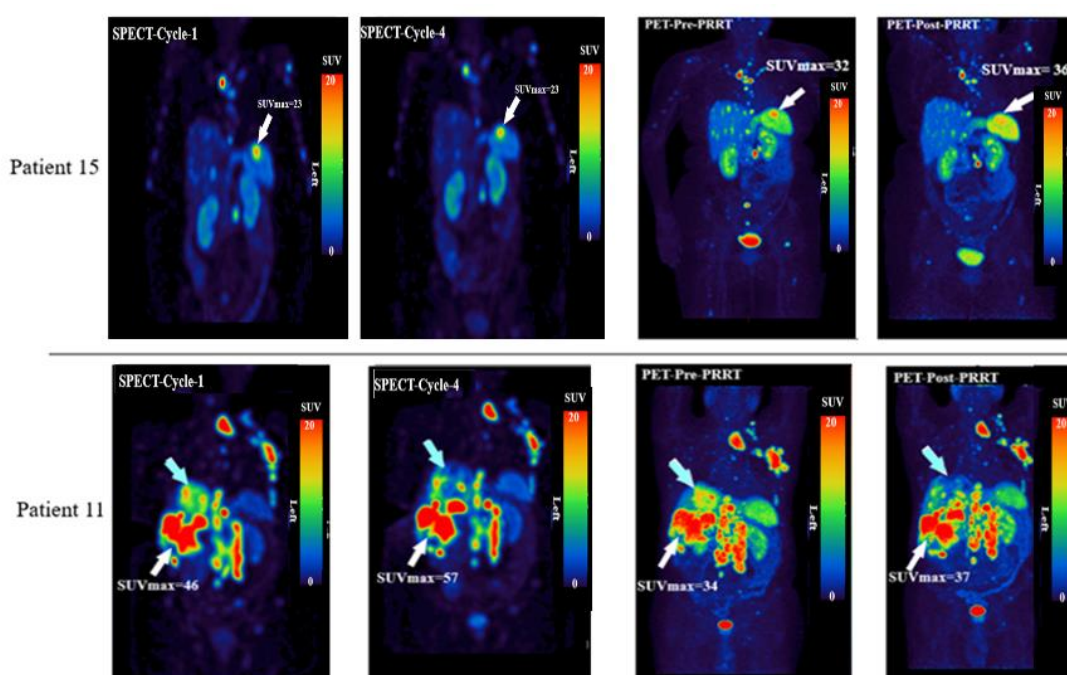
Figure 4-3: Examples of MRT response assessment in two NET patients with different disease burden. SPECT/CT at 24-h following PRRT cycles 1 and 4 and PET/CT pre- and post PRRT MIP images showing patient 15 (top) with a stable disease with no significant SUV change (<30%) and patient. 11 (bottom) with mixed response, upper lobe liver lesion (blue arrow) reduced to background liver SUV, and the lower right lobe liver lesion was increased by 23% in SPECT-cycle-4 and by 9% in post-PRRT PET. The remaining lesions in patient 11 were stable with no SUVmax changes.

Figure 4-4 showed a significant, positive Spearman's correlation between the SUV_{peak} ($r_s =$ 0.75) and SUV_{max} ($r_s = 0.71$) when comparing values derived from SPECT/CT and PET/CT ($P < 0.05$). The four outliers at the lower right side of the graph presented significant increases in the post-PRRT SUV-PET/CT measurements despite a decrease in SUV-SPECT/CT measurements following Cycle 4. Three outliers represented three lesions in one patient (Dota-3) who showed a decrease in mean lesional SUV_{max}-SPECT by 37% and an increase of 162% in PET. However, both CgA and CgB were reduced by 17% and 37%, respectively. The fourth outlier representing mean SUV_{max} of the liver lesion (Dota-16) that was reduced by 21% in SPECT and increased by 151% in PET. Dota-16 patient showed an increase in CgA by 31%, however, CgB decreased by 28%. In contrast, another liver lesion in the same patient (Dota-16) showed a similar SUV_{max} change in SPECT and PET (-16%). The changes in SUV values between SPECT and PET imaging after PRRT may be attributed to a few different factors. One of the main considerations is the difference in the physical properties of the radionuclides used in SPECT and PET imaging. SPECT imaging typically uses gamma-emitting isotopes which have a lower energy and a longer half-life compared to the positron-emitting isotopes used in PET imaging. Due to physical characteristics of the modality, PET imaging may detect more subtle changes in tracer uptake and has a higher spatial resolution. On the other hand, ^{68}Ga is confined to early uptake phase and in some cases may only partially reflect steady state uptake (Ortega et al., 2021; Thuillier et al., 2021).
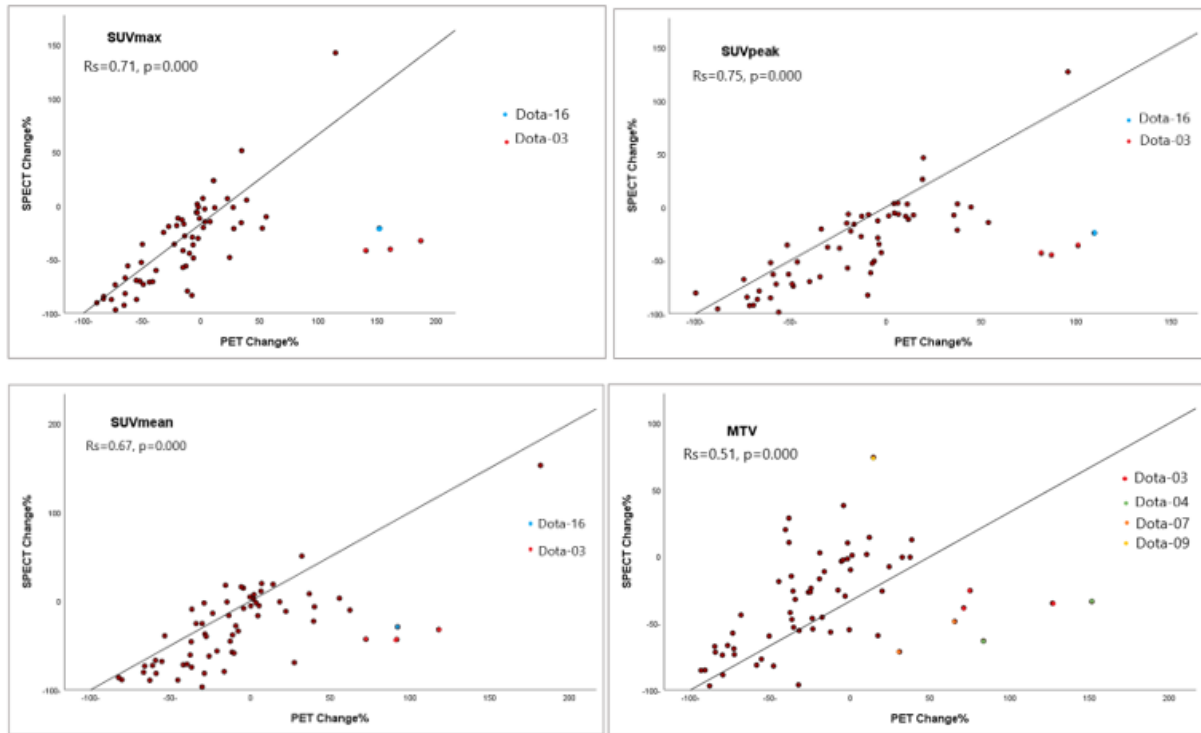
Figure 4-4: Simple scatter graph with reference line showed Spearman's (r_s) correlation (2-tailed) between PET and SPECT lesional SUV & MTV change.

A Bland-Altman agreement plot for differences between SPECT/CT and PET/CT measurements compared with the mean values is shown in figure 4-5. The limits of agreement (LoA) were defined as the mean difference ± 2 standard deviations. The points on the plot were uniformly scattered between the LoA, suggesting good agreement between both SPECT CT and PET CT derived SUV measurements. Approximately 95% of lesions showed SUV-SPECT/CT and PET/CT measurements that were within the LoA on the Bland-Altman plot.
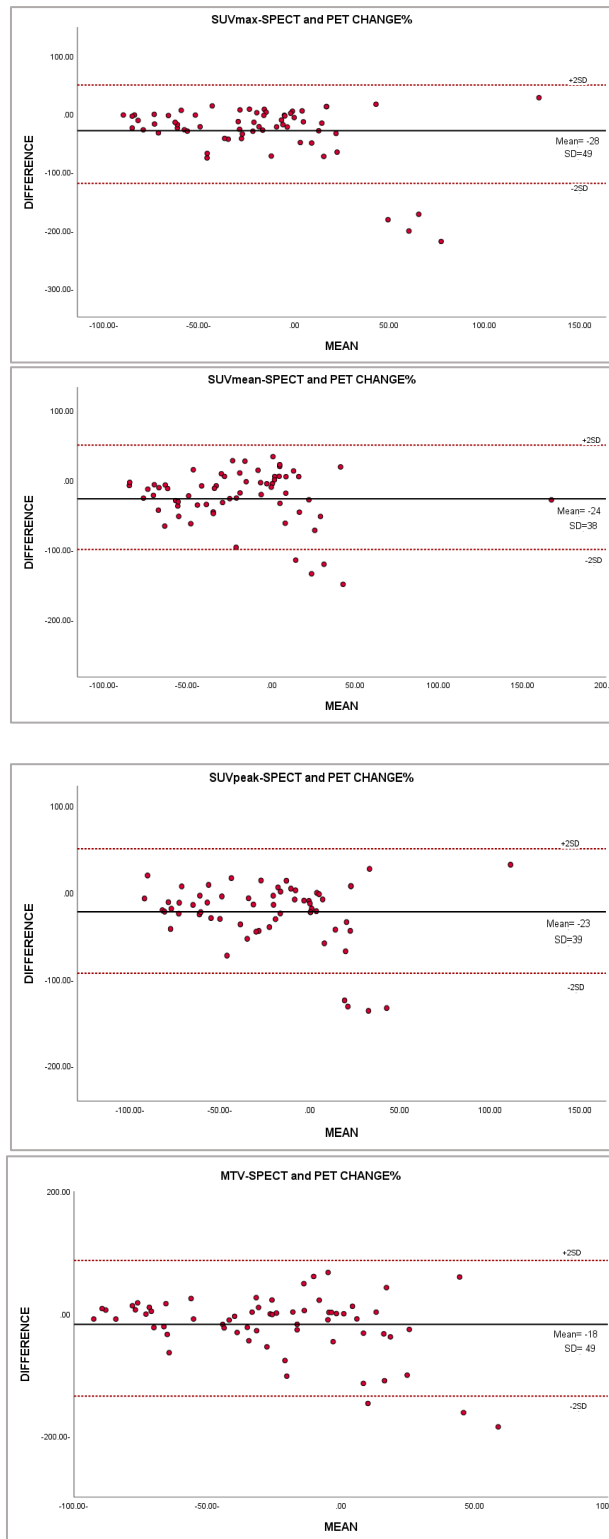
Figure 4-5: A Bland-Altman agreement plots with the difference between SPECT & PET measurements against the mean. The limits of agreement (LoA) are defined as the mean difference ± 2 SD of differences.

4.4.2. Non-target Tissue SUV Changes

Table 4-4 shows descriptive statistics (mean, maximum, and standard deviation) for the SPECT/CT and PET/CT SUV metrics in non-target tissues. Non-target tissues in the liver, spleen and kidneys showed differences in the SUV metrics obtained by SPECT/CT at Cycles 1 and 4. Increased SUV measurements were observed at Cycle 4 for the liver, spleen, and right and left kidneys (17%, 20%, 11%, and 14%, respectively). Comparable increases in the same organs were observed for SUV-PET/CT measurements (11%, 20%, 7%, and 11%, respectively). However, renal SUV metrics showed no significant difference in liver and spleen background ratio between SPECT/CT at cycles one and four ($p > 0.05$).

Functional and anatomical volumes were defined using SPECT and CT images, respectively. A total of 14 spleens, 13 right kidneys, and 15 left kidneys were analysed using a 33% threshold for SPECT functional volume and multiple ROIs manual drawing on CT to create the anatomical VOI in both cycles. One spleen and two right kidneys were excluded from analysis due to splenectomy and two right kidneys were nearby the high uptake liver lesions. Significant correlations ($p < 0.01$) were found between functional and anatomical volumes for the spleen, right kidney, and left kidney ($R = 0.86$, 0.79, and 0.76, respectively). The median differences between the functional and anatomical volumes were not significant for the spleen and right kidney ($p = 0.81$ and 0.74, respectively). However, the left kidney showed significant differences between the anatomical and functional volumes ($p = 0.008$). This may be due to scatter from high uptake in the adjacent organ (spleen) and justifies analysis of the right and left kidneys separately.

Table 4-4: Descriptive statistics of non-target organs SUV metrics at cycle one and four [^{177}Lu] Lu-DOTA-TATE PRRT and pre & post-PRRT [^{68}Ga] Ga-DOTA-TATE.

Non-target organs SUV	SPECT/CT-PRRT Cycle 1			SPECT/CT-PRRT Cycle 4		
	Maximum	Mean	±SD	Maximum	Mean	±SD
Liver Background:						
SUVmean	3.14	1.05	0.47	3.30	1.32	0.53
SUVmax	4.45	1.60	0.69	6.03	1.98	1.05
SUVpeak	3.97	1.63	0.95	4.20	1.66	0.84
Spleen Background:						
SUVmean	10.30	5.43	2.08	12.40	6.39	2.90
SUVmax	12.60	7.23	2.49	17.50	8.76	3.62
SUVpeak	12.20	6.78	2.45	17.20	8.21	3.61
Right Kidney:						
SUVmean	7.55	4.33	1.35	8.28	5.16	1.65
SUVmax	36.46	10.36	6.79	31.95	10.74	5.79
SUVpeak	22.29	8.72	3.92	21.37	9.55	3.86
Left Kidney:						
SUVmean	7.72	4.39	1.47	8.89	5.12	1.70
SUVmax	14.32	8.63	2.48	16.91	9.75	3.00
SUVpeak	13.61	8.11	2.40	15.91	9.16	2.79

Non-target organs SUV	PET/CT Pre-PRRT			PET/CT Post-PRRT		
	Maximum	Mean	±SD	Maximum	Mean	±SD
Liver Background:						
SUVmean	9.41	5.51	1.78	9.22	6.21	1.86
SUVmax	13.03	7.73	2.58	11.94	8.49	2.19
SUVpeak	14.20	6.56	2.63	10.54	7.21	2.00
Spleen Background:						
SUVmean	31.30	15.98	6.37	31.44	18.57	6.74
SUVmax	44.00	19.87	8.35	39.76	23.51	8.17
SUVpeak	37.00	17.78	7.20	36.05	21.44	7.66
Right Kidney:						
SUVmean	18.37	10.68	2.93	18.09	11.95	3.20
SUVmax	76.29	33.43	16.29	81.80	34.97	17.71
SUVpeak	50.64	24.04	9.72	44.26	24.77	8.62

Left Kidney:						
SUVmean	16.74	9.93	3.21	18.72	11.43	2.98
SUVmax	43.90	26.80	9.22	62.40	28.77	12.59
SUVpeak	28.41	19.41	5.65	31.37	21.73	5.79

4.4.3. Lesion to Liver and Lesion to Spleen Ratios

The SPECT/CT and PET/CT lesional SUV_{max} measurements were compared with the background SUV_{mean} and SUV_{max} results in the healthy liver and spleen tissue. The lesional SUV_{max} showed a strong linear correlation with both the background SUV_{mean} and SUV_{max} (r_s = 0.9, p < 0.05), as shown in figure 4-6. Good agreement was observed between background SUV_{max} measurements for the liver and spleen when comparing SPECT/CT with PET/CT (Fig. 4-7). Changes in the lesions overall SUV_{max} to the spleen (LTS) and lesion to liver (LTL) ratios following the completion of PRRT showed significant positive, linear correlations (r_s = 0.8, p < 0.05) in both SPECT/CT and PET/CT measurements (Fig. 4-8). Overall, SPECT LTL and LTS ratios (Cycle-1 ratios 30:1 and 5.6:1, and cycle-4 ratios 18:1 and 3:1, respectively) reduced post-therapy by 40±33% and 46±25%, respectively. However, PET LTL and LTS ratios (pre-PRRT ratios 6.5:1 and 2.2:1 and post-PRRT ratios 5:1 and 1.7:1, respectively) reduced by 23±35% and -25±29%, respectively.
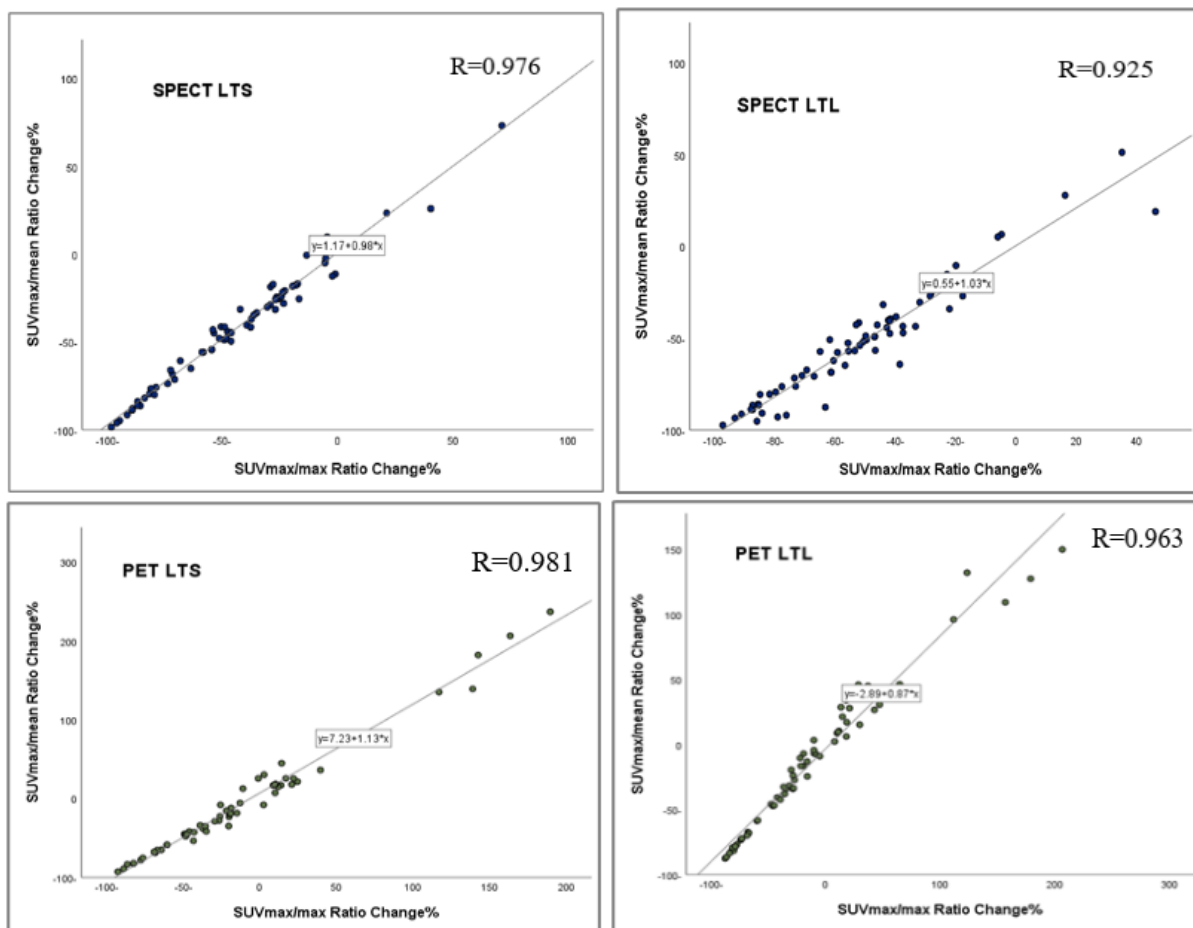
Figure 4-6: Simple scatter graph with reference line showed a linear correlation between lesion to the background (LTS & LTL) SUVmax/mean and max/max in both PET and SPECT.
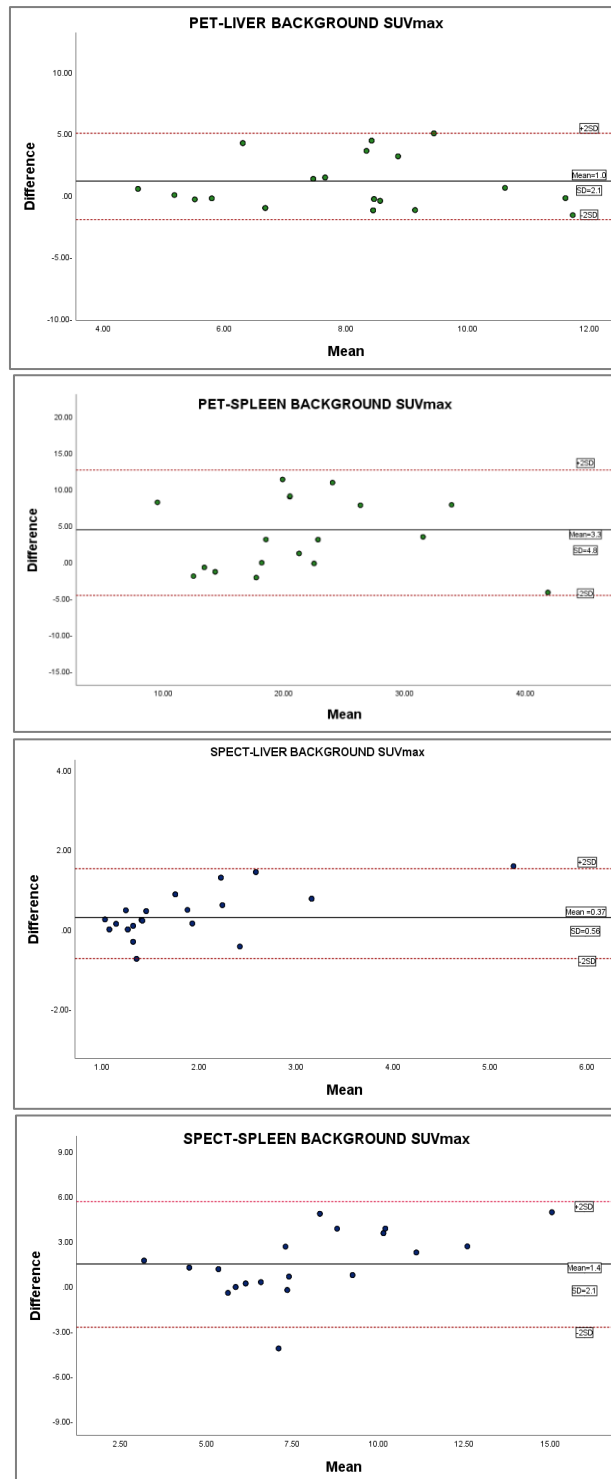
Figure 4-7: A Bland-Altman agreements plot with the difference between liver and spleen background SUVmax measurements (in cycles 1 and 4 for SPECT/CT and pre- and post-PRRT PET/CT imaging) against the mean. The limits of agreement (LoA) as the mean difference ± 2 SD of differences.
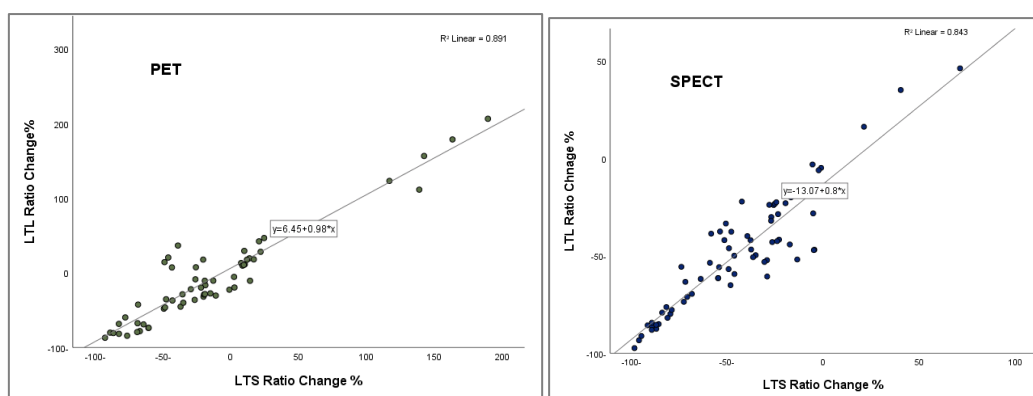
Figure 4-8: Simple scatter graph with a reference line showed a linear correlation between lesion to liver (LTL) and lesion to spleen (LTS) ratio change in PET/CT and SPECT/CT.

4.4.4. Biochemistry and Haematology

Renal (eGFR and creatinine) and liver (ALT, ALP, albumin, and bilirubin) biochemistry function profiles showed no significant changes between PRRT cycles, as shown in Table 4-5. RBC, WBC, PLT, and Hb values decreased after PRRT ($p < 0.05$), but these changes were not defined as clinically significant haematological toxicity (National Cancer Institute [NCI] CTCAE Grades 0–1; Table 4-5)(Cancer Therapy Evaluation Program, 2017)). Overall, CgA values were significantly reduced by mean -27% $\pm$ 30 % after PRRT ($p < 0.05$). CgA and CgB showed a significant ($p < 0.05$) moderate, positive correlation with SUV-SPECT/CT metrics (r_s=0.3 and 0.5, respectively), as shown in Table 4-6. However, all PET/CT quantitative metrics were weakly correlated with CgA, and weak or no correlations were observed for CgB. Weak correlation might be because of small sample size.

Comparing SUV values from SPECT/PET with biochemical data is a promising approach to gain a deeper understanding of the physiological and pathological processes. However, careful consideration of statistical methods, sample sizes, data normalization, and clinical context is necessary to draw meaningful conclusions from such comparisons.

Table 4-5: Biochemical & Haematological Data measurements pre- and post-PRRT.

	Pre-PRRT				Post-PRRT			
	Minimum	Maximum	Mean	±SD	Minimum	Maximum	Mean	±SD
e-GFR	37.0	97.0	69.7	15.7	40.0	102.0	66.5	15.7
Creatinine	65.0	136.0	88.2	21.1	61.0	154.0	84.3	22.9
Haemoglobin	101.0	152.0	127.5	12.3	94.0	140.0	121.5	11.7
RBC	2.9	5.2	4.3	0.5	2.7	4.6	3.7	0.5
WBC	4.0	10.6	6.6	1.5	2.9	8.0	4.6	1.3
PLT	139.0	372.0	226.5	63.4	75.0	259.0	178.1	43.9
ALT	9.0	52.0	20.5	11.1	11.0	70.0	21.2	12.5
ALP	47.0	188.0	97.5	38.8	51.0	258.0	113.6	62.3
Bilirubin	3.0	21.0	9.8	5.3	5.0	25.0	10.7	5.5
Albumin	36.0	49.0	44.3	3.2	33.0	51.0	43.7	4.2
CgA*	20.0	37819.0	3060.2	8484.4	17.0	40000.0	2812.9	8869.0
CgB**	67.0	2017.0	386.2	468.8	74.0	7408.0	676.0	1644.7

* Nor-metadrenaline and **Metadrenaline were assessed for olfactory neuroblastoma and Paraganglioma patients.

Table 4-6: CgA and CgB Spearman's correlation coefficient (rs) with SPECT and PET Quantitative metrics.

SPECT

Spearman's rho		SUV_{mean}	SUV_{max}	SUV_{peak}	MTV	LTL	LTS
CgA	Correlation Coefficient	.347**	.355**	.354**	.463**	.396**	.446**
	Sig. (2-tailed)	.003	.002	.002	.000	.001	.000
CgB	Correlation Coefficient	.535**	.568**	.599**	.417**	.299*	.439**
	Sig. (2-tailed)	.000	.000	.000	.000	.011	.000

PET

		SUV_{mean}	SUV_{max}	SUV_{peak}	MTV	LTL	LTS
CgA	Correlation Coefficient	.301*	.271*	.318*	.280*	.254*	.371**
	Sig. (2-tailed)	.016	.031	.012	.025	.043	.003
CgB	Correlation Coefficient		.275*	.358**			.313*
	Sig. (2-tailed)		.028	.004			.015

*. Correlation is significant at the 0.05 level (2-tailed).
**. Correlation is significant at the 0.01 level (2-tailed).

4.5. Discussion

To the best of our knowledge, this is the first study to show that quantified SUV-SPECT/CT has the potential to predict response to PRRT. We compared the changes in SPECT/CT-measured SUV in NET patients undergoing PRRT with changes in PET/CT-measured SUV before and after therapy for the target tissue (lesion) and non-target tissues in addition to comparisons with biochemical markers.

We considered three SUV metrics as predictors of response; SUV_{max} of a single lesion, overall SUV_{max} of up to five lesions, LTL, and LTS SUV_{max} change. PERCIST defined metabolic response using only [^{18}F]-fluorodeoxyglucose (FDG) (Joo Hyun et al., 2016). PERCIST considers complete metabolic response when the lesional uptake returns to background levels and no new FDG-avid lesions appear. The partial metabolic response is defined as a decrease of SUV $\geq$30% from baseline (Joo Hyun et al., 2016). In FDG PET/CT studies, increased SUV_{max} is significantly associated with aggressive cancerous tissue and prognostic assessment and is a validated metabolic response indicator (Tang et al., 2020). We applied PERCIST criteria to our SPECT and PET SUV assessment of response to therapy, having previously optimised and validated our protocols using phantom imaging as presented in chapter-3.

Although some attempts have been made to address the assessment of NET PRRT response by relating [^{68}Ga] Ga- DOTA-TATE PET/CT quantitative data to PERCIST guidelines (Haug et al., 2010; Komek et al., 2019; Sharma et al., 2019; Ilan et al., 2020 Tang et al., 2020; Ortega et al., 2021), few studies have investigated changes in [^{68}Ga] Ga- DOTA-TATE SUV_{max} after PRRT (Q. Liu et al., 2021; Joo Hyun et al., 2016; Sainz-Esteban et al., 2012; Sharma et al., 2019). Studies investigating metabolic responses using SUV quantitative data derived from PRRT response assessments using SPECT/CT based on [^{177}Lu] Lu- DOTA-TATE measurements during PRRT are lacking.

Our study confirmed a strong positive correlation between SUV_{mean}, SUV_{max}, and SUV_{peak} in estimating changes between cycles 1 and 4 of PRRT ($r_s=0.9$, $P<0.05$). We recommend using SUV_{max} as it is least affected by VOI delineation and image noise. All prominent highest uptake lesions defined on pre-PRRT baseline PET/CT corresponded with those defined on SPECT-CT following the first cycle of PRRT. We showed that the change of SUV_{max} of a prominent single lesion and averaged SUV_{max} of several lesions strongly correlate for SPECT and PET ($R=0.84$ and 0.95, $p<0.001$, respectively). Notably, SUV_{max} of the maximum peptide-avid lesion in either SPECT or baseline PET is not always the lesion that responds best to PRRT. For instance, we recorded two patients (number 16 and 18) with the highest scoring lesions at baseline, SPECT-$SUV_{max} = 40$, which reduced by 17% and 82%, respectively post treatment. SUV changes varied between different target lesions in individual patients. Two patients (numbers 2 and 11) were reported to have a mixed response, showing an example of differential treatment response within the same patient. Lesions with stable and partial response showed higher SUV_{max} at SPECT and PET baseline than those with progressive disease. This result is consistent with a previous study of ^{68}Ga- DOTA-TATE prior to Lu-DOTA-TATE therapy of 37 NET patients (Teker & Elboga, 2021). The study showed that longer progression-free survival (PFS) of 26 months was associated with higher mean lesional SUV_{max} (34.15 ± 17.89) compared to shorter PFS (8.4 months) with lower SUV_{max} (14.69 ± 9.17) (Teker & Elboga, 2021). This discrepancy could be explained by NET heterogeneity and differences in SSTR expression leading to inter- and intra-patient peptide avidity and differential tumour responses.

Significant changes were identified for SUV_{mean}, SUV_{max}, and SUV_{peak} values between Cycles 1 and 4 of PRRT ($p < 0.001$). The majority of SPECT/CT and PET/CT responders' lesions (89% and 66%, respectively) showed SUV_{max} reductions, averaging 45% and 34% respectively. The average change in SUV_{max} -PET/CT measured for all lesions of -13% was

comparable to the reported changes in SUV_{max} after PRRT of -19.6% and -11.9% in other studies (Haug et al., 2010; Sainz-Esteban et al., 2012). Liu et al. reported a decrease in the percentage change in [^{68}Ga] Ga- DOTA-TATE PET/CT SUV_{max} by $-11.9\% \pm 37.9\%$ after three [^{177}Lu] Lu-Dota-EB-Tate-PRRT cycles, with a mean, injected activity (IA) of 3.97 ± 0.84 GBq (Q. Liu et al., 2021).

Our study demonstrated a strong positive correlation between SPECT/CT and PET/CT changes in SUV_{max} and SUV_{peak}. Some patients showed comparable SUV_{max} -SPECT/CT and PET/CT measurements. This result agrees well with the existing study showed strong positive linear correlations between pre-PRRT [^{68}Ga] Ga- DOTA-TATE PET/CT SUV_{max} and [^{177}Lu] Lu-DOTA-TATE PRRT voxel uptake and absorbed dose (Hänscheid et al., 2012). In 14 patients [^{177}Lu] Lu- DOTA-TATE SUV values were higher than those measured by [^{68}Ga] Ga- DOTA-TATE, possibly as the result of the timing of scans post-injection (24 hr and 1 hr, respectively). [^{68}Ga] Ga- DOTA-TATE shows the highest SUV_{max} at 3 hr rather than at 1 and 2 hr, according to Velikyan et al.(Velikyan et al., 2014). However, six patients showed higher [^{68}Ga] Ga-DOTA-TATE pre-therapy SUV_{max} compared with the values measured 24 hours after Cycle 1 of PRRT [^{177}Lu] Lu- DOTA-TATE SPECT/CT.

Liver background SUV_{mean} or SUV_{max} measurements showed no significant differences between SPECT/CT and PET/CT values ($p > 0.05$). However, spleen and kidney SUV_{mean} and SUV_{max} changed significantly during the second measurement relative to the first measurement for both PET/CT and SPECT/CT in patients who responded favourably to PRRT ($p < 0.05$). This may reflect increased SSTR expression due to an inflammatory response in the liver and spleen (Ortega et al., 2021).

SUV_{mean} -SPECT/CT and PET/CT measurements increased by 18% for the spleen, 19% for the right kidney, and 16% for the left kidney. Minimal liver background SUV variation indicates

the stability of the scanner calibration and function, resulting in minimal SUV error (Adams et al., 2010). Our ^{68}Ga- DOTA-TATE SUV threshold estimation of ≥ 11.6 is comparable to the published threshold of >13 (Sharma et al., 2019). Higher SUV_{max} thresholds (17.9 and 16.4) were reported for ^{68}Ga-DOTA-TOC (Öksüz, M. Ö et al., 2014; Kratochwil C. et al., 2014). Changes in the LTL and LTS SUV ratios measured by SPECT/CT and PET/CT showed strong linear correlations ($R^2 = 0.8$), with good agreements between the lesional SUV_{max} measurements and the liver and spleen SUV_{max} and SUV_{mean} measurements. We recommend using changes in LTL SUV unless there is evidence of liver disease, in which case LTS can be used to assess response to PRRT.

Lesion to liver and spleen ratio can show when the lesion SUV_{max} becomes equal to normal background uptake for each patient. The SPECT/CT LTL and LTS SUV measurements decreased by mean percentages of 40±33.4% and 46±25.6%, respectively. PET/CT LTL and LTS SUV measurements decreased by mean percentages of 23±35% and -25±29%, respectively. A recent study reported a correlation between values measured after Cycle 1 of [^{177}Lu] Lu- DOTA-TATE SPECT/CT and the pre-PRRT values measured using [^{68}Ga] Ga-DOTA-TATE /DOTA-NOC PET/CT scans (Thuillier et al., 2021). Thuillier et al. reported that the LTL and LTS SUV ratios were comparable between SPECT/CT and PET/CT for small lesions (MTV < 3 mL). This agreed with our finding, showing that high [^{177}Lu] Lu- DOTA-TATE LTL and LTS values correlated with [^{68}Ga] Ga- DOTA-TATE LTL and LTS ($p = 0.02$ and $p = 0.001$, respectively).

Biochemical tumour markers showed weak to moderate correlations with changes in SUV measured by either SPECT/CT or PET/CT. The majority of patients showed agreement between SPECT/CT and PET/CT-measured changes in SUV_{max} and CgA tumour markers (84% and 69%, respectively). Agreement between these three metrics was observed in 63% of our sample. Additionally, CgA changes showed no significant difference to SPECT-SUV_{max}

changes of single and multiple lesions (p=0.6 and 0.38, respectively). However, significant differences were reported between CgA changes and PET-SUV$_{max}$ of single and multiple lesions (p=0.036 and 0.050, respectively). Bodei et al. (2020) reported that PRRT response did not correlate with CgA changes (Bodei et al., 2020). Occasionally, an increase in CgA can be caused by tumour progression or by cell damage following PRRT.

This study reported no significant hematotoxicity or nephrotoxicity in grades 3 and 4 according to the CTCA grading system. This result is consistent with incidences of ≤3% in previous studies on a large cohort of [177]Lu- DOTA-TATE (Bergsma et al., 2016; Bodei et al., 2016, 2020; Bongiovanni et al., 2022; Sabet et al., 2013; J. R. Strosberg et al., 2021).

In summary, our findings agreed with the prospective application of SPECT- SUV$_{max}$, average SUV$_{max}$, LTL, and LTS to predict PRRT response clinical outcome. For SUV-PET, a recent review reported that only eight studies investigated the role of [68]Ga- DOTA-TATE in PRRT response assessment using SUV metrics (Lee et al., 2022). Some studies experimentally demonstrated that the previously mentioned SUV metrics are reliable predictors (Ilan et al., 2020; Ortega et al., 2021; Sharma et al., 2019; Teker & Elboga, 2021). Generally, averaged SUV$_{max}$ and LTL could be used as predictive markers to determine PRRT response.

This study proved the ability and feasibility of quantitative SPECT and PET SUV metrics and their role in PRRT management. These obtained results justify further development of the quantitative SUV method for more standardised and harmonised investigations to define responses to PRRT criteria for SPECT and PET.

Despite the success demonstrated, a significant limitation was the small sample size and retrospective data, which were not controlled for data acquisition and imaging modalities. Finally, there was a large mean time interval between the pre-and post-PRRT [68]Ga- DOTA-TATE (60± 38.5 days and102± 25.3 days, respectively) and post-PRRT biochemistry data

(100± 49 days). This reflects variations in real-world data collection that occur in routine clinical practice and latterly, the impact of the Covid-19 pandemic.

A general issue is that we applied the SUV-PET threshold ≥30% to the SUV-SPECT response assessment during PRRT. However, this threshold cannot be directly translated to SUV-SPECT, as SPECT's imaging characteristics differ from PET. Therefore, it is important to establish separate thresholds for assessing tumour response using SUV-SPECT measurements.

4.6. Conclusion

Currently, MRT doses are prescribed as fixed amounts of radionuclide activity at pre-determined intervals, regardless of the burden of disease or physiological uptake associated with each individual patient. Few centres undertake post-treatment imaging to assess response prospectively between cycles, and evidence to support the concept of a response–adapted treatment approach is therefore lacking. Our study found that quantitative SPECT/CT was reliable for evaluating PRRT responses, allowing for the use of SUV-SPECT/CT measurements as a clinical evaluation marker in between MRT cycles. In theory, monitoring MRT response prospectively might facilitate the optimisation and individualisation of MRT to improve the safety and treatment outcomes for each patient. The precise documentation of each patient's PRRT-corrected administered activity, scan time, and body weight are crucial for accurate 3D SUV-SPECT/CT reconstruction.

CHAPTER 5

5. Patient-Led Whole-Body Retention Monitoring - Feasibility, Accuracy and Application to Molecular Radiotherapy (MRT)

Abstract

Introduction/Aims: Optimising the outcomes of MRT would benefit from reliable measurement of absorbed radiation doses delivered to target tissues and healthy organs. Post-treatment imaging is often performed 24-48 hours after MRT administration. This a) limits the reliability of dose estimates and b) results in patients being provided with generic radiation safety advice, based on worst-case assumptions of radiopharmaceutical retention. The drive towards personalised treatment requires the development and validation of dosimetry-based MRT, particularly for therapies that account for a high percentage of treatments such as ^{131}I-NaI-Sodium iodide, and ^{177}Lu-DOTA-TATE.

In this study, long-term whole-body retention data was derived from patient-led whole-body dose monitoring and combined with post-treatment early distribution whole-body imaging. We postulate that this approach will provide reliable whole-body absorbed dose estimates and allow personalised radiation protection advice, which might significantly improve the patient experience.

Methods: Patients undergoing molecular radionuclide therapy using ^{177}Lu-DOTA-TATE (7.4GBq) for neuroendocrine tumours and ^{131}I-NaI for benign (600-800 GBq) and malignant thyroid disease (1.1-7.4 GBq) were included. Planar whole-body images 24-48 hr following ^{177}Lu-DOTA-TATE and ^{131}I-NaI administration were acquired to assess early uptake. Three ^{177}Lu-DOTA-TATE patients had 4 time-point whole-body scans. Patient-led whole-body retention measurements using a hand-held radiation monitor were used to follow each patient's time course of radioactivity clearance for four weeks post-therapy. Pearson's correlation and the Bland-Altman agreement plot were applied to compare patient-led and imaging-derived retained whole-body activity.

Results: A significant correlation was shown between patient-led and imaging-derived retained whole-body activity (A_r) (r=0.8, p<0.05) for all MRT groups. ^{177}Lu-DOTA-TATE multi-time-points data sets showed comparable mean whole-body absorbed dose estimates for both imaging and patient-led measurements (457 ± 62 mGy, 253 ± 24 mGy, and 150.5 ± 10.6 mGy for patients no. 1,2 & 3 respectively). Both methods observed a strong linear correlation in whole-body absorbed dose estimation (r=0.99, p<0.05). The Bland-Altman analysis confirmed a good agreement between both methods.

Conclusion: These data show the feasibility of patient-led measurements. This study supports the concept of integrating patient-led radiation monitoring into MRT planning and may be useful in future for single imaging time point dosimetry. It can be considered a feasible tool for WB retention estimates with good accuracy compared to serial quantitative imaging and offers convenience to the patient by avoiding repeated hospital visits. In addition to enabling an alternative dose calculation, this approach supports personalised radiation protection guidance.

5.1. Introduction

Molecular radiotherapy (MRT) refers to the use of radiopharmaceuticals to treat benign and malignant diseases. Optimising the outcomes of MRT would benefit from reliable measurement of absorbed radiation doses delivered to target tissues and healthy organs. The use of MRT in the UK expanded significantly between 2007 and 2017 both in terms of the number of patients treated and the number of individual treatments administered (82% and 250% increase respectively) (Rojas et al., 2019). Sodium iodide [^{131}I] (NaI) treatment for differentiated thyroid cancer (DTC) increased by 35% between 2007 and 2017(Rojas et al., 2019). Further expansion is predicted following European Medicines Agency approval (EMA, 2017) and National Institute for Health and Care Excellence (NICE) recommendations (NICE, 2018) regarding PRRT for neuroendocrine tumours (NETs) using ^{177}Lu-DOTA-TATE (Rojas et al., 2019) and advances in radioligand therapy for prostate cancer (Sartor et al., 2021).

Different dosimetry methods can assess whole-body retention based on available resources. Time-activity curves (TACs) from blood, urine and whole-body scans (WBS) following radiotherapy are familiar sources of input data. However, whole-body and SPECT/CT imaging can estimate biokinetic data in different tissues over time (Ljungberg et al., 2016; Zaknun et al., 2013). The accuracy of TAC estimation is highly dependent on the sampling time and data integrity, with a minimum of three-time points for each biological uptake and elimination phase (Hindorf et al., 2010; Lassmann et al., 2011). However, the total number of time points needed for dosimetry data to completely describe the activity as a function of time after administration depends on the pharmacokinetics of the radiopharmaceutical administered to each patient (Hindorf et al., 2010). A recent study assessed the tumour-absorbed dosimetry using multi-time-point SPECT/CT imaging following MRT and suggested using at least four time-points

SPECT/CT to reduce the uncertainty of the bi-exponential time activity curve (TAC) fitting (Finocchiaro et al., 2020).

In 2015, a study for long-term retention of ^{177}Lu-DOTA-TATE activity was presented by Gleisner et al. using planar whole-body gamma camera imaging and high-purity germanium (HPGe) detectors 5–10 weeks following administration. The study reported higher retention of radioactivity using detector measurements and whole-body gamma imaging at 1–3 time points between 5–10 weeks than was predicted from curve fitting from the first-week 4-time-point post-PRRT (Gleisner et al., 2015). Moreover, the study showed that four time-point whole-body gamma imaging between 1–7 days post-PRRT cannot accurately estimate the TAC tail (Gleisner et al., 2015).

Flux et al. presented a curve fitting ^{131}I activity–time model for DTC patients that required at least three points for each phase acquired over 10 days, initially with a ceiling-mounted Geiger counter in the therapy room and later with a whole-body shielded NaI counter (Flux et al., 2002).

Pre-therapy dosimetry using serial blood and whole-body scintigraphy (WBS) was used to predict TACs following high-activity ^{131}I therapy for advanced DTC (Verburg et al., 2010). In the study, the TAC was calculated based on serial whole-body gamma imaging and post-therapy blood sampling (Hänscheid et al., 2009). Several dosimetry methods were applied to estimate whole-body retention following radioactive iodine (RAI) therapy for DTC patients. Dosimetry was performed with SPECT, a Geiger counter, blood (Flux et al., 2010), a pressurised ionisation chamber (Barquero et al., 2008), NaI (Tl) detector gamma spectrometry system, urine (Nascimento et al., 2010), and a serial Geiger–Muller detector (Willegaignon et al., 2006).

Several studies have investigated the role of thyroid imaging dosimetry using SPECT/CT following ^{131}I for DTC patients (Fujita et al., 2020; Taprogge et al., 2019; Wadsley et al., 2017). Activity retention in thyroid remnants was determined from 3–4 SPECT acquisitions, blood sampling, and whole-body external dose rate. Predicted and observed whole-body and blood retentions were in agreement (Taprogge et al., 2021).

Oral administration of sodium iodide for treating thyrotoxicosis (hyperthyroidism) was first described in 1923 (Chapman & Evans, 1946) and is now well established. Thyrotoxicosis due to autoimmune hyperthyroidism (previously toxic diffuse goitre or Graves' disease), solitary toxic nodular adenoma, and multinodular goitre (Plummer's disease) are accepted indications for RAI therapy in addition to antithyroid drugs and as an alternative to surgery (Stokkel et al., 2010).

For post-therapy dosimetry in thyrotoxicosis, a recent study reported a strong correlation (r = 0.89) between a single SPECT image-based and four time-point external dose rate measurements using a thyroid uptake NaI crystal system in the prediction of the thyroid-absorbed dose following RAI therapy (Fujita et al., 2020). Serial measurements using a NaI (Tl)-detector following RAI therapy for thyrotoxicosis showed good agreement between the generated time-dependent retention curve and measurement points (Andersson & Mattsson, 2021). A thermoluminescence dosimeter was used to measure the radiation dose received by family members of patients with thyrotoxicosis or thyroid cancer treated with [131]I (Pant et al., 2006). Doses received by partners and children of patients with thyrotoxicosis treated with RAI as out-patients revealed that 11% of children aged ≤3 years received more than 1 mSv (Barrington et al., 1999).

A small study by Gils et al. (2017) was the only work to prove the feasibility of using serial measurements for up to 3 weeks with a thyroid collar detector and single SPECT acquisition

to determine the uptake profile and absorbed dose of the thyroid following ^{131}I therapy in three female patients with thyrotoxicosis. Their results revealed differences in the dynamic thyroid uptake profiles of each patient, which added to the potential value of the collar detector dosimetry method (K. van Gils et al., 2017).

To date, investigations into whole-body retention in MRT have been based on multi-time-point whole-body planar and SPECT/CT imaging. However, whole-body retention evaluation via imaging rarely continues past 7 days post-MRT administration. Multiple hospital visits and significant resource implications are the primary constraints that limit the applicability and consistency of serial whole-body radioactivity retention measurements.

Optimising the outcome of MRT would benefit from reliable measurement of absorbed radiation doses delivered to target tissues and healthy organs. In our centre single time point post-treatment imaging is performed 24–48 hours after MRT administration. This is useful to confirm radiopharmaceutical biodistribution but does not contribute to individual dosimetry measurements. The drive towards personalised treatment requires the development and validation of dosimetry-based MRT, especially for therapies that account for a high percentage of treatments, such as ^{177}Lu-DOTA-TATE and ^{131}I.

Our study investigated a novel approach using long-term patient-led whole-body retention measurements for patients undergoing lutetium ^{177}Lu-DOTA-TATE PRRT for NETs and sodium-iodide [^{131}I] therapy for benign and malignant thyroid disease.

5.2. Aims

In this chapter, the main objective is to investigate the use of long-term whole-body retention data derived from patient-led whole-body dose monitoring combined with early post-treatment whole-body imaging. The study also assessed the patients' acceptance of using a patient-led radiation monitor.

We hypothesised that this approach would:

1. Be feasible by assessing hand-held device linearity and accuracy.
2. Provide reliable estimates of whole-body retained activity (A_r) and absorbed dose (D) by comparing patient-led data to quantitative whole-body planar and SPECT/CT imaging.
3. Improve patient experience.

5.3. Methods

5.3.1. Ethical Approval

This study was approved by Guy's and St Thomas Foundation Trust Clinical Audit Committee (No.10515) and Health Research Authority (HRA) and Health and Care Research Wales (HCRW) (REC ref. 21/SC/0262, IRAS no. 288352). All procedures performed in studies involving human participants were in accordance with the ethical standards of the institution and with the 1964 Helsinki Declaration and its later amendments or comparable ethical standards.

5.3.2. Human Subjects

Patients undergoing molecular radionuclide therapy using ^{177}Lu-DOTA-TATE (7.4 GBq) for NET and ^{131}I-NaI for benign (600–800 MBq) and malignant (1.1–7.4 GBq) thyroid disease were included.

To assess early uptake, we acquired single planar whole-body and SPECT/CT gamma images at 24 hours following ^{177}Lu-DOTA-TATE administration. Three patients who received ^{177}Lu-DOTA-TATE had four time-point WBS (a total of 12 data points). Whole-body image activity measurements were derived as the GM of anterior and posterior views using Eq.5-5 to minimise the effects of organ depth and photon attenuation. Imaging acquisition and reconstruction protocols are detailed in Chapter 3 with respect to phantom SUV quantification.

For DTC patients we acquired single planar whole-body and SPECT/CT gamma images at 48 hours following [^{131}I] NaI administration; This was to align imaging with the Trust's routine clinical protocols. All DTC subjects underwent total thyroidectomy and received an injection of rhTSH to attain a serum thyroid-stimulating hormone (TSH) level >30 mIU/L (Avram et al., 2022). All patients were instructed to follow a low-iodine diet for 2 weeks prior to therapy. Blood sampling for measurement of serum TSH, thyroglobulin (Tg), anti-Tg antibody (TgAb), thyroxine (T4), triiodothyronine (T3), and glomerular filtration rate (GFR) was performed on the day of RAI therapy, prior to its administration. DTC patients who received >1.1 GBq were hospitalised in an isolated lead-shielded ward for 48 hours post-RAI administration. Then, patients were released from hospital once the survey-metre dose rate reading at 1 m from the patient was ≤ 800 MBq of retained whole-body activity. Patients who received 1.1 GBq stayed in a lead-shielded therapy room in the nuclear medicine department for 4–6 hours post-RAI administration with dose rate monitoring at a 1 m distance every 1–2 hours until their whole-body dose rate measurements met the legal threshold for discharge (≤ 800 MBq).

Patients with thyrotoxicosis underwent only planar whole-body gamma imaging at 24 hours following RAI administration.

A hand-held Geiger–Muller counter (ATOMTEX model AT6130, Belarus Rep., BIC Technology Ltd, UK) was used to track the time course of radioactivity in individual patients. It records the count rate measurement of impulses, generated in the Geiger–Muller counter tube, under the influence of X-ray, gamma (γ), and beta (β) radiation.

Patient-led whole-body retention measurements using a hand-held radiation monitor were used by all MRT groups. Whole-body activity retention and absorbed dose measurements were derived from 4 weeks of patient-led records (two measurements/day in the first 2 weeks followed by once daily in the last 2 weeks) started immediately after MRT administration. For consistency of measurements, patients were instructed to hold the monitor at arm's length in front of the body while resting elbow by body side at waist level (Detailed instruction in Appendix A). Therefore, we introduced the term "*Selfie*", as patients refer to this tool as such. For inclusivity of patients' ability, no specific instructions were issued on whether measurements were to be taken sitting down or standing up, provided that the same position was used throughout the series of measurements (Fig. 5-1).
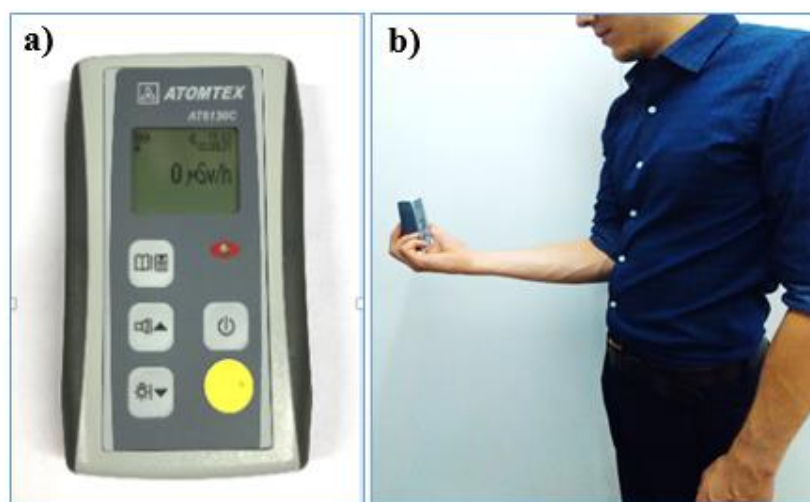
Figure 5-1: a. Hand-held Geiger–Muller counter (ATOMTEX) and the patient instructed to hold the monitor at arm's length in front of the body while resting elbow by body side at waist level (b).

Patient-led data were collected and analysed to assess patterns of external dose rate change over time and were correlated to 2D/3D quantitative radionuclide imaging data.

Patient-led data that were included in this analysis are as follows:

- Retrospective analysis of 20 patients (37 datasets) following cycles 1 and 4 of PRRT-Lu-DOTA-TATE. Three datasets (Dota-10 cycles 1 and 4, and Dota-19 cycle-4) were not returned.

- Prospective analysis of 20 patients (17 datasets) following ^{131}I therapy for DTC. Three datasets were excluded: two patient-led measurements were not returned, and one patient recorded measurements for only 3 days.

- Prospective analysis of 9 patients (8 datasets) following ^{131}I therapy for thyrotoxicosis. One patient's dataset was excluded due to inconsistency of recorded data (15 patients approached and 5 patients declined to take part in the study).

More details on patient groups demographics in Appendix table B, D, and F.

5.3.3. Assessment of Patient-led Measurements

Linearity

In this study, an assessment of the linearity of ATOMTEX measurements under relevant clinical conditions (mainly count rate and isotope energy) was performed using vials containing ^{131}I-NaI and ^{177}Lu-DOTA-TATE. Higher activity (7.85GBq) levels corresponded to the typically administered highest activities for NET therapies. For ^{131}I a maximum activity of 2.83GBq was used due to radiation protection considerations in our local protocol in the facility

available for these measurements. Low activities (^{177}Lu: 380MBq and ^{131}I: 355 MBq) were also considered for comparison measurements assumed to be free of dead-time effects. The vial was placed on a flat surface, and multiple-dose rate measurements were recorded at different distances using the Atomtex 6130 device. Then, we used the inverse-square law equation (Eq.5-1) to calculate the dose rate from a 2-metre distance reading. Finally, the relative error between the measured dose rate using the patient-led method and the calculated dose rate from a 2-m distance was calculated and expressed in % (Eq.5-2).

$$I_2 = I_1 * (D_1/D_2)^2 \qquad\qquad Eq.5\text{-}1$$

$$I_1 = \frac{I_2}{(D_1/D_2)^2} \qquad\qquad Eq.5\text{-}2$$

I_2 represents the measured dose rate at a 2-metre distance (D_2,), and I_1 represents the calculated dose rate at a certain distance (D_1).

The relative error (RE) can be calculated by calculating absolute error (Δx) first if x is the actual activity (Dose-calibrator) and x_0 is the measured activity (patient-led and static planar imaging) (Eq.5-3,4)

$$\Delta x = x_0 - x \qquad\qquad Eq.5\text{-}3$$

$$RE\% = (\Delta x/x) * 100 \qquad\qquad Eq.5\text{-}4$$

Multiple Time-points Patient-led and Scintigraphy Data

^{177}Lu patient-led measurements were validated using three patients' retrospective data from four sequential time-point gamma-camera WBS and patient-led measurements. Whole-body absorbed dose was estimated (Eq.5-9) using patient-led and quantitative 2D WBS data. Then we assessed the correlation between both methods.

Atomtex measurements of ^{131}I activity were compared to a series of static planar gamma images (5-minute scan duration) for the neck phantom with two bags of sodium chloride saline 0.9% (500 ml each) placed on the anterior part of the phantom to mimic the attenuation effect of a deeper lesion. A vial containing 3.4 GBq of ^{131}I solution was placed in the holder and inserted into the phantom (Fig.5-2). Three measurements were taken: activity measurement using a dose calibrator (CRC-15R serial number151976, instrument under routine quality control of the hospital and with annual calibration against the National Physics Laboratory, NPL), dose rate measurement using the Atomtex positioned 30 cm from the source and count rate measurement from static gamma images. All measurements were taken consecutively at multiple time points: 0, 24, 48, 96, and 165 hours. The 24-hour static image was not included due to system maintenance. Gamma camera static anterior and posterior images were taken using a dual-head scintillation scanner (INTEVO BOLD-Siemens, Erlangen, Germany). Parameters were consistent for all acquired scans, as shown in table 5-1.

Imaging data were processed using Hermes Hybrid 3D 3.01 software (Hermes Medical Solutions, Stockholm, Sweden). An elliptical region of interest was placed over the vial on the anterior image and then mirrored onto the posterior one.

Figure 5-2: Neck phantom with two bags of sodium chloride saline 0.9% (500 ml each) placed on the anterior part of the phantom to mimic the attenuation effect of a deeper lesion.

Table 5-1: Dual-head gamma camera planar STATIC acquisition parameters.

Detector 1 distance from the bed	14.2 cm
Detector 2 distance from the bed	22.4 cm
Scan bed position	Vertical centre 19.2 cm
Collimator	High-energy general-purpose collimator (HEGP)
Matrix	256 x 256
Image duration	5 min
Energy window centre	364 KeV
Zoom	1

The anterior and posterior geometric mean (GM) counts (Eq.5-5) were converted to count rate values considering scan duration in seconds (counts per second [CPS]) (Eq.5-6). The static image calibration factor (CF) was calculated using the same phantom setting, without saline bags, as a product of CPS divided by activity (MBq) (Eq.5-7).

$$GM = \sqrt[2]{Ca \cdot Cp} \qquad\qquad Eq.5\text{-}5$$

$$CPS = GM/t \qquad\qquad Eq.5\text{-}6$$

$$CF\ (CPS/MBq) = \frac{CPS}{A(MBq)} \qquad\qquad Eq.5\text{-}7$$

Where:

GM: Geometric mean, Ca: Anterior counts, Cp: Posterior counts, t: scan duration in seconds, A: Activity (MBq), CF: Calibration factor (CPS/MBq).

Then, all measurements (Table 5-2) were normalised to fractions (Table 5-3) so that all data referred to the initial activity at time zero (fraction of 1).

Table 5-2: ^{131}I neck phantom dose rate measurement using Atomtex 6130 monitor and activity measurements using a dose calibrator and static image.

Elapsed Time (hr)	Atomtex 6130 Dose Rate mSv/hr	Activity GBq (Dose Calibrator)	Activity GBq (Static Image)
0	1.44	3.36	1.95
24	1.30	3.09	-
48	1.13	2.85	1.76
96	0.90	2.41	1.51
165	0.70	1.86	1.24

Table 5-3: ^{131}I fractional dose rate using Atomtex 6130 monitor and activity measurements using a dose calibrator and static image.

	^{131}I- NORMALISED		
Elapsed Time (hr)	Atomtex 6130 Dose Rate mSv/hr	Activity GBq (Dose Calibrator)	Activity GBq (Static Image)
0	1	1	1
24	0.90	0.92	-
48	0.78	0.85	0.90
96	0.63	0.72	0.77
165	0.49	0.55	0.64

Patient-led vs. Standard External Dose Rate Measurements

A standard external dose rate measurement was also performed at 2 meters from the patient as per routine clinical protocol by a trained clinical scientist. These measurements are routinely used to assess hospital discharge criteria based on comparing each measurement to the initial dose rate immediately after administration of MRT.

The external dose rates change using patient-led at arm's length (typically 0.38 m from the anterior mid-abdomen) compared to a 2-m distance using an energy-compensated Geiger–Muller tube (Radalert professional model 1202, UK). Measurements were recorded

immediately following MRT administration and at 24 hr for NET patients and at 48 hr for DTC patients. Dose rate changes using both methods were assessed for agreement.

5.3.4. Whole-body Retained Activity and Absorbed Dose Calculations

First, whole-body retention was analysed using patient-led data and compared to quantitative WBS and SPECT/CT estimation for NET and DTC patients. Thyrotoxicosis patients had only patient-led and WBS data for comparison. All MRT groups' patient-led whole-body retention was normalised to fractions describing the radiopharmaceutical clearance, with fast and slow excretion rates, half-lives, and area under the curve (AUC) values calculated. Data were scaled by dose rate (µSv/hr) and integrated to 700 hours post-administration.

Retained whole-body activity (A_r) at a certain time point following MRT administration was calculated as a product of dose rate (D_{rate}) fraction and administered initial activity A_0, as shown in equation 5-8:

$$A_r(MBq) = D_{rate} \cdot A_0 \qquad\qquad Eq.5\text{-}8$$

Whole-body mean absorbed dose (D) was calculated according to MIRD as the product of the integral activity ($\tilde{A}$), and the S-value was derived using equations Eq. 5-9,10,11 (Howell et al., 1999).

$$D(mGy) = \tilde{A} \cdot S_{(Wb \leftarrow Wb)} \qquad\qquad Eq.5\text{-}9$$

$$\tilde{A} = A_0 \cdot \tau \qquad\qquad Eq.5\text{-}10$$

$$\tilde{A} = A_0 \cdot AUC \qquad\qquad Eq.5\text{-}11$$

where A_0 is the initial activity (MBq), and τ is the residence time (hr), also known as the AUC. $S_{(wb\leftarrow wb)\,was}$ calculated for each patient using the following dose conversion factors for reference male weight of 70 kg and female weight of 57 kg:

$S_{(wb\leftarrow wb)\,ref}$ (male) = 3.49 10^{-7} mGy MBq^{-1} s^{-1} $\qquad\qquad$ m_{ref}=70kg

$S_{(wb\leftarrow wb)\,ref}$ (female) = 4.49 10^{-7} mGy MBq^{-1} s^{-1} $\qquad\qquad$ m_{ref}=57kg

At this point, scaling to body weight was calculated for the patient weight (m_p) compared to the reference weight (m_{ref}), according to the formula:

$$S_{(Wb\leftarrow Wb)}mGy/MBq/s = S_{(Wb\leftarrow Wb)ref} \cdot (m_{ref}/m_p) \qquad\qquad Eq.5\text{-}12$$

Then, the S-value was multiplied by 3600 s (total seconds in 24 hours) to obtain a value in mGy (MBq hr)$^{-1}$.

Whole-body absorbed dose was estimated for all MRT groups using long-term sequential patient-led data. For NET patients with multiple time-points WBS, whole-body absorbed doses were estimated and correlated with patient-led estimation for validation purposes.

5.3.5. Patient-led Compliance Survey

The study questionnaire consisted of two parts. Part '**A**' included questions about demographic information, including respondent age, gender, therapy type, and experience with patient-led monitoring (Table 5-4).

Part '**B**' included eight statements to assess ease of use and acceptance (Table 5-5). The questionnaire was developed in a way that allows respondents to grade their responses on a 5-

point Likert scale: strongly disagree = 1, disagree = 2, neither = 3, agree = 4 and strongly agree = 5.

The reliability of the questionnaire was measured using the alpha coefficient to be 0.67. Cronbach's alpha for internal consistency should not be less than 0.50 for newly developed instruments, and values between 0.65 and 0.8 are generally acceptable (Singh, 2017).

All are positive statements except statement 4, so it is the item that showed differences in the direction from other items. There was one participant who did not respond to statement no.3 and another one to statement no.4 (missing values replaced by a simple mean).

Table 5-4 : Patient-led questionnaire - sociodemographic information scale.

Variable Item	Response Options
Age	(Open).......
Gender	Male/Female
Patient-led experience	Yes/No
Therapy type	DTC/Thyrotoxicosis

Table 5-5: Patient-led questionnaire statements to evaluate patients' acceptance of the patient-led monitor

Statement
1. The patient-led monitor was straightforward to use at home.
2. I had enough information to work the patient-led monitor when I got home.
3. Using the patient-led monitor helped me to feel involved in my treatment.
4. It was a nuisance to have to take measurements each day.
5. It was reassuring to see the numbers go down.
6. Using the patient-led monitor helped me to follow the radiation advice I was given.
7. I would be happy to use the patient-led monitor again.
8. I would recommend other people to use a patient-led monitor.

5.3.6. Statistical Analysis

The following statistical analysis was applied to the data presented in this and the next chapter. SPSS software (IBM Corp. SPSS Statistics *2019* v26.0 for Windows; Armonk, NY) was used for descriptive (mean $\pm$ SD, maximum [Max], minimum [Min], and percentage [%]) and inferential analyses. The one-sample Kolmogorov–Smirnov normality test was used to verify the normal distribution of data. A paired-sample t-test was used to evaluate the differences among normally distributed data. Spearman's correlation coefficient (r_s) was calculated for nonparametric data, whereas Pearson's correlation coefficient (R) was calculated for normally distributed data. A *P* value <0.05 was considered significant. Patient-led dose rate measurement normalisation, AUC, and mono- and bi-exponential non-linear curve fitting were performed using GraphPad Prism version 9.0.1 for Windows (GraphPad Software, San Diego, California USA). Microsoft Excel for Microsoft 365 MSO (version 2018) was used to generate charts with basic mathematical functions (error bars).

5.4. Results

In this section, first, we presented the result of the patient-led validation method using ^{177}Lu and ^{131}I as follows:

- Linearity.

- Multiple time points patient-led and Scintigraphy.

- Patient-led vs. Standard External Dose Rate Measurements.

Then the results for each MRT group (^{177}Lu-DOTA-TATE- NET, ^{131}I-DTC, and ^{131}I-Thyrotoxicosis) will be presented as follows:

- Whole-body activity retention estimation using Single Time-Point Patient-led, WBS, and SPECT/CT (SPECT/CT not acquired for Thyrotoxicosis patients).

- Whole-body absorbed dose estimation using sequential long-term patient-led data.

Finally, we presented the patient compliance survey results toward using *Selfie*.

5.4.1. Assessment of Patient-led Measurements

Linearity

Lu-177 dose rate measurements are shown in (Fig.5-3); Results indicate a close agreement between calculated expected dose rate and ATOMTEX measurement for distances approaching those practically relevant in the study, even when patient body attenuation is not taken into account. Data showed high RE percentages at a 20-cm distance (RE=14% and 15%, for high and low vial activity respectively) with moderate RE ≤10% recorded at 30–100 cm distances.

I-131 2.83 GBq activity produced RE >30% at 20- and 30-cm distances and <30% at 40–100-cm distances. Lower I-131 activity produced RE ≤10% from 30–100 cm distances (Fig. 5-4).
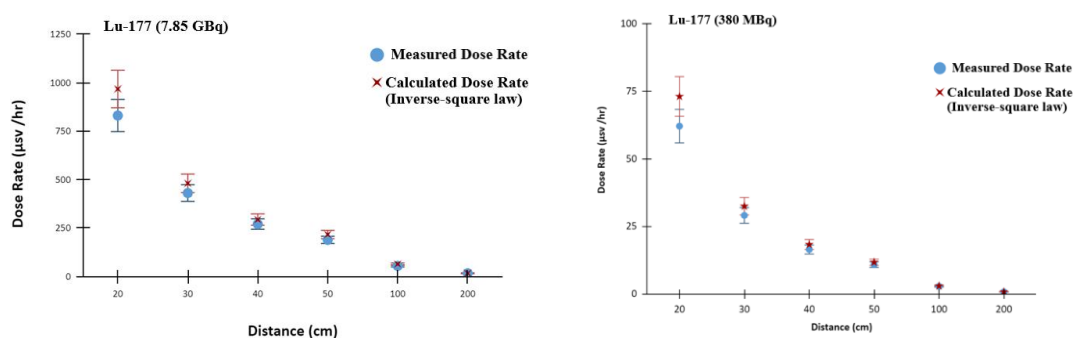
Figure 5-3: Lu-177 high (7850MBq) and low (380MBq) activity vial measurements at different distances. Measured (Dose-calibrator) and calculated dose rate (using inverse square law from 2-m distance measurements) showed consistency in both measurements..
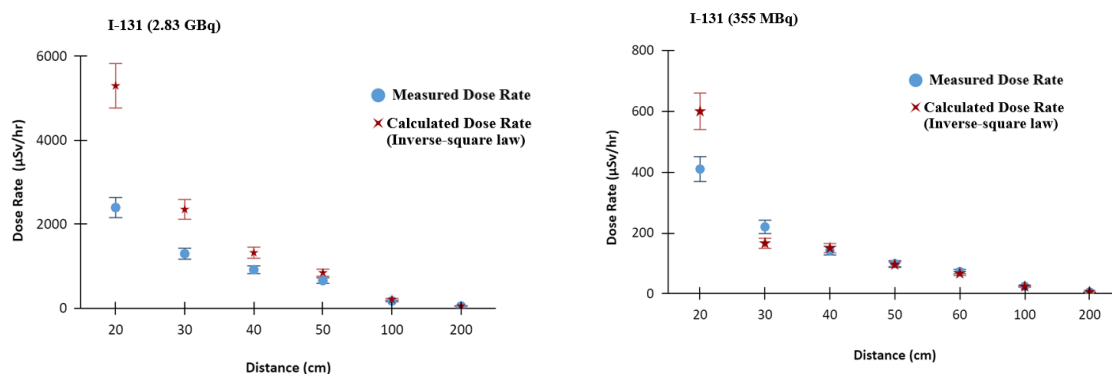
Figure 5-4: I-131 high and low activity vial measurements at different distances. Measured and calculated dose rate (using inverse square law from 2-m distance measurements) showed consistency in the dose rate.

For both I-131 and Lu-177 (Fig. 5-3 and 5-4), Atomtex 6130 measurements followed closely an inverse square law approximation, especially at 40- and 50-cm distances, which corresponded to the patient's clinical practice. In addition, the linearity of measurements at high and low activity remained relatively constant at all distances assessed, indicating that dead time effects at these activity levels can be considered negligible. Clearly, for measurements at shorter source-to-detector distance, count rate performance should be considered as a potential source of error. In practice, source-to-detector distance between 30 – 40 cm is relevant for patient-led measurements. However, in practice due to the distributed nature of activity in the body and a reduced count rate as a result of patient self-attenuation, could potentially limit the impact of count rate performance seen in this experimental setup.

Multiple Time-Point Patient-Led and Scintigraphy Comparison

Whole-body retention and absorbed dose estimates derived from multiple time points using patient-led and WBS data were compared for NET patients. Twelve whole-body scans and patient-led datasets were acquired from three ^{177}Lu-DOTA-TATE patients at four-time points and showed comparable estimation of whole body retained activity (MBq) and absorbed dose (mGy) with a strong positive linear correlation (R=0.99, p<0.001) (Fig. 5-5). The mean

absorbed dose estimates were comparable for both imaging and patient-led measurements (457

± 62 mGy, 253 ± 24 mGy, and 150.5 ± 10.6 mGy for patients no. 1,2 & 3 respectively).
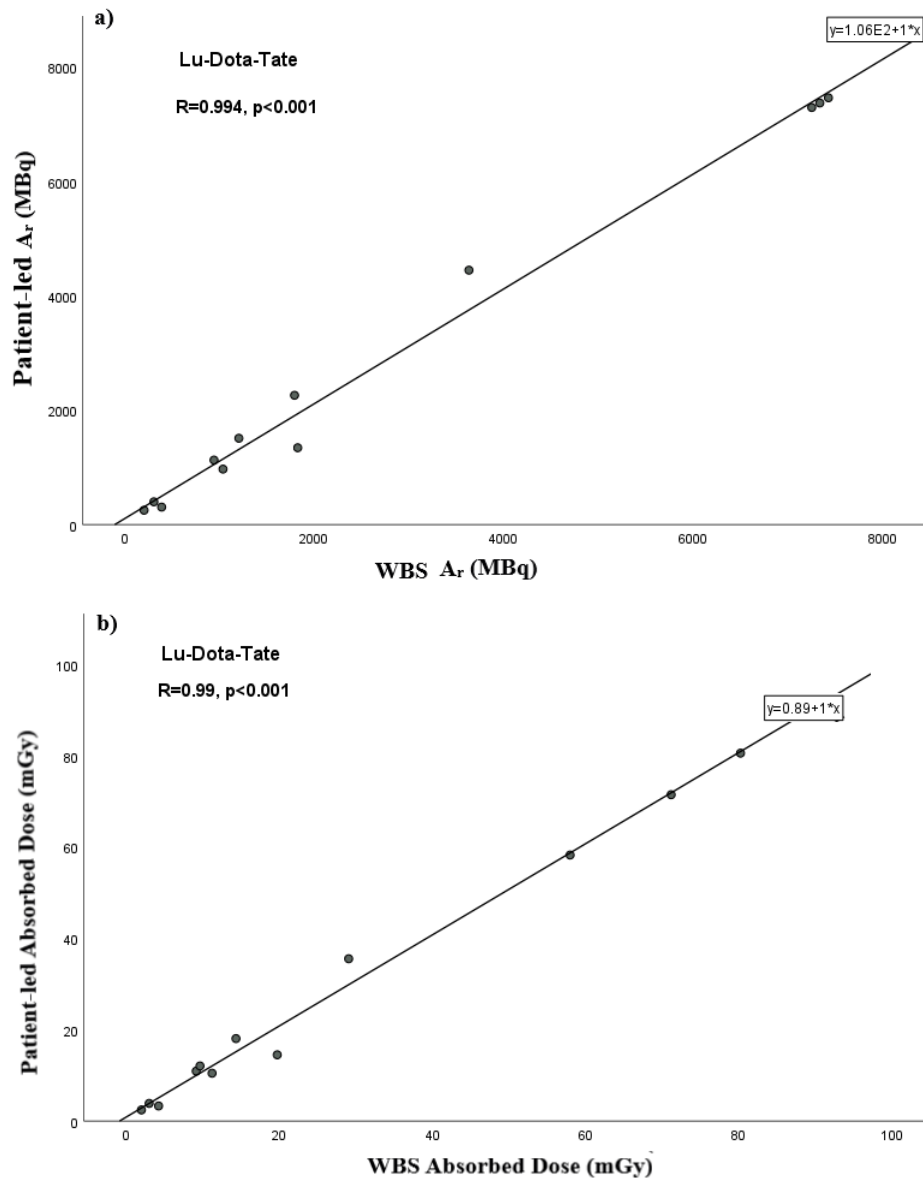
Figure 5-5: Multi-time-point dosimetry using WBS images and patient-led dose rate measurements for three PRRT patients (12 data points). a) Whole body retained activity, A_r (MBq)and b) Whole body absorbed dose (mGy). A very strong positive linear correlation was observed between the proposed methods.

I-131 neck phantom measurements using three different methods (Atomtex-6130, planar static

imaging, and dose calibrator) showed good agreement levels between all measurements, with

relative error RE ≤10% at 0, 24, and 48 hours (Fig. 5-6). Late measurements at 96 and 190

hours showed higher RE ≤20% between planar imaging and Atomtex measurements. The RE increased with time due to radioactive decay of 131I. Moreover, the count rate of radioactive decay events follows a Poisson distribution, which means that the uncertainty in the number of counts recorded increases with the square root of the number of counts. With fewer counts being recorded as the activity diminishes, the relative error can increase.
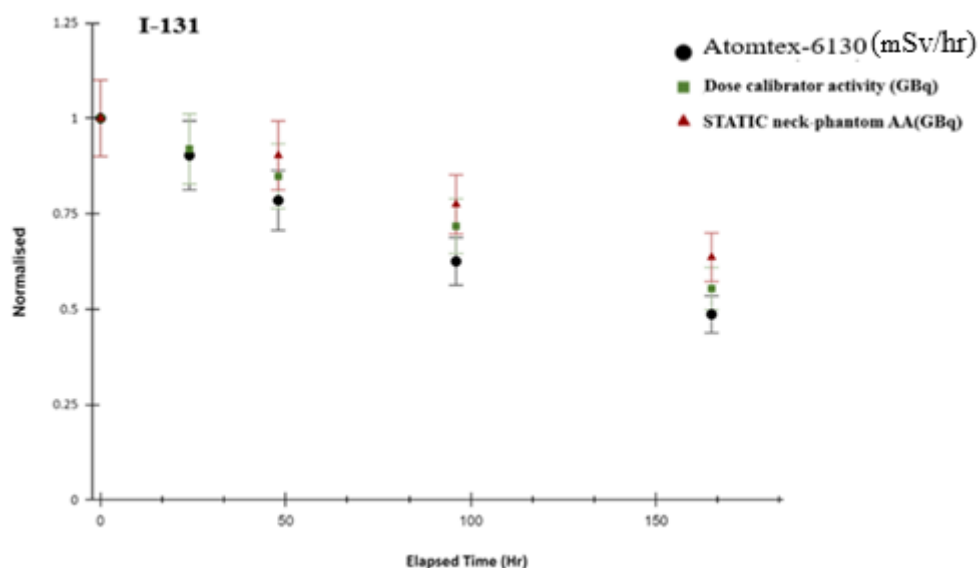
Figure 5-6: I-131 neck phantom normalised static images converted count rate to activity (GBq), dose calibrator activity measurements (GBq), and Atomtex-6130 dose rate measurements (μSv/hr) with 10% RE bars. Multi-time-point assessments from 0 to 190 hours show linearity of measurements using different methods.

Patient-led vs. 2-m Distance External Dose Rate Measurements

Change in dose rates of ^{177}Lu-DOTA-TATE over 24 hours from PRRT administration based on patient-led data and concurrent standard 2-m external dose rate measured by a trained clinical scientist (n=32) is shown in figure 5-7 with overall mean change of 74.2± 11.6% and 75.9 ± 9.7% respectively. Figure 5-7 shows a strong positive linear correlation between patient-led measurements and 2-m distance dose rate changes (R=0.82, p<0.001). Possible sources of the variation; perhaps changes in the redistribution of radioactivity during that time can affect more the Atomtex measurement as it is performed at closer geometry (arm's length).
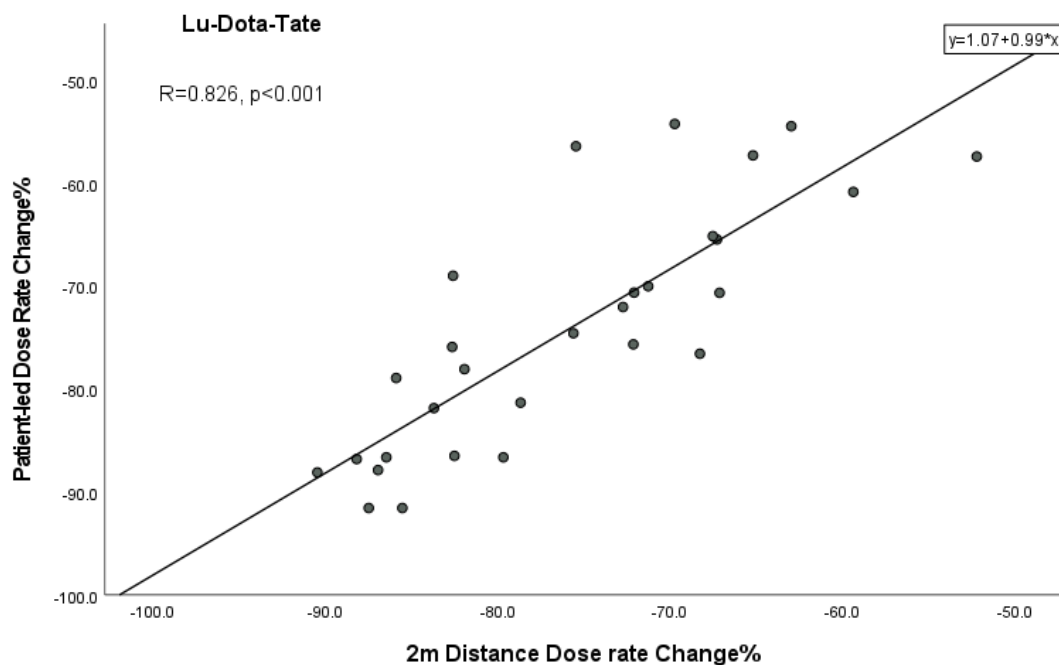
Figure 5-7: Whole-body dose rate change (%) 24 hours after PRRT administration based on concurrent patient-led and 2-m-distance measurements.

The mean dose rates of ^{131}I-DTC patient-led and concurrent standard 2-m external dose rate data (n=9) over 48 hrs after RAI is shown in figure 5-8 with overall mean change of 90.2 ±8.6 % and 90.1 ±9.6 % respectively. Figure 5-8 shows a strong positive linear correlation between patient-led and 2-m distance whole-body dose rate change (R=0.91, p<0.001). Patient-led measurements showed comparable accuracy to routine practice of acquiring 2m external dose rate measurements following MRT administration.
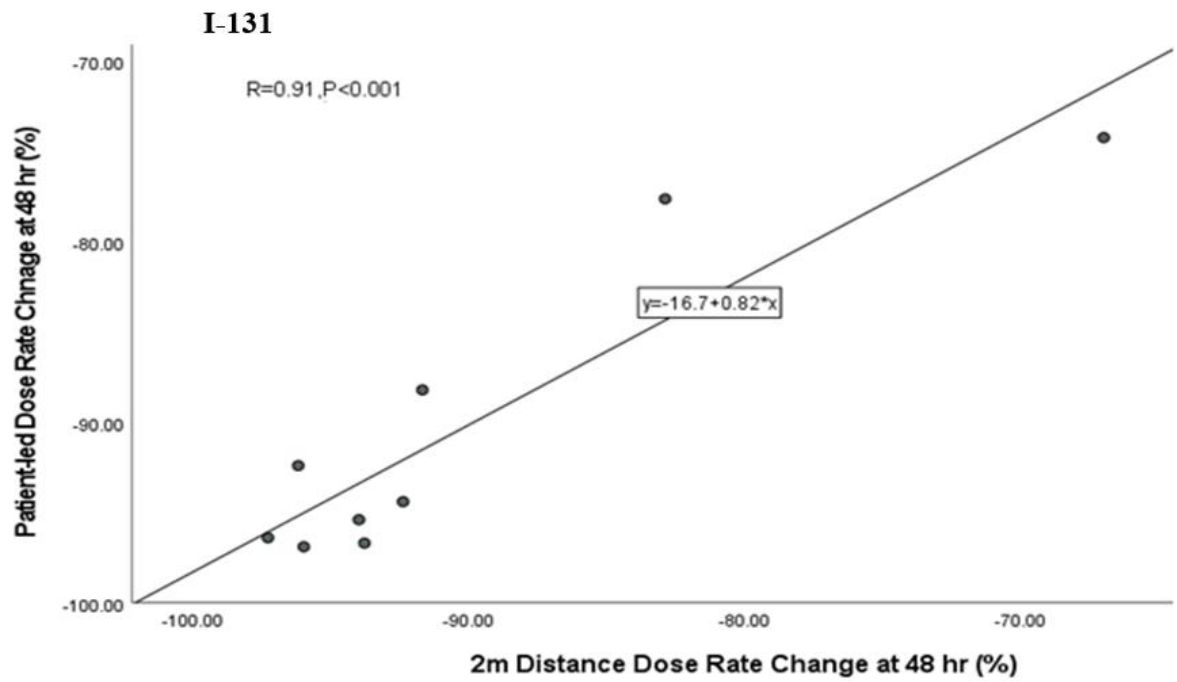
Figure 5-8: Whole-body dose rate change (%) 48 hours after RAI administration for DTC patients using patient-led and 2-m distance measurements.

5.4.2. Comparison of Patient-led Data to Imaging Following ^{177}Lu-DOTA-TATE-MRT

In this study, we included 19 NET patients with WBS and SPECT/CT images and patient-led measurements following PRRT cycles 1 and 4, which produced a total of 38 WBS and SPECT/CT datasets and 37 patient-led datasets (one dataset was illegible for inclusion due to inconsistent patient-led measurements undertaken by the patient). Data from 19 NET patients (11 females and 8 males, summarised in Appendix B) were analysed, with a mean age of 61.2 $\pm$ 8.4 years. Mean injected ^{177}Lu-DOTA-TATE activity was 7632 $\pm$ 224 MBq (7081-8000 MBq) for cycle 1 PRRT and 7273 $\pm$ 900 MBq (3780-7843 MBq) for cycle 4 (more details in Appendix B). Patient with ID DOTA-6 received the lowest activity at cycle 4 (3780 MBq) due to recorded toxicity as per Common Terminology Criteria for Adverse Events v5.0 (CTCAE) (eGFR 38ml/min/1.73m², grade-3 CTCA and Hb 9.4 g/dL, grade-2 CTCA) (Cancer Therapy Evaluation Program, 2017).

The mean duration of the recorded dose rate using patient-led monitors was 25 $\pm$ 5 days for NET patients.

Whole-body Activity Retention Estimation Using Patient-led, WBS, and SPECT/CT

The mean whole-body retained activity 24 hours after ^{177}Lu-DOTA-TATE administration based on each of the three dosimetry methods (WBS, SPECT/CT, and patient-led) for cycles 1 and 4 are shown in figure 5-9. A good correlation was observed between patient-led and WBS (R=0.78) and SPECT/CT(R=0.82). Whole-body retention was comparable between the three methods (WBS, SPECT/CT, and patient-led) for cycles 1 and 4 (21 $\pm$ 5% and 19 $\pm$ 6%, respectively). The mean whole-body retention at 24 hr for PRRT patients using WBS,

SPECT/CT, and patient-led measurement was 15%, 23%, and 24 % for cycle 1 and 13%, 20%, and 25% for cycle 4, respectively.

A strong positive linear correlation of remaining activity A_r (in MBq) was observed 24 hours following PRRT cycles 1 and 4 using quantitative images of WBS and SPECT/CT and patient-led dosimetry (R=0.8, p=0.00) (Fig.5-9).

The reason for WBS underestimation compared to SPECT may be that attenuation and scatter correction were not included in the WBS approach. We estimated the 0.406 cm^{-1} attenuation of the source at 10 cm deep in the tissue given the linear attenuation coefficient (μ) of ^{177}Lu (208 Kev). Moreover, the deviation for line-of-identity seen between WBS and SPECT could be related scatter, attenuation, and dead-time effects.
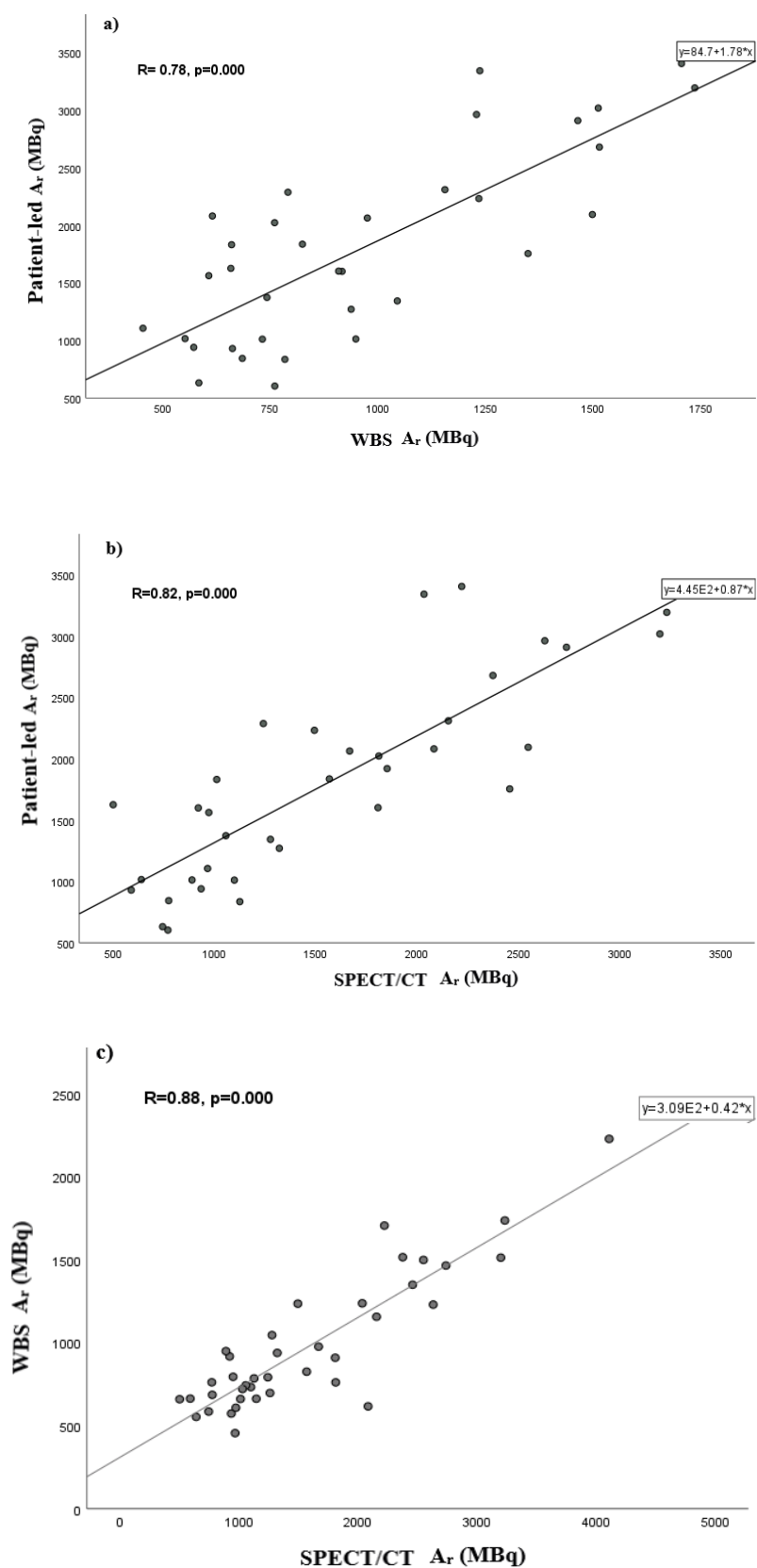
Figure 5-9: Scatter plot of whole-body retained activity (A$_r$) estimation 24 hours after PRRT administration for cycles 1 and 4. a) patient-led monitoring and whole-body scan (WBS), b) patient-led monitoring and SPECT/CT (with scatter and attenuation correction), and c) SPECT/CT (with scatter and attenuation correction) and WBS.

Whole-body Absorbed Dose Estimation Using Sequential Long-Term Patient-Led Data

With the reassurance of the previous data showing agreement of ^{177}Lu activity estimates at the time-points assessed against professional-led dose rate measurements and quantitative SPECT/CT, we pursued the calculation of whole-body absorbed dose as per the MIRD scheme. The mean whole-body absorbed dose based on patient-led dosimetry method was calculated for cycles 1 and 4 (329.6±196.6 mGy and 278±108.8mGy, respectively) and decreased by 22.8 ± 1% in cycle 4 (more details shown in Appendix C). Patient DOTA-20 showed the highest absorbed dose by > 50% reduction (Fig. 5-10). However, five patients showed an increase in the absorbed dose (details for each patient can be found in Appendix C). These absorbed dose results cannot be directly compared to a dosimetric gold standard as additional SPECT/CT imaging was not available for all of the patients in the cohort. However, seen in combination with activity estimates comparisons and the dose estimates from the three WBS data series (Fig 5-5) showing good agreement (R=99, linear coefficient of 0.99), they are provided here as demonstration of the potential of the methodology and the feasibility of the approach in a clinical setting.
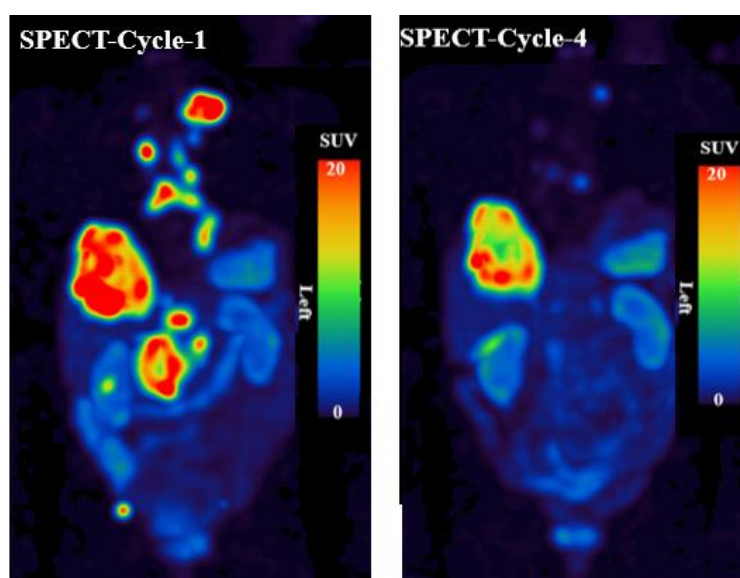
Figure 5-10: Patient DOTA-20's SPECT/CT maximum-intensity projection (MIP) images 24 hours following PRRT cycles 1 and 4. This patient exhibited a 54% reduction in absorbed dose (mGy), and the total lesion means SUVmax was reduced by 68%.

5.4.3. Comparison of Patient-led Data to Imaging Following ^{131}I MRT for DTC

20 DTC patients had planar WBS and SPECT/CT whole-body images, and patient-led measurements following ablation or metastatic therapy (WBS=20, SPECT/CT=19, patient-led=18).

A total of 10 females and 10 males referred for RAI ablation therapy (n=14) and follow-up (FU) therapy for metastatic disease (n=6) were recruited prospectively, with a mean age of 45.5 ± 13.5 years. The mean administered ^{131}I-NaI activity for ablation was 3232 ± 1455 MBq, and 5578 ± 1552 MBq for FU metastatic therapy (more details on the patient group can be found in Appendix D). The mean duration of the recorded dose rate using patient-led monitors was 27 ± 3 days for DTC patients.

This paragraph provides an overview of the profile and clinical background of the patient group included in the study. Biochemistry data were analysed for DTC patients before and 2–3 months after RAI therapy. All patients achieved the target TSH level >30 pmol/L following rhTSH stimulation (range 39.8-269.7 pmol/L). Estimated GFR (eGFR) measurements confirmed adequate renal function (range 54 – 134 mL/min). The highest stimulated Tg was recorded for patients Thyca-2 and Thyca-4 (10798 ug/L and 5573 ug/L, respectively). A representative example of a patient (Thyca-4) showing iodine avid metastatic disease is shown in figure 5-11. By comparison, RAI WBS and SPECT/CT from patient Thyca-2 showed only remnant thyroid tissue uptake, with no evidence of iodine-avid metastatic disease (Fig. 5-12). Subsequent FDG PET/CT demonstrated, multiple intensely (^{18}F)-fluorodeoxyglucose (FDG)-avid bilateral pulmonary metastases. Eight patients (3 ablations and 5 FU) showed no evidence of iodine-avid uptake into remnant thyroidal tissues or extra-thyroidal metastases on SPECT/CT. Possible explanations include very low volume thyroid remnants/ metastases which were below the

resolution of gamma camera imaging or non-Iodine avid metastatic disease. As a result, no uptake was shown on whole-body planar and SPECT/CT gamma camera images, despite focal uptake on FDG-PET/CT (Fig. 5-12).
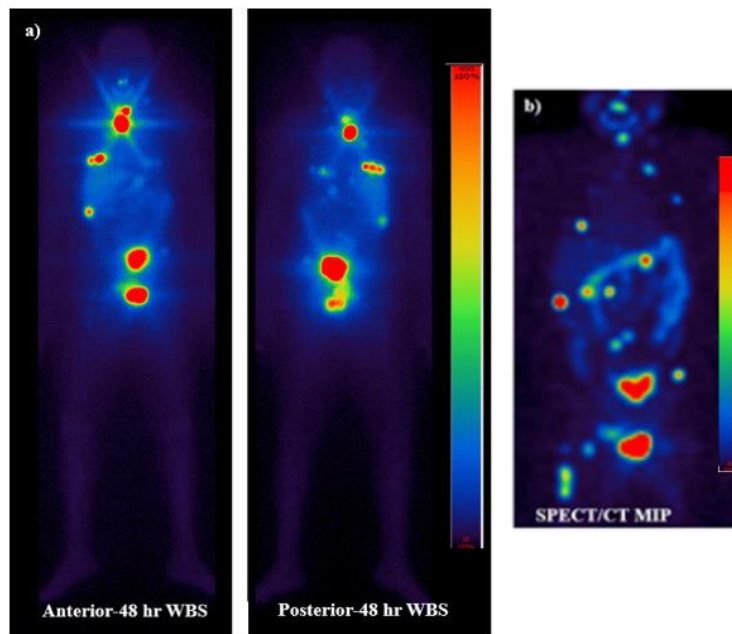
Figure 5-11: DTC patient Thyca-4 received 7930 MBq of ^{131}I for follow-up (FU) therapy. 48-hour imaging showed good uptake in the thyroid bed, lung, liver, and skeletal metastases. a) WBS and b) SPECT/CT.
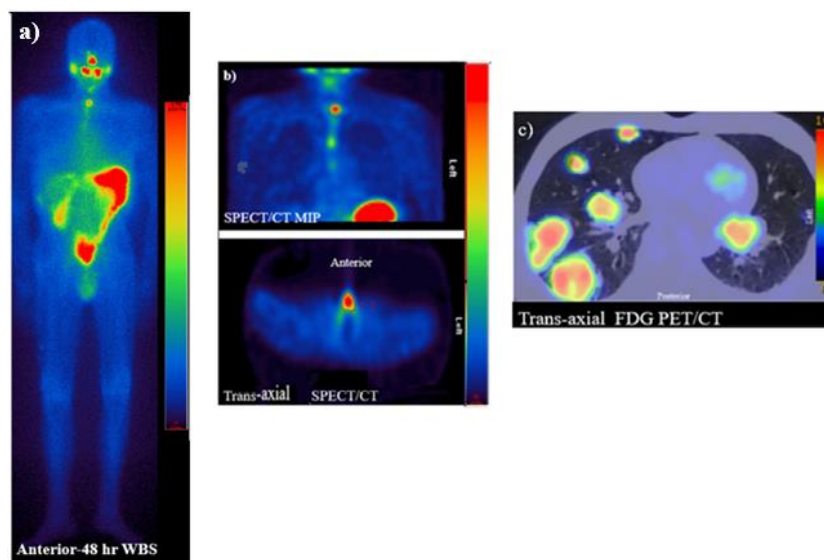
Figure 5-12: DTC patient Thyca-2 received 5780 MBq of ^{131}I for ablation therapy. 48-hour imaging showed remnant thyroid tissue uptake and no evidence of iodine-avid metastatic disease. a) WBS anterior view and b) SPECT/CT, c) FDG-PET/CT shows evidence of FDG-avid lung metastases.

Whole-body Activity Retention Estimation at Single Time-Point based on Patient-led, WBS, and SPECT/CT

Estimated activity at 48 hours post RAI administration, based on patient-led, WBS and SPECT measurements are shown in figure 5-13. The mean whole-body retained activity 48 hours after ^{131}I administration was comparable between WBS, SPECT/CT, and patient-led measurement for ablation and FU therapies (7 ± 2.5% and 3.7 ± 1.2%, respectively). The whole-body retention values were 7%, 4%, and 9 % for ablation and 4%, 2%, and 5% for FU using WBS, SPECT/CT, and patient-led measurement, respectively.

A strong positive linear correlation was observed with the estimated retained activity at 48 hours following RAI for DTC ablation and FU therapy using quantitative images from WBS (247±330MBq and 213±148MBq, respectively), SPECT/CT (141±169MBq and 1123±102MBq, respectively), and patient-led (309±309MBq and 225±92MBq, respectively). The strongest linear correlation was observed between SPECT/CT and WBS (R=0.97, p<0.001) followed by WBS and patient-led (R=0.92, p<0.001), and the lowest observed between SPECT/CT and patient-led (R=0.88, p<0.001) (Fig.5-13).
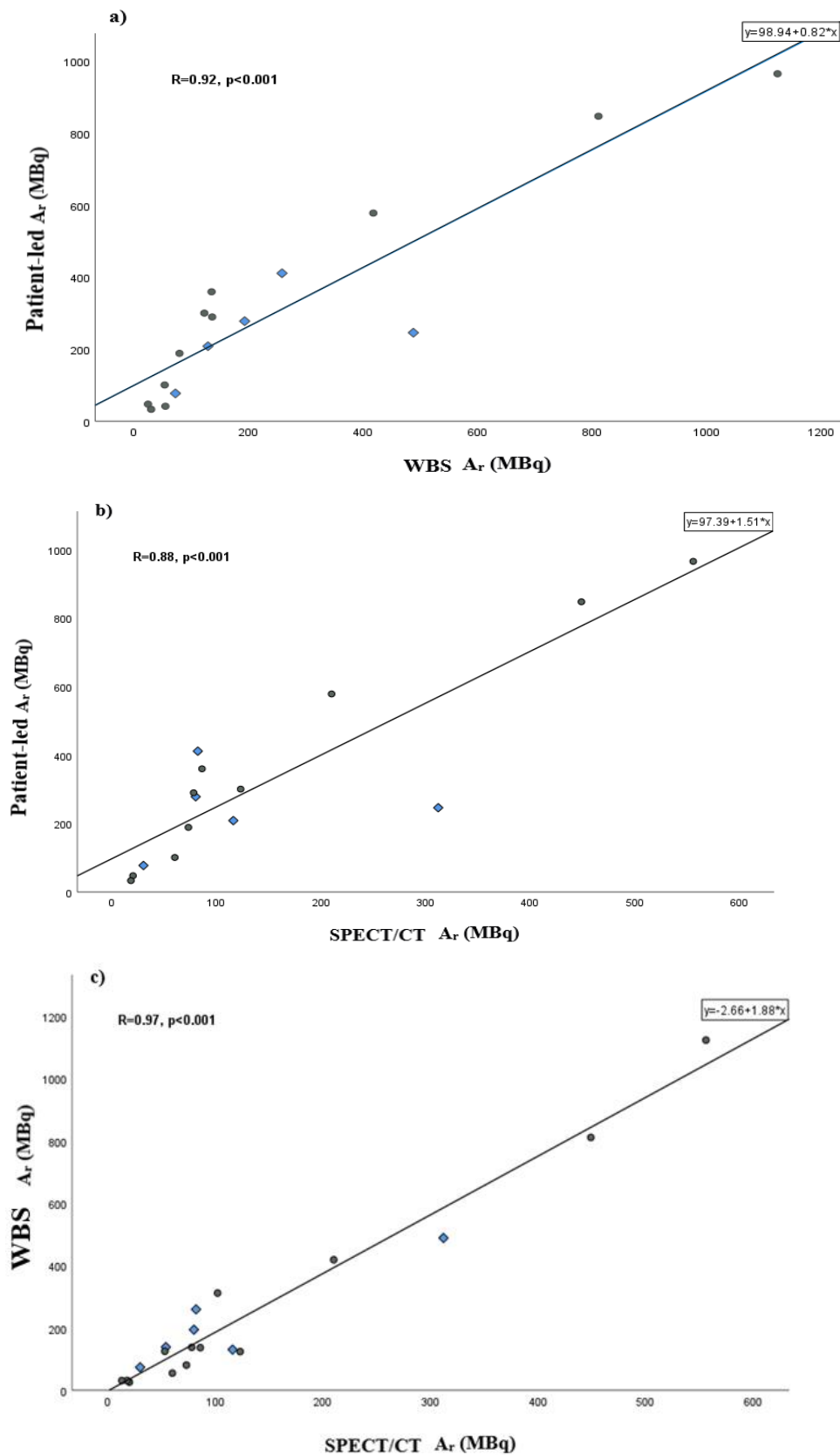
Figure 5-13: Scatter plot of a retained activity (A_r) estimation 48 hours following ^{131}I DTC ablation (circle marker) and FU (diamond marker) therapy plotted between a) patient-led measurement and WBS, b) patient-led measurement and SPECT/CT, and c) SPECT/CT and WBS.

Whole-body Absorbed Dose Estimation Using Sequential Long-Term Patient-Led Data

With the reassurance of the previous data showing agreement of ^{131}I activity estimates at the time-points assessed against patient-led dose rate measurements and quantitative SPECT/CT, we pursued the calculation of whole-body absorbed dose as per the MIRD scheme. Absorbed dose (D) (mGy) calculations using a patient-led estimate for DTC patients (n=17) (detailed absorbed dose per patient can be found in Appendix E). The mean absorbed dose for ablation and FU therapies were 77 ± 49 mGy and 120 ± 52 mGy, respectively (Fig. 5-14). These ^{131}I data cannot be directly compared to a dosimetric gold standard as additional SPECT/CT imaging was not available for these patients. However, seen in combination with activity estimates comparisons, they are provided here as demonstration of the potential of the methodology and the feasibility of the approach in a clinical setting.
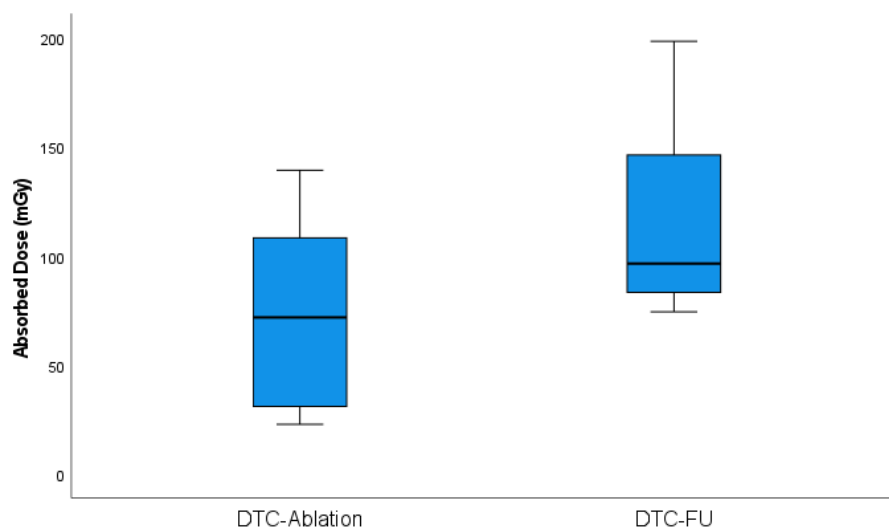
Figure 5-14: Box plot of mean, maximum, and minimum whole-body absorbed dose (mGy) by DTC ablation and FU therapy patients.

5.4.4. Comparison of Patient-led Data to Imaging Following ^{131}I MRT for Thyrotoxicosis

Fifteen thyrotoxic patients were referred for radioiodine therapy between January and June 2022 of whom 9 proceeded to treatment and completed WBS and patient-led monitoring. Seven females and two males with a mean age of 48.1 ± 18.5 years were treated with RAI therapy prospectively. The mean administered ^{131}I-NaI activity was 681 ± 83.5 MBq. The mean duration of the recorded dose rate using patient-led monitors was 21.57 ± 5.79 days for thyrotoxicosis patients.

Patients were treated for Graves' disease (n=6), toxic multi-nodular goitre (n=2), and toxic solitary thyroid nodule (n=1). Mean 20-minute Tc-99m thyroid uptake was 12.8 ± 13.5%, (normal range 0.4% and 4%) (more details about the patient cohort can be found in Appendix F). Whole-body gamma imaging at 24 hours revealed different RAI retention and count rate for each patient.

The biochemistry data were analysed for thyrotoxicosis patients before and 2–3 months after RAI therapy. Persisting hyperthyroidism was reported in six patients with TSH <0.27 mU/L.

Whole-body Activity Retention Estimation at Single Time-Point by Patient-Led measurements and WBS

The mean dose rate of thyrotoxicosis patients using the patient-led monitor at arm's length from the anterior mid-abdomen immediately after ^{131}I administration was 210 ± 66 µSv/h. Dose rate measurements led to estimates of retained activity as previously described. Results compared to WBS-derived estimates can be seen in figure 5-15. The mean whole-body retained activity 24 hours after ^{131}I administration was comparable between WBS 351.4±155.8 MBq (180-632.7 MBq) and patient-led measurements 402.7±154.5 MBq (189.7-682 MBq).

A strong positive linear correlation of residual activity estimation in MBq was observed 24 hours following RAI thyrotoxicosis therapy between quantitative WBS and patient-led dosimetry (R=0.88, p<0.01) with a linear fit coefficient of 0.78 and a low bias of 120 MBq (Fig. 5-15). The pattern is not dissimilar to that seen in figure 5-13a between *Selfie* and WBS data at wider range of activity levels (higher administered activity but imaging 48 hours post-administration).
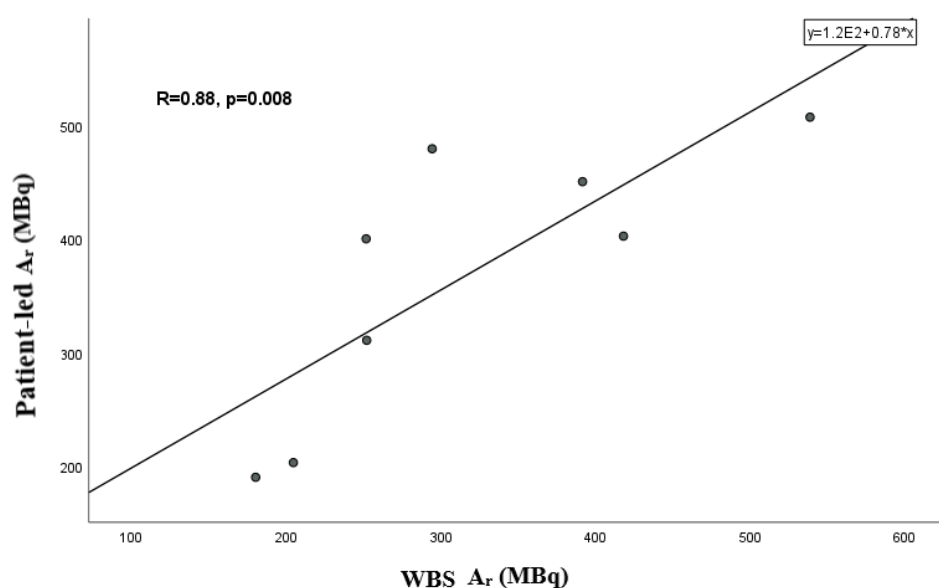
Figure 5-15: Scatter plot of A$_r$ estimation 24 hours following RAI thyrotoxicosis therapy based on patient-led measurements and WBS.

Whole-body absorbed dose estimation using sequential long-term patient-led data.

With the reassurance of these and previous data showing agreement of ^{131}I activity estimates at the time-points assessed against professional-led dose rate measurements, WBS and quantitative SPECT/CT, we pursued calculation of whole-body absorbed dose as per the MIRD scheme. Although these data cannot be directly compared to a dosimetric gold standard in the absence of additional imaging they are provided here as demonstration of the potential of the methodology and the feasibility of the approach in a clinical setting.

Absorbed dose (D) (in mGy) calculations using patient-led estimates for eight thyrotoxic patients. The mean whole-body absorbed dose was 108 ± 63 mGy (38-245mGy) (Appendix G).

In addition to WB absorbed dose, it would also be possible to calculate dose to the thyroid based on a thyroid-to-whole-body fractional estimates from WBS and the ^{131}I residence times from the *Selfie* data.

5.4.5. Patient-led User Compliance Survey

Eighteen patients responded to the patient-led *ease of use* survey (age: 48.9 y $\pm$ 14.9 y, 10 female and 8 male, 12 DTC and 6 thyrotoxic).

Table 5-6 shows the respondents' mean scores for each statement. The respondents agreed / strongly agreed (4.5±0.2) with all statements (except statement 4). Disagreed to strongly disagreed (1.7±0.8) responded to statement 4, which stated negative opinion regarding using patient-led. The evidence seems to indicate that five-point Likert scales ensure respondents reflected a strong level of acceptance of using the patient-led radiation monitor.

Table 5-6: Patient-led radiation monitor questionnaire mean statement responses.

Statement		Mean	±SD
1.	The patient-led monitor was straightforward to use at home.	4.72	.46
2.	I had enough information to work the patient-led monitor when I got home.	4.83	.38
3.	Using the patient-led monitor helped me to feel involved in my treatment.	4.64	.60
4.	It was nuisance to have to take measurements each day.	1.7	.81
5.	It was reassuring to see the numbers go down.	4.55	.61
6.	Using the patient-led monitor helped me follow the radiation advice I was given.	4.16	1.0
7.	I would be happy to use the patient-led monitor again.	4.66	.59
8.	I would recommend other people to use a patient-led monitor.	4.44	.78

5.5. Discussion

The first part of this study assessed the linearity of patient-led dose rate monitoring under relevant clinical conditions for radioisotopes ^{177}Lu and ^{131}I using vial measurements at certain distances. Patient-led measurements were validated with a neck-phantom static gamma imaging series for ^{177}Lu, and a four-time points whole-body gamma imaging series for three ^{177}Lu-DOTA-TATE patients. Patient-led measurements at 30–50 cm showed an acceptable RE ≤10% when compared with gamma imaging for ^{177}Lu and ^{131}I. Patient-led whole-body retention estimation at 24–48 hours was strongly correlated with dose rate measurements at a 2-m distance, WBS, and SPECT/CT during the patient's hospitalisation.

In this chapter, the ability of using patient-led measurements (*Selfie* data) to accurately estimate retain activity levels following administration of MRT at a clinical setting, was assessed against external dose rate measurements undertaken by medical physics staff and imaging in the form of planar scintigraphy and quantitative SPECT. Results showed a strong positive linear correlation between patient-led and WBS (R=0.78 and 0.92) and SPECT/CT (R=0.82 and 0.88) for the ^{177}Lu and ^{131}I-DTC estimates, respectively. Quantitative SPECT/CT is currently the

gold standard for such measurements. Results support the use of patient-led measurements for retained activity estimates after MRT administration over a longer period of several days and with minimal patient involvement (hospital visits) and imaging facilities workload. This is the first study to demonstrate the feasibility and accuracy of patient-led measurements by following various MRT groups. The results of this work show little variation from established imaging with WBS and SPECT/CT. Patient-led measurements may therefore prove able to resolve limitations related to the costly and time-consuming dosimetry approaches. Their potential to augment dosimetry alongside imaging in less imaging-heavy protocols for dosimetry by providing a better-informed alternative to population biodistribution for single time-point dosimetry (Hou et al., 2021; Willowson, Eslick, et al., 2018) , was not investigated in this work but seems to have strong potential as a direction for future studies.

Our proposed method using patient-led monitoring can be used to estimate activity retention and whole-body absorbed dose. In most centres, dosimetry following each PRRT cycle is not routinely applied to estimate the cumulative radiation dose and to correlate with MRT response and toxicities (Martinez et al., 2022). Even for ^{131}I DTC therapy, which is the oldest radionuclide therapy, the use of dosimetry is inconsistent and not standardised internationally (Martinez et al., 2022). The use of the mean kinetics model for all treated patients with a fixed activity was shown to be incompatible with outlier data and supports the concept of individual activity prescription. Individualised dosimetry-based MRT methods need to be harmonised among healthcare providers (Devasia et al., 2021b; Haug, 2020).

This study demonstrated a significant correlation between patient-led, WBS, and SPECT/CT dosimetry in estimating residual activity and whole-body retention. NET patients had a mean relative whole-body retention of 21 ± 5% and 19 ± 6% in PRRT cycles 1 and 4, respectively. A recent study reported comparable whole-body retention of 24 ± 7% using serial WBS at 24 hours following PRRT administration (Levart et al., 2019). In 72% of the NET patients in our

study, whole-body absorbed doses declined by 22.7 ± 15.8%, with a range from -7% to 54%, between PRRT cycles 1 and 4. As shown in figure 5-10, patient DOTA-20 exhibited a 54% reduction in whole-body absorbed dose, and the total-lesion mean SUV_{max} was reduced by 68% (Chapter 4). Although, administered activities were similar (7623 ± 47 MBq) in both cycles, two NET patients (Dota-1 & 2) showed an increase in whole-body absorbed doses by 67% and 30%, respectively. These patients showed stable disease responses to PRRT on SUV-SPECT/CT as shown in chapter 4. Both patients (DOTA-1&2) showed reduced eGFR by 18% and 8%, respectively. Retained ^{177}Lu-DOTA-TATE activity relies heavily on somatostatin avidity, radiopharmaceutical biodistribution, and renal function (Levart et al., 2019). Higher whole-body absorbed doses and longer activity retention increase the risk of radiation exposure to others such as the public and family members.

The overall measured retention at discharge (48 hours) for DTC ablation and FU therapy was 7 ± 2.5% and 3.7 ± 1.2% of the administered activity respectively. Hänscheid et al. reported equivalent whole-body retention of 6.9 ± 5.7% for DTC ablation therapy (Hänscheid et al., 2006). A study by Hong et al. reported DTC therapy retention comparable to FU therapy at 2.6%, but higher ablation retention of 12.9% (Hong et al., 2017). The difference in retention for ablation between this study and other studies could be related to the different sample sizes (n=118) (Hong et al., 2017). Another study reported 13.5 ± 11.9% [131]I retention for DTC patients (n=166), including ablation and subsequent therapies (Klain et al., 2021). RAI retention for thyrotoxicosis patients at 24 hours showed a longer retained ^{131}I activity compared with DTC patients. Lower retention in DTC patients related to the smaller thyroid remnants following completeness thyroidectomy surgery. Current UK practice mandates that thyroid cancer surgery is always undertaken by specialist thyroid surgeons. As a result, we postulate that our patients may have had smaller thyroid remnants than historical or non-UK subjects.

Whole-body retention and absorbed dose varied considerably between individual patients in the same MRT groups. The amount of retained activity varies from one patient to the other depending on the disease burden, radiopharmaceutical biodistribution and excretion. Longer retention, effective half-lives and higher whole-body absorbed radiation doses were observed in patients with significant remnant thyroid tissue, as in the ablation patient Thyca-02, than in patients with metastatic disease, such as FU patient Thyca-04 (Fig. 5-16). The main reason for longer retention in ablation patients is the normal physiological function of remnants of thyroid tissue which is driven by the thyroid-stimulating hormone (TSH) concentration in the blood (Hänscheid et al., 2006). One ablation patient (Thyca-02) showed non-iodine-avid pulmonary metastases. Non-iodine-avid metastases were reported due to rhTSH stimulation instead of thyroid hormone withdrawal (Driedger & Kotowycz, 2004; Lawhn-Heath et al., 2020). Although in this case, FDG avidity suggests de-differentiated, iodine refractory disease. Another reason for longer whole-body retention could be the patient's age, large thyroid remnants and extrathyroidal disease (Klain et al., 2021).
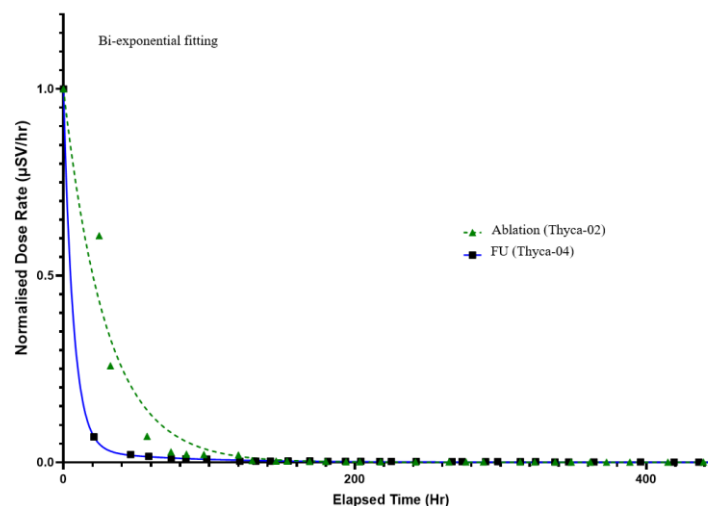
Figure 5-16: Representative examples of whole-body retention using bi-exponential curve fitting for ablation (dotted line) and FU (solid line) DTC patients treated with ^{131}I. Longer retention was observed in ablation therapy compared with FU therapy.

For thyrotoxicosis patients, more precautions need to be applied when selecting the exponential model. Bi- and mono-exponential models showed a very good fit to thyrotoxicosis data (as we will see in chapter 6), with a higher R^2 achieved with the bi-exponential model ($R^2=0.98 \pm 0.01$ and $R^2=0.93 \pm 0.04$, respectively). Our thyrotoxicosis data showed the longest retention in patients with high Tc-99m uptake. The highest (245mGy) and lowest (38mGy) whole body absorbed dose was observed for thyrotoxicosis patient's Hyper-10 and Hyper-4, respectively. As shown in figure 5-17, Hyper-4 exhibited the shortest retention compared with patient Hyper-10, and this can be linked to the Tc-99m uptake percentage prior to RAI (0.2% and 20%, respectively).
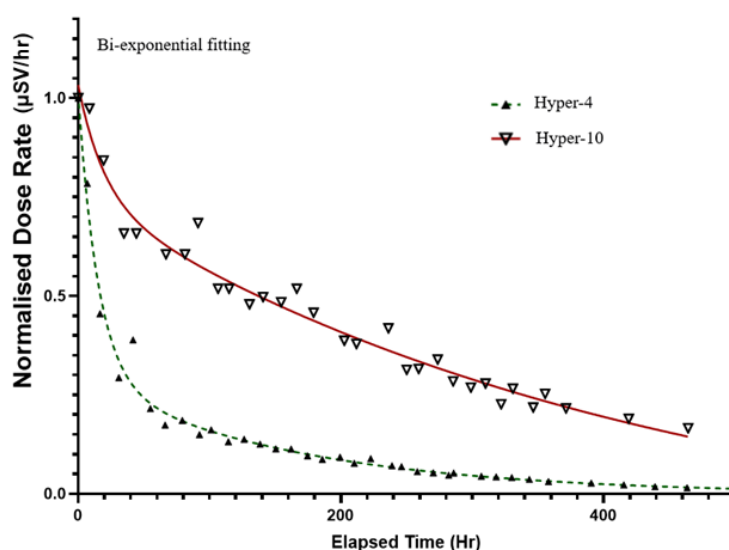
Figure 5-17: Representative examples of whole-body retention using bi-exponential curve fitting for thyrotoxicosis patients treated with ^{131}I. Longer retention was observed in patient Hyper-10, who had high TPO-Ab and 20% pre-therapy Tc-99m thyroid uptake. Patient Hyper-4 reported the lowest pre-therapy Tc-99m thyroid uptake (0.9%).

To create an appropriate TAC and to determine the cumulative activity, a minimum of three-time points sequential quantitative imaging is required. Therefore, the latest time points should be after two effective half-lives of the radiopharmaceutical (Huizing et al., 2018). Recently, researchers assessed the feasibility of single time-point SPECT/CT and reported that the

accuracy varied strongly between individuals due to patient-specific radiopharmaceutical clearance times (Hou et al., 2021).

The patient-led acceptance questionnaire showed positive feedback from all respondents for 28 days of data recording. Patients strongly agreed that *Selfie* is a straightforward device to use (4.72±0.46) and would have been happy to use it again (4.83±0.38). Patients did not find it a nuisance to take *Selfie* measurements each day (1.7±0.8). The five-point Likert scales ensured the *Selfie* was well-tolerated by the participating patients following MRT administration.

5.6. Conclusion

This study supports the concept of integrating patient-led radiation monitoring into MRT monitoring; the accuracy of this approach is comparable to that of serial quantitative imaging for whole-body activity estimates. Patient-led monitoring at home avoids the inconvenience of repeated hospital visits. In addition to allowing whole-body activity retention and absorbed dose calculations, we speculate this approach would support prospective personalised radiation protection guidance, which might positively impact the patient experience. Therefore, the next chapter will explore the role of patient-led data in tailoring patients' radiation restrictions.

CHAPTER 6

6. Application of Patient-Led Measurements to Tailor Radiation Restrictions Following MRT

Abstract

Introduction/Aims: There is an increasing need to understand whole-body activity retention and excretion in MRT for radiation risk assessment for patients, carers, and the public. However, the post-MRT imaging is limited to 1-3 days following radiopharmaceutical administration. As a result, patients are provided with generic radiation safety advice based on worst-case assumptions of radiopharmaceutical retention. As far as we know, no previous research has investigated ^{131}I and ^{177}Lu retention estimation over four weeks with daily dose rate measurements. We hypothesise that using patient-led data will show considerable inter-patient variability among groups of patients undergoing the same type of MRT. We pursue an assessment of personalised radiation restrictions using the best-fitting nonlinear regression model derived from patient-led data.

Methods: Patients undergoing molecular radionuclide therapy using ^{177}Lu-DOTA-TATE (7.4GBq) for neuroendocrine tumours and ^{131}I-NaI for benign (600-800 GBq) and malignant thyroid disease (1.1-7.4 GBq) were included. Patient-led whole-body retention measurements using a hand-held radiation monitor followed each patient's time of radioactivity clearance for four weeks post-therapy. Cohort analysis of 37, 17, and eight patient-led datasets following MRT administration of PRRT-^{177}Lu-DOTA-TATE, ^{131}I for DTC, and Thyrotoxicosis were included. The exponential non-linear regression analysis using the least squares method to fit the data was performed on GraphPad.

Results: ^{177}Lu-DOTA-TATE patient-led bi-exponential nonlinear regression showed that sleeping apart from the partner-tailored restriction was shorter in cycles 1 and 4 by 2 and 3 days, respectively, than the referenced restriction (15 days). Tailored restrictions for contact with children aged 2–5 y and 5–11 y were also longer than those referenced. For ^{131}I-DTC, patient-led data overestimated referenced restrictions in all categories except for one ablation patient. Three thyrotoxicosis patients showed shorter tailored restrictions than referenced advice, whereas the restrictions would have been extended for four patients, especially for the protection of children aged 2–11 y.

Conclusion: Tailored radiation restriction using patient-led whole-body retention measurements proved feasible for following the time course of radioactivity clearance in post-MRT. The best-fitting nonlinear regression model was illustrated for different MRT. This might enhance the feasibility of applying this approach to larger MRT populations.

6.1. Introduction

In the previous chapter we assessed the ability of patient-led *Selfie* data to provide accurate dose rate measurements and activity estimates following MRT and demonstrated its feasibility to be used over a longer period to provide whole-body retention patterns. In this chapter we investigate the application of this method in order to personalise MRT, firstly by tailoring radiation restrictions to patients and their close contacts.

Protection of patients, carers, and public safety requires optimising and personalising radiation protection restrictions using existing radiation protection measures ("Common Strategic Research Agenda for Radiation Protection in Medicine," 2017). Five medicals societies (European Association of Nuclear Medicine, EANM; European Federation of Organizations for Medical Physics, EFOMP; European Federation of Radiographer Societies, EFRS; European Society of Radiology, ESR; European Society for Radiotherapy and Oncology, ESTRO) involved in ionising radiation have identified measurement and quantification of ionising radiation as an urgent research area for effective patient care and efficiency in terms of radiation protection. Developing optimal dosimetry protocols in nuclear medicine is an essential priority for radiation safety in MRT. Optimisation requires standardisation and validation of implemented dosimetry methods using a phantom model ("Common Strategic Research Agenda for Radiation Protection in Medicine," 2017).

The international commission on radiological protection (ICRP) limits the annual equivalent dose for members of the public to 1 mSv (ICRP, 1991). This radiation dose limit applies to any family member or member of the public who is in close contact with an MRT patient after their release from the hospital. However, the family member and public dose limit is influenced by many factors, including the administered activity, the amount of radioactivity retained by the patient, the effective half-life, and the duration of close contact with the patient. Patients with

extensive metastases are expected to show higher whole-body radiopharmaceutical retention and longer effective half-life. As a result, the radiation dose to exposed members the public may also be increased.

The first published recommendations on radiological protection of patients, staff, and members of the public specific to radiopharmaceutical therapy were released in 2019 (ICRP, 2019). Currently, MRT patients who receive a fixed quantity of radiation follow similar radiation restrictions when released from isolation wards. In the UK, patients receiving RAI are released to the public with restrictions on their whole-body activity of ≤800 MBq. PRRT patients routinely receive fixed activity of ^{177}Lu-DOTA-TATE 7.4GBq/cycle. Patients with thyrotoxicosis are typically treated with 400–800 MBq of ^{131}I, whereas DTC patients receive a higher administered activity of radioactive iodine (RAI) (1.1–7.4 GBq) depending on whether the indication is thyroid remnant ablation or treatment of metastatic disease (Avram et al., 2022; ICRP, 1991, 2004, 2019; Sisson et al., 2011; Stokkel et al., 2010).

A recent study by Han et al. (2021) reported differences in external dose rates using a Geiger–Mueller tube in 238 DTC patients who had received 2.96-7.4 GBq ^{131}I. Radiation protection restrictions based on administered activity were more stringent than those based on measured effective dose equivalent rates at the time of discharge. This demonstrates the necessity for individualising radiation restriction guidelines (Han et al., 2021). Lee and Park (2010) had calculated discharge times from isolation following ^{131}I therapy for DTC patients based on external dose rate whole-body retention measurements. Patients who were given generic restrictions showed considerable variation; 27% of their sample could leave the isolation room within 24 hours and 77% could leave within 48 hours (Lee & Park, 2010). Effective doses received by the children and partners of patients were reported to be lower in thyroid cancer patients than for patients treated for thyrotoxicosis (Beckers, 1997).

There is an increasing need to understand whole-body activity retention and excretion in MRT for radiation risk assessment for patients, carers, and the public. While individualised dosimetry following MRT is not well established, individual biokinetic models of patients undergoing MRT have been used to evaluate significant differences between patients, the efficacy of therapy and the optimisation of repeated treatment planning (Barquero et al., 2008; Craig et al., 2020; Grudzinski et al., 2010).

Considerations, such as cost, patient convenience, quality of life and radiation protection are important drivers for developing flexible and personalised hospitalisation and radiation restriction plans for MRT patients. The previous chapter (Ch-5) showed that dose rates, activity estimates and TACs can be determined from long-term patient-led measurements and might be useful to guide personalising radiation restrictions. This approach proved to be comparable to imaging for whole-body estimates, feasible and patient friendly. As far as we know, no previous research has investigated ^{131}I and ^{177}Lu retention estimation over four weeks with daily dose rate measurements. We hypothesise that using patient-led data will show considerable inter-patient variability among groups of patients undergoing the same type of MRT. We pursue an assessment of personalised radiation restrictions using the best-fitting nonlinear regression model derived from patient-led data.

6.2. Aims

In this study, we aimed to investigate tailoring radiation protection advice to individual patients' radioactivity retention profiles by:

- Exploring the best fitting nonlinear regression model of acquired long-term (28 days) patient-led data.

- Tailoring radiation restrictions per individual and comparing them to clinical standard reference restrictions.

- Evaluating the impact of modelling restrictions based on short (8 day) versus long-term (28 day) patient-led data.

6.3. Methods

This section follows on from the collection of patient-led *Selfie* data described in the previous chapter. Data collection and statistical analysis were presented; Patient-led data and their proposed application to personalised radiation restrictions are presented for each MRT group in the following order: ^{177}Lu-Dota-Tate, ^{131}I-DTC, and ^{131}I-Thyrotoxicosis.

6.3.1. Tailored Radiation Protection Restrictions (Best Fit model)

Nonlinear regression analysis using mono- and bi-exponential curve fitting was applied to the whole-body activity retention data using GraphPad Prism version 9.0.1 for Windows (GraphPad Software, San Diego, California, USA).

The normalised dose rate (μSv/hr) was plotted against elapsed time, and exponential non-linear regression analysis using the method of least squares to fit the data was performed on GraphPad to derive the relationship between the two variables. The least square method minimises the sum of squares of the vertical distances between the data points and the curve. R^2 is the square of the correlation coefficient between the actual and predicted Y values, and it quantifies the goodness of curve fit.

Patient-led whole-body dose rate measurements for NET patients were analysed following cycles 1 and 4 of PRRT. Currently, PRRT patients received the same radiation protection restriction in both cycles. The DTC study population comprised of two groups, the ablation group (1st therapy) and the follow-up (FU) group (metastatic therapy), and each group was

categorised into four different radiation restriction guidelines based on administered activities: 1.1, 3.7, 5.5, and 7.4 GBq.

For the thyrotoxicosis group, bi-exponential and mono-exponential non-linear regression analysis were used to calculate patients' radiation protection restrictions.

Bi-exponential Decay Model

The bi-exponential clearance model is a two-phase model using the sum of fast and slow exponential clearance. The two clearance components (fast and slow) are each defined by a rate constant (K) and a predicted Y value. The starting Y values are defined by the following equations (H. J. Motulsky, 2016):

$$Y = Plateau + SpanFast * e^{(-KFast*x)} + SpanSlow * e^{(-KSlow*x)} \qquad Eq.6\text{-}1$$

$$SpanFast = (Y0 - Plateau) * PercentFast * 0.01 \qquad Eq.6\text{-}2$$

$$SpanSlow = (Y0 - Plateau) * (100 - PercentFast) * 0.01 \qquad Eq.6\text{-}3$$

X: Time

Y: Starts at Plateau + SpanFast + SpanSlow, then decays, with two phases, down to Plateau.

Y0: Value of Y at X=0, in the same units as Y. We constrain Y0 to be between zero and one (1>Y0>0).

PercentFast: The fraction of the Y signal due to the fast phase as a per cent.

Kslow: Slow decay constant rate per day.

Kfast: Fast decay constant rate per day.

Plateau is the Y value at infinite times, expressed in the same units as Y. We constrain our plateau to zero.

Span is the difference between Y0 and Plateau, expressed in the same units as Y values.

Referenced and Tailored Restrictions

Referenced standard written restrictions issued by Guys and St Thomas Hospital, starting immediately after MRT administration, were discussed with patients before MRT administration to comply with UK legislation (ICRP, 2004; IPEM, 2002; IRR2017, 2017) (Table 6-1). There are no specific restrictions regarding public and private transportation. Generally, the patient was advised to limit journey times so as not to exceed one hour and to avoid prolonged close contact with individual members of the public while travelling. In some cases, where the patient longer journey times were anticipated, advice was based on individualised calculations and risk assessment based on the dose rate at the time of discharge from hospital.

These restrictions were derived by use of dose-modelling methods outlined by Barrington et al. following RAI therapy for DTC and thyrotoxicosis patients (Barrington et al., 1996, 1999) in which the following assumptions were applied:

1. For private transport, the driver would sit 1.0 m from the patient, and no other traveller would present in the vehicle. For public transport, the patient would sit 0.1 m from fellow travellers. (We calculated the allowed maximum public and private transport journey time (hours) after leaving the hospital).
2. On return to work, the patient would sit 1.0 m away from the same work fellow for a working day of 8 hours.
3. Sleep apart from a partner; patients would spend 6 hours at 1.0 m, followed by 8 hours at 0.1 m (asleep) next to the partner.
4. For children, three age groups were defined based on assumed periods of time spent by a child in close contact with a patient:
   I. Child (<2 years) would spend 15 periods of close contact (0.1 m) of 35 minutes during every 24-hour period with the patient.

II. Child (2–5 years) would spend 4 hours at 0.1 m and 8 hours at 1.0 m from the patient.

III. Child >5 years would spend 2 hours at 0.1 m and 4 hours at 1 m from the patient.

We used the above assumptions to tailor patient radiation restrictions following discharge from hospital after MRT administration.

Table 6-1: Standard restrictions advised by Guys and St Thomas Hospital for patients undergoing MRT. Restricted contact (days) following radiopharmaceutical administration for different categories of member of the public.

Referenced Radiation Restrictions (days)

	^{131}I-DTC 1st Treatment (Ablation)				^{131}I-DTC Follow-up Therapy (FU)			^{131}I-Thyrotoxicosis	^{177}Lu-DOTA-TATE
	1100 MBq	3700 MBq	5500 MBq	7400 MBq	3700 MBq	5500 MBq	7400 MBq	601–800 MBq	7400 MBq
Going out	3	11	13	15	2	3	3	17	7
Returning to work	7	15	17	19	3	3	4	17	7
Contact with a pregnant woman	3	11	13	15	2	3	3	16	15
Sleep apart from partner	13	19	21	23	4	4	5	26	15
Child <2 years old	14	20	22	24	4	5	5	27	15
Child 2–5 years old	11	17	19	21	4	4	4	22	10
Child >5 years old	7	13	16	17	3	3	4	16	7

Referenced and tailored restrictions were calculated to comply with the recommended dose limit of 1 mSv/cycle for household members and the public following I-131 therapy. A dose limit not exceeding 5 mSv averaged over 5 years (ICRP, 2004; Silberstein et al., 2012; Sisson et al., 2011) was applied to the contacts of patients receiving ^{177}Lu-DOTA-TATE PRRT. The constraint per procedure was 0.3 mSv for pregnant women and members of the public, such as public and private transport and co-workers, and 1 mSv for members of the same household.

Dose rate measurements (µSv/hr/MBq) were scaled by inverse square law for 0.1-, 0.5-, and 1.0-m distances from the 0.38 m patient-led first dose rate measurement following activity administration. Then, the fast and slow effective half-life, $T_{eff(F)}$ and $T_{eff(S)}$, were calculated from the following equations (Cormack & Shearer, 1998):

$$T_{eff(F)} = SPAN_{fast} \cdot (e^{-K_{fast} \cdot x} \cdot x \ /K_{fast}) \cdot (1 - e^{-K_{fast} \cdot x}) \qquad Eq.6\text{-}4$$
$$T_{eff(S)} = SPAN_{slow} \cdot (e^{-K_{slow} \cdot x} \ /K_{slow}) \cdot (1 - e^{-K_{slow} \cdot x}) \qquad Eq.6\text{-}5$$

Finally, exposure to another individual in µSv was calculated using dose rate (D_R, µSv/Day) at 0.1 and 1 m distances and $T_{eff(S)}$ from the following equation.

$$Exposure = T_{eff(S)} \cdot D_R \qquad\qquad\qquad Eq.6\text{-}6$$

6.3.2. Eight (8) Days Patient-led Fitting Model

We assessed the correlation between bi-exponential fitting parameters using patient-led measurements for at least 8 days. This approach evaluates the implications of using a shorter period of patient-led measurements for calculating radiation restrictions reflecting the need to inform patients as early as possible on the specific radiation restriction path that should be followed. We aimed to assess the shortest period that was more than or equal to the radioisotopes' physical half-lives (^{177}Lu=6.7 days and ^{131}I=8 days).

We analysed patient-led data from day zero to eight by applying nonlinear regression bi-exponential and mono-exponential curves. The exact method was replicated from the previous section. The fitting coefficients and half-lives were correlated with 28 days data set for each MRT group.

6.4. Results

In this section, results of tailored radiation restrictions using a patient-led data best-fitting model are presented for each MRT group in the following order (^{177}Lu-Dota-Tate, ^{131}I-DTC, and ^{131}I-Thyrotoxicosis). Then the results of the correlation between the 8- and 28-day fitting model are presented as an assessment of whether radiation restrictions can be tailored based on earlier dose rate readings.

6.4.1. Tailoring Radiation Protection Restrictions (Best fit model)

^{177}Lu-DOTA-TATE Neuroendocrine Tumours Therapy

Thirty-seven patient-led whole-body retention bi-exponential non-linear regression curve fitting parameters for NET patients following ^{177}Lu-DOTA-TATE PRRT cycles 1 and 4 were analysed. The bi-exponential model of fast and slow half-lives corresponding fast and slow whole-body excretion, respectively. The cohort PRRT cycle 1 fast half-life of 7.3 ± 8.9 hr (2.3-42.6 hr) decreased at cycle 4 to 5.8 ± 2.8 hr (3.0-12.9 hr) whereas slow half-life showed a slight increase between cycles 1 and 4 (84.3 ± 19.3 hr (59.8-133.6 hr) and 88.1 ± 25.3 hr (41.3-150.3 hr), respectively). Curve fitting coefficients were applied for each data. The mean, fast, and slow whole-body excretion fitting values as per equation 6-1 were:

Cycle 1 PRRT bi-exponential curve fitting

$$Y_{mean} = 0.75 \cdot e^{(-3.38x)} + 0.25 \cdot e^{(-0.21x)}$$

$$Y_{fast} = 0.93 \cdot e^{(-7.1x)} + 0.07 \cdot e^{(-0.28x)}$$

$$Y_{slow} = 0.35 \cdot e^{(-0.39x)} + 0.65 \cdot e^{(-0.12x)}$$

*Cycle 4 PRRT bi-exponential curve fitting***:**

$$Y_{mean} = 0.75 \cdot e^{(-3.34x)} + 0.25 \cdot e^{(-0.21x)}$$

$$Y_{fast} = 0.91 \cdot e^{(-5.42x)} + 0.09 \cdot e^{(-0.4x)}$$

$$Y_{slow} = 0.55 \cdot e^{(-1.28x)} + 0.45 \cdot e^{(-0.11x)}$$

The bi-exponential model goodness of fit was excellent with minimal error (cycle 1: $R^2=1 \pm 0.01$ and sum of squares = $0.01 \pm .01$, cycle 4: $R^2=1 \pm 0.01$ and sum of squares = 0.004 ± 0.004). Figure 6-1 shows the variation in bi-exponential whole-body retention curves of PRRT cycles 1 and 4 between NET patients treated uniformly with the same ^{177}Lu-DOTA-TATE activity (7.4GBq +/- 10%). NET patient DOTA-20 exhibited faster whole-body clearance (shorter whole-body retention) in cycle 4 (half-lives slow = 78.9 hr and fast = 6.9 hr) compared with cycle 1 (half-lives slow = 92 hr and fast = 42.6 hr) (Fig. 6-2). This example poses interesting questions about tailoring radiation restrictions, and perhaps in future, tailoring treatment.
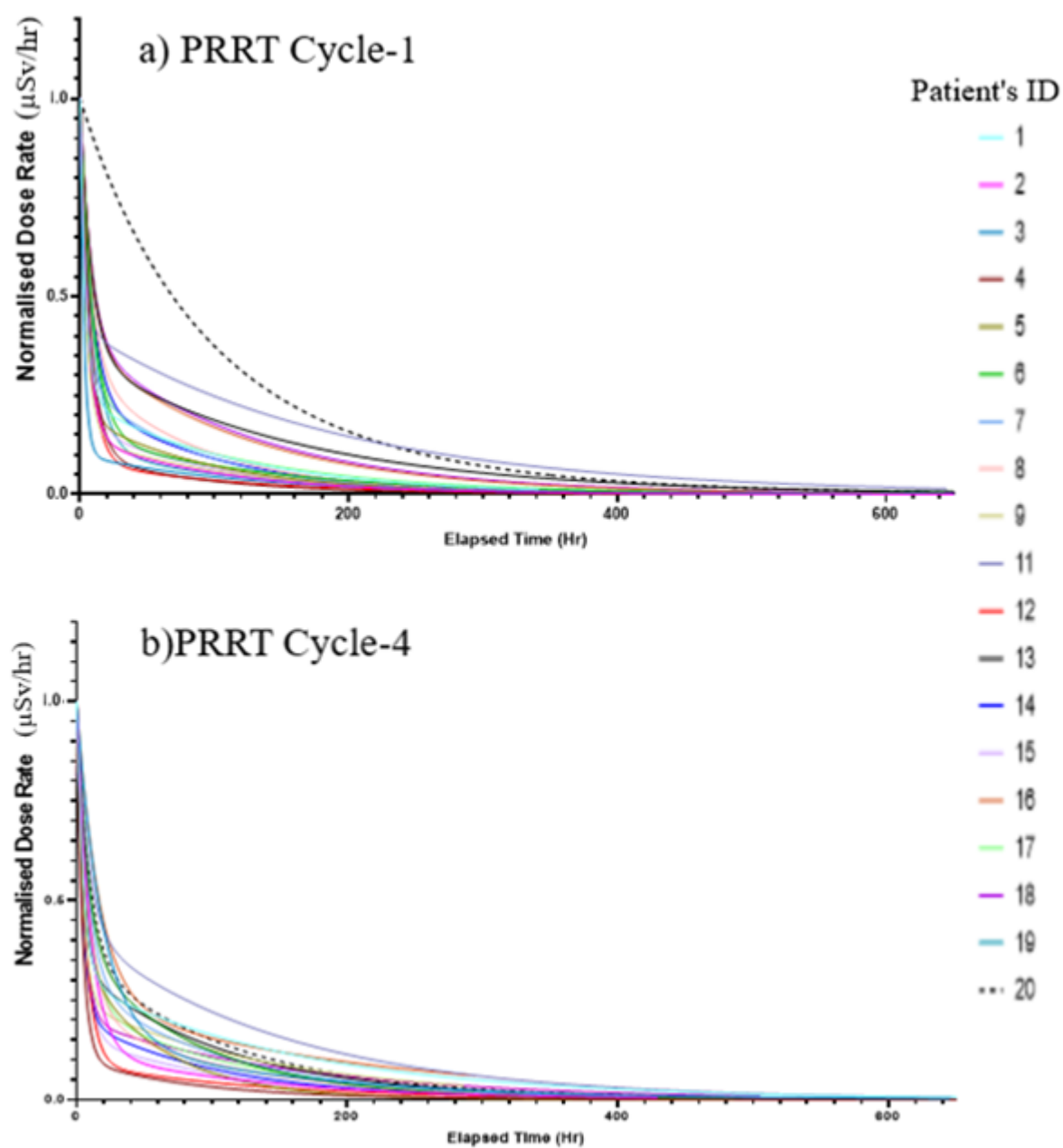
Figure 6-1: Bi-exponential whole-body retention curve of a) cycle 1 and b) cycle 4 of PRRT showing variation between NET patients treated uniformly with the same activity of Lu-DOTA-TATE.
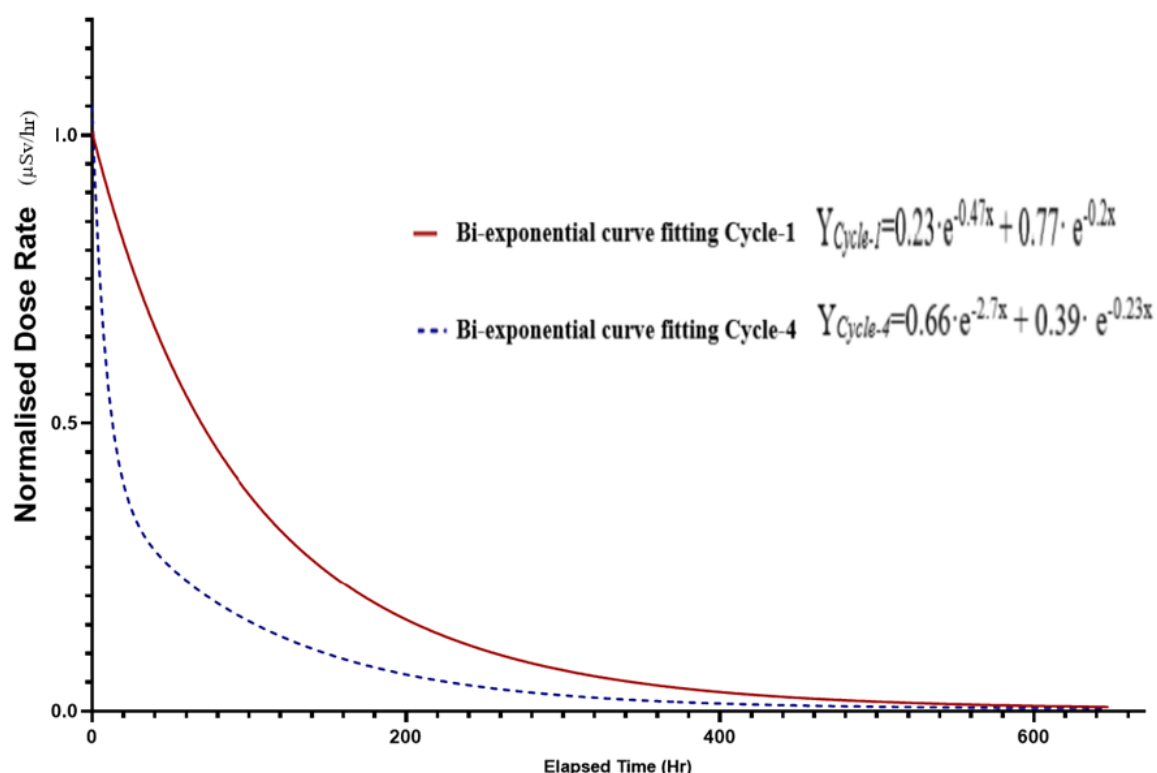
Figure 6-2: NET patient DOTA-20's PRRT cycles 1 and 4 patient-led bi-exponential curve fitting showed a faster whole-body clearance at cycle 4 compared with cycle 1.

Tailored radiation protection restrictions were calculated daily for NET patients using bi-exponential fitting parameters (Fig. 6-3). Referenced restrictions in the first two categories concerning members of the public were overestimated on average by 6.7 ± 0.54 days compared with tailored restrictions that could have been derived using the patient-led method. Restrictions for family members, including the restriction of sleeping apart from partners and children (<2 y, 2–5 y, and 5–11 y), showed considerable variation between tailored restrictions and referenced restrictions in NET patients. Table 6-2 shows the descriptive statistics of tailored restrictions for ^{177}Lu-DOTA-TATE PRRT cycles 1 and 4. The journey time for public and private transport to limit the members of the public exposure to ≤0.3mSv were as follows; Cycle-1 public and private transport journey time (9.14 ± 26.19 hr and 56 ± 32.9 hr,

respectively). Cycle-4 public and private transport journey time (8.8± 4.7 hr and 61.9±33.7 hr, respectively).
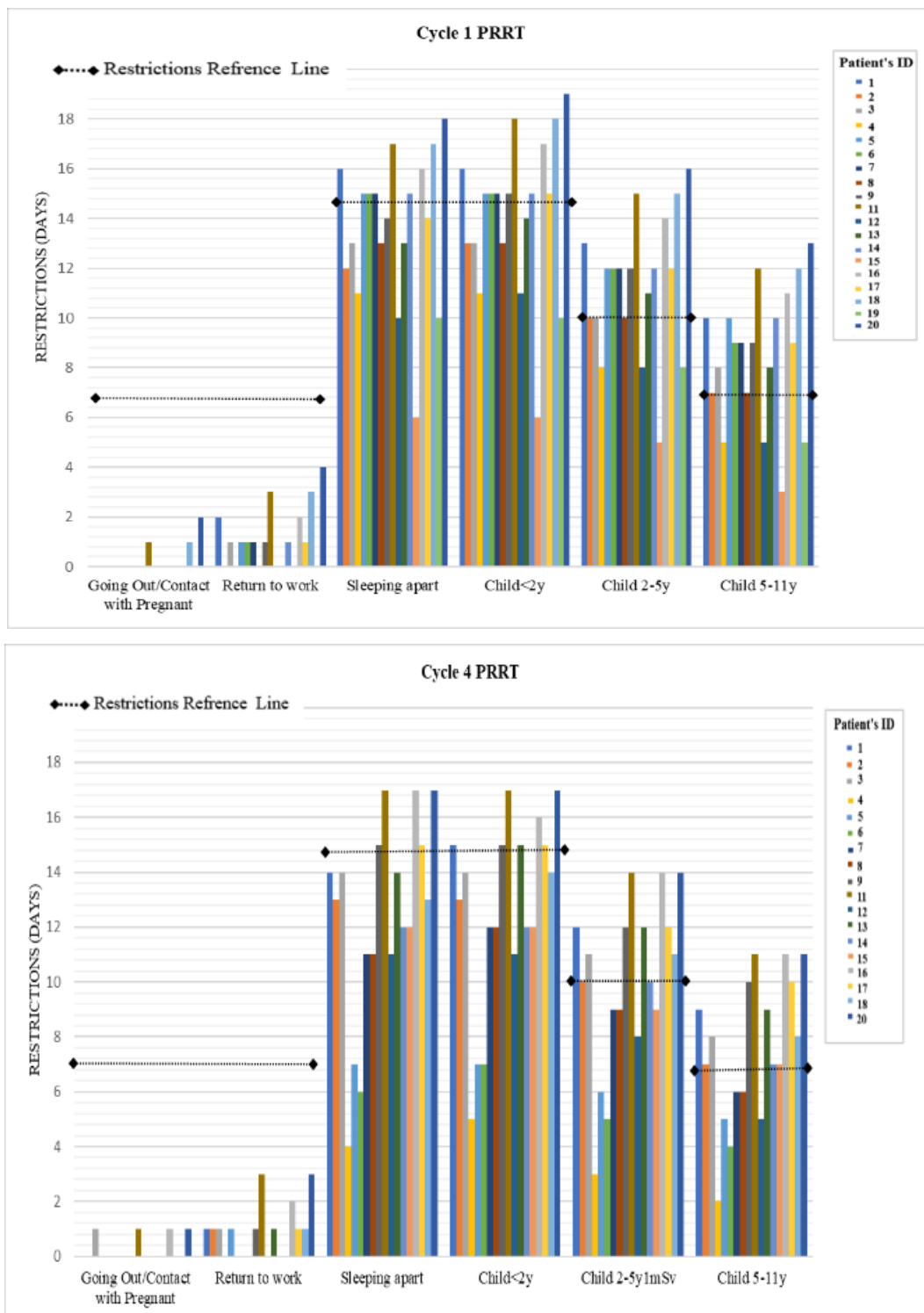
Figure 6-3: Tailored radiation restrictions (using patient-led data) in days plotted by group categories for NET patients following PRRT cycles 1 and 4. The reference line (dotted black line) represents the generic restriction advice given to the patients following PRRT administration.

Table 6-2: 177Lu-DOTA-TATE PRRT cycles 1 and 4 Descriptive statistics (mean, ±SD, Max, and Min) of tailored restriction days using patient-led and whole-body bi-exponential fitting parameters.

	Generic restrictions (Day)	PRRT Cycle 1				PRRT Cycle 4			
		Mean	*±SD*	*Max*	*Min*	*Mean*	*±SD*	*Max*	*Min*
Going out/Contact with a pregnant person *(4 hrs contact at 1 m)*	*7*	*0.2*	*0.5*	*2.0*	*0.0*	*0.2*	*0.4*	*1.0*	*0.0*
Return to work *(8 hrs contact at 1 m, 7 days a week)*	*7*	*1.1*	*1.2*	*4.0*	*0.0*	*0.9*	*1.0*	*3.0*	*0.0*
Sleeping apart *(6 hrs at 1 m during the day and 8 hrs sleep time at 0.1 m)*	*15*	*13.7*	*2.9*	*18.0*	*6.0*	*12.4*	*3.7*	*17.0*	*4.0*
Child <2 y *(8 hrs at 0.1 m)*	*15*	*14.2*	*3.1*	*19.0*	*6.0*	*12.7*	*3.4*	*17.0*	*5.0*
Child 2–5 y *(4 hrs at 0.1 m and 8 hrs at 1 m)*	*10*	*11.3*	*2.8*	*16.0*	*5.0*	*10.1*	*3.1*	*14.0*	*3.0*
Child 5–11y *(2 hrs at 0.1 m and 4 hrs at 1 m)*	*7*	*8.5*	*2.7*	*13.0*	*3.0*	*7.6*	*2.6*	*11.0*	*2.0*

The sleeping apart from the partner-tailored restriction was shorter in cycles 1 and 4 by 2 and 3 days, respectively than the referenced restriction (15 days). Tailored restrictions for contact with children aged 2–5 y and 5–11 y was also longer in cycle 1 (by 2 ± 2.8 and 2 ± 2.7 days, respectively) and cycle 4 (by 1 ± 3.1 and 1 ± 2.6 days, respectively) than the referenced restrictions. However, children <2 y old showed less onerous tailored restrictions by 1 ± 3.1 days and 3 ± 3.4 days following cycle 1 and cycle 4, respectively. On an individual basis, some patients showed a reduction in contact restriction by 4 days (Fig. 6-4, a) and 8 days (Fig. 6-4, b) which was consistent with visual assessment of reduced uptake on SPECT/CT images. On the other hand, longer radiation restrictions would have been advisable for patients showing stable disease on SPECT/CT images by ≥ 4 days (Fig. 6-5).
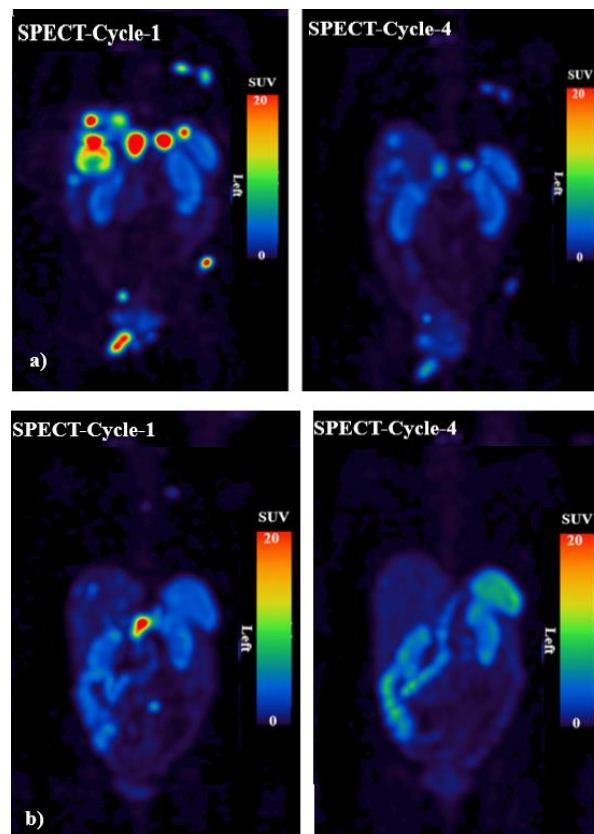
Figure 6-4: Examples of two PRRT patients' SPECT/CT MIP images. a) Patient DOTA-7 showed a reduction in restrictions following cycle 4 PRRT by 4 days, and b) patient DOTA-5 showed a reduction by 8 days.
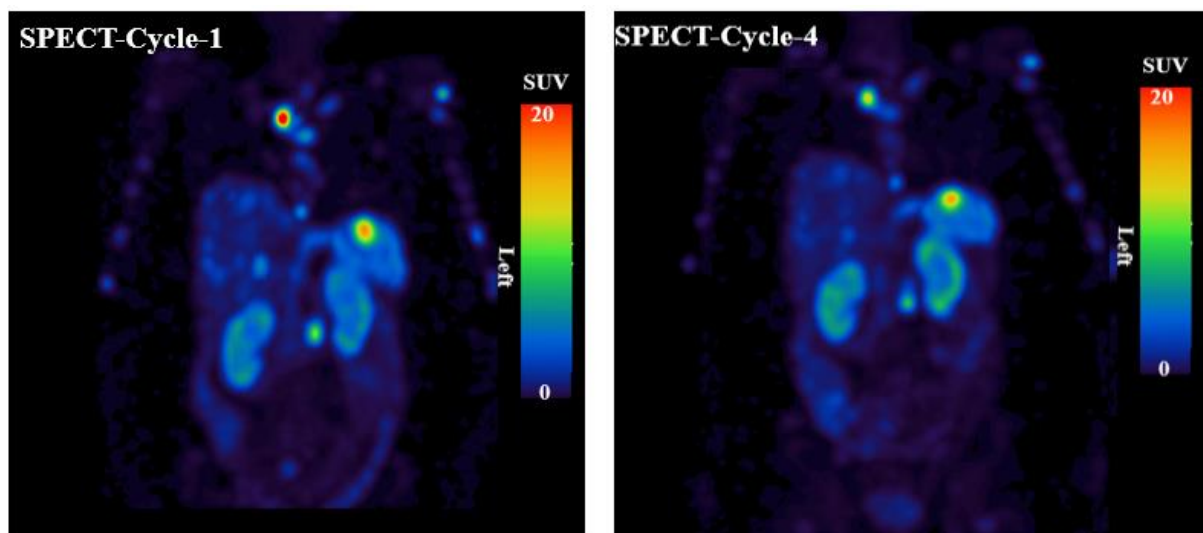
Figure 6-5: Example of SPECT/CT MIP image following PRRT cycles 1 and 4. Patient DOTA-15 showed increased radiation restriction by 6 days for sleeping apart from a partner and contact with children <2 years old, and by 4 days regarding contact with children >2–11 years old.

^{131}I-Differentiated Thyroid Cancer Therapy

Seventeen patient-led and whole-body retention bi- and mono-exponential non-linear regression curve fitting parameters for thyroid DTC were analysed. The bi-exponential model's fast and slow half-lives (10.2 ± 3.8 hr (2.5-14.5 hr) and 33.3 ± 33.6 hr (10.4-122.7 hr), respectively) demonstrated fast and slow whole-body excretion, respectively. The mean, fast, and slow whole-body excretion fitting values were calculated as per equation 6-1:

Bi-exponential curve fitting

$$Y_{mean} = 0.63 \cdot e^{(-1.82x)} + 0.39 \cdot e^{(-0.91x)}$$

$$Y_{fast} = 1 \cdot e^{(-6.53x)} + 0.27 \cdot e^{(-1.59x)}$$

$$Y_{slow} = 0.82 \cdot e^{(-1.34x)} + 0.9 \cdot e^{(-0.17x)}$$

Mono-exponential curve fitting:

$$Y_{mean} = 1 \cdot e^{(-1.59x)}$$

$$Y_{max} = 1.08 \cdot e^{(-3.05x)}$$

$$Y_{min} = 1.02 \cdot e^{(-0.79x)}$$

The bi-exponential model showed goodness of fit with almost ideal fitting with minimal error compared with the mono-exponential model (bi-exponential: R^2=0.99 ± 0.01 and sum of squares = 0.01 ± 0.02, mono-exponential: R^2=0.99 ± 0.02 and sum of squares = 0.02 ± .03).

Tailored radiation protection restrictions for DTC ablation (Fig. 6-6) and FU patients (Fig. 6-7) were calculated using bi-exponential fitting parameters. Overestimation of referenced restrictions was observed in all categories for ablation therapy patients, except for one subject (Thyca-20), compared with tailored restrictions using the patient-led method. Restrictions for family members, including sleeping apart from partners and children (<2 y, 2–5 y, and 5–11 y), showed considerable variation in DTC patients between tailored restrictions and referenced

restrictions. Table 6-3 shows the descriptive statistics of tailored restrictions for ablation and FU RAI therapy. The journey time for public and private transport to limit the public member exposure to ≤0.3mSv were 21.6±26.4 hr and 57.8± 53.8 hr, respectively.

The tailored restriction for sleeping apart from the partner was 7.6 ± 7.5 days and 4.2 ± 1.3 days for ablation and FU therapies, respectively. In general, the duration of tailored and referenced restrictions was similar for FU therapies whereas a considerable reduction in all categories of tailored restrictions duration compared with referenced advice was reported for ablation therapies.
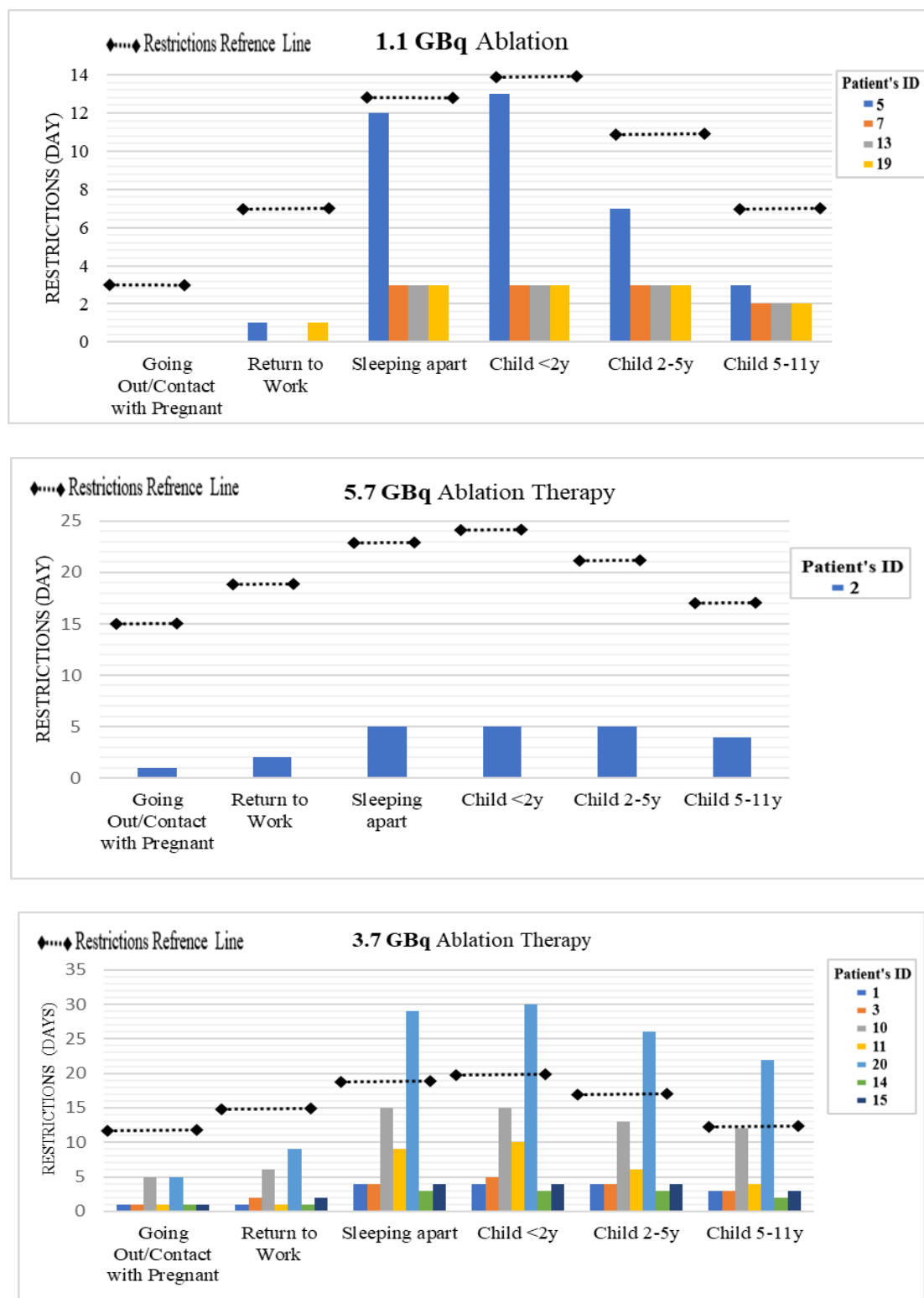
Figure 6-6: Tailored radiation restrictions (using patient-led data) in days plotted by group for DTC- ablation patients following ^{131}I therapy. Reference line (dotted black line) represents the standard restriction advice given to the patients following MRT as part of GSTT standard of care. Referenced restrictions were based on the type of therapy (ablation or FU) and the amount of administered activity.
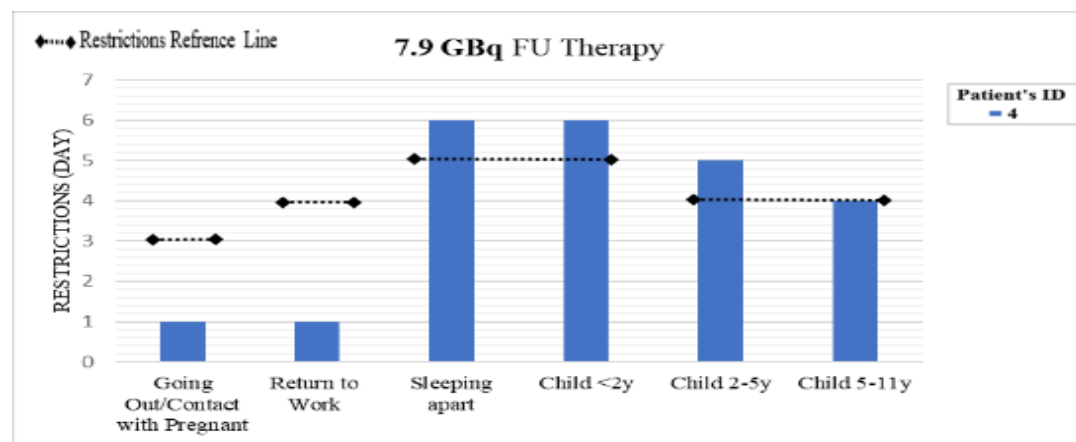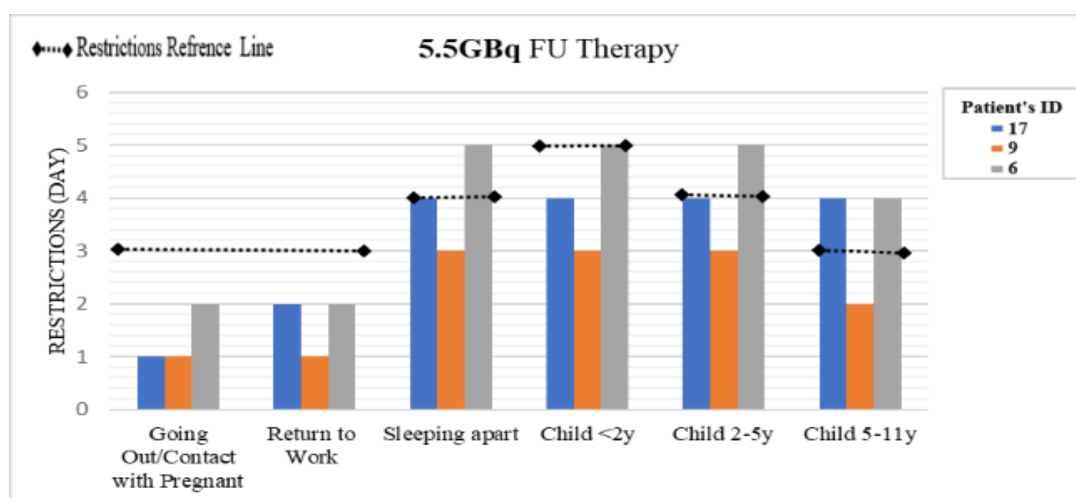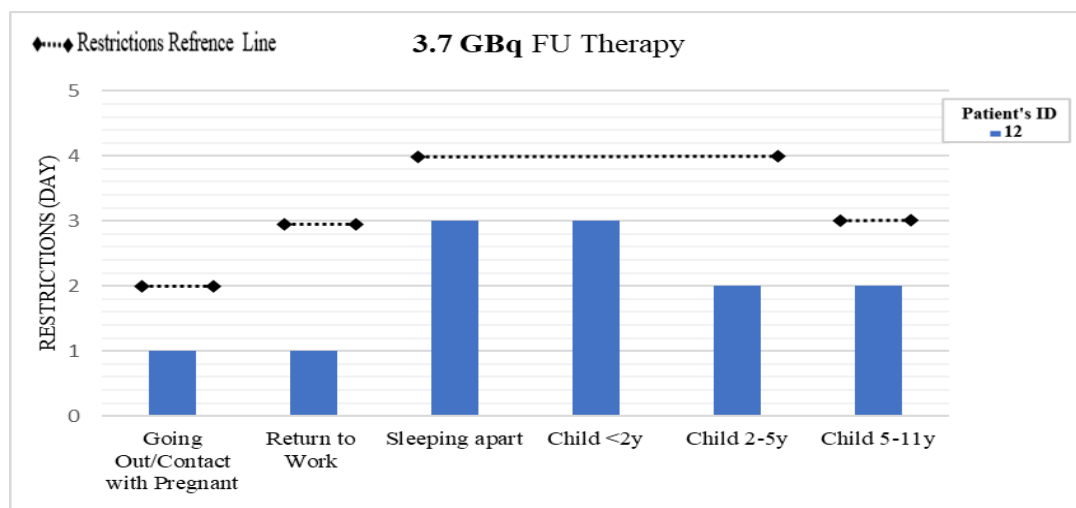
Figure 6-7: Tailored radiation restrictions (using patient-led data) in days plotted by group for DTC-FU patients following ^{131}I therapy. Reference line (dotted black line) represents the standard restriction advice given to the patients following MRT as part of GSTT standard of care.

Table 6-3: Descriptive statistics (mean, ±SD, Max, and Min) of tailored restriction days using patient-led and whole-body bi-exponential fitting parameters for DTC ablation and FU RAI therapy.

	THYCA-Ablation				THYCA-FU			
	Mean	±SD	Max	Min	Mean	±SD	Max	Min
Going out/Contact with a pregnant person (4 hrs contact at 1 m)	*1.33*	*1.78*	*5*	*0*	*1.20*	*0.45*	*2*	*1*
Return to work (8 hrs contact at 1 m, 7 days a week)	*2.17*	*2.66*	*9*	*0*	*1.40*	*0.55*	*2*	*1*
Sleeping apart (6 hrs at 1 m during the day and 8 hrs sleep time at 0.1 m)	*7.83*	*7.77*	*29*	*3*	*4.20*	*1.30*	*6*	*3*
Child <2 y (8 hrs at 0.1 m)	*8.17*	*8.04*	*30*	*3*	*4.20*	*1.30*	*6*	*3*
Child 2–5 y (4 hrs at 0.1 m and 8 hrs at 1 m)	*6.75*	*6.69*	*26*	*3*	*3.80*	*1.30*	*5*	*2*
Child 5–11 y (2 hrs at 0.1 m and 4 hrs at 1 m)	*5.17*	*5.97*	*22*	*2*	*3.20*	*1.10*	*4*	*2*

^{131}I-Thyrotoxicosis Therapy

Eight patient-led whole-body retention bi- and mono-exponential non-linear regression curve fitting parameters for thyrotoxicosis patients were analysed. Two patients were excluded from the restrictions analysis due to inconsistent return of patient-led data. The bi-exponential model fast and slow half-lives (12.3 ± 4.5 hr (8.6-21.8 hr) and 147 ± 25.8 hr (113.5-174.8 hr), respectively) corresponding to fast and slow whole-body excretion, respectively. Patients 9 and 10 exhibited increased slow half-life (333 hrs, and 296 hrs, respectively), exceeding the ^{131}I physical half-life (192.47 hrs)); this may be probably due to errors with data collection which couldn't be resolved or investigated by the time of data analysis. The mean, fast, and slow whole-body excretion fitting values were calculated as per equation 6-1:

Bi-exponential curve fitting

$$Y_{mean} = 0.39 \cdot e^{(-1.46x)} + 0.58 \cdot e^{(-0.1x)}$$

$$Y_{fast} = 0.72 \cdot e^{(-1.92x)} + 0.29 \cdot e^{(-0.15x)}$$

$$Y_{slow} = 0.19 \cdot e^{(-0.76x)} + 0.78 \cdot e^{(-0.05x)}$$

Mono-exponential curve fitting:

$$Y_{mean} = 0.88 \cdot e^{(-0.29x)}$$

$$Y_{fast} = 0.93 \cdot e^{(-0.74x)}$$

$$Y_{slow} = 0.77 \cdot e^{(-0.14x)}$$

The bi-exponential model provided goodness of fit with almost ideal fitting with minimal error compared with the mono-exponential model (bi-exponential: $R^2=0.98 \pm 0.01$ and sum of squares $=0.00 \pm 0.04$, mono-exponential: $R^2=0.99 \pm 0.02$ and sum of squares $= 0.03 \pm 0.02$). Figure 6-8 shows an example of short (Hyper-4) and long (Hyper-10) whole-body retention in thyrotoxic patients, with comparable bi- and mono- exponential curve fitting.

Hyper-4

Dose Rate

Mono-exponential $Y = 0.93 \cdot e^{(-0.72x)}$

Bi-exponential $Y = 0.72 \cdot e^{(-1.5x)} + 0.29 \cdot e^{(-0.15x)}$

Hyper-10

Dose Rate

Mono-exponential fittir $Y = 0.92 \cdot e^{(-0.14x)}$

Bi-exponential fitting $Y = 0.21 \cdot e^{(-1.23x)} + 0.78 \cdot e^{(-0.06x)}$
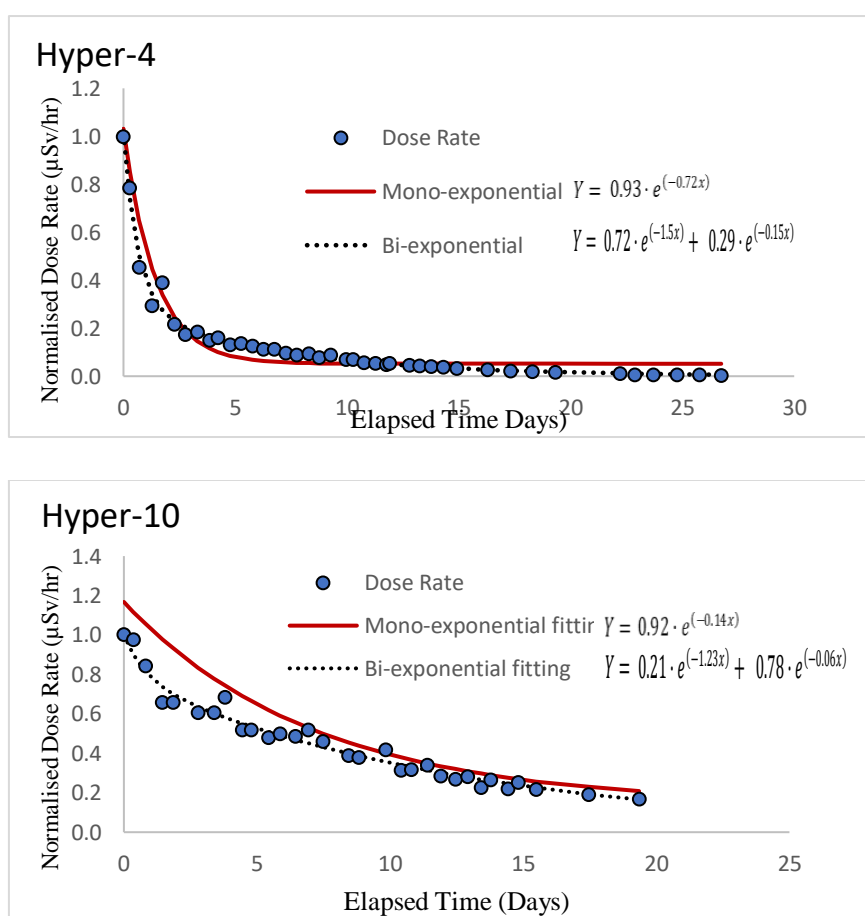
Figure 6-8: Mono- and bi-exponentials curve fitting for thyrotoxicosis patients: a) very fast whole-body clearance (Hyper-4) and b) very slow whole-body clearance (Hyper-10).

Tailored radiation protection restrictions for thyrotoxicosis RAI therapies were calculated using patient-led bi-exponential fitting parameters. The bi-exponential model resulted in an illogical overestimation of tailored restrictions, the estimated slow half-life being longer than the physical half-life of ^{131}I in some cases. We therefore applied a mono-exponential model, which resulted in more rational restrictions considering the effective half-life of RAI in thyrotoxic patients (Table 6-4). The journey times for public and private transport to limit the public member exposure to ≤0.3mSv were 1.8±0.53 hr and 12.9± 3.68 hr, respectively.

Three patients (Hyper-1, 4 and 9) showed shorter tailored restrictions than referenced one's advice whereas the duration of restrictions would have been extended for four patients (Hyper-3, 6, 8, and 10) especially for the protection of children aged 2–11 y (Fig.6-9). The variability among the cohort suggests that it is probably worth investigating this approach of tailored restrictions further.

Table 6-4: Patient-led mono-exponential fitting parameters used to calculate tailored restrictions for thyrotoxicosis patients following RAI therapy.

	Mono- Exponential Tailored Restriction Days							*STATISTICS*			
Patient ID	**1**	**3**	**4**	**6**	**8**	**9**	**10**	**Mean**	**±SD**	**MAX**	**MIN**
Going out/Contact with a pregnant person (4 hrs contact at 1 m)	*0*	*5*	*0*	*3*	*7*	*2*	*13*	*4.3*	*4.6*	*13*	*0*
Return to work (8 hrs contact at 1 m, 7 days a week)	*1*	*9*	*1*	*7*	*12*	*5*	*19*	*7.7*	*6.4*	*19*	*1*
Sleeping apart (6 hrs at 1 m during the day and 8 hrs sleep time at 0.1 m)	*8*	*26*	*5*	*27*	*35*	*18*	*44*	*23.3*	*14.0*	*44*	*5*
Child <2 y (8 hrs at 0.1 m)	*8*	*29*	*5*	*27*	*36*	*19*	*45*	*24.1*	*14.5*	*45*	*5*
Child 2–5 y (4 hrs at 0.1 m and 8 hrs at 1 m)	*6*	*25*	*4*	*23*	*30*	*16*	*40*	*20.6*	*12.9*	*40*	*4*
Child 5–11 y (2 hrs at 0.1 m and 4 hrs at 1 m)	*5*	*21*	*4*	*19*	*26*	*13*	*34*	*17.4*	*10.9*	*34*	*4*
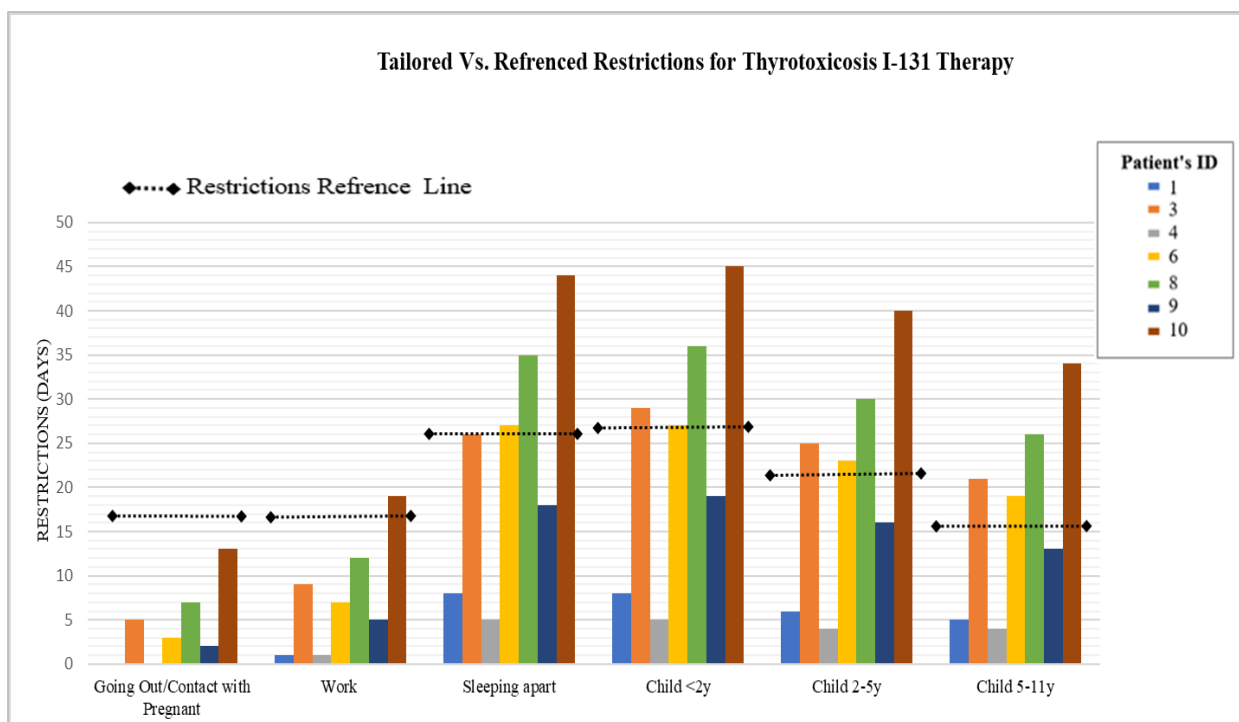
Figure 6-9: Thyrotoxicosis patients referenced and tailored radiation restrictions following RAI therapy. Mono-exponential curve fitting parameters were used for restriction calculation.

6.4.2. Eight (8) Days Prediction of Patient-led Data Fitting Model

The patient-led whole-body measurements recorded for 28 days following PRRT and RAI therapy for DTC showed a strong positive linear correlation with 8-day measurements (Table 6-5). However, NET patients' 8-day measurements showed increased plateau values of 0.04 ± 0.04 compared with 0.0 ± 0.01 at 28 days of measurement. The plateau values are consistent with the radiation background value measured using the patient-led method (0.03 ± 0.02 µSv/hr).

Table 6-5: Paired sample correlation coefficient between 28- and 8-day patient-led measurements for NET and DTC patients using a bi-exponential fitting model.

Bi-exponential Fitting Parameters	NET			DTC		
	Correlation	Significance		Correlation	Significance	
		One-sided p	Two-sided p		One-sided p	Two-sided p
Y0	0.746	<.001	<.001	1	<.001	<.001
PercentFast	0.938	<.001	<.001	0.88	<.001	<.001
Plateau	0.161	0.261	0.523	1	<.001	<.001
SpanFast	0.959	<.001	<.001	0.998	0.000	0.000
Kfast/D	0.961	<.001	<.001	1	<.001	<.001
SpanSlow	0.964	<.001	<.001	0.88	0.000	0.000
Kslow/D	0.65	0.002	0.004	0.99	<.001	<.001
Half-life (Slow)	0.7	<.001	0.001	0.99	<.001	<.001
Half-life (Fast)	0.612	0.005	0.009	1	<.001	<.001

Thyrotoxicosis patients showed inconsistent slow half-life values at 8 days, according to patient-led measurements using a bi-exponential fitting model. Therefore, we applied the plateau constraint 0, which produced a strong correlation between fitting parameters, except for span fast, span slow, and slow half-life ($R \leq 0.40$, $p > 0.05$) (Table 6-6). However, mono-

exponential fitting for 28 and 8 days showed a very strong linear correlation coefficient for all

fitting parameters (Table 6-7) with and without constrained plateau to zero and 1>Y0>0.

Table 6-6: Paired sample correlation coefficient between 28- and 8-day patient-led measurements for thyrotoxicosis patients using a bi-exponential fitting model with plateau and Y0 constraints.

Bi-exponential Fitting Parameters	Thyrotoxicosis with constraints		
	Correlation	Significance	
		One-sided p	Two-sided p
Y0	0.906	0.002	0.005
PercentFast	0.851	0.008	0.015
SpanFast	0.408	0.182	0.364
Kfast/D	0.986	0.000	0.000
SpanSlow	0.397	0.189	0.379
Kslow/D	0.726	0.032	0.065
Half-life (Slow)	0.282	0.27	0.54
Half-life (Fast)	0.986	0.000	0.000

Table 6-7: Paired sample correlation coefficient between 28- and 8-day patient-led measurements for thyrotoxicosis patients using a mono-exponential fitting model a) without plateau and Y0 constraint and b) with plateau and Y0 constraints.

Mono-exponential Fitting Parameters	a. Thyrotoxicosis without constraints		
	Correlation	Significance	
		One-sided p	Two-sided p
Y0	0.876	0.005	0.01
K/D	0.936	<.001	0.002
Half-life	0.846	0.008	0.016

Mono-exponential Fitting Parameters	b. Thyrotoxicosis with constraints		
	Correlation	Significance	
		One-sided p	Two-sided p
Y0	0.988	0.000	0.000
K/D	0.997	0.000	0.000
Half-life	0.994	0.000	0.000

6.5. Discussion

The results obtained here have implications for personalising MRT radiation protection restrictions and suggest that our approach using a patient-led monitor is a promising alternative to serial WBS and SPECT/CT imaging which tend to be resource heavy. It is essential to take account of patient-specific radiopharmaceutical biokinetics to determine individual MRT patients' radiation protection restrictions. (B. Liu et al., 2015). Our study showed that the bi-exponential model fitted very well for patient-led data in the MRT groups studied. For tailored radiation restriction calculation, bi-exponential and mono-exponential fitting parameters were used for NET and DTC patients and for Thyrotoxic subjects respectively.

NET patients showed variable duration of restrictions following PRRT administration among the same group in PRRT cycles 1 and 4. Restrictions decreased for some patients following cycle 4, which, we postulate, was related to a favourable therapy response (Fig.6-4). In contrast, longer contact restrictions were required by some patients who showed stable disease and /or no response after 4 cycles of PRRT (Fig. 6-5). The mean contact restriction with partners (8 days) and children reported by Levart et al. was markedly shorter than reported in our study. However, the return-to-work contact restriction was in line with our findings on 1 day (Levart et al., 2019).

Different fitting exponential model approaches, such as using a mono-exponential fit for ablation and bi-exponential for FU DTC patients, have been studied (Klain et al., 2021). Patient-led effective half-lives for ablation and FU (31.9 ± 30 hrs and 15.4 ± 9.5 hrs, respectively) were comparable to reported WBS serial effective half-lives of 26.1 ± 11.7 hours and 14.6 ± 4.6 hours, respectively (Klain et al., 2021). In contrast, longer effective half-lives have been reported for DTC ablation, such as 67.6 ± 48.8 hours (Hänscheid et al., 2006). Effective ^{131}I half-life determination using serial diagnostic WBS, and blood sampling were

reported with a strong correlation coefficient with probe (NaI scintillator) measurements (T_{eff}=15.6 ± 5.2 hours) ($R^2 = 0.992$ and $R^2 = 0.854$, respectively) (Freesmeyer et al., 2019).

In our study, thyrotoxicosis patients showed long estimations of contact restrictions using a bi-exponential model, which dropped by ~50% using mono-exponential fitting parameters. For example, thyrotoxicosis patient Hyper-4 had the lowest whole-body absorbed dose (38 mGy) and the lowest retained activity at 24 hours based on WBS (180 MBq) and the patient-led methods (189 MBq).

Liu et al. used post-therapy four time-point WBS to calculate restrictions for Graves' disease patients after ^{131}I therapy. For patients treated with 740 MBq, the restricted period to sleep apart from their partner was 11 days and avoid returning to work for 10 days. In our study, the minimum and maximum restricted periods for sleeping apart were 5 and 44 days (23 ± 13 days), respectively, and return to work after 7.7 ± 6.4 days. In our small thyrotoxicosis cohort who received similar ^{131}I activities (681 ± 83.5 MBq), observed biokinetic variability resulted in a wide range of patient-specific restrictions. This is in keeping with ^{131}I biokinetic variability reported among a larger cohort of 72 patients with Graves' disease (Liu B. et al., 2015). It should be noted that a number of reasons, having to do with the reorganisation of the clinical service at the tail-end of COVID-19 restrictions, resulted in recruitment of a significantly smaller cohort of thyrotoxicosis patients than was initially planned.

Patients' biokinetics are significantly influenced by many covariates, including disease burden, radiopharmaceutical biodistribution, renal function, and patient preparation method, such as the use of rhTSH or thyroid hormone withdrawal prior to radioiodine therapy for DTC (Taprogge et al., 2021). The adjusted ICRP model showed significant variation from the existing model, suggesting that the rate constants for each patient could be calculated based on physiological uptake and clearance (Taprogge et al., 2021).

For private transportation, NET and DTC patients showed similar long-journey restrictions of 58.9 hr and 57.9 hr, respectively. Thyrotoxicosis patients showed the averaged private transportation journey length of 12.9 hr. Though, public transportation showed the averaged journey length from 21.6 hr for DTC patients, followed by 8.9 hr for NET patients, and the least of 1.8 hr for Thyrotoxicosis patients. Overall, our results indicated that tailored contact restrictions with pregnant women and returning to work for all MRT groups were noticeably shorter than the referenced restrictions that the patient were advised to follow.

Finally, this study supported the feasibility of a personalised biokinetic model, despite our limited sample size, across a wide range of patient-led data. There is a need to adjust population pharmacokinetic models to describe the rate constants of specific patient populations for specific MRT groups (Taprogge et al., 2021). We investigated how soon we could stop collecting patient-led data without compromising the equivalent fit to the 28-day data curve. Applying 8 days of patient-led bi-exponential fitting data results in a very strong correlation with all PRRT and DTC RAI therapy groups. This can assist with future clinical implementation of a tailored approach to radiation restrictions. In addition, collecting long-term whole-body retention data allows personalised calculation of WB absorbed doses and in future, combining such data with discrete imaging may lead to tailored versions of single-time point dosimetry approaches.

6.6. Conclusion

Tailored radiation restriction using patient-led whole-body retention measurements obtained with a hand-held radiation monitor proved to be feasible for following the time course of radioactivity clearance in each patient for 3–4 weeks post-therapy. We illustrated the best fitting nonlinear regression model for different MRT. Furthermore, minimising the monitoring period to 8 days (twice a day) was sufficient to fit the non-linear regression exponential curve

to calculate patient-specific radiation restrictions. This might enhance the feasibility of applying this approach to larger MRT populations.

CHAPTER 7

7. Summary, Limitations, and Future Work

7.1. Summary

The improved understanding of factors driving cancer progression and response to therapy in benign and malignant diseases has significantly contributed to developments associated with theranostic SPECT and PET probes, leading to the optimisation of quantitative imaging and potentially dosimetry. It is reasonable to assume that the outcome of MRT would depend on the absorbed radiation dose delivered to target tissues and healthy organs. It is standard practice to undertake early qualitative post-treatment gamma imaging for visual assessment of therapeutic radiopharmaceutical distribution but quantitative assessments such as SUV or dosimetric assessment are not performed routinely. Furthermore, in the absence of individual data, patients are provided with generic radiation safety advice based on worst-case assumptions of radiopharmaceutical retention.

The main objectives of this thesis were, therefore, to explore the feasibility of undertaking quantitative SPECT/CT and PET/CT. Then, to combine quantitative whole-body scans and SPECT/CT imaging with post-treatment, patient-led whole-body dose rate measurements to support individual MRT treatment planning. Finally, to apply patient-led, whole-body dose rate measurements to provide personalised radiation protection advice for patients undergoing MRT. This thesis addressed these novel goals using phantom studies for optimisation and validation using patient cohorts. To the best of my knowledge, this is the first study that explored the SUV serial changes between PET/CT and SPECT/CT and the application of long-term whole-body retention data obtained from patient-led monitoring in patients undergoing MRT.

As mentioned in chapter 1, this research's null hypotheses aimed for two primary outcomes to determine a) the potential of monitoring MRT impact prospectively based on post-treatment quantitative imaging, and b) the impact of patient-led external dose rate monitoring versus

standard, generic, post-treatment radiation protection advice in terms of restriction duration and patient satisfaction.

Chapter 2 reviewed the role of quantitative SUV-SPECT/CT on NET molecular response assessment during ^{177}Lu-DOTA-TATE MRT cycles. A systematic review undertaken according to PRISMA guidelines showed a lack of studies utilising SUV-SPECT/CT in ^{177}Lu-DOTA-TATE as surrogate metrics of therapy response. This demonstrates the potential in developing a quantitative SUV-SPECT/CT protocol in PRRT describing the acquisition and processing factors toward optimisation. This was the motivation for undertaking studies to develop an optimised quantitative SUV-SPECT/CT protocol discussed in Chapter 3.

Phantom data were used to optimise and validate quantitative SPECT/CT. Calibration factor, coefficient of variation, relative error, concentration recovery coefficient and iterative reconstruction algorithm were assessed for each SPECT/CT system and relevant collimator type. The phantom simulation study confirmed the feasibility of quantitative SUV-SPECT/CT with optimised reliability for ^{177}Lu and ^{131}I. The main challenge in quantitative SPECT/CT is the partial volume effect (PVE). This is an inherent issue of the limited spatial resolution of radionuclide imaging and, in addition, an issue with high-energy collimators due to septal scatter and penetration. However, the PVE can be somehow limited by the optimisation of data acquisition and reconstruction parameters and could potentially be compensated for by the NEMA phantom using the sphere's validation method. PVE occurs when the activity from a small lesion is spread out and diluted across multiple pixels due to the limited spatial resolution of the imaging system. This can result in an underestimation of the true activity concentration of the lesion. We used the NEMA phantom 6-spheres activity concentration recovery coefficient (cRC) factor to correct this effect. The cRC factor varies depending on the size, shape, and location of the lesion, as well as the imaging system and reconstruction algorithm used. Therefore, we determined the cRC factor for sphere size. In clinical data, correct, accurate

measurement of lesion size is important for applying proper correction factor of cRC in the quantitative analysis of SPECT functional imaging. Our NEMA phantom study showed that the cRC factor should be applied to lesions less than 37 ml a correction factor that accounts for the spread of activity outside the lesion region. However, in cases where the lesion size is small or difficult to visualize on non-enhanced CT reference images registered with SPECT, it may be challenging to accurately determine the exact anatomical dimensions or volume of the lesion. This is due to the lower spatial resolution of SPECT imaging compared to CT, which can lead to an underestimation of the lesion size. Therefore, contrast-enhanced CT and Magnetic Resonance Imaging (MRI) anatomical images can be used pre-MRT to provide more detailed information than non-enhanced images, particularly in cases where the lesion is small or difficult to visualize.

In Chapter 4, phantom-optimised acquisition and image reconstruction protocols was applied to imaging data acquired from a cohort of NET patients. The main findings were as follows:

- Significant SUV-SPECT/CT differences were observed between PRRT cycles 1 and 4 and between pre-and post-PRRT SUV-PET/CT measurements ($p < 0.05$). A decrease in SUV_{max}-SPECT/CT was observed in 89% of 74 lesions during PRRT ranging from -0.25% to -97% (mean: $-45\% \pm 29.6\%$). The remaining eight lesions (12%) increased by $32\% \pm 47.3\%$. The SUV_{max} measured by PET/CT was reduced by a mean of $34\% \pm 27.5\%$ in 66% of lesions (n=42). However, 22 lesions showed an increase in the SUV_{max}-PET/CT of $50\% \pm 58.7\%$.

- Significant positive correlations were reported among all SUV-SPECT/CT metrics (SUV_{mean}, SUV_{max}, SUV_{peak}, and MTV) (r_s=0.9, P<0.05).

- Increased SUV-SPECT/CT measurements were observed at Cycle 4 for the liver, spleen and both kidneys, and comparable increases in the same organs were observed for SUV-PET/CT measurements. However, both kidneys' SUV metrics showed no

significant difference in liver and spleen background ratio between SPECT/CT at cycles one and four (P>0.05). No correlation was found between kidneys SUV and e-GFR change.

- The lesional SUV_{max} showed strong linear correlations with the liver background SUV_{mean} and SUV_{max} ($r_s = 0.9$, $P < 0.05$). Changes in the LTS and LTL ratios showed significant and strong, positive, linear correlations ($r_s = 0.8$, $P < 0.05$) in both SPECT/CT and PET/CT measurements. LTL and LTS reduced post-therapy by $40\pm33.4\%$ and $46\pm25.6\%$ in SPECT and by $20\pm35\%$ and $-25\pm29\%$ in PET, respectively.

- A significant, strong, positive Spearman's correlation was shown between the SUV_{peak} ($r_s = 0.75$) and SUV_{max} ($r_s = 0.71$) when comparing values derived from SPECT/CT and PET/CT (p<0.05). Approximately 95% of the lesions showed SUV-SPECT/CT and PET/CT measurements within the Limits of Agreement on the Bland-Altman plot. Finally, CgA values were significantly reduced by mean $-27\% \pm 29.7\%$ after PRRT ($P < 0.05$). CgA and CgB showed a significant ($P < 0.05$) moderate, positive correlation with SUV-SPECT/CT metrics, as shown in table 4-7. By comparison, PET/CT quantitative metrics were weakly correlated with CgA, and weak or no correlations were observed for CgB.

SUV-SPECT/CT metrics changes during ^{177}Lu-DOTA-TATE PRRT are important for optimising treatment outcomes, minimising side effects and improving the overall clinical relevance of PRRT for NETs. A decrease in tumour SUV after PRRT treatment may indicate a favourable response to the treatment in terms of reduced somatostatin receptor expression and/, or metabolic tumour volume. By contrast an increase in lesional SUV suggests a less favourable response.

SUV-SPECT/CT can detect specific metabolic changes in a tumour's response to treatment earlier than other monitoring methods, such as contrast CT, which require a change in tumour

size to assess efficacy. Monitoring patients via blood count and chemistry provides additional important information about the patient's overall health status, potential side effects of treatment and change in tumour markers. Therefore, different methods provide complementary information, and it is vital that qualified medical professionals interpret SUV-SPECT results in the context of a patient's overall clinical status, medical history, and other relevant diagnostic tests.

The choice of the best SUV-SPECT metric for assessing treatment response during Peptide Receptor Radionuclide Therapy (PRRT) in patients with neuroendocrine tumours (NETs) is an area of ongoing research and debate.

Lesion SUV_{max} is a commonly used metric for assessing tumour response in PET-FDG imaging. It reflects the highest level of radiotracer uptake within a tumour and can be used to measure changes in tumour metabolic activity over time and it's independent of operator.

SUV_{max} of lesion-to-liver (LTL) or lesion-to-spleen ratios (LTS) may be more reliable metrics for assessing treatment response during PRRT in NETs. These ratios consider variations in normal organ uptake of the radiotracer, which can be affected by factors such as patient anatomy and treatment timing.

The main advantage of using LTL/LTS ratios is that they may be less prone to variability than lesion SUV_{max} alone. This is because normal liver and spleen uptake are relatively stable over time and can serve as a reference point for measuring changes in tumour uptake during therapy. We suggested using the LTL ratio as a metric to assess response to PRRT, LTS being a sensible alternative in patients with extensive hepatic metastases.

The choice of the best response metric may depend on individual patient factors, imaging protocols, and clinical goals. It is important for clinicians to interpret imaging results in the context of each patient's unique clinical history and overall treatment plan.

We reported some patients with different SUV changes between SPECT and PET. While both SPECT and PET imaging use radiotracers to visualize metabolic activity, inherent physical and instrumentational differences in these techniques affect SUV measurements. A key difference between SPECT and PET imaging is the type of radiation detected. SPECT detects gamma radiation emitted by a radiotracer, while PET detects positron emission. As gamma photons are less energetic than positrons, SPECT images have higher noise and lower spatial resolution leading to less precise measurements of SUV compared to PET images. Moreover, different kinetics of ^{177}Lu and ^{68}Ga and imaging interval time following injection may cause the observed SUV difference between SPECT and PET.

Another factor that can contribute to differences in SUV measurements between SPECT and PET is the type of radiotracer used. Different radiotracers have different physical and biological properties, including uptake and clearance rates, which can influence SUV measurement. Lastly, fundamental differences between the capability and resolution of equipment used for SPECT and PET imaging influence the accuracy and precision of SUV measurements.

In summary, the differences in SUV changes between SPECT and PET may be due to the inherent technical differences in the imaging techniques, as well as differences in the radiotracers used and imaging protocols. It is important to consider these factors when interpreting SUV measurements in clinical practice.

Chapter 5 and 6 presented a comprehensive investigation into the first use of long-term patient-led measurements to evaluate therapeutic radiopharmaceutical retention. The patient-led dosimetry primary outcomes link to null hypotheses described in chapter 1 as follows:

- ^{177}Lu-DOTA-TATE and I-131 MRT whole-body dosimetry from patient-led measurements showed a strong correlation with a single time-point quantitative whole-body scan and SPECT/CT dosimetry.

- ^{177}Lu-DOTA-TATE and I-131 MRT whole-body dosimetry from patient-led measurements correlated well with conventional 2-metre external dose rate measurements (R=0.7 and 0.91, respectively).

- Patient-led measurements could have led to changes to generic radiation restrictions for some patients, which is evidence of the need for tailored restrictions.

- Patient-led non-linear curve regression for eight days correlated with 28 days of curve fitting parameters.

- Patients accepted using the patient-led recording for 28 days.

Tailoring radiation restrictions following molecular radiotherapy (MRT) can have a positive impact on minimising exposure of members of the public and family. Based on our data, it might be feasible to adjust patients' restrictions prospectively based on individual whole-body retention data acquired by self-monitoring. Some of the impacts are:

- Ensuring that MRT is carried out in compliance with radiation safety regulations, which require that measures be put in place to minimise radiation exposure to the public and family members.

- Patients and their families can experience anxiety about the potential risks of radiation exposure. Tailoring radiation restrictions can help to reduce this anxiety by providing real time evidence of decreasing radiation levels, minimizing the potential exposure to the public and family.

- Adjustments to the treatment plan, such as increasing the time between treatment sessions in patients with prolonged retention may be feasible. This can impact the overall treatment schedule and may require additional monitoring.

An important factor in (molecular) radiotherapy remains the knowledge and, when possible, the optimisation of absorbed dose delivery to target tissues and healthy organs. Whilst this

work demonstrated the robust use of quantitative metrics derived from imaging as well as the reliability of longer term continual whole-body retention data, the issue of estimation of absorbed doses in a practical manner that is not perceived as resource-heavy by the Nuclear Medicine community, remains. Efforts to address this issue include the use of single time point dosimetry (Hou et al., 2021; Willowson et al., 2018) to limit the number of imaging data points required for the estimation of a dosimetric profile to be delivered. The method developed in this work could potentially help further guide these approaches to more accurate patient-specific approaches. This would require further work to develop models that could guide the definition of organ time-activity-curves by sparse or single-time-point imaging and limited by the envelop whole-body curve provided by patient-led monitoring. Such methods would require development of models specific to the MRT radiopharmaceutical with appropriate validation for the patient cohort intended. The time available for this project has not allowed such developments to be further explored in the present work even though it remains as area of interest for future work.

Finally, we have shown that this approach uniquely provides the evidence necessary to support consideration of an individual patient's situation and balance the risks and benefits of radiation restrictions to optimise treatment outcomes while minimising the risks to the public and family.

Chapters 4, 5 and 6 demonstrated the novel application of SUV-SPECT/CT as a prospective clinical evaluation marker during PRRT and of patient-led measurements to personalise radiation protection guidance and absorbed dose estimation.

To conclude, the experiments using the phantom simulations and patient data confirmed the feasibility and reliability of the proposed quantitative imaging and patient-led dosimetry methods.

7.2. Limitations

There are several limitations to our study. First, only 48 patients from three MRT categories were included in this work. This small mixed cohort of prospective and retrospective data reflects the negative impact of the COVID-19 pandemic, during which the IRAS submission was suspended. Ethical approval was granted in December 2021 and prospective data collection started in January 2022.

Radioiodine supplies were interrupted from February 2022 till April 2022 and clinic cancellations occurred due to staff shortages.

The use of quantitative SUV-SPECT to assess response prospectively over the course of repeated treatment cycles has limitations, and it is essential to be aware of these to avoid misinterpretation of the results. Some of the limitations of SUV-SPECT in assessing therapy response and how they could be overcome are:

- SPECT has lower spatial resolution than PET, making it difficult to localize the area of interest precisely. This can be overcome with phantom imaging optimisation and standardisation protocol as explained in chapter 3. Some new developments along the direction of overcoming resolution limitations of SPECT include the synergetic reconstruction of SPECT data informed by the (superior resolution) PET (Marquis et al., 2021).

- Variations in imaging protocols, such as the time interval between the injection of the radiotracer and the imaging acquisition, can affect the SUV measurements. Standardisation of imaging protocols can help reduce variability and improve the accuracy of SUV measurements. It remains to be seen if future applications of innovative methodology such as Total Body PET (Cherry et al., 2018) may offer longer term data on radiopharmaceutical organ retention thanks to a substantially improved sensitivity; this would allow a more

accurate understanding of radiopharmaceutical biokinetics and a fairer comparison with SPECT data.

- Biological factors, such as differences in the metabolism of the radiotracer, can influence SUV measurements. This limitation can be overcome by using radiotracers with known biological properties and by comparing the SUV measurements at different time points to assess changes in response to therapy.

- SUV-SPECT measurements can be influenced by the partial volume effect (PVE). PVE can be compensated for by applying recovery coefficients derived from NEMA phantom studies using the sphere's validation method. To accurately measure lesion size, pre- and post-PRRT anatomical imaging such as contrast-enhanced CT and MRI may be required. These imaging techniques can provide high-resolution images of the anatomy and help to identify the precise location and size of the lesion. By comparing the pre- and post-PRRT images, it is possible to track the changes in the lesion size over time and correlate these changes with the functional changes observed in SPECT imaging. This limitation can also be offset by careful interpretation of SUV measurements in the context of the patient's clinical history and other diagnostic tests. In addition, definition of ROIs for SUV analysis may be further improved by standardisation of definition criteria or even using deep-learning or artificial intelligence (AI) approaches (Arabi et al., 2021) to reduce bias and variability.

- A CT reference image is required to calculate SUV in an area of interest. The resulting additional exposure to ionising radiation is potentially harmful to patients, particularly those who require frequent imaging studies. The relative risk posed by this exposure is considered low by comparison with the radiation dose received during therapy however and in this patient, population is outweighed by the potential clinical value of the SUV data generated. The option of following SUV changes across four PRRT cycles by applying the CT image acquired after the first treatment to subsequent SPECT images might be considered but would

require patient position and scanner settings to be reproduced accurately to register the SPECT and CT successfully.

Tailoring patient's individual radiation restrictions after MRT is a feasible approach that could be applied prospectively in the future. However, some factors that might affect the impact of this approach include:

- Availability of radiation monitoring equipment can vary depending on the healthcare facility and could limit the feasibility of widescale adoption.

- Radiation safety regulations vary between countries and regions and may impact the feasibility of tailoring patient's radiation restriction after MRT. Healthcare facilities must comply with these regulations to ensure patient and public safety.

- Patient compliance with the radiation restriction guidelines to minimise the risk of exposure to family members and the public. Education and counselling regarding the importance of compliance may be required, especially if patients unexpectedly need to extend the restrictions to ensure safety for others.

7.3. Future work

The reported findings of this thesis identified the following opportunities for future work:

- A further investigation of PET/CT and SPECT/CT in both in-vivo and in-vitro systems performance harmonisation to achieve comparability of image quality and SUV metrics of 68Ga- DOTA-TATE with 177Lu- DOTA-TATE.

- Applying SUV-SPECT/CT in cycles 2 and 3 PRRT and comparing changes across all four cycles of PRRT. SUV-SPECT changes could provide insights into the kinetics of radiopharmaceutical uptake and clearance in the tumour. This information can be used to optimise treatment protocols and improve the therapeutic efficacy of PRRT. Moreover, early changes in SUV-SPECT during PRRT could be used as a prognostic indicator for treatment outcomes. Patients who show a significant decrease in SUV-SPECT after a few treatment sessions may have better long-term treatment responses compared to those with minimal changes.

- Investigating the feasibility of quantitative SUV-SPECT/CT in emerging types of MRT such as 177Lu-FAPI (Fibroblast Activation Protein Inhibitor) and 177Lu-PSMA (Prostate-Specific Membrane Antigen). FAPI is a small molecule that specifically targets and binds to fibroblast activation protein (FAP), which is overexpressed on the surface of cancer-associated fibroblasts (CAFs) of the stroma of many epithelial cancers (Huang et al., 2022; Liu et al., 2022). Both 177Lu-PSMA and FAPI therapies are currently being evaluated in clinical trials as a potential treatment option for advanced prostate and epithelial cancers, respectively (Jackson et al., 2022; Mair et al., 2018; Sjögreen Gleisner et al., 2022).

- Investigating the feasibility of quantitative SUV-SPECT/CT in emerging alpha particle therapy such as Actinium-225 labelled PSMA/FAPI.

- Standardisation of pre- and post-therapy diagnostic imaging acquisition and processing using SPECT/CT with advanced Cadmium Zinc Telluride detector (CZT) and PET systems.

- The results of the patient-led monitoring carried out in this thesis also suggest the feasibility of this dosimetry method which would involve a larger patient cohort to understand the best-to-fit pharmacokinetic model for emerging MRT groups, such as PSMA and FAPI, and assess more covariates. Moreover, to assess the potential of adapting MRT activity prescription based on post-treatment quantitative imaging.

- Applying the reported exponential whole-body retention model to prospective patients' data and correlating this with serial quantitative WBS and SPECT/CT imaging. Assessment in a larger patient cohort would be essential to support implementation in routine clinical practice.

- Developing an automated process to save the patient-led monitor's recording with accurate date and time and link it to software for example via a mobile phone application. This would assist archiving and analysis, would eliminate the patient's effort for manual recording and would allow patients to access real time feedback. This development might accelerate the radiation protection restrictions assessment process and the patient could be advised to follow updated restrictions based on their daily dose rate measurements.

- Integrating quantitative SUV-SPECT/CT imaging into future research protocols and clinical practice for MRT by incorporating it into the treatment planning and follow-up process. Clinical trials can be designed to include quantitative SUV-SPECT imaging as part of the treatment response evaluation. This might help to assess the efficacy of the treatment, determine the optimal activity for subsequent cycles and confirm the clinical relevance of SUV-SPECT as a technique for prospective response monitoring.

- Establishing guidelines for interpreting SUV-SPECT measurements to facilitate consistent and reliable interpretation of the imaging results.

- Providing education and training to clinicians and researchers to ensure that they are familiar with the use of quantitative SUV-SPECT imaging in MRT and how to interpret the results.

Some other developments such as the use of AI for region of interest (ROI) standardisation and the development of models to inform organ time activity curve (TACs) based on sparse/single-time-point

imaging with serial patient-led data for the full dosimetric evaluation of MRT have also been discussed in this chapter and would be exciting directions for building upon the work developed in this study for future improvements in MRT. Growing interest in MRT and new developments, including the discovery of novel molecular targeting agents and the use of alpha emitting radionuclides underlines the importance of optimising MRT to fully realise the huge potential of theranostics in clinical practice.

Appendices

A. SELFIE Instruction leaflet.

Guy's and St Thomas' **NHS**
NHS Foundation Trust

Lefteris Livieratos, PhD
Nuclear Medicine Physicist
Tel +44 (0)20 7 188 3802
FAX +44 (0)20 7 188 4094
email: Lefteris.Livieratos@gstt.nhs.uk

Department of Nuclear Medicine
Guy's Hospital
St Thomas St, London. SE1 9RT
Tel +44 (0)20 7188 4112

Thank you taking part in this study. Please find contact details above, together with the following instructions for self-monitoring at home after your treatment (SELFIE project). Please contact us if you have any questions and return the radiation monitor in the pre-paid envelope provided.

Selfie Instructions for Patients:

1. Turn on the SELFIE monitor using the ON/OFF switch.

2. Hold the monitor at arm's length in front of you while resting your elbow by your side at waist height. It doesn't matter whether you are sitting down or standing up, provided that you use the same position every time, so make sure that it feels comfortable from the start.

3. Please try to use this position carefully for every measurement you record.

4. The SELFIE monitor shows a number at the top of the screen. This will keep changing for a few seconds after you switch the monitor on.

5. Wait for 1 minute, then write down the number shown on the screen on your form with the time and date.

6. Turn the SELFIE monitor off by pressing the ON/OFF button three times.

7. Please take measurements at any time of the day, ideally once in the morning and once in the afternoon, for 28 days after your treatment.

8. If you forget or can't take a measurement for any reason, don't worry - just restart and carry on when you can.

9. Sometimes, the afternoon measurement might be slightly higher than the morning one. This is not a cause for concern.

10. There is no right or wrong reading or target level at the end of the 28-day measurement period.

11. If you don't want to keep taking measurements anymore, just send us what you have recorded so far and return the sheet and monitor to us in the prepaid envelope provided.

Very many thanks for your help.

I confirm that I am willing to undertake 'Selfie 'monitoring when I leave the hospital.

I understand that anonymised information from 'Selfie 'records will be used to find out more about how radiation levels change in different people after radionuclide treatment

I understand that I can change my mind and stop taking 'Selfie 'measurements at any time.

NAME   ....

SIGNATURE   ....

DATE   ....

Number to write down

ON/OFF button

The SELFIE monitor looks like this

Hold the SELFIE monitor like this

B. PRRT patients' general characteristics and injected activity for PRRT cycles 1 and 4.

Patient ID	General characteristics		Injected activity (MBq)	
	Gender	Age (y)	Cycle 1	Cycle 4
1	M	65	7974	7754
2	F	38	7541	7843
3	F	71	7539	7511
4	F	56	7830	7807
5	F	59	7626	7378
6	F	73	7616	3780
7	F	69	8000	7630
8	M	65	7175	7343
9	M	62	7592	7626
11	M	71	7790	7186
12	F	69	7668	7744
13	F	55	7596	7450
14	M	61	7697	7460
15	F	52	7810	7369
16	M	63	7880	7596
17	F	57	7779	7114
18	F	56	7567	7057
19	M	63	7081	7370
20	M	63	7590	7656
Mean		61.28	7632.06	7273.33
±SD		8.46	224.72	900.10
Max		73.00	8000.00	7843.00
Min		38.00	7081.00	3780.00

C. PRRT cycles 1 and 4 whole-body absorbed dose (D, mGy) calculations using patient-led data.

Patient ID (DOTA-)	AUC		m_{ref}/m_p	$S_{(Wb-Wb)}$ mGy/MBq/hr	Cycle-1 $\tilde{A}$(MBq*hr)	Cycle-4 $\tilde{A}$(MBq*hr)	Cycle-1 D(mGy)	Cycle-4 D(mGy)
	Cycle-1	Cycle-4						
1	28.78	49.53	0.86	0.00109	229491.7	384056.0	249.2	417.0
2	19.93	24.97	0.79	0.00128	150292.1	195840.0	192.3	250.6
3	16.67	13.97	0.92	0.00149	125675.1	104929.0	186.8	155.9
4	21.25	12.83	0.69	0.00111	166387.5	100164.0	184.7	111.2
5	24.44	26.89	0.77	0.00125	186379.4	198394.0	232.1	247.0
6	28.61	36.98	1.19	0.00192	217893.8	139784.0	418.2	268.3
7	57.85	31.73	0.7	0.00114	230000.0	301461.0	526.4	275.3
8	33.19	30.14	0.57	0.00072	238138.3	221318.0	171.7	159.5
9	14.52		0.9	0.00113	110235.8		124.3	
11	83.3	70.99	0.7	0.00088	648907.0	510134.0	570.7	448.7
12	20.99	17.49	0.98	0.00159	160951.3	135443.0	255.7	215.2
13	59.88	39.6	0.6	0.00097	454848.5	295020.0	441.1	286.1
14	30.46	29.18	0.86	0.00109	234450.6	217683.0	254.6	236.4
15	22.57	22.11	0.6	0.00097	176271.7	162929.0	171.0	158.0
16	47.91	46.11	1.13	0.00142	377530.8	350252.0	535.5	496.8
17	34.8	34.04	0.61	0.00098	270709.2	242161.0	265.3	237.4
18	57.72	38.91	0.76	0.00123	436767.2	274588.0	536.6	337.3
20	105.7	47.96	0.88	0.0011	802263.0	367182.0	882.0	403.7
Mean	39.3	33.7	0.8	0.0	289844.1	245655.9	329.6	278.9
±SD	24.9	14.6	0.2	0.0	187969.6	108223.2	196.6	108.8
Max	105.7	70.9	1.2	0.0	802263.0	510134.0	882.0	496.8
Min	14.5	12.8	0.6	0.0	110235.8	100164.0	124.3	111.2

D. DTC patients' general characteristics and A_r for ablation and follow-up (FU) ^{131}I therapy.

Patient ID (ThyCa-)	General characteristics		Administered activity	Type of Therapy	Gamma-imaging uptake at 48 hours
	Gender	Age (y)	(MBq)		
1	F	56	3950	Ablation	Uptake into remnant thyroid tissue
2	M	60	5780	Ablation	Uptake into remnant thyroid tissue
3	M	44	3770	Ablation	Uptake into remnant thyroid tissue
4	F	49	7930	Follow-up (FU)	Evidence of iodine-avid metastatic disease
5	M	43	1183	Ablation	Uptake into remnant thyroid tissue
6	M	64	6040	Follow-up (FU)	No uptake
7	F	61	1100	Ablation	Uptake into remnant thyroid tissue
8	F	34	3810	Follow-up (FU)	No uptake
9	M	45	5950	Follow-up (FU)	No uptake
10	M	72	3860	Ablation	No uptake
11	F	39	3860	Ablation	No uptake
12	F	50	3860	Follow-up (FU)	No uptake
13	M	53	1154	Ablation	Uptake into remnant thyroid tissue
14	F	24	3870	Ablation	Uptake into remnant thyroid tissue
15	M	26	3950	Ablation	Uptake into remnant thyroid tissue
16	F	46	3870	Ablation	Uptake into remnant thyroid tissue
17	F	40	5880	Follow-up (FU)	No uptake
18	F	29	3890	Ablation	No uptake
19	M	25	1173	Ablation	Uptake into remnant thyroid tissue
20	M	50	3850	Ablation	Uptake into remnant thyroid tissue

E. DTC patients' absorbed dose calculations using patient-led data.

Patient ID (ThyCa-)	AUC	m_{ref}/m_p	$S_{(Wb-Wb)}$ mGY/MBq/hr	Ã(MBq*hr)	D (mGy)
1	20.52	0.83	0.00134	81054.0	108.2
2	20.81	0.92	0.00116	120281.8	139.2
3	18.59	0.81	0.00102	70084.3	71.7
4	13.81	0.83	0.00134	109513.3	146.2
5	17.65	0.86	0.00109	20880.0	22.7
6	13.33	0.75	0.00095	78520.0	74.3
7	21.07	0.83	0.00134	23177.0	30.9
9	11.77	0.95	0.00119	70031.5	83.2
10	49.02	0.68	0.00085	189217.2	161.6
11	18.08	0.53	0.00086	69788.8	60.1
12	14.1	1.10	0.00177	54426.0	96.4
13	20.37	1.00	0.00126	23507.0	29.5
14	13.22	0.73	0.00118	51161.4	60.4
15	22.16	0.76	0.00096	87532.0	83.7
17	20.51	1.02	0.00165	120540.0	198.3
19	15.42	0.82	0.00133	18064.2	24.0
20	44.27	0.65	0.00081	170439.5	138.8
Mean	20.86	0.83	0.00118	79895.2	90.0
±SD	10.27	0.14	0.00027	49902.3	52.2
Max	49.02	1.10	0.00177	189217.2	198.3
Min	11.77	0.53	0.00081	18064.2	22.7

F. Thyrotoxicosis patients' general characteristics, AA, diagnosis, and thyroid uptake before ^{131}I therapy.

Patient ID (Hyper-)	General characteristics				Administered activity	Diagnosis	Technetium-Tc-99m thyroid uptake (%)
	Gender	Age (y)	Weight (kg)	Height (cm)	(MBq)		
1	M	57	83	174	605	Toxic solitary thyroid nodule	2.3%
3	F	62	96	164	800	Toxic multinodular goitre	39.0%
4	M	69	79	169	612	Graves' disease	0.9%
5	F	22	43	160	718	Graves' disease	13.7%
6	F	63	64	161	621	Graves' disease	2.7%
7	F	20	67.8	166	619	Graves' disease	
8	F	57	91	177	617	Toxic multinodular goitre	10.8%
9	F	51	96	169	799	Graves' disease (2nd therapy)	
10	F	32	53	156	746	Graves' disease	20.0%
Mean		48.1	74.8	166.2	681.9		12.8%
±SD		18.5	19.0	6.8	83.5		13.5%
Max		69.0	96.0	177.0	800		39.0%
Min		20.0	43.0	156.0	605		0.9%

G. Thyrotoxicosis absorbed dose calculation using patient-led data.

Patient ID (Hyper-)	AUC	m_{ref}/m_p	$S_{(Wb-Wb)}$ mGY/MBq/hr	$\tilde{A}$ (MBq*hr)	D (mGy)
1	81	0.84	0.00106	49005	51.9
3	157	0.59	0.00096	125600	120.5
4	56	0.89	0.00111	34272	38.2
6	137	0.89	0.00144	85077	122.5
7	106	0.84	0.00135	65614	88.9
8	172	0.63	0.00101	106124	107.4
9	118	0.59	0.00096	94282	90.5
10	189	1.08	0.00174	140994	245.1
Mean	127.00	0.79	0.00120	87621	108.1
±SD	45.59	0.17	0.00028	36851	63.1
Max	189.00	1.08	0.00174	140994	245.1
Min	56.00	0.59	0.00096	34272	38.2

References

Adams, M. C., Turkington, T. G., Wilson, J. M., & Wong, T. Z. (2010). A Systematic Review of the Factors Affecting Accuracy of SUV Measurements. American Journal of Roentgenology, 195(2), 310–320. https://doi.org/10.2214/AJR.10.4923

Ahn, B. C. (2016). Personalized Medicine Based on Theranostic Radioiodine Molecular Imaging for Differentiated Thyroid Cancer. In BioMed Research International (Vol. 2016). Hindawi Limited. https://doi.org/10.1155/2016/1680464

Aloj, L., Giger, O., Mendichovszky, I. A., Challis, B. G., Ronel, M., Harper, I., Cheow, H., Hoopen, R. ten, Pitfield, D., Gallagher, F. A., Attili, B., McLean, M., Jones, R. L., Dileo, P., Bulusu, V. R., Maher, E. R., & Casey, R. T. (2021). The role of [68 Ga]Ga-DOTATATE PET/CT in wild-type KIT/PDGFRA gastrointestinal stromal tumours (GIST). EJNMMI Research, 11(1). https://doi.org/10.1186/s13550-021-00747-0

Ambrosini, V., Zanoni, L., Filice, A., Lamberti, G., Argalia, G., Fortunati, E., Campana, D., Versari, A., & Fanti, S. (2022). Radiolabeled Somatostatin Analogues for Diagnosis and Treatment of Neuroendocrine Tumors. Cancers, 14(4), 1055. https://doi.org/10.3390/cancers14041055

Andersson, M., & Mattsson, S. (2021). Improved Patient Dosimetry at Radioiodine Therapy by Combining the ICRP Compartment Model and the EANM Pre-Therapeutic Standard Procedure for Benign Thyroid Diseases. Frontiers in Endocrinology, 12. https://doi.org/10.3389/fendo.2021.634955

Andreou, C., Pal, S., Rotter, L., Yang, J., & Kircher, M. F. (2017). Molecular Imaging in Nanotechnology and Theranostics. Molecular Imaging and Biology, 19(3), 363–372. https://doi.org/10.1007/s11307-017-1056-z

Arabi, H., AkhavanAllaf, A., Sanaat, A., Shiri, I., & Zaidi, H. (2021). The promise of artificial intelligence and deep learning in PET and SPECT imaging. Physica Medica, 83, 122–137. https://doi.org/10.1016/j.ejmp.2021.03.008

Atkinson, C., Ganeshan, B., Endozo, R., Wan, S., Aldridge, M. D., Groves, A. M., Bomanji, J. B., & Gaze, M. N. (2021). Radiomics-Based Texture Analysis of 68Ga-DOTATATE Positron Emission Tomography and Computed Tomography Images as a Prognostic Biomarker in Adults with Neuroendocrine Cancers Treated With 177Lu-DOTATATE. Frontiers in Oncology, 11. https://doi.org/10.3389/fonc.2021.686235

Avram, A. M., Giovanella, L., Greenspan, B., Lawson, S. A., Luster, M., van Nostrand, D., Peacock, J. G., Ovčariček, P. P., Silberstein, E., Tulchinsky, M., Verburg, F. A., & Vrachimis, A. (2022). SNMMI Procedure Standard/EANM Practice Guideline for Nuclear Medicine Evaluation and Therapy of Differentiated Thyroid Cancer: Abbreviated Version. Journal of Nuclear Medicine : Official Publication, Society of Nuclear Medicine, 63(6), 15N-35N.

Bailey, D. L., Hennessy, T. M., Willowson, K. P., Henry, E. C., Chan, D. L. H., Aslani, A., & Roach, P. J. (2015). In vivo quantification of 177Lu with planar whole-body and SPECT/CT gamma camera imaging. EJNMMI Physics, 2(1), 1–17. https://doi.org/10.1186/s40658-015-0123-2

Bailey, D. L., & Willowson, K. P. (2013). An Evidence-Based Review of Quantitative SPECT Imaging and Potential Clinical Applications. Journal of Nuclear Medicine, 54(1), 83–89. https://doi.org/10.2967/jnumed.112.111476

Barquero, R., Basurto, F., Vega-Carrillo, H. R., Iñiguez, M. P., Ferrer, N., & Esteban, R. (2008). Correlation Between External Exposure and Activity in Patients Undergoing 131 I Thyroid Cancer Therapy.

Barrington, S. F., Kettle, A. G., O'Doherty, M. J., Wells, C. P., Somer, E. J. R., & Coakley, A. J. (1996). Radiation dose rates from patients receiving iodine-131 therapy for carcinoma of the thyroid. European Journal of Nuclear Medicine, 23(2), 123–130. https://doi.org/10.1007/BF01731834

Barrington, S. F., O'Doherty, M. J., Kettle, A. G., Thomson, W. H., Mountford, P. J., Burrell, D. N., Farrell, R. J., Batchelor, S., Seed, P., & Harding, L. K. (1999). Radiation exposure of the families of outpatients treated with radioiodine (iodine-131) for hyperthyroidism. European Journal of Nuclear Medicine and Molecular Imaging, 26(7), 686–692. https://doi.org/10.1007/s002590050438

Beauregard, J. M., Hofman, M. S., Pereira, J. M., Eu, P., & Hicks, R. J. (2011). Quantitative 177Lu SPECT (QSPECT) imaging using a commercially available SPECT/CT system. Cancer Imaging, 11(1), 56–66. https://doi.org/10.1102/1470-7330.2011.0012

BECKERS, C. (1997). Regulations and Policies on Radioiodine [131] I Therapy in Europe. Thyroid, 7(2), 221–224. https://doi.org/10.1089/thy.1997.7.221

Bergsma, H., Konijnenberg, M. W., Kam, B. L. R., Teunissen, J. J. M., Kooij, P. P., de Herder, W. W., Franssen, G. J. H., van Eijck, C. H. J., Krenning, E. P., & Kwekkeboom, D. J. (2016). Subacute haematotoxicity after PRRT with 177Lu-DOTA-octreotate: prognostic factors, incidence, and course. European Journal of Nuclear Medicine and Molecular Imaging, 43(3), 453–463. https://doi.org/10.1007/s00259-015-3193-4

Bevilacqua, A., Calabrò, D., Malavasi, S., Ricci, C., Casadei, R., Campana, D., Baiocco, S., Fanti, S., & Ambrosini, V. (2021). A [68ga]ga-dotanoc pet/ct radiomic model for non-invasive prediction of tumour grade in pancreatic neuroendocrine tumours. Diagnostics, 11(5). https://doi.org/10.3390/diagnostics11050870

Bodei, L., Kidd, M. S., Singh, A., van der Zwan, W. A., Severi, S., Drozdov, I. A., Malczewska, A., Baum, R. P., Kwekkeboom, D. J., Paganelli, G., Krenning, E. P., & Modlin, I. M. (2020). PRRT neuroendocrine tumor response monitored using circulating transcript analysis: the NETest. European Journal of Nuclear Medicine and Molecular Imaging, 47(4), 895–906. https://doi.org/10.1007/s00259-019-04601-3

Bodei, L., Kwekkeboom, D. J., Kidd, M., Modlin, I. M., & Krenning, E. P. (2016). Radiolabeled Somatostatin Analogue Therapy of Gastroenteropancreatic Cancer. Seminars in Nuclear Medicine, 46(3), 225–238. https://doi.org/10.1053/j.semnuclmed.2015.12.003

Bongiovanni, A., Nicolini, S., Ibrahim, T., Foca, F., Sansovini, M., di Paolo, A., Grassi, I., Liverani, C., Calabrese, C., Ranallo, N., Matteucci, F., Paganelli, G., & Severi, S. (2022). 177Lu-DOTATATE Efficacy and Safety in Functioning Neuroendocrine Tumors: A Joint Analysis of Phase II Prospective Clinical Trials. Cancers, 14(24). https://doi.org/10.3390/cancers14246022

Bozkurt, M. F., & Özcan, Z. (2018). The Evolving Role of Nuclear Medicine and Molecular Imaging: Theranostics and Personalized Therapeutic Applications. Malecular Imaging and Radionuclide Therapy, 1–2. https://doi.org/10.4274/mirt.30502

Cancer Therapy Evaluation Program. (2017). Common Terminology Criteria for Adverse Events, Version 5.0, DCTD, NCI, NIH, DHHS.https://ctep.cancer.gov/protocoldevelopment/electronic_applications/ctc.htm#ctc_50.

Carollo, A., Papi, S., & Chinol, M. (2015). Lutetium-177 Labeled Peptides: The European Institute of Oncology Experience. Current Radiopharmaceuticals, 9(1), 19–32. https://doi.org/10.2174/1874471008666150313111633

Chang, C. A., Pattison, D. A., Tothill, R. W., Kong, G., Akhurst, T. J., Hicks, R. J., & Hofman, M. S. (2016). 68Ga-DOTATATE and 18F-FDG PET/CT in Paraganglioma and Pheochromocytoma: utility, patterns, and heterogeneity. Cancer Imaging, 16(1), 22. https://doi.org/10.1186/s40644-016-0084-2

Chapman, E. M., & Evans, R. D. (1946). The Treatment of Hyperthyroidism with Radioactive Iodine. JAMA, 131(2), 86–91. https://doi.org/10.1001/jama.1946.02870190010003

Cherry, S. R., Jones, T., Karp, J. S., Qi, J., Moses, W. W., & Badawi, R. D. (2018). Total-Body PET: Maximizing Sensitivity to Create New Opportunities for Clinical Research and Patient Care. Journal of nuclear medicine : official publication, Society of Nuclear Medicine, 59(1), 3–12. https://doi.org/10.2967/jnumed.116.184028

Chicheportiche, A., Sason, M., Godefroy, J., Krausz, Y., Zidan, M., Oleinikov, K., Meirovitz, A., Gross, D. J., Grozinsky-Glasberg, S., & Ben-Haim, S. (2021). Simple model for estimation of absorbed dose by organs and tumors after PRRT from a single SPECT/CT study. EJNMMI Physics, 8(1), 63. https://doi.org/10.1186/s40658-021-00409-z

Choudhury, parTha, & GupTa, manoj. (2018). TheranosTics and precision medicine special feaTure: review arTicle differentiated thyroid cancer theranostics: radioiodine and beyond.

Colombo, I., Overchuk, M., Chen, J., Reilly, R. M., Zheng, G., & Lheureux, S. (2017). Molecular imaging in drug development: Update and challenges for radiolabeled antibodies and nanotechnology. Methods, 130, 23–35. https://doi.org/10.1016/j.ymeth.2017.07.018

Common strategic research agenda for radiation protection in medicine. (2017). Insights into Imaging, 8(2), 183–197. https://doi.org/10.1007/s13244-016-0538-x

Cormack, J., & Shearer, J. (1998). Calculation of radiation exposures from patients to whom radioactive materials have been administered. Physics in Medicine and Biology, 43(3), 501–516. https://doi.org/10.1088/0031-9155/43/3/003

Craig, A. J., Rojas, B., Wevrett, J. L., Hamer, E., Fenwick, A., & Gregory, R. (2020). IPEM topical report: current molecular radiotherapy service provision and guidance on the implications of setting up a dosimetry service. Physics in Medicine & Biology, 65(24), 245038. https://doi.org/10.1088/1361-6560/abc707

Cremonesi, M., Ferrari, M. E., Bodei, L., Chiesa, C., Sarnelli, A., Garibaldi, C., Pacilio, M., Strigari, L., Summers, P. E., Orecchia, R., Grana, C. M., & Botta, F. (2018). Correlation of dose with toxicity and tumour response to 90Y- and 177Lu-PRRT provides the basis for optimization through individualized treatment planning. European Journal of Nuclear Medicine and Molecular Imaging, 45(13), 2426–2441. https://doi.org/10.1007/s00259-018-4044-x

Dal Maso, L., Tavilla, A., Pacini, F., Serraino, D., van Dijk, B. A. C., Chirlaque, M. D., Capocaccia, R., Larrañaga, N., Colonna, M., Agius, D., Ardanaz, E., Rubió-Casadevall, J., Kowalska, A., Virdone, S., Mallone, S., Amash, H., de Angelis, R., Hackl, M., Zielonke, N., … White, C. (2017). Survival of 86,690 patients with thyroid cancer: A population-based study in 29 European countries from EUROCARE-5. European Journal of Cancer, 77, 140–152. https://doi.org/10.1016/j.ejca.2017.02.023

D'Arienzo, M., & Cox, M. (2017). Uncertainty Analysis in the Calibration of an Emission Tomography System for Quantitative Imaging. Computational and Mathematical Methods in Medicine, 2017, 1–9. https://doi.org/10.1155/2017/9830386

D'Arienzo, M., Cozzella, M. L., Fazio, A., de Felice, P., Iaccarino, G., D'Andrea, M., Ungania, S., Cazzato, M., Schmidt, K., Kimiaei, S., & Strigari, L. (2016). Quantitative 177Lu SPECT imaging using advanced correction algorithms in non-reference geometry. Physica Medica, 32(12), 1745–1752. https://doi.org/10.1016/j.ejmp.2016.09.014.

Därr, R., Kuhn, M., Bode, C., Bornstein, S. R., Pacak, K., Lenders, J. W. M., & Eisenhofer, G. (2017). Accuracy of recommended sampling and assay methods for the determination of plasma-free and urinary fractionated metanephrines in the diagnosis of pheochromocytoma and paraganglioma: a systematic review. Endocrine, 56(3), 495–503. https://doi.org/10.1007/s12020-017-1300-y

de la Vieja, A., & Riesco-Eizaguirre, G. (2021). Radio-iodide treatment: From molecular aspects to the clinical view. In Cancers (Vol. 13, Issue 5, pp. 1–21). MDPI AG. https://doi.org/10.3390/cancers13050995

de Pont, C., Halders, S., Bucerius, J., Mottaghy, F., & Brans, B. (2013). 124I PET/CT in the pretherapeutic staging of differentiated thyroid carcinoma: comparison with posttherapy 131I SPECT/CT. European Journal of Nuclear Medicine and Molecular Imaging, 40(5), 693–700. https://doi.org/10.1007/s00259-012-2331-5

del Prete, M., Buteau, F.-A., Arsenault, F., Saighi, N., Bouchard, L.-O., Beaulieu, A., & Beauregard, J.-M. (2019). Personalized 177Lu-octreotate peptide receptor radionuclide therapy of neuroendocrine tumours: initial results from the P-PRRT trial. European Journal of Nuclear Medicine and Molecular Imaging, 46(3), 728–742. https://doi.org/10.1007/s00259-018-4209-7

del Prete, M., Buteau, F.-A., & Beauregard, J.-M. (2017). Personalized 177Lu-octreotate peptide receptor radionuclide therapy of neuroendocrine tumours: a simulation study. European Journal of Nuclear Medicine and Molecular Imaging, 44(9), 1490–1500. https://doi.org/10.1007/s00259-017-3688-2

Desy, A., Bouvet, G. F., Frezza, A., Després, P., & Beauregard, J. M. (2020). Impact of dead time on quantitative 177Lu-SPECT (QSPECT) and kidney dosimetry during PRRT. EJNMMI Physics, 7(1). https://doi.org/10.1186/s40658-020-00303-0

Devasia, T. P., Dewaraja, Y. K., Frey, K. A., Wong, K. K., & Schipper, M. J. (2021). A Novel Time–Activity Information-Sharing Approach Using Nonlinear Mixed Models for Patient-Specific Dosimetry with Reduced Imaging Time Points: Application in SPECT/CT After [177] Lu-DOTATATE. Journal of Nuclear Medicine, 62(8), 1118–1125. https://doi.org/10.2967/jnumed.120.256255

Dewaraja, Y. K., Frey, E. C., Sgouros, G., Brill, A. B., Roberson, P., Zanzonico, P. B., & Ljungberg, M. (2012). MIRD pamphlet no. 23: Quantitative SPECT for patient-specific 3-dimensional dosimetry in internal radionuclide therapy. In Journal of Nuclear Medicine (Vol. 53, Issue 8, pp. 1310–1325). https://doi.org/10.2967/jnumed.111.100123

Dewaraja, Y. K., Ljungberg, M., Green, A. J., Zanzonico, P. B., Frey, E. C., Bolch, W. E., Brill, A. B., Dunphy, M., Fisher, D. R., Howell, R. W., Meredith, R. F., Sgouros, G., & Wessels, B. W. (2013). MIRD pamphlet No. 24: Guidelines for quantitative 131I SPECT in dosimetry applications. Journal of Nuclear Medicine, 54(12), 2182–2188. https://doi.org/10.2967/jnumed.113.122390

Dewaraja, Y. K., Wilderman, S. J., Ljungberg, M., Koral, K. F., Zasadny, K., & Kaminiski, M. S. (2005). Accurate Dosimetry in 131 I Radionuclide Therapy Using Patient-Specific, 3-Dimensional Methods for SPECT Reconstruction and Absorbed Dose Calculation. In J Nucl Med (Vol. 46, Issue 5).

Driedger, A. A., & Kotowycz, N. (2004). Two Cases of Thyroid Carcinoma That Were Not Stimulated by Recombinant Human Thyrotropin. Journal of Clinical Endocrinology and Metabolism, 89(2), 585–590. https://doi.org/10.1210/jc.2003-031650

Drude, N., Tienken, L., & Mottaghy, F. M. (2017). Theranostic and nanotheranostic probes in nuclear medicine. Methods, 130, 14–22. https://doi.org/10.1016/j.ymeth.2017.07.004

EMA. (2017). Lutathera. European Medicines Agency. Available at: Https://Www.Ema.Europa.Eu/En/Medicines/Human/EPAR/Lutathera (Accessed: January 18, 2023).

Emmett, L., Willowson, K., Violet, J., Shin, J., Blanksby, A., & Lee, J. (2017). Lutetium [177] PSMA radionuclide therapy for men with prostate cancer: a review of the current literature and discussion of practical aspects of therapy. Journal of Medical Radiation Sciences, 64(1), 52–60. https://doi.org/10.1002/jmrs.227

European Association of Nuclear Medicine (EANM). (2017). Internal Dosimetry Task Force Report on: Treatment Planning for Molecular Radiotherapy: Potential And Prospects. https://www.eanm.org/content-eanm/uploads/documents/EANM_2017_iDTF-Report_online.pdf.

Esser, J. P., Krenning, E. P., Teunissen, J. J. M., Kooij, P. P. M., van Gameren, A. L. H., Bakker, W. H., & Kwekkeboom, D. J. (2006). Comparison of [177Lu-DOTA0,Tyr3]octreotate and [177Lu-DOTA0,Tyr3]octreotide: Which peptide is preferable for PRRT? European Journal of Nuclear Medicine and Molecular Imaging, 33(11), 1346–1351. https://doi.org/10.1007/s00259-006-0172-9.

Ezziddin, S., Khalaf, F., Vanezi, M., Haslerud, T., Mayer, K., al Zreiqat, A., Willinek, W., Biersack, H.-J., & Sabet, A. (2014). Outcome of peptide receptor radionuclide therapy with 177Lu-octreotate in advanced grade 1/2 pancreatic neuroendocrine tumours. European Journal of Nuclear Medicine and Molecular Imaging, 41(5), 925–933. https://doi.org/10.1007/s00259-013-2677-3

Fahey, F. H., Grant, F. D., & Thrall, J. H. (2017). Saul Hertz, MD, and the birth of radionuclide therapy. EJNMMI physics, 4(1), 15. https://doi.org/10.1186/s40658-017-0182-7

Feelders, R. A., Hofland, L. J., Kwekkeboom, D. J., Lamberts, StevenW., & de Herder, W. W. (2012). Neuroendocrine Tumors. In Handbook of Neuroendocrinology (pp. 761–778). Elsevier. https://doi.org/10.1016/B978-0-12-375097-6.10035-6

Finocchiaro, D., Gear, J. I., Fioroni, F., Flux, G. D., Murray, I., Castellani, G., Versari, A., Iori, M., & Grassi, E. (2020). Uncertainty analysis of tumour absorbed dose calculations in molecular radiotherapy. EJNMMI Physics, 7(1). https://doi.org/10.1186/s40658-020-00328-5

Flux, G. D., Guy, M. J., Beddows, R., Pryor, M., & Flower, M. A. (2002). Estimation and implications of random errors in whole-body dosimetry for targetedradionuclide therapy. In MEDICINE AND BIOLOGY Phys. Med. Biol (Vol. 47).

Flux, G. D., Haq, M., Chittenden, S. J., Buckley, S., Hindorf, C., Newbold, K., & Harmer, C. L. (2010). A dose-effect correlation for radioiodine ablation in differentiated thyroid cancer. European Journal of Nuclear Medicine and Molecular Imaging, 37(2), 270–275. https://doi.org/10.1007/s00259-009-1261-3

Fournier, L., Costaridou, L., Bidaut, L., Michoux, N., Lecouvet, F. E., de Geus-Oei, L. F., Boellaard, R., Oprea-Lager, D. E., Obuchowski, N. A., Caroli, A., Kunz, W. G., Oei, E. H., O'Connor, J. P. B., Mayerhoefer, M. E., Franca, M., Alberich-Bayarri, A., Deroose, C. M., Loewe, C., Manniesing, R., … European Society of Radiology. (2021). Incorporating radiomics into clinical

trials: expert consensus endorsed by the European Society of Radiology on considerations for data-driven compared to biologically driven quantitative biomarkers. European Radiology, 31(8), 6001–6012. https://doi.org/10.1007/s00330-020-07598-8

Freesmeyer, M., Gühne, F., Kühnel, C., Opfermann, T., Winkens, T., & Werner, A. (2019). Determination of effective half-life of 131 I in patients with differentiated thyroid carcinoma: comparison of cystatin C and creatinine-based estimation of renal function. Endocrine, 63(3), 554–562. https://doi.org/10.1007/s12020-018-1800-4

Freudenberg, L. S., Jentzen, W., Müller, S. P., & Bockisch, A. (2008). Disseminated iodine-avid lung metastases in differentiated thyroid cancer: a challenge to 124I PET. European Journal of Nuclear Medicine and Molecular Imaging, 35(3), 502–508. https://doi.org/10.1007/s00259-007-0601-4

Frey, E. C., Humm, J. L., & Ljungberg, M. (2012). Accuracy and Precision of Radioactivity Quantification in Nuclear Medicine Images. Seminars in Nuclear Medicine, 42(3), 208–218. https://doi.org/10.1053/j.semnuclmed.2011.11.003

Fujita, N., Koshiba, Y., Abe, S., & Kato, K. (2020). Investigation of post-therapeutic image-based thyroid dosimetry using quantitative SPECT/CT, iodine biokinetics, and the MIRD's voxel S values in Graves' disease. EJNMMI Physics, 7(1), 6. https://doi.org/10.1186/s40658-020-0274-7

Gålne, A., Almquist, H., Almquist, M., Hindorf, C., Ohlsson, T., Nordenström, E., Sundlöv, A., & Trägårdh, E. (2019). A Prospective Observational Study to Evaluate the Effects of Long-Acting Somatostatin Analogs on ^{68}Ga-DOTATATE Uptake in Patients with Neuroendocrine Tumors. Journal of Nuclear Medicine, 60(12), 1717–1723. https://doi.org/10.2967/jnumed.119.226332

Gear, J., Chiesa, C., Lassmann, M., Gabiña, P. M., Tran-Gia, J., Stokke, C., & Flux, G. (2020). EANM Dosimetry Committee series on standard operational procedures for internal dosimetry for 131I mIBG treatment of neuroendocrine tumours. EJNMMI Physics, 7(1). https://doi.org/10.1186/s40658-020-0282-7

Gleisner, K. S., Brolin, G., Sundlöv, A., Mjekiqi, E., O'Stlund, K., Tennvall, J., & Larsson, E. (2015). Long-term retention of 177Lu/177mLu-DOTATATE in patients investigated by γ-spectrometry and γ-camera imaging. Journal of Nuclear Medicine, 56(7), 976–984. https://doi.org/10.2967/jnumed.115.155390

Gosewisch, A., Delker, A., Tattenberg, S., Ilhan, H., Todica, A., Brosch, J., Vomacka, L., Brunegraf, A., Gildehaus, F. J., Ziegler, S., Bartenstein, P., & Böning, G. (2018). Patient-specific image-based bone marrow dosimetry in Lu-177-[DOTA0, Tyr3]-Octreotate and Lu-177-DKFZ-PSMA-617 therapy: investigation of a new hybrid image approach. EJNMMI Research, 8(1), 76. https://doi.org/10.1186/s13550-018-0427-z

Gregory, R. A., Murray, I., Gear, J., Leek, F., Chittenden, S., Fenwick, A., Wevrett, J., Scuffham, J., Tipping, J., Murby, B., Jeans, S., Stuffins, M., Michopoulou, S., Guy, M., Morgan, D., Hallam, A., Hall, D., Polydor, H., Brown, C., … Flux, G. (2019). Standardised quantitative radioiodine SPECT/CT Imaging for multicentre dosimetry trials in molecular radiotherapy. Physics in Medicine and Biology, 64(24). https://doi.org/10.1088/1361-6560/ab5b6c

Grudzinski, J. J., Burnette, R. R., Weichert, J. P., & Jeraj, R. (2010). Dosimetric effectiveness of targeted radionuclide therapy based on a pharmacokinetic landscape. Cancer Biotherapy and Radiopharmaceuticals, 25(4), 417–426. https://doi.org/10.1089/cbr.2009.0754

H. J. Motulsky. (2016, March). GraphPad Curve Fitting Guide. Http://Www.Graphpad.Com/Guides/Prism/7/Curve-Fitting/Index.Htm.

Haddad, R. I., Bischoff, L., Ball, D., Bernet, V., Blomain, E., Busaidy, N. L., Campbell, M., Dickson, P., Duh, Q.-Y., Ehya, H., Goldner, W. S., Guo, T., Haymart, M., Holt, S., Hunt, J. P., Iagaru, A., Kandeel, F., Lamonica, D. M., Mandel, S., … Darlow, S. (2022). Thyroid Carcinoma, Version 2.2022, NCCN Clinical Practice Guidelines in Oncology. Journal of the National Comprehensive Cancer Network, 20(8), 925–951. https://doi.org/10.6004/jnccn.2022.0040

Han, S., Jin, S., Yoo, S. H., Lee, H. S., Lee, S. H., Jeon, M. J., & Ryu, J. S. (2021). A practical individualized radiation precaution based on the dose rate at release time after inpatient 131I ablation therapy. PLoS ONE, 16(5 May). https://doi.org/10.1371/journal.pone.0251627

Hänscheid, H., Lapa, C., Buck, A. K., Lassmann, M., & Werner, R. A. (2018). Dose Mapping After Endoradiotherapy with ^{177} Lu-DOTATATE/DOTATOC by a Single Measurement After 4 Days. Journal of Nuclear Medicine, 59(1), 75–81. https://doi.org/10.2967/jnumed.117.193706

Hänscheid, H., Lassmann, M., Luster, M., Kloos, R. T., & Reiners, C. (2009). Blood dosimetry from a single measurement of the whole-body radioiodine retention in patients with differentiated thyroid carcinoma. Endocrine-Related Cancer, 16(4), 1283–1289. https://doi.org/10.1677/ERC-09-0076

Hänscheid, H., Lassmann, M., Luster, M., Thomas, S. R., Pacini, F., Ceccarelli, C., Ladenson, P. W., Wahl, R. L., Schlumberger, M., Ricard, M., Driedger, A., Kloos, R. T., Sherman, S. I., Haugen, B. R., Carriere, V., Corone, C., & Reiners, C. (2006). Iodine biokinetics and dosimetry in radioiodine therapy of thyroid cancer: procedures and results of a prospective international controlled study of ablation after rhTSH or hormone withdrawal. Journal of Nuclear Medicine: Official Publication, Society of Nuclear Medicine, 47(4), 648–654.

Hänscheid, H., Sweeney, R. A., Flentje, M., Buck, A. K., Löhr, M., Samnick, S., Kreissl, M., & Verburg, F. A. (2012). PET SUV correlates with radionuclide uptake in peptide receptor therapy in meningioma. European Journal of Nuclear Medicine and Molecular Imaging, 39(8), 1284–1288. https://doi.org/10.1007/s00259-012-2124-x

Harris, P. E., & Zhernosekov, K. (2022). The evolution of PRRT for the treatment of neuroendocrine tumors; What comes next? Frontiers in Endocrinology, 13. https://doi.org/10.3389/fendo.2022.941832

Haug, A. R. (2020). PRRT of neuroendocrine tumors: individualized dosimetry or fixed dose scheme? EJNMMI Research, 10(1). https://doi.org/10.1186/s13550-020-00623-3

Haug, A. R., Auernhammer, C. J., Wängler, B., Schmidt, G. P., Uebleis, C., Göke, B., Cumming, P., Bartenstein, P., Tiling, R., & Hacker, M. (2010). ^{68} Ga-DOTATATE PET/CT for the Early Prediction of Response to Somatostatin Receptor–Mediated Radionuclide Therapy in Patients with Well-Differentiated Neuroendocrine Tumors. Journal of Nuclear Medicine, 51(9), 1349–1356. https://doi.org/10.2967/jnumed.110.075002

Hennrich, U., & Kopka, K. (2019). Lutathera®: The First FDA- and EMA-Approved Radiopharmaceutical for Peptide Receptor Radionuclide Therapy. Pharmaceuticals, 12(3), 114. https://doi.org/10.3390/ph12030114

Hindorf, C., Glatting, G., Chiesa, C., Lindén, O., & Flux, G. (2010). EANM dosimetry committee guidelines for bone marrow and whole-body dosimetry. In European Journal of Nuclear Medicine and Molecular Imaging (Vol. 37, Issue 6, pp. 1238–1250). https://doi.org/10.1007/s00259-010-1422-4

Hippeläinen, E., Tenhunen, M., Mäenpää, H., & Sohlberg, A. (2016). Quantitative accuracy of 177Lu SPECT reconstruction using different compensation methods: phantom and patient studies. EJNMMI Research, 6(1), 16. https://doi.org/10.1186/s13550-016-0172-0

Hong, C. M., Kim, C. Y., Son, S. H., Jung, J. hoon, Lee, C. H., Jeong, J. H., Jeong, S. Y., Lee, S. W., Lee, J., & Ahn, B. C. (2017). I-131 biokinetics of remnant normal thyroid tissue and residual thyroid cancer in patients with differentiated thyroid cancer: comparison between recombinant human TSH administration and thyroid hormone withdrawal. Annals of Nuclear Medicine, 31(8), 582–589. https://doi.org/10.1007/s12149-017-1188-x

Hou, X., Brosch, J., Uribe, C., Desy, A., Böning, G., Beauregard, J. M., Celler, A., & Rahmim, A. (2021). Feasibility of Single-Time-Point Dosimetry for Radiopharmaceutical Therapies. Journal of Nuclear Medicine, 62(7), 1006–1011. https://doi.org/10.2967/jnumed.120.254656

Howell, R. W., Wessels, B. W., Loevinger, R., Watson, E. E., Bolch, W. E., Brill, A. B., Charkes, N. D., Fisher, D. R., Hays, M. T., Robertson, J. S., Siegel, J. A., & Thomas, S. R. (1999). The MIRD perspective 1999. Medical Internal Radiation Dose Committee. Journal of Nuclear Medicine: Official Publication, Society of Nuclear Medicine, 40(1), 3S-10S.

Huang, R., Pu, Y., Huang, S., Yang, C., Yang, F., Pu, Y., Li, J., Chen, L., & Huang, Y. (2022). FAPI-PET/CT in Cancer Imaging: A Potential Novel Molecule of the Century. In Frontiers in Oncology (Vol. 12). Frontiers Media S.A. https://doi.org/10.3389/fonc.2022.854658.

Huizing, D. M. V., de Wit-van der Veen, B. J., Verheij, M., & Stokkel, M. P. M. (2018). Dosimetry methods and clinical applications in peptide receptor radionuclide therapy for neuroendocrine tumours: a literature review. In EJNMMI Research (Vol. 8). Springer Verlag. https://doi.org/10.1186/s13550-018-0443-z

Huizing, D. M. V., Peters, S. M. B., Versleijen, M. W. J., Martens, E., Verheij, M., Sinaasappel, M., Stokkel, M. P. M., & de Wit-van der Veen, B. J. (2020). A head-to-head comparison between two commercial software packages for hybrid dosimetry after peptide receptor radionuclide therapy. EJNMMI Physics, 7(1). https://doi.org/10.1186/s40658-020-00308-9

IAEA International Atomic Energy Agency, Quantitative Nuclear Medicine Imaging: Concepts, Requirements and Methods, IAEA Human Health Reports No. 9, IAEA, Vienna (2014). https://www-pub.iaea.org/MTCD/Publications/PDF/Pub1605_web.pdf (Accessed May 2019).

ICRP. (1991). 1990 Recommendations of the International Commission on Radiological Protection. Annals of the ICRP, 21(1–3), 1–201.

ICRP. (2004). Release of patients after therapy with unsealed radionuclides. Annals of the ICRP, 34(2), v–vi. https://doi.org/10.1016/j.icrp.2004.08.001

ICRP. (2019). Radiological Protection in Therapy with Radiopharmaceuticals. ICRP Publication 140, Ann. ICRP 48(1). www.icrp.org,

Ilan, E., Velikyan, I., Sandström, M., Sundin, A., & Lubberink, M. (2020). Tumor-to-blood ratio for assessment of somatostatin receptor density in neuroendocrine tumors using 68Ga-DOTATOC and 68Ga-DOTATATE. Journal of Nuclear Medicine, 61(2), 217–221. https://doi.org/10.2967/jnumed.119.228072

IPEM. (2002). Legal Aspects, Nuclear Medicine, Occupational Exposure, Occupational Safety, Public Health, Radiation Protection, Radiological Personnel, Recommendations. Journal of Radiological Protection; ISSN 0952-4746, 22(3), 334–335.

IRR2017. (2017). The Ionising Radiations Regulations 2017 (SI 2017 No.1075). https://www.legislation.gov.uk/uksi/2017/1075.

Jackson, P., Hofman, M., McIntosh, L., Buteau, J. P., & Ravi Kumar, A. (2022). Radiation Dosimetry in 177Lu-PSMA-617 Therapy. In Seminars in Nuclear Medicine (Vol. 52, Issue 2, pp. 243–254). W.B. Saunders. https://doi.org/10.1053/j.semnuclmed.2021.11.003.

Jadvar, H. (2014). Radionuclide Imaging of Cancer Therapy. In Cancer Theranostics (pp. 45–54). Elsevier. https://doi.org/10.1016/B978-0-12-407722-5.00004-9

Jha, A. K., Mithun, S., Purandare, N. C., Kumar, R., Rangarajan, V., Wee, L., & Dekker, A. (2022). Radiomics: a quantitative imaging biomarker in precision oncology. In Nuclear Medicine Communications (Vol. 43, Issue 5, pp. 483–493). Lippincott Williams and Wilkins. https://doi.org/10.1097/MNM.0000000000001543

Joo Hyun, O., Lodge, M. A., & Wahl, R. L. (2016). Practical percist: A simplified guide to PET response criteria in solid tumors 1.0. Radiology, 280(2), 576–584. https://doi.org/10.1148/radiol.2016142043

Kapoor, M., & Kasi, A. (2022). Octreotide Scan.

Kayani, I., Conry, B. G., Groves, A. M., Win, T., Dickson, J., Caplin, M., & Bomanji, J. B. (2009). A Comparison of ^{68}Ga-DOTATATE and ^{18}F-FDG PET/CT in Pulmonary Neuroendocrine Tumors. Journal of Nuclear Medicine, 50(12), 1927–1932. https://doi.org/10.2967/jnumed.109.066639

Khorjekar, G. R., van Nostrand, D., Garcia, C., O'Neil, J., Moreau, S., Atkins, F. B., Mete, M., Orquiza, M. H., Burman, K., & Wartofsky, L. (2014). Do Negative [124]I Pretherapy Positron Emission Tomography Scans in Patients with Elevated Serum Thyroglobulin Levels Predict Negative [131]I Posttherapy Scans? Thyroid, 24(9), 1394–1399. https://doi.org/10.1089/thy.2013.0713

Klain, M., Nappi, C., de Risi, M., Piscopo, L., Volpe, F., Manganelli, M., Caiazzo, E., Bianco, D., Schlumberger, M., & Cuocolo, A. (2021). Whole-body radioiodine effective half-life in patients with differentiated thyroid cancer. Diagnostics, 11(10). https://doi.org/10.3390/diagnostics11101740

Klubo-Gwiezdzinska, J., van Nostrand, D., Atkins, F., Burman, K., Jonklaas, J., Mete, M., & Wartofsky, L. (2011). Efficacy of Dosimetric Versus Empiric Prescribed Activity of 131I for Therapy of Differentiated Thyroid Cancer. The Journal of Clinical Endocrinology & Metabolism, 96(10), 3217–3225. https://doi.org/10.1210/jc.2011-0494

Komek, H., Can, C., Urakçi, Z., & Kepenek, F. (2019). Comparison of (18F) FDG PET/CT and (68Ga)DOTATATE PET/CT imaging methods in terms of detection of histological subtype and related SUVmax values in patients with pulmonary carcinoid tumors. Nuclear Medicine Communications, 40(5), 517–524. https://doi.org/10.1097/MNM.0000000000000985

Kozak, O. v, Sukach, G. G., Korchinskaya, O. I., Trembach, A. M., Turicina, V. L., & Voit, N. U. (2005). Hierarchy of treatment variables affecting outcome of 131I therapy in thyroid cancer patients with lung metastases. Experimental Oncology, 27(2), 150–155.

Kramer-Marek, G., & Capala, J. (2012). The role of nuclear medicine in modern therapy of cancer. Tumor Biology, 33(3), 629–640. https://doi.org/10.1007/s13277-012-0373-8

Lassmann, M., Chiesa, C., Flux, G., & Bardiès, M. (2011). EANM Dosimetry Committee guidance document: good practice of clinical dosimetry reporting. European Journal of Nuclear Medicine and Molecular Imaging, 38(1), 192–200. https://doi.org/10.1007/s00259-010-1549-3

Lassmann, M., & Eberlein, U. (2018). The Relevance of Dosimetry in Precision Medicine. Journal of Nuclear Medicine, 59(10), 1494–1499. https://doi.org/10.2967/jnumed.117.206649

Laudicella, R., Comelli, A., Liberini, V., Vento, A., Stefano, A., Spataro, A., Crocè, L., Baldari, S., Bambaci, M., Deandreis, D., Arico', D., Ippolito, M., Gaeta, M., Alongi, P., Minutoli, F., Burger, I. A., & Baldari, S. (2022). [68 Ga] DOTATOC PET/CT Radiomics to Predict the Response in

GEP-NETs Undergoing [177 Lu] DOTATOC PRRT: The "Theragnomics" Concept. Cancers, 14(4). https://doi.org/10.3390/cancers14040984

Lawhn-Heath, C., Flavell, R., Chuang, E., & Liu, C. (2020). Failure of iodine uptake in microscopic pulmonary metastases after recombinant human thyroid-stimulating hormone stimulation. World Journal of Nuclear Medicine, 19(01), 61–64. https://doi.org/10.4103/wjnm.wjnm_29_19

Lee, J. H., & Park, S. G. (2010). Estimation of the release time from isolation for patients with differentiated thyroid cancer treated with high-dose I-131. Nuclear Medicine and Molecular Imaging, 44(4), 241–245. https://doi.org/10.1007/s13139-010-0041-0

Lee, O. N. Y., Tan, K. V., Tripathi, V., Yuan, H., Chan, W. W.-L., & Chiu, K. W. H. (2022). The Role of 68Ga-DOTA-SSA PET/CT in the Management and Prediction of Peptide Receptor Radionuclide Therapy Response for Patients with Neuroendocrine Tumors. Clinical Nuclear Medicine, 47(9), 781–793. https://doi.org/10.1097/RLU.0000000000004235

Levart, D., Kalogianni, E., Corcoran, B., Mulholland, N., & Vivian, G. (2019). Radiation precautions for inpatient and outpatient 177Lu-DOTATATE peptide receptor radionuclide therapy of neuroendocrine tumours. EJNMMI Physics, 6(1). https://doi.org/10.1186/s40658-019-0243-1

Lewis, A., Atkinson, B., Bell, P., Courtney, H., McCance, D., Mullan, K., & Hunter, S. (2013). Outcome of 131I therapy in hyperthyroidism using a 550MBq fixed dose regimen. The Ulster Medical Journal, 82(2), 85–88.

Liberini, V., de Santi, B., Rampado, O., Gallio, E., Dionisi, B., Ceci, F., Polverari, G., Thuillier, P., Molinari, F., & Deandreis, D. (2021). Impact of segmentation and discretization on radiomic features in 68Ga-DOTA-TOC PET/CT images of neuroendocrine tumor. EJNMMI Physics, 8(1). https://doi.org/10.1186/s40658-021-00367-6

Liberini, V., Huellner, M. W., Grimaldi, S., Finessi, M., Thuillier, P., Muni, A., Pellerito, R. E., Papotti, M. G., Piovesan, A., Arvat, E., & Deandreis, D. (2020). The Challenge of Evaluating Response to Peptide Receptor Radionuclide Therapy in Gastroenteropancreatic Neuroendocrine Tumors: The Present and the Future. Diagnostics, 10(12), 1083. https://doi.org/10.3390/diagnostics10121083

Liberini, V., Rampado, O., Gallio, E., de Santi, B., Ceci, F., Dionisi, B., Thuillier, P., Ciuffreda, L., Piovesan, A., Fioroni, F., Versari, A., Molinari, F., & Deandreis, D. (2021). 68Ga-DOTATOC PET/CT-Based Radiomic Analysis and PRRT Outcome: A Preliminary Evaluation Based on an Exploratory Radiomic Analysis on Two Patients. Frontiers in Medicine, 7. https://doi.org/10.3389/fmed.2020.601853

Liu, B., Tian, R., Peng, W., He, Y., Huang, R., & Kuang, A. (2015). Radiation safety precautions in 131I therapy of Graves' disease based on actual biokinetic measurements. Journal of Clinical Endocrinology and Metabolism, 100(8), 2934–2941. https://doi.org/10.1210/jc.2015-1682

Liu, Q., Zang, J., Sui, H., Ren, J., Guo, H., Wang, H., Wang, R., Jacobson, O., Zhang, J., Cheng, Y., Zhu, Z., & Chen, X. (2021). Peptide Receptor Radionuclide Therapy of Late-Stage Neuroendocrine Tumor Patients with Multiple Cycles of 177Lu-DOTA-EB-TATE. Journal of Nuclear Medicine: Official Publication, Society of Nuclear Medicine, 62(3), 386–392. https://doi.org/10.2967/jnumed.120.248658

Liu, Y., Watabe, T., Kaneda-Nakashima, K., Shirakami, Y., Naka, S., Ooe, K., Toyoshima, A., Nagata, K., Haberkorn, U., Kratochwil, C., Shinohara, A., Hatazawa, J., & Giesel, F. (2022). Fibroblast activation protein targeted therapy using [177Lu]FAPI-46 compared with [225Ac]FAPI-46 in a pancreatic cancer model. European Journal of Nuclear Medicine and Molecular Imaging, 49(3), 871–880. https://doi.org/10.1007/s00259-021-05554-2

Ljungberg, M., Celler, A., Konijnenberg, M. W., Eckerman, K. F., Dewaraja, Y. K., & Sjögreen-Gleisner, K. (2016). MIRD Pamphlet No. 26: Joint EANM/MIRD Guidelines for Quantitative [177] Lu SPECT Applied for Dosimetry of Radiopharmaceutical Therapy. Journal of Nuclear Medicine, 57(1), 151–162. https://doi.org/10.2967/jnumed.115.159012

Ljungberg, M., & Sjögreen Gleisner, K. (2016). Personalized Dosimetry for Radionuclide Therapy Using Molecular Imaging Tools. Biomedicines, 4(4), 25. https://doi.org/10.3390/biomedicines4040025

Lu, W., Onofrey, J. A., Lu, Y., Shi, L., Ma, T., Liu, Y., & Liu, C. (2019). An investigation of quantitative accuracy for deep learning based denoising in oncological PET. Physics in Medicine & Biology, 64(16), 165019. https://doi.org/10.1088/1361-6560/ab3242

Luster, M., Clarke, S. E., Dietlein, M., Lassmann, M., Lind, P., Oyen, W. J. G., Tennvall, J., & Bombardieri, E. (2008). Guidelines for radioiodine therapy of differentiated thyroid cancer. In European Journal of Nuclear Medicine and Molecular Imaging (Vol. 35, Issue 10, pp. 1941–1959). https://doi.org/10.1007/s00259-008-0883-1

Luster, M., Pfestroff, A., Hänscheid, H., & Verburg, F. A. (2017). Radioiodine Therapy. In Seminars in Nuclear Medicine (Vol. 47, Issue 2, pp. 126–134). W.B. Saunders. https://doi.org/10.1053/j.semnuclmed.2016.10.002

Ma, C., Xie, J., & Kuang, A. (2005). Is empiric 131I therapy justified for patients with positive thyroglobulin and negative 131I whole-body scanning results? Journal of Nuclear Medicine: Official Publication, Society of Nuclear Medicine, 46(7), 1164–1170.

Mair, C., Warwitz, B., Fink, K., Scarpa, L., Nilica, B., Maffey-Steffan, J., Buxbaum, S., & Virgolini, I. J. (2018). Radiation exposure after 177Lu-DOTATATE and 177Lu-PSMA-617 therapy. Annals of Nuclear Medicine, 32(7), 499–502. https://doi.org/10.1007/s12149-018-1264-x

Martinez, J., Fung, E. K., Prof, A., Flavell, R. R., Lawhn-Heath, C., Hope, T. A., Martinez, J., Fung, E. K., Shin, J., & Seo, Y. (2022). Dosimetry in radionuclide therapy: the clinical role of measuring radiation dose. In Review Lancet Oncol (Vol. 23). www.thelancet.com/oncology

Marquis, H., Deidda, D., Gillman, A., Willowson, K. P., Gholami, Y., Hioki, T., Eslick, E., Thielemans, K., & Bailey, D. L. (2021). Theranostic SPECT reconstruction for improved resolution: application to radionuclide therapy dosimetry. EJNMMI physics, 8(1), 16. https://doi.org/10.1186/s40658-021-00362-x

Mete, O., Asa, S. L., Gill, A. J., Kimura, N., de Krijger, R. R., & Tischler, A. (2022). Overview of the 2022 WHO Classification of Paragangliomas and Pheochromocytomas. In Endocrine Pathology (Vol. 33, Issue 1, pp. 90–114). Springer. https://doi.org/10.1007/s12022-022-09704-6

Mezzenga, E., D'Errico, V., D'Arienzo, M., Strigari, L., Panagiota, K., Matteucci, F., Severi, S., Paganelli, G., Fenwick, A., Bianchini, D., Marcocci, F., & Sarnelli, A. (2017). Quantitative accuracy of 177Lu SPECT imaging for molecular radiotherapy. PLOS ONE, 12(8), e0182888. https://doi.org/10.1371/journal.pone.0182888

Mínguez, P., Flux, G., Genollá, J., Delgado, A., Rodeño, E., & Sjögreen Gleisner, K. (2016). Whole-remnant and maximum-voxel SPECT/CT dosimetry in [131] I-NaI treatments of differentiated thyroid cancer. Medical Physics, 43(10), 5279–5287. https://doi.org/10.1118/1.4961742

Monaghan, P. J., Lamarca, A., Valle, J. W., Hubner, R. A., Mansoor, W., Trainer, P. J., & Darby, D. (2016). Routine measurement of plasma chromogranin B has limited clinical utility in the management of patients with neuroendocrine tumours. Clinical Endocrinology, 84(3), 348–352. https://doi.org/10.1111/cen.12985

Morphis, M., van Staden, J. A., du Raan, H., & Ljungberg, M. (2021). Evaluation of Iodine-123 and Iodine-131 SPECT activity quantification: a Monte Carlo study. EJNMMI Physics, 8(1). https://doi.org/10.1186/s40658-021-00407-1

Mujica-Mota, R., Varley-Campbell, J., Tikhonova, I., Cooper, C., Griffin, E., Haasova, M., Peters, J., Lucherini, S., Talens-Bou, J., Long, L., Sherriff, D., Napier, M., Ramage, J., & Hoyle, M. (2018). Everolimus, lutetium-177 DOTATATE and sunitinib for advanced, unresectable, or metastatic neuroendocrine tumours with disease progression: a systematic review and cost-effectiveness analysis. Health Technology Assessment, 22(49), 1–326. https://doi.org/10.3310/hta22490

Nascimento, A. C. H., Lipsztein, J. L., Corbo, R., & Rebelo, A. M. O. (2010). 131I biokinetics and cytogenetic dose estimates in ablation treatment of thyroid CARCINOMA. Health Physics, 99(4), 457–463. https://doi.org/10.1097/HP.0b013e3181c8f9ea

NICE. (2018). Technology appraisal guidance [TA539] Lutetium (177Lu) oxodotreotide for treating unresectable or metastatic neuroendocrine tumours. National Institute for Health and Care Excellence. Available at: Https://Www.Nice.Org.Uk/About/What-We-Do/Our-Programmes/NICE-Guidance/NICE-Technology-Appraisal-Guidance (Accessed: January 18, 2023).

Nussey S. (2001). Endocrinology: An Integrated Approach.; Chapter 3, The thyroid gland. Available from: https://www.ncbi.nlm.nih.gov/books/NBK28/. BIOS Scientific Publishers.

Opalińska, M., Morawiec-Sławek, K., Kania-Kuc, A., al Maraih, I., Sowa-Staszczak, A., & Hubalewska-Dydejczyk, A. (2022). Potential value of pre- and post-therapy [68Ga] Ga-DOTA-TATE PET/CT in the prognosis of response to PRRT in disseminated neuroendocrine tumors. Frontiers in Endocrinology, 13. https://doi.org/10.3389/fendo.2022.929391

Ortega, C., Wong, R. K. S., Schaefferkoetter, J., Veit-Haibach, P., Myrehaug, S., Juergens, R., Laidley, D., Anconina, R., Liu, A., & Metser, U. (2021). Quantitative ^{68}Ga-DOTATATE PET/CT Parameters for the Prediction of Therapy Response in Patients with Progressive Metastatic Neuroendocrine Tumors Treated with ^{177}Lu-DOTATATE. Journal of Nuclear Medicine, 62(10), 1406–1414. https://doi.org/10.2967/jnumed.120.256727

Page, M. J., Moher, D., Bossuyt, P. M., Boutron, I., Hoffmann, T. C., Mulrow, C. D., Shamseer, L., Tetzlaff, J. M., Akl, E. A., Brennan, S. E., Chou, R., Glanville, J., Grimshaw, J. M., Hróbjartsson, A., Lalu, M. M., Li, T., Loder, E. W., Mayo-Wilson, E., Mcdonald, S., … Mckenzie, J. E. (2021). PRISMA 2020 explanation and elaboration: Updated guidance and exemplars for reporting systematic reviews. In The BMJ (Vol. 372). BMJ Publishing Group. https://doi.org/10.1136/bmj.n160

Panagiotidis, E., Alshammari, A., Michopoulou, S., Skoura, E., Naik, K., Maragkoudakis, E., Mohmaduvesh, M., Al-Harbi, M., Belda, M., Caplin, M. E., Toumpanakis, C., & Bomanji, J. (2017). Comparison of the Impact of ^{68}Ga-DOTATATE and ^{18}F-FDG PET/CT on Clinical Management in Patients with Neuroendocrine Tumors. Journal of Nuclear Medicine, 58(1), 91–96. https://doi.org/10.2967/jnumed.116.178095

Pant, G. S., Sharma, S. K., Bal, C. S., Kumar, R., & Rath, G. K. (2006). Radiation dose to family members of hyperthyroidism and thyroid cancer patients treated with 131I. Radiation Protection Dosimetry, 118(1), 22–27. https://doi.org/10.1093/rpd/nci337

Perros, P., Boelaert, K., Colley, S., Evans, C., Evans, R. M., Gerrard BA, G., Gilbert, J., Harrison, B., Johnson, S. J., Giles, T. E., Moss, L., Lewington, V., Newbold, K., Taylor, J., Thakker, R. v, Watkinson, J., & Williams, G. R. (2014). Guidelines for the management of thyroid cancer. Clinical Endocrinology, 81, 1–122. https://doi.org/10.1111/cen.12515

Poeppel, T. D., Binse, I., Petersenn, S., Lahner, H., Schott, M., Antoch, G., Brandau, W., Bockisch, A., & Boy, C. (2011). 68Ga-DOTATOC versus 68Ga-DOTATATE PET/CT in functional imaging of neuroendocrine tumors. Journal of Nuclear Medicine, 52(12), 1864–1870. https://doi.org/10.2967/jnumed.111.091165

Poeppel, T. D., Binse, I., Petersenn, S., Lahner, H., Schott, M., Antoch, G., Brandau, W., Bockisch, A., & Boy, C. (2013). Differential Uptake of 68Ga-DOTATOC and 68Ga-DOTATATE in PET/CT of Gastroenteropancreatic Neuroendocrine Tumors (pp. 353–371). https://doi.org/10.1007/978-3-642-27994-2_18

Popoveniuc, G., & Jonklaas, J. (2012). Thyroid Nodules. Medical Clinics of North America, 96(2), 329–349. https://doi.org/10.1016/j.mcna.2012.02.002

Prosperi, D., Gentiloni Silveri, G., Panzuto, F., Faggiano, A., Russo, V. M., Caruso, D., Polici, M., Lauri, C., Filice, A., Laghi, A., & Signore, A. (2022). Nuclear Medicine and Radiological Imaging of Pancreatic Neuroendocrine Neoplasms: A Multidisciplinary Update. In Journal of Clinical Medicine (Vol. 11, Issue 22). MDPI. https://doi.org/10.3390/jcm11226836

Ragab, A., Wu, J., Ding, X., Clark, A., Mischen, B., Chauhan, A., Oates, M. E., Anthony, L., & el Khouli, R. (2022). 68Ga-DOTATATE PET/CT: The Optimum Standardized Uptake Value (SUV) Internal Reference. Academic Radiology, 29(1), 95–106. https://doi.org/10.1016/j.acra.2020.08.028

Ramage, J. K., Ahmed, A., Ardill, J., Bax, N., Breen, D. J., Caplin, M. E., Corrie, P., Davar, J., Davies, A. H., Lewington, V., Meyer, T., Newell-Price, J., Poston, G., Reed, N., Rockall, A., Steward, W., Thakker, R. V, Toubanakis, C., Valle, J., … Grossman, A. B. (2012). Guidelines for the management of gastroenteropancreatic neuroendocrine (including carcinoid) tumours (NETs). Gut, 61(1), 6–32. https://doi.org/10.1136/gutjnl-2011-300831

Reubi, J. C., Schär, J.-C., Waser, B., Wenger, S., Heppeler, A., Schmitt, J. S., & Mäcke, H. R. (2000). Affinity profiles for human somatostatin receptor subtypes SST1-SST5 of somatostatin radiotracers selected for scintigraphic and radiotherapeutic use. European Journal of Nuclear Medicine and Molecular Imaging, 27(3), 273–282. https://doi.org/10.1007/s002590050034

Rindi, G., Mete, O., Uccella, S., Basturk, O., la Rosa, S., Brosens, L. A. A., Ezzat, S., de Herder, W. W., Klimstra, D. S., Papotti, M., & Asa, S. L. (2022). Overview of the 2022 WHO Classification of Neuroendocrine Neoplasms. In Endocrine Pathology (Vol. 33, Issue 1, pp. 115–154). Springer. https://doi.org/10.1007/s12022-022-09708-2

Rojas, B., McGowan, D. R., Guy, M. J., Tipping, J., Aldridge, M., & Gear, J. (2019). Eighty per cent more patients in 10 years of UK molecular radiotherapy. Nuclear Medicine Communications, 40(7), 657–661. https://doi.org/10.1097/MNM.0000000000001020

Roth, D., Gustafsson, J., Warfvinge, C. F., Sundlöv, A., Åkesson, A., Tennvall, J., & Gleisner, K. S. (2022). Dosimetric Quantities in Neuroendocrine Tumors over Treatment Cycles with [177] Lu-DOTATATE. Journal of Nuclear Medicine, 63(3), 399–405. https://doi.org/10.2967/jnumed.121.262069

Rubello, D., Salvatori, M., Ardito, G., Mariani, G., Al-Nahhas, A., Gross, M. D., Muzzio, P. C., & Pelizzo, M. R. (2007). Iodine-131 radio-guided surgery in differentiated thyroid cancer: Outcome on 31 patients and review of the literature. Biomedicine & Pharmacotherapy, 61(8), 477–481. https://doi.org/10.1016/j.biopha.2007.07.010

Sabet, A., Ezziddin, K., Pape, U.-F., Ahmadzadehfar, H., Mayer, K., Pöppel, T., Guhlke, S., Biersack, H.-J., & Ezziddin, S. (2013). Long-Term Hematotoxicity After Peptide Receptor Radionuclide Therapy with [177] Lu-Octreotate. Journal of Nuclear Medicine, 54(11), 1857–1861. https://doi.org/10.2967/jnumed.112.119347

Sainz-Esteban, A., Prasad, V., Schuchardt, C., Zachert, C., Carril, J. M., & Baum, R. P. (2012). Comparison of sequential planar 177Lu-DOTA-TATE dosimetry scans with 68Ga-DOTA-TATE PET/CT images in patients with metastasized neuroendocrine tumours undergoing peptide receptor radionuclide therapy. European Journal of Nuclear Medicine and Molecular Imaging, 39(3), 501–511. https://doi.org/10.1007/s00259-011-2003-x

Saito, S., Sakurada, T., Yamamoto, M., Yoshida, K., Kaise, K., Kaise, N., & Yoshinaga, K. (1980). Long-term results of radioiodine (131I) therapy in 331 patients with Graves' disease. The Tohoku Journal of Experimental Medicine, 132(1), 1–10. https://doi.org/10.1620/tjem.132.1

Saleh, M., Bhosale, P. R., Yano, M., Itani, M., Elsayes, A. K., Halperin, D., Bergsland, E. K., & Morani, A. C. (2022). New frontiers in imaging including radiomics updates for pancreatic neuroendocrine neoplasms. Abdominal Radiology, 47(9), 3078–3100. https://doi.org/10.1007/s00261-020-02833-8

Sanders, J. C., Kuwert, T., Hornegger, J., & Ritt, P. (2015). Quantitative SPECT/CT Imaging of 177Lu with In Vivo Validation in Patients Undergoing Peptide Receptor Radionuclide Therapy. Molecular Imaging and Biology, 17(4), 585–593. https://doi.org/10.1007/s11307-014-0806-4

Santoro, L., Pitalot, L., Trauchessec, D., Mora-Ramirez, E., Kotzki, P. O., Bardiès, M., & Deshayes, E. (2021). Clinical implementation of PLANET® Dose for dosimetric assessment after [177Lu]Lu-DOTA-TATE: comparison with Dosimetry Toolkit® and OLINDA/EXM® V1.0. EJNMMI Research, 11(1), 1. https://doi.org/10.1186/s13550-020-00737-8

Sartor, O., de Bono, J., Chi, K. N., Fizazi, K., Herrmann, K., Rahbar, K., Tagawa, S. T., Nordquist, L. T., Vaishampayan, N., El-Haddad, G., Park, C. H., Beer, T. M., Armour, A., Pérez-Contreras, W. J., DeSilvio, M., Kpamegan, E., Gericke, G., Messmann, R. A., Morris, M. J., & Krause, B. J. (2021). Lutetium-177–PSMA-617 for Metastatic Castration-Resistant Prostate Cancer. New England Journal of Medicine, 385(12), 1091–1103. https://doi.org/10.1056/NEJMoa2107322

Saw, M. M. (2013). Early Experience with 68Ga-DOTATATE Preparation (pp. 177–188). https://doi.org/10.1007/978-3-642-27994-2_10

Sharma, R., Wang, W. M., Yusuf, S., Evans, J., Ramaswami, R., Wernig, F., Frilling, A., Mauri, F., Al-Nahhas, A., Aboagye, E. O., & Barwick, T. D. (2019). 68Ga-DOTATATE PET/CT parameters predict response to peptide receptor radionuclide therapy in neuroendocrine tumours. Radiotherapy and Oncology, 141, 108–115. https://doi.org/10.1016/j.radonc.2019.09.003

Silberstein, E. B., Alavi, A., Balon, H. R., Clarke, S. E. M., Divgi, C., Gelfand, M. J., Goldsmith, S. J., Jadvar, H., Marcus, C. S., Martin, W. H., Parker, J. A., Royal, H. D., Sarkar, S. D., Stabin, M., & Waxman, A. D. (2012). The SNMMI Practice Guideline for Therapy of Thyroid Disease with ^{131}I 3.0. Journal of Nuclear Medicine, 53(10), 1633–1651. https://doi.org/10.2967/jnumed.112.105148

Singh, A. S. (2017). Common procedures for development, validity, and reliability of a questionnaire.. International Journal of Economics, 5(5), 790–801.

Sisson, J. C., Freitas, J., McDougall, I. R., Dauer, L. T., Hurley, J. R., Brierley, J. D., Edinboro, C. H., Rosenthal, D., Thomas, M. J., Wexler, J. A., Asamoah, E., Avram, A. M., Milas, M., & Greenlee, C. (2011). Radiation safety in the treatment of patients with thyroid diseases by radioiodine 131I: Practice recommendations of the american thyroid association. Thyroid, 21(4), 335–346. https://doi.org/10.1089/thy.2010.0403

Sjögreen Gleisner, K., Chouin, N., Gabina, P. M., Cicone, F., Gnesin, S., Stokke, C., Konijnenberg, M., Cremonesi, M., Verburg, F. A., Bernhardt, P., Eberlein, U., & Gear, J. (2022). EANM dosimetry committee recommendations for dosimetry of 177Lu-labelled somatostatin-receptor-

and PSMA-targeting ligands. European Journal of Nuclear Medicine and Molecular Imaging, 49(6), 1778–1809. https://doi.org/10.1007/s00259-022-05727-7

Sjögreen, K., Ljungberg, M., & Strand, S.-E. (2002). An activity quantification method based on registration of CT and whole-body scintillation camera images, with application to 131I. Journal of Nuclear Medicine: Official Publication, Society of Nuclear Medicine, 43(7), 972–982.

Sorbye, H., Kong, G., & Grozinsky-Glasberg, S. (2020). PRRT in high-grade gastroenteropancreatic neuroendocrine neoplasms (WHO G3). Endocrine-Related Cancer, 27(3), R67–R77. https://doi.org/10.1530/ERC-19-0400

Srirajaskanthan, R., Kayani, I., Quigley, A. M., Soh, J., Caplin, M. E., & Bomanji, J. (2010). The Role of [68] Ga-DOTATATE PET in Patients with Neuroendocrine Tumors and Negative or Equivocal Findings on [111] In-DTPA-Octreotide Scintigraphy. Journal of Nuclear Medicine, 51(6), 875–882. https://doi.org/10.2967/jnumed.109.066134

Sterne, J. A., Hernán, M. A., Reeves, B. C., Savović, J., Berkman, N. D., Viswanathan, M., Henry, D., Altman, D. G., Ansari, M. T., Boutron, I., Carpenter, J. R., Chan, A.-W., Churchill, R., Deeks, J. J., Hróbjartsson, A., Kirkham, J., Jüni, P., Loke, Y. K., Pigott, T. D., … Higgins, J. P. (2016). ROBINS-I: a tool for assessing risk of bias in non-randomised studies of interventions. BMJ, i4919. https://doi.org/10.1136/bmj.i4919

Stokkel, M. P. M., Handkiewicz Junak, D., Lassmann, M., Dietlein, M., & Luster, M. (2010). EANM procedure guidelines for therapy of benign thyroid disease. In European Journal of Nuclear Medicine and Molecular Imaging (Vol. 37, Issue 11, pp. 2218–2228). https://doi.org/10.1007/s00259-010-1536-8

Strosberg, J., El-Haddad, G., Wolin, E., Hendifar, A., Yao, J., Chasen, B., Mittra, E., Kunz, P. L., Kulke, M. H., Jacene, H., Bushnell, D., O'Dorisio, T. M., Baum, R. P., Kulkarni, H. R., Caplin, M., Lebtahi, R., Hobday, T., Delpassand, E., van Cutsem, E., … Krenning, E. (2017). Phase 3 Trial of [177] Lu-Dotatate for Midgut Neuroendocrine Tumors. New England Journal of Medicine, 376(2), 125–135. https://doi.org/10.1056/NEJMoa1607427

Strosberg, J. R., Caplin, M. E., Kunz, P. L., Ruszniewski, P. B., Bodei, L., Hendifar, A., Mittra, E., Wolin, E. M., Yao, J. C., Pavel, M. E., Grande, E., van Cutsem, E., Seregni, E., Duarte, H., Gericke, G., Bartalotta, A., Mariani, M. F., Demange, A., Mutevelic, S., & Krenning, E. P. (2021). 177Lu-Dotatate plus long-acting octreotide versus high-dose long-acting octreotide in patients with midgut neuroendocrine tumours (NETTER-1): final overall survival and long-term safety results from an open-label, randomised, controlled, phase 3 trial. The Lancet Oncology, 22(12), 1752–1763. https://doi.org/10.1016/S1470-2045(21)00572-6

Svensson, J., Hagmarker, L., Magnander, T., Wängberg, B., & Bernhardt, P. (2016). Radiation exposure of the spleen during (177)Lu-DOTATATE treatment and its correlation with haematological toxicity and spleen volume. EJNMMI Physics, 3(1), 15. https://doi.org/10.1186/s40658-016-0153-4

Svensson, J., Rydén, T., Hagmarker, L., Hemmingsson, J., Wängberg, B., & Bernhardt, P. (2016). A novel planar image-based method for bone marrow dosimetry in (177) Lu-DOTATATE treatment correlates with haematological toxicity. EJNMMI Physics, 3(1), 21. https://doi.org/10.1186/s40658-016-0157-0

Tamhane, S., & Gharib, H. (2016). Thyroid nodule update on diagnosis and management. Clinical Diabetes and Endocrinology, 2(1), 17. https://doi.org/10.1186/s40842-016-0035-7

Tang, L., Wang, X. J., Baba, H., & Giganti, F. (2020). Gastric cancer and image-derived quantitative parameters: Part 2—a critical review of DCE-MRI and 18F-FDG PET/CT findings. In European

Radiology (Vol. 30, Issue 1, pp. 247–260). Springer. https://doi.org/10.1007/s00330-019-06370-x

Taprogge, J., Carnegie-Peake, L., Murray, I., Gear, J. I., & Flux, G. D. (2021). Adjustment of the iodine ICRP population pharmacokinetic model for the use in thyroid cancer patients after thyroidectomy. Journal of Radiological Protection, 41(4). https://doi.org/10.1088/1361-6498/ac149a

Taprogge, J., Leek, F., & Flux, G. D. (2019). Physics aspects of setting up a multicenter clinical trial involving internal dosimetry of radioiodine treatment of differentiated thyroid cancer. In Quarterly Journal of Nuclear Medicine and Molecular Imaging (Vol. 63, Issue 3, pp. 271–277). Edizioni Minerva Medica. https://doi.org/10.23736/S1824-4785.19.03202-3

Taprogge, J., Leek, F., Schurrat, T., Tran-Gia, J., Vallot, D., Bardiès, M., Eberlein, U., Lassmann, M., Schlögl, S., Vergara Gil, A., Buck, A., Clayton, N., Courbon, F., Lapa, C., Luster, M., Mora-Ramirez, E., Newbold, K., Schumann, S., Verburg, F., … Flux, G. D. (2020). Setting up a quantitative SPECT imaging network for a European multi-centre dosimetry study of radioiodine treatment for thyroid cancer as part of the MEDIRAD project. EJNMMI Physics, 7(1). https://doi.org/10.1186/s40658-020-00332-9

Teker, F., & Elboga, U. (2021). Is SUVmax a useful marker for progression-free survival 177 in patients with metastatic GEP-NET receiving Lu-DOTATATE therapy? In Hell J Nucl Med (Vol. 24, Issue 2). www.nuclmed.gr

Thuillier, P., Maajem, M., Schick, U., Blanc-Beguin, F., Hennebicq, S., Metges, J. P., Salaun, P. Y., Kerlan, V., Bourhis, D., & Abgral, R. (2021). Clinical Assessment of 177Lu-DOTATATE Quantification by Comparison of SUV-Based Parameters Measured on Both Post-PRRT SPECT/CT and 68Ga-DOTATOC PET/CT in Patients with Neuroendocrine Tumors: A Feasibility Study. Clinical Nuclear Medicine, 46(2), 111–118. https://doi.org/10.1097/RLU.0000000000003412

Tran-Gia, J., & Lassmann, M. (2019). Characterization of Noise and Resolution for Quantitative ^{177}Lu SPECT/CT with xSPECT Quant. Journal of Nuclear Medicine, 60(1), 50–59. https://doi.org/10.2967/jnumed.118.211094

van Gils, C. A. J., Beijst, C., van Rooij, R., & de Jong, H. W. A. M. (2016). Impact of reconstruction parameters on quantitative I-131 SPECT. Physics in Medicine and Biology, 61(14), 5166–5182. https://doi.org/10.1088/0031-9155/61/14/5166

van Gils, K., Brinks, P., Lavalaye, J., Verberne, H. J., & Habraken, J. B. A. (2017). A method to measure the absorbed dose of the thyroid during I-131 therapy, using a collar detector system and a SPECT acquisition. Medical Physics, 44(10), 5450–5456. https://doi.org/10.1002/mp.12472

Velikyan, I. (2014). Radionuclides for Imaging and Therapy in Oncology. In Wong SXiaoyuan Chen & Stephen Wong (Eds.), Cancer Theranostics (pp. 285–325). Elsevier.

Velikyan, I., Sundin, A., Sörensen, J., Lubberink, M., Sandström, M., Garske-Román, U., Lundqvist, H., Granberg, D., & Eriksson, B. (2014). Quantitative and qualitative intrapatient comparison of 68Ga-DOTATOC and 68Ga-DOTATATE: net uptake rate for accurate quantification. Journal of Nuclear Medicine: Official Publication, Society of Nuclear Medicine, 55(2), 204–210. https://doi.org/10.2967/jnumed.113.126177

Verburg, F. A., Hänscheid, H., Biko, J., Hategan, M. C., Lassmann, M., Kreissl, M. C., Reiners, C., & Luster, M. (2010). Dosimetry-guided high-activity 131I therapy in patients with advanced differentiated thyroid carcinoma: Initial experience. European Journal of Nuclear Medicine and Molecular Imaging, 37(5), 896–903. https://doi.org/10.1007/s00259-009-1303-x

Verburg, F. A., Luster, M., Giovanella, L., Lassmann, M., Chiesa, C., Chouin, N., & Flux, G. (2017). The "reset button" revisited: why high activity 131I therapy of advanced differentiated thyroid cancer after dosimetry is advantageous for patients. European Journal of Nuclear Medicine and Molecular Imaging, 44(6), 915–917. https://doi.org/10.1007/s00259-017-3649-9

Vergnaud, L., Giraudet, A.-L., Moreau, A., Salvadori, J., Imperiale, A., Baudier, T., Badel, J.-N., & Sarrut, D. (2022). Patient-specific dosimetry adapted to variable number of SPECT/CT time-points per cycle for ^{177}Lu-DOTATATE therapy. EJNMMI Physics, 9(1), 37. https://doi.org/10.1186/s40658-022-00462-2

Wadsley, J., Gregory, R., Flux, G., Newbold, K., Du, Y., Moss, L., Hall, A., Flanagan, L., & Brown, S. R. (2017). SELIMETRY—a multicentre I-131 dosimetry trial: a clinical perspective. The British Journal of Radiology, 90(1073), 20160637. https://doi.org/10.1259/bjr.20160637

Wahl, R. L., Jacene, H., Kasamon, Y., & Lodge, M. A. (2009). From RECIST to PERCIST: Evolving considerations for PET response criteria in solid tumors. In Journal of Nuclear Medicine (Vol. 50, Issue SUPPL. 1). https://doi.org/10.2967/jnumed.108.057307

Wang, X., Li, X., & Ren, Y. (2016). Radionuclide imaging and treatment of thyroid cancer. Frontiers in Bioscience, 21(6), 4449. https://doi.org/10.2741/4449

Willegaignon, J., Stabin, M. G., Guimar??es, M. I. C., Malvestiti, L. F., Sapienza, M. T., Maroni, M., & Sordi, G.-M. A. A. (2006). Evaluation Of the Potential Absorbed Doses From Patients Based On Whole-Body 131i Clearance In Thyroid Cancer Therapy. Health Physics, 91(2), 123–127. https://doi.org/10.1097/01.HP.0000206041.25242.c0

Willowson, K. P., Eslick, E., Ryu, H., Poon, A., Bernard, E. J., & Bailey, D. L. (2018). Feasibility and accuracy of single time point imaging for renal dosimetry following 177 Lu-DOTATATE ('Lutate') therapy. EJNMMI Physics, 5(1). https://doi.org/10.1186/s40658-018-0232-9

Willowson, K. P., Ryu, H., Jackson, P., Singh, A., Eslick, E., & Bailey, D. L. (2018). A Comparison of 2D and 3D Kidney Absorbed Dose Measures in Patients Receiving 177Lu-DOTATATE. Asia Oceania Journal of Nuclear Medicine & Biology, 6(2), 113–119. https://doi.org/10.22038/aojnmb.2018.26105.1182

Yang, J., Kan, Y., Ge, B. H., Yuan, L., Li, C., & Zhao, W. (2014). Diagnostic role of Gallium-68 DOTATOC and Gallium-68 DOTATATE PET in patients with neuroendocrine tumors: a meta-analysis. Acta Radiologica, 55(4), 389–398. https://doi.org/10.1177/0284185113496679

Zaidi, Habib. (2005). Quantum analysis in nuclear medicine imaging. Springer.

Zaknun, J. J., Bodei, L., Mueller-Brand, J., Pavel, M. E., Baum, R. P., Hörsch, D., O'Dorisio, M. S., O'Dorisiol, T. M., Howe, J. R., Cremonesi, M., & Kwekkeboom, D. J. (2013). The joint IAEA, EANM, and SNMMI practical guidance on peptide receptor radionuclide therapy (PRRNT) in neuroendocrine tumours. In European Journal of Nuclear Medicine and Molecular Imaging (Vol. 40, Issue 5, pp. 800–816). Springer Verlag. https://doi.org/10.1007/s00259-012-2330-6

Zhang, H., Tian, M., Carrio, I., Civelek, A. C., & Fujibayashi, Y. (2015). Molecular Image-Guided Theranostic and Personalized Medicine 2014. BioMed Research International, 2015, 1–2. https://doi.org/10.1155/2015/258612

Zhang, J., Song, Q., Cai, L., Xie, Y., & Chen, Y. (2020). The efficacy of 177Lu-DOTATATE peptide receptor radionuclide therapy (PRRT) in patients with metastatic neuroendocrine tumours: a systematic review and meta-analysis. Journal of Cancer Research and Clinical Oncology, 146(6), 1533–1543. https://doi.org/10.1007/s00432-020-03181-2

Zhao, W., Esquinas, P. L., Frezza, A., Hou, X., Beauregard, J. M., & Celler, A. (2019). Accuracy of kidney dosimetry performed using simplified time activity curve modelling methods: A 177Lu-

DOTATATE patient study. Physics in Medicine and Biology, 64(17). https://doi.org/10.1088/1361-6560/ab3039

Zhao, W., Esquinas, P. L., Hou, X., Uribe, C. F., Gonzalez, M., Beauregard, J.-M., Dewaraja, Y. K., & Celler, A. (2018). Determination of gamma camera calibration factors for quantitation of therapeutic radioisotopes. EJNMMI Physics, 5(1), 8. https://doi.org/10.1186/s40658-018-0208-9

Zhu, W., Cheng, Y., Wang, X., Yao, S., Bai, C., Zhao, H., Jia, R., Xu, J., & Huo, L. (2020). Head-to-Head Comparison of [68] Ga-DOTA-JR11 and [68] Ga-DOTATATE PET/CT in Patients with Metastatic, Well-Differentiated Neuroendocrine Tumors: A Prospective Study. Journal of Nuclear Medicine, 61(6), 897–903. https://doi.org/10.2967/jnumed.119.235093

Zidan, J., Hefer, E., Iosilevski, G., Drumea, K., Stein, M. E., Kuten, A., & Israel, O. (2004). Efficacy of i131 ablation therapy using different doses as determined by postoperative thyroid scan uptake in patients with differentiated thyroid cancer. International Journal of Radiation Oncology*Biology*Physics, 59(5), 1330–1336. https://doi.org/10.1016/j.ijrobp.2004.01.036

Zimmerman, B. E., Grošev, D., Buvat, I., Coca Pérez, M. A., Frey, E. C., Green, A., Krisanachinda, A., Lassmann, M., Ljungberg, M., Pozzo, L., Quadir, K. A., Terán Gretter, M. A., van Staden, J., & Poli, G. L. (2017). Multi-centre evaluation of accuracy and reproducibility of planar and SPECT image quantification: An IAEA phantom study. Zeitschrift Für Medizinische Physik, 27(2), 98–112. https://doi.org/10.1016/j.zemedi.2016.03.008